Photonic solutions towards optical waveform synthesis

Couny, Francois

Award date:
2008

Awarding institution:
University of Bath

Photonic Solutions towards Optical Waveform Synthesis

submitted by

François Couny

for the degree of Doctor of Philosophy

of the

University of Bath

Department of Physics

January 2008

ABSTRACT

This thesis presents the development of photonic tools towards the realisation of an optical intensity waveform synthesiser and of an attosecond pulse synthesiser based on the generation and Fourier synthesis of a continuous-wave coherent spectral comb spanning more than 3 octaves (UV to mid-IR) by use of a gas-filled hollow core photonic crystal fibre (HC-PCF).

Towards these long-term goals, two types of HC-PCF are developed. The first fibre is the well-established photonic band gap hollow core fibre offering a low optical loss over a narrow frequency range. The second fibre is the large-pitch Kagomé hollow core fibre, whose unusual guidance mechanism and remarkable ultra-broadband transmission characteristics are identified here.

In anticipation to integrating the proposed synthesiser in a compact, all-fibre system, a photonic "micro-cell" is developed, utilising the exceptional ability of the fibre to confine light and gas in a micrometer-scale hollow core over a long interaction length with low optical loss. Gas loading and hermetic splicing techniques are implemented to create portable and highly efficient gas-laser devices.

In addition, the thesis reports on new experimental approaches leading to the identification of the resonators responsible for the guidance in photonic band gap hollow core fibre.

Finally, the compact and highly efficient photonic micro-cells based on H_2-filled photonic band gap fibres are demonstrated to lower the threshold of stimulated Raman scattering with both pulsed and continuous-wave lasers, leading to the realisation of the first single-pass gas-fibre Raman laser with a single-frequency output and 50% conversion efficiency. An outstanding property of these gas-filled HC-PCF is that they can be designed to maintain the highly-coherent transient regime of amplification even for ultra-long interaction times. As a result, gas-laser devices based on H_2-filled large-pitch Kagomé fibre have been demonstrated to generate and guide a multi-octave frequency comb via higher-order Raman scattering using low power, nanosecond laser pulses.

PREFACE

At the heart of the emerging atto-science is a desire to study and control ultra-fast physical and chemical processes. This new endeavour generates new scientific and engineering challenges as it requires the creation of new, ultra-fast tools that can only belong to the realm of photonics science. The keystone to this technology is the ability to harvest ultra-short, shaped laser light bursts. Methods based on High Harmonic Generation (HHG) have already demonstrated attosecond (10^{-18}s) compression of femtosecond (10^{-15}s) pulses through the generation of a phase-locked optical frequency comb. However, the high demand on laser power and engineering difficulties of this technique means that new routes are being explored. One of these routes consists of coherently and adiabatically driving a Raman active medium by the use of two high power lasers. The resulting Raman sidebands have been shown to exhibit similar properties than those obtained via HHG, though with a much lower non-linear threshold and less strain on the experimental procedure. In an effort to further this research, F. Benabid proposed that these recent developments could be combined with breakthroughs in the technology of hollow core photonic crystal fibres (HC-PCF) to successfully develop compact and self-contained photonic solutions operating in the continuous wave (CW) regime that would lead to the synthesis of arbitrary optical intensity waveforms, including attosecond pulses. Prior to the realisation of the synthesiser, a series of technological milestones, presented in this thesis, needs to be reached.

The proposed photonic solutions required to create the waveform synthesiser are based on the exploitation of the unique properties offered by the HC-PCF, as presented in Chapter 1. A HC-PCF consists of a micrometer-scale air-hole surrounded by a photonic crystal cladding formed by hundreds of capillaries running along the length of the fibre that confine the light tightly inside the core by photonic band gap within a limited optical bandwidth. The low optical attenuation achieved in these fibres allows highly efficient non-linear interactions to take place between a gas trapped inside the hollow core and a laser radiation propagating along the fibre. A gas-filled HC-PCF could then be used for stimulated Raman scattering (SRS) at ultra-low light power in the CW regime and for generating the coherent frequency comb required for the realisation of the synthesiser via the process of coherent SRS.

The ever increasing interest for these hollow-core fibres means that their development has advanced at a great pace over recent years. However, a more profound understanding of the fibre's guidance mechanism is still required to control the fibre properties and tailor them for gas-laser applications. Of particular interest is any physical insight that could be gained regarding the optimization of its transmission bandwidth and the removal of unwanted modes guided in the cladding structure instead of the hollow core region. This understanding can be explored by devising experiments to look at the photonic metrology of this type of fibre. In Chapter 2, the experimental direct visualisation of the photonic band gap and the study of the peculiar propagation of Bloch modes in the fibre's photonic crystal cladding shed light on the origin of the photonic band gap effect and open new routes toward optimizing HC-PCF for non-linear interaction such as Raman scattering.

Another, more practical, challenge resides in the preparation of gas-filled HC-PCF for such non-linear experiments. Indeed, the gas filling process and the realisation of an all-fibre gas-filled HC-PCF micro-cell to be used as a compact, highly efficient non-linear device pose several engineering difficulties. Chapter 3 describes the challenging preparation of micro-cells with high internal gas pressure or at vacuum pressure, as well as the solutions adopted for creating such devices.

The central part of this thesis is composed of 3 chapters concerning the study of stimulated Raman scattering in H_2-filled HC-PCF. Chapter 4 contains the theoretical work that was developed concurrently to the reported experiments of chapter 5. Particular care is taken to study the modified Raman linewidth and Raman gain arising from the tight confinement of the gas trapped between the core walls. The extreme efficiency of HC-PCF gas cell as a Raman amplifier is demonstrated by a series of experiments where ultra-low threshold SRS is achieved with an ultra-high conversion efficiency from the pump laser radiation to the Raman lines. For the first time, these micro-cells give access to ultra-long nanosecond pulses for Raman amplification in the transient regime, maintaining a high degree of molecular coherence, previously limited to pulses shorter than the Raman dephasing time. Further work presented in Chapter 6 describes the realisation of a CW gas-fibre Raman laser in a single pass configuration with 99.99% of the output power at the Stokes frequency and 50% conversion efficiency. This laser is the first of the building blocks towards the optical synthesiser.

To explore the transient regime of coherent Raman amplification to its full potential and to successfully generate and guide mutually coherent Raman sidebands spanning a broad frequency range, an alternative class of HC-PCF is required that lifts the bandwidth limitation imposed by the photonic band gap fibre. A new type of fibre, based on the large pitch Kagomé-lattice structure, is presented in Chapter 7 as the ideal solution for large frequency comb generation. The identification of a novel guidance mechanism, akin to a photonic Von-Neumann Wigner bound state within a continuum, permits the optimisation of the bandwidth and the fabrication of a fibre with a transmission spectrum spanning nearly 1000THz. This fibre is then used in Chapter 8 for the efficient generation of coherent Raman scattering in the transient regime of Raman scattering. The frequency comb is broader, the pump threshold lower and pulse width longer than previously reported techniques, making it a good contender as an optical synthesiser in the pulsed regime.

The final chapter of the thesis presents an inventory of what is available in the new photonic toolbox based on HC-PCF: a highly efficient CW Raman converter and a fibre that has been demonstrated to generate and guide a broad, coherent frequency comb. The foreseeable prospect of CW Raman sidebands using the tools developed in this thesis is also discussed.

ACKNOWLEDGEMENTS

First and foremost, I would like to thank Dr Fetah Benabid for supporting me throughout these three years during which so much has happened. I believe we have very similar approaches to physics which made working together an enjoyable and enriching experience. The project presented in this thesis called for many skills, from plumbing to quantum optics and Fetah has always been there to support me, both as a supervisor and as a friend (usually over a cup of coffee).

I would like to thank Professor Philip St. J. Russell, for offering me the opportunity to do the PhD in the first place. Without him, I would not have embarked upon this adventure.

I thank the members of the Physics department at the University of Bath. Particularly, I'd like to thank Phil S. Light, who started his PhD with me and with whom I worked on several projects. Phil had an invaluable input on various parts of the work presented here and is also a great friend. I would also like to thank Professors Tim A. Birks and Jonathan C. Knight; Matt Burnett and Stephan Maier for helping with the SNOM experiment presented in Chapter 2; the French connection of the department: Geraud Bouwmans, Nicolas Joly, Georges Humbert, Jean-Marc Rollin, Alexandre Kudlinski, Alexandre Reinhart and Frederic Gérome; and all the great people that I had the privilege to meet and work with during my time at the University of Bath: Georges Kakarantsas, Sergio Leon-Saval, Fabio Biancalana, Greg Antonopoulos, Arismar Cerqueira Sodré Junior and John Pottage, to only cite a few.

This list would not be complete without acknowledging Dr Brian J. Mangan and Dr P. John Roberts, who made an incredible impact on my life as a researcher and as an individual. Most of the fibre modelling work presented throughout this thesis was performed by John and provided critical insight to the experimental work.

Finally, I would like to thank my family for believing in me and for their constant support despite the distance.

This thesis is dedicated to my wife Michelle, who's always there for me and whose support has been amazing throughout the years, and to my daughter Laila.

Contents

List of Figures

List of Tables

Chapter 1

Introduction

This opening chapter first presents the principles behind the guidance mechanisms of hollow core photonic crystal fibre (HC-PCF) and how the fibre's properties make it a perfect platform for gas-laser interaction applications. The second part of the chapter introduces the non-linear optical processes of stimulated Raman scattering (SRS) and coherent Raman sidebands generation in gas-filled HC-PCF that could lead to the future realisation of an optical waveform synthesiser.

1.1 Hollow Core Photonic Crystal Fibre

The development of non-linear and quantum optics applications based on gas-phase material has been impeded by the lack of a suitable technology for creating devices that guide light in a single transverse mode over long interaction lengths while still offering a high level of integration in a practical and compact set-up or device. This constraint meant that gas-phase materials have for a long time been overlooked in favour of their solid-phase counterparts, even for applications where the former outperformed the latter. The recent development of an optical fibre guiding in a hollow air-core, the hollow core photonic crystal fibre (Fig 1.1), lifts these limitations and hold the promise of reviving gas-based applications.

Contrary to the conventional index-guiding optical fibres that guide by total internal reflection (TIR) such as step-index fibres or some solid core photonic crystal fibres, the HC-PCF guidance mechanism is based on a photonic crystal cladding that acts as an

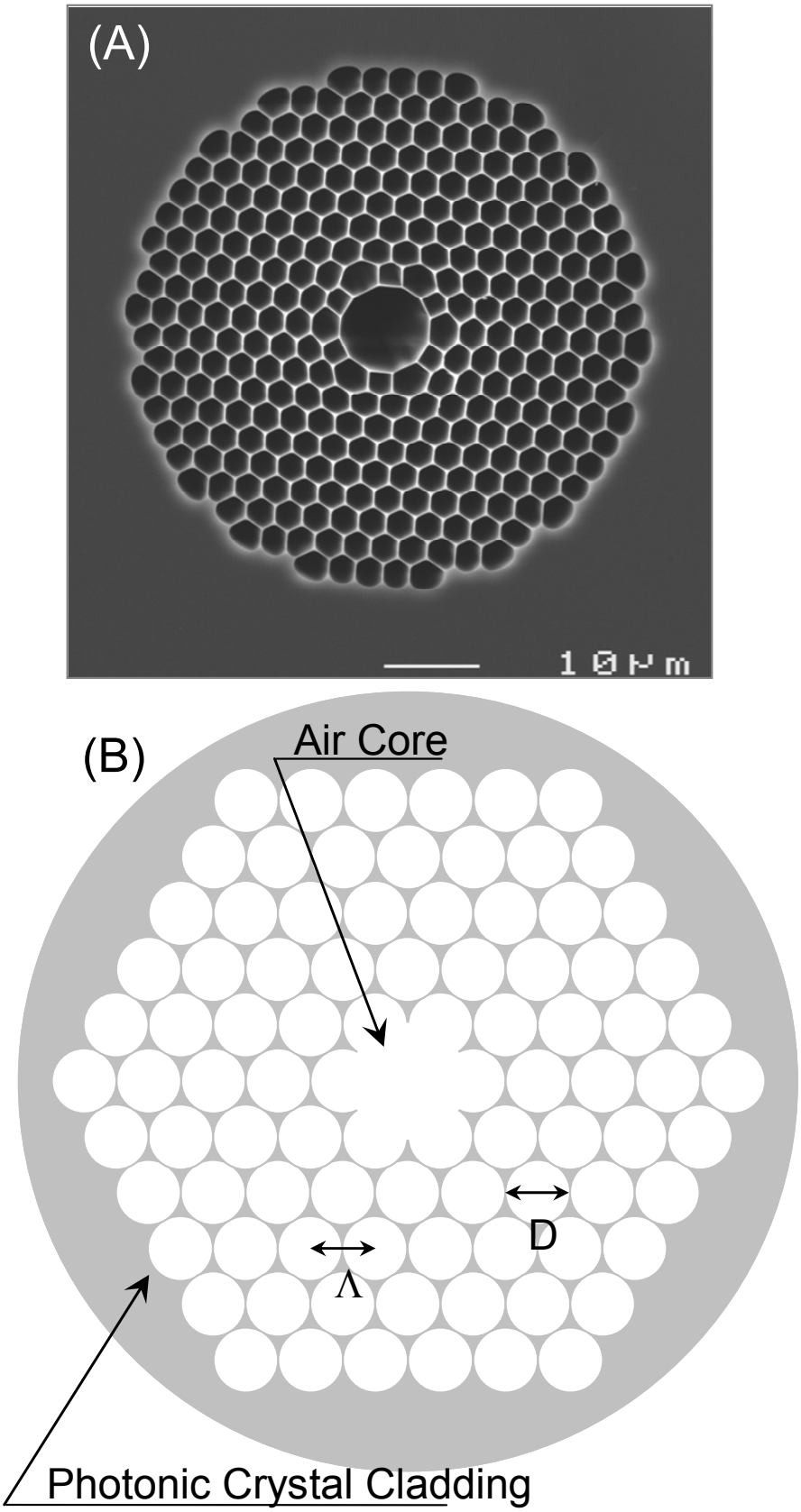

Fig. 1.1 (Top) Scanning electron micrograph of the end face of a fabricated HC-PCF with a triangular arrangement of holes; (Bottom) Schematic representation of the fibre with the definition of the cladding pitch Λ and the diameter D of holes.

effective light barrier surrounding the central core defect (Fig 1.1). In this type of confinement, the refractive index of the fibre core is no longer critical to achieve guidance and light can potentially be guided in an air- or gas-filled core.

This introductory section presents the standard understanding of the photonic band gap effect (PBG). Rapid progress has been made over recent years in explaining fully the complex mechanism behind the guidance. The work presented in Chapter 2 of this thesis played a part in this progress, presenting experimental evidence of the link between the PBG guidance mechanism and the tight binding model of solid state physics.

Moreover, the photonic band gap is not the sole waveguiding mechanism in these hollow core fibres. Indeed, a class of these fibres can also guide light in another, less intuitive way by a process analogous to the Von Neumann-Wigner electronic bound states within a continuum of quantum physics. This novel type of guidance is identified for the first time in this thesis and presented in more details in Chapter 7.

1.1.1 Concept of photonic band gap guidance in HC-PCF

Guidance through an air hole cannot be achieved by total internal reflection as the index of the core would be lower than that of the cladding. Some degree of guidance could be gained by using a capillary, but this process suffers from a very high attenuation [1].

The idea of a hollow core photonic crystal fibre emerged from the suggestion, made by Philip St. J. Russell, that efficient air-core guidance in fibre could be achieved by adding a photonic crystal cladding around the core to confine the light in the air core by mean of out-of-plane photonic band gap [2].

Out of Plane Photonic Band Gap

Until 1991, the hunt for photonic band gaps in photonic crystal structures concentrated on in-plane propagation in periodic dielectric structures with strong refractive index contrast [3,4]. By considering propagation out of the periodic plane for an infinite photonic crystal lattice [5], Birks et al. [6] formally identified specific spectral regions of total exclusion of the light from inside the structure. This was done by casting Maxwell - Helmholtz equation as an eigenvalues problem [7]:

$$\left(\nabla^2 + k^2 n^2\right)h + \nabla\left(\ln n^2\right)\times\left(\nabla\times h\right) = \beta^2 h \tag{1.1}$$

where h is the transverse component of the magnetic field, n represents the dielectric function of the cladding structure, k is the free-space wavenumber, and β is the axial wavenumber component, also called the propagation constant. The generated result is a

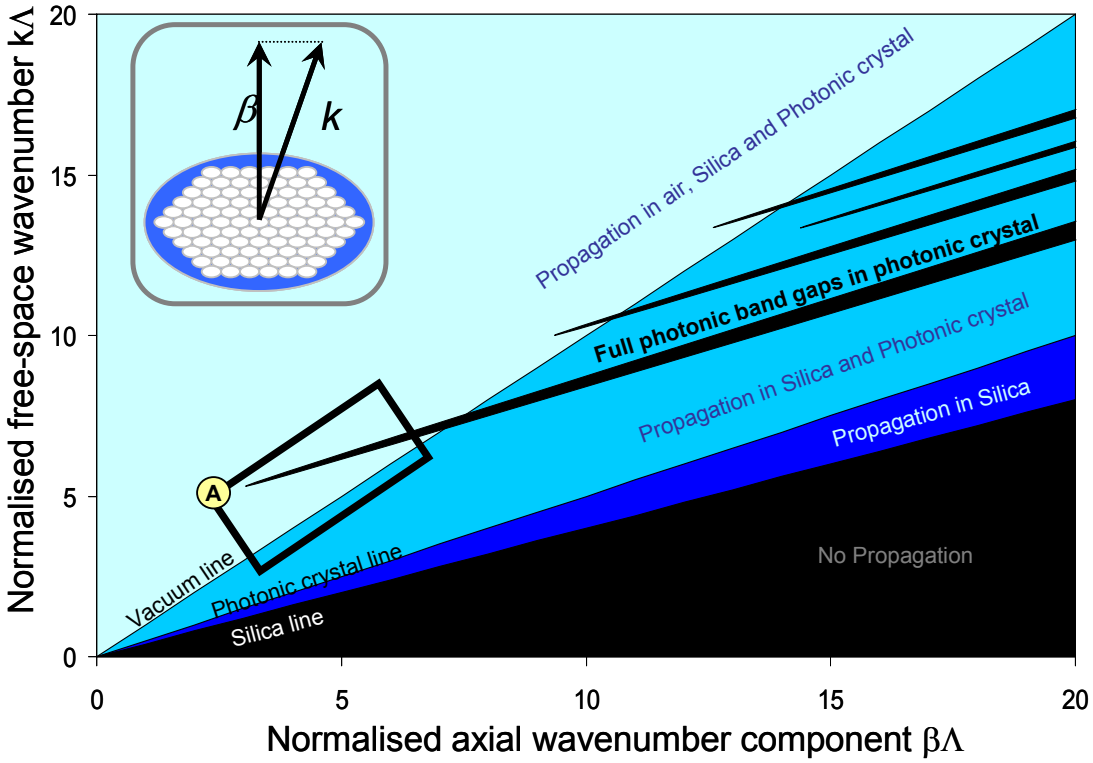

Fig. 1.2 Typical propagation/band diagram of the photonic crystal from [6] (often called "finger" plot) showing regions where propagation is possible in silica, photonic crystal and air; (Inset) Definition of the free-space wavenumber k and its axial component β in this out-of-plane configuration.

propagation diagram of the structure such as the one represented schematically in Figure 1.2 as a function of the dimensionless normalised parameters $k\Lambda$ and $\beta\Lambda$, where Λ is the pitch of the structure (see Fig 1.1). Band gaps, where no solution exists to Eq. (1.1), can open up for ranges of non-zero values of (β,k), mapping out "finger" shaped regions (represented in black in Fig 1.2) where light is excluded from the photonic crystal. This representation illustrates the fruitful crossing of guided optics (propagation diagram) with solid state physics (band gap diagram).

Certain defects in the photonic crystal break the transverse periodicity of the structure and light becomes effectively trapped inside it*. Remarkably, the refractive index of this core defect is less critical than for TIR and can actually be lower than that of the cladding. If one or more of these PBG regions extends above the vacuum dispersion line (air-line, $k=\beta$), air-core guidance becomes possible over a particular frequency range (rectangle A in Fig 1.2). Fortunately, the refractive indices of pure silica and air create

* Providing the defect can accommodate guidance of light at the (β,k) of the PBG

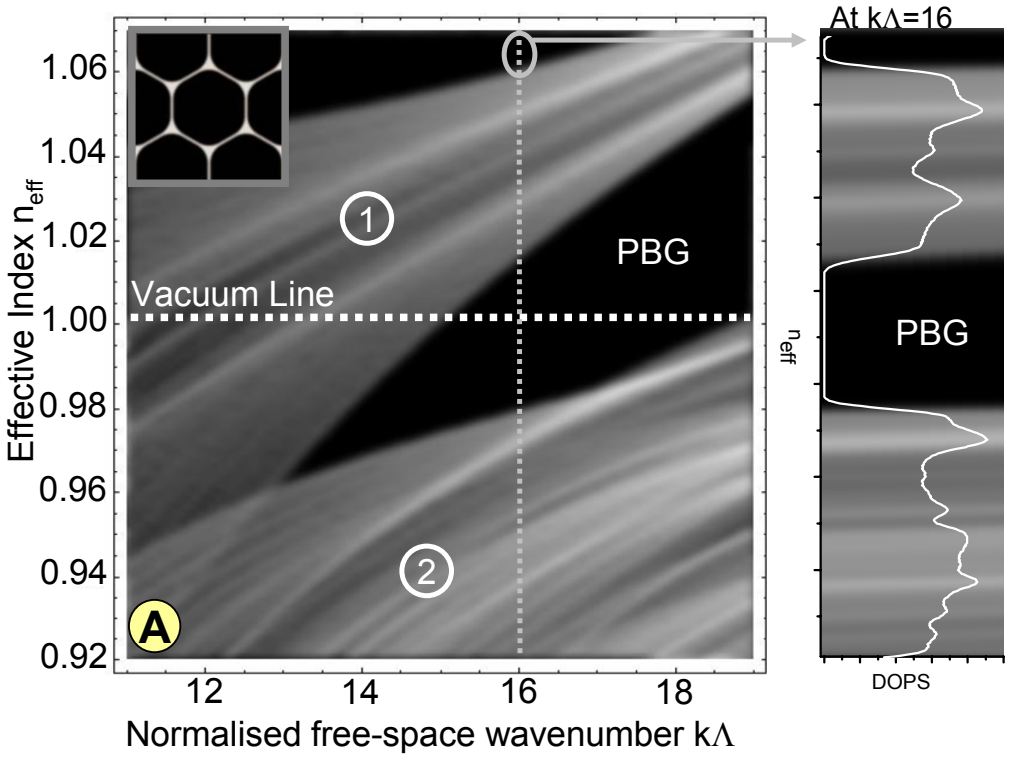

Fig. 1.3 Calculated density of photonic state (DOPS) diagram of an infinite photonic crystal (as represented in the inset) corresponding to rectangle A of Fig 1.2. The photonic band gap (PBG) is surrounded by two regions of high DOPS. Region 1 comes from a class of modes propagating mainly in the glass apices of the structure, while modes from region 2 propagate predominantly in air. (Right) Sample at $k\Lambda$=16 showing the sharp edges of the PBG.

such a favourable concurrence and an air-guiding PBG fibre can be realised with a µm-scale lattice pitch Λ for guidance in the visible and near infra-red ($k\Lambda$<20). The limited bandwidth of the PBG means the structure's pitch need to be adapted in order to guide a particular wavelength range.

Density of Photonic State plots

Conventionally, numerical simulations are limited to finding the photonic band gap regions where Eq. (1.1) possesses no solution. However, more information about the PBG can be gained by representing the density of photonic states (DOPS) of the structure. The DOPS is, by definition, the number of electromagnetic modes per unit cell and per unit length, within the infinitesimal wavenumber and propagation constant range (k, $k+\delta k$) and (β, $\beta+\delta\beta$), respectively [7]. Various software for the resolution of Eq. (1.1), either by the finite element method [8,9] or by the plane wave expansion method [10,11], are now available commercially and generate DOPS plots as in Fig 1.3, calculated for a perfectly

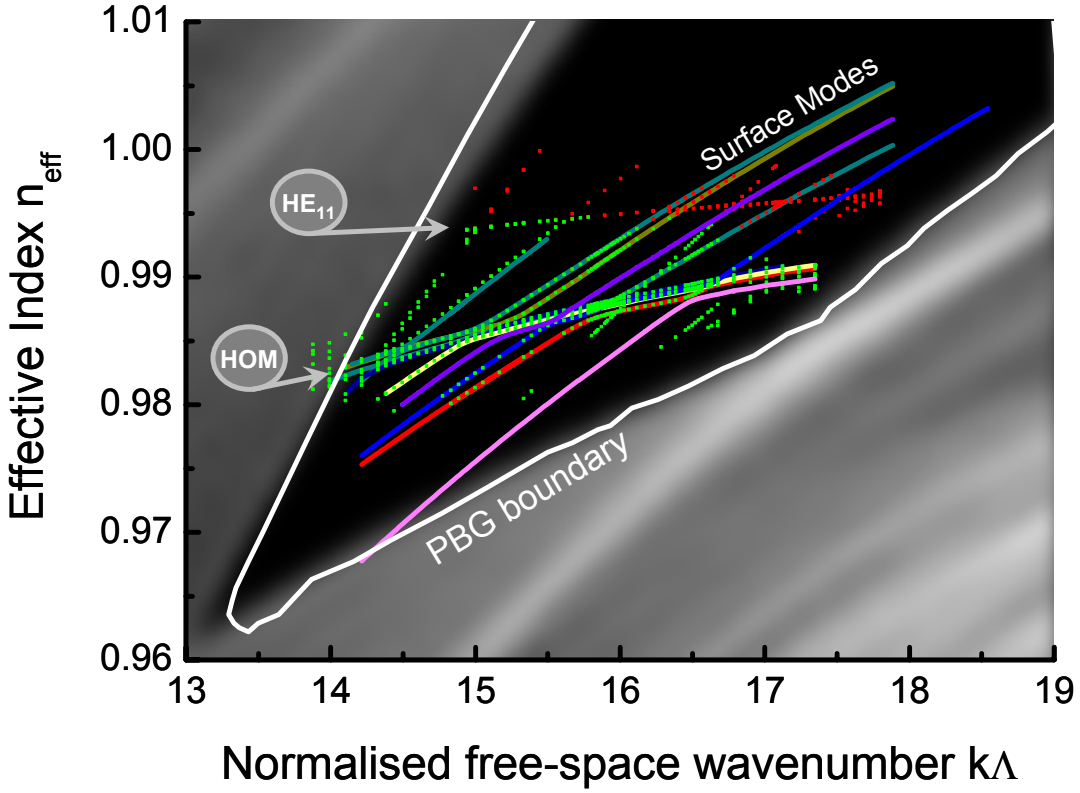

Fig. 1.4 DOPS diagram of the region of the PBG falling below the vacuum line (n_{eff}=1). Inside the PBG, defect-guided modes can be calculated and their trajectories identified using the plane wave method [10]. The trajectory of the core-guided fundamental (HE_{11}) mode and other high order modes (HOM) are identified, as well as surface modes (solid lines). Anti-crossing events between core-guided and surface modes are also observed.

periodic hexagonal cladding with a pitch Λ of 2.15 µm and an air-filling fraction of 92%. The cladding modes supported by the photonic structure add up to form banded regions of high DOPS (bright regions 1 and 2 in Fig 1.3). When the DOPS falls to zero (dark regions in Fig 1.3), light cannot propagate and photonic band gap confinement occurs.

Although quite powerful at giving the position and characteristics of PBG, these methods do not give any insight into the origin of the PBG. Recent theoretical work based on a resonator picture, akin to the tight binding model in solid state physics [12], gives a different approach to the problem of PBG formation [13]. By studying the modes supported by the photonic cladding of a HC-PCF, one can experimentally identify the various resonators participating to the creation of the PBG. Details of how these resonators are identified are presented in Chapter 2 of this thesis.

Modal properties

Light can be guided with low attenuation in an air core defect providing that the photonic crystal cladding exhibits a PBG above the air-line ($n_{eff}<1$) and that the core shape accommodates modes within the range (β,k) of propagation constant of the PBG. For example, air-guidance is achieved in circular core defects with a diameter larger than the pitch of the fibre cladding [14]. Within the PBG, the lowest-order "fundamental"* mode (Fig 1.5A) is the mode with the highest propagation constant β and therefore the closest to the air line (HE_{11} in Fig 1.4). In case of large cores, higher-order air-guided modes (Fig 1.5B, C and E) can propagate at lower n_{eff} (HOM in Fig 1.4). Within the PBG boundaries, the dispersion of these air-guided modes is flatter than that of silica-guided cladding modes, and their trajectory in the DOPS diagram is a near-horizontal line in Fig 1.4, limited on either side by the continuum of modes creating the PBG's edges. Close to these boundaries, the core modes couples to the continuum, leading to high loss and increased dispersion. This effectively limits the operating bandwidth of the hollow core PCF to a narrow range. As a result, the pitch Λ of the fibre's cladding has to be chosen carefully for the fibre to guide at a given wavelength. In addition to this optical bandwidth limitation imposed by the photonic crystal cladding, a further constraint is caused by the interaction of the air-guided modes with surface modes. These modes, called surface mode by analogy to electronic surface states in solid state physics [15], originate at the interface between the photonic crystal cladding and the core defect (Fig 1.5F) [16,17]. Due to the large amount of light propagating in the silica core surround, the dispersion of these modes, represented as solid lines in Fig 1.4, has a steeper slope than the air-core modes and can occasionally intersect with them inside the PBG. If the surface and core mode have the same β and some degree of symmetry and spatial overlap, an "anti-crossing" occurs where the dispersion curves of the modes repel each other (Fig 1.6 and Fig 1.5D), leading to a dramatic increase in the transfer of energy from the core mode to the high attenuation surface mode. These high attenuation regions at the frequency of these anti-crossings further reduce the operational bandwidth and affect the overall transmission of the HC-PCF. It is also interesting to note that these surface modes have two cut-off frequencies and as a consequence cannot be identified as a TIR guiding process.

Light in a HC-PCF can therefore be guided either in the core, in the cladding or in one of the surface modes. More importantly, leakage and energy exchange from one waveguide to another means that a direct observation of the photonic band gap is possible, by simply

* Unlike a conventional waveguide, the real fundamental mode, i.e. the mode with the largest β value is in fact a mode that lies in the cladding, called the space-filling mode and not a core-guided mode. Further details can be found in chapter 2 of this thesis.

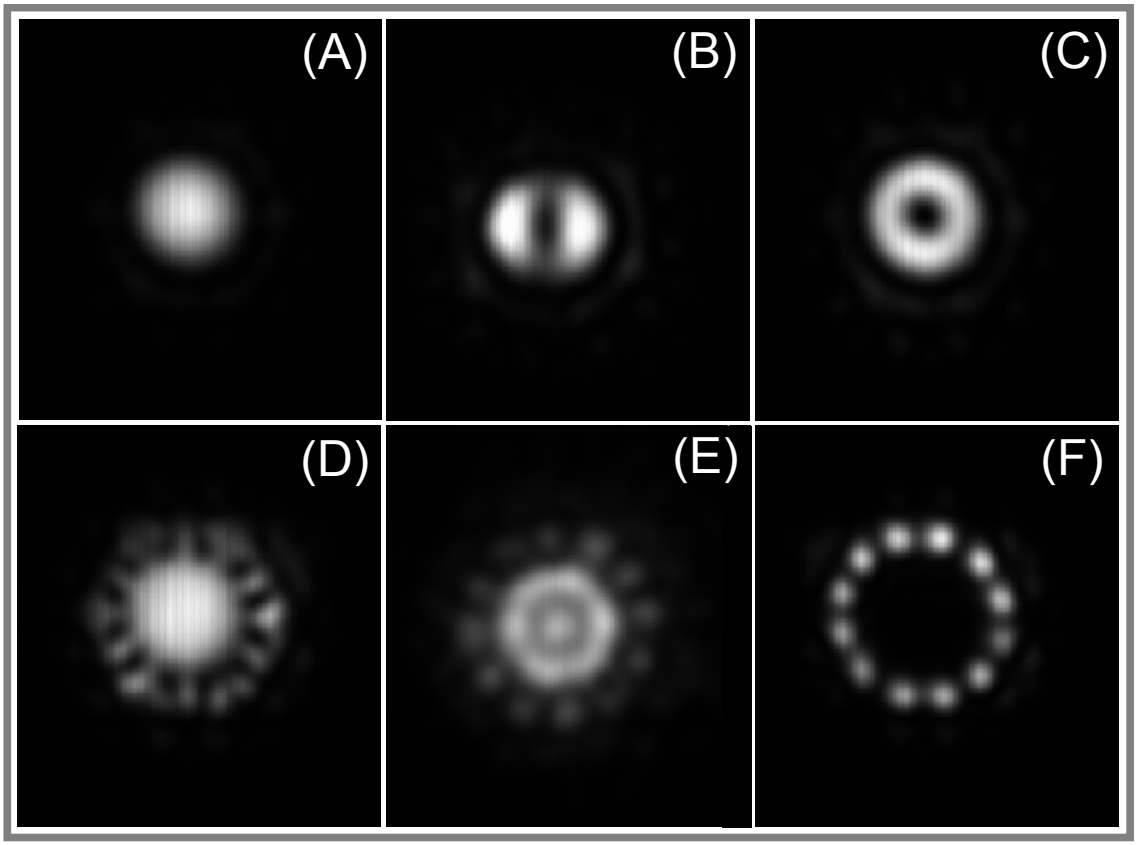

Fig. 1.5 Experimental near-field profiles for a 7 cell defect core HC-PCF guiding at 1300nm. (A) Fundamental mode HE_{11}; (B,C) High order core modes TE_{01} and TE_{01}^{*} respectively; (D) anticrossing between fundamental and surface modes; (E) high order core mode; (F) Surface mode.

collecting the light scattered from the side of the fibre, as presented in Chapter 2 of this thesis. A very good corroboration with the modal properties identified above is obtained, substantiating both the theoretical and experimental results obtained over the past decade regarding photonic band gap guidance.

Evidence of another hollow core wave-guidance mechanism

One can see from the above that guidance is correlated to the absence of photonic states. This correlation, however, seems to fall apart for a certain type of HC-PCF. Indeed, hollow-core fibres with large pitch (i.e. operating at high frequencies $k\Lambda$>50) have been experimentally observed to guide light over an extremely broad optical wavelength range with relatively low attenuation, low dispersion and a surprisingly high light-in-air fraction, even though their calculated DOPS diagram does not exhibit any PBG at these frequencies that would allow air-guidance over such a span.

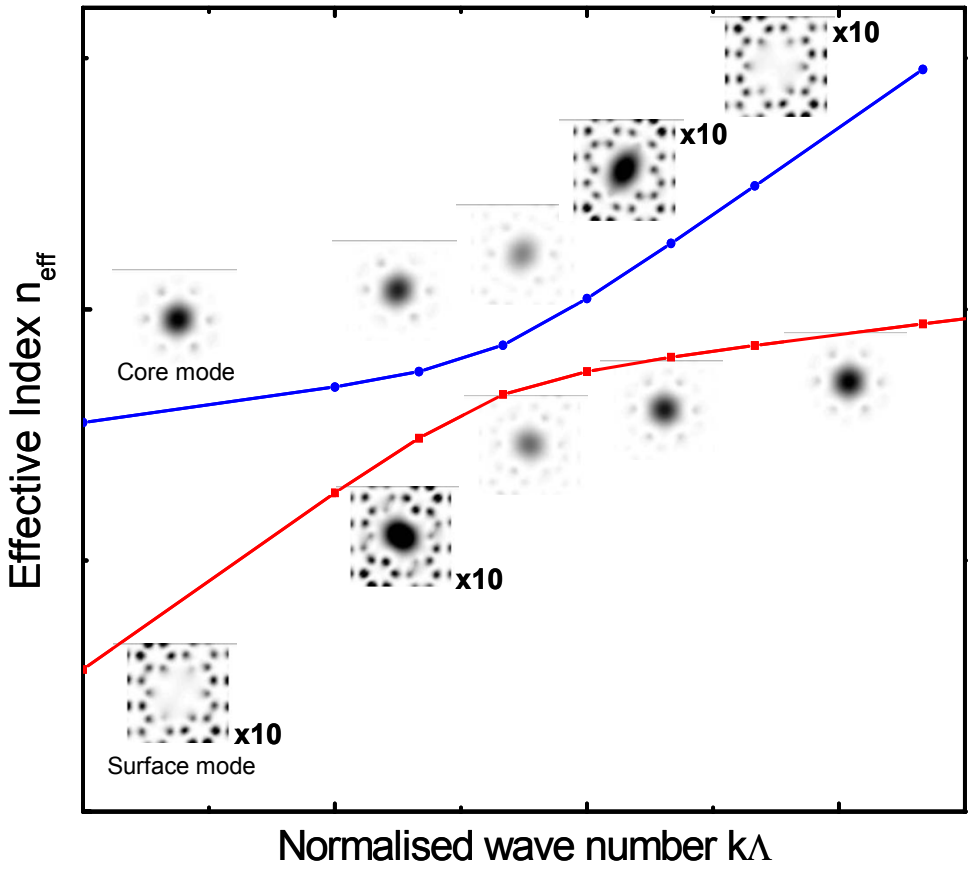

Fig. 1.6 Trajectories of the fundamental core mode and a surface mode as they interact around an anti-crossing event; The large exchange of energy is observed at the point of anti-crossing, leading to a peak in the attenuation spectrum. The intensity of the surface mode is magnified by 10 (x10).

The first observation of this type of guidance was made in 2002 in a Kagomé-structured fibre* [18]. The physical process by which the optical guidance occurs in this fibre remained a mystery for a long time as it was established later that, at the transmission wavelengths, the photonic structure of the Kagomé cladding exhibits a low number of photonic states that would create a degree of mode-hybridization between the hollow-core mode and the cladding modes [19]. Consequently, this observation did not fully explain the dramatic reduction in confinement loss observed in these fibres compared to a simple hollow capillary with the same core diameter and the fibre was disregarded as a potential contender to achieve low loss HC-PCF, especially following the subsequent development of a triangular-lattice HC-PCF exhibiting a full PBG.

* from the Japanese "Kago" *bamboo basket* and "me" *woven pattern*. The cladding is made up of thin parallel sheets of silica that intersect to form a tessalated 'star-of-david' pattern.

Chapter 7 of this thesis presents a new point of view on this photonic guidance mystery. From this change of perspective, a new type of air guidance emerges where the core mode can be thought of as a bound state within a continuum of cladding modes, comparable to bound states predicted by Von-Neumann and Wigner in the early years of quantum physics [20]. The recognition of this new guidance mechanism revives the interest for these atypical fibres and makes possible their optimisation within the framework of ultra-broadband, low-loss guidance.

1.1.2 Fabrication of state-of-the-art HC-PCF

The fabrication method of HC-PCF is based on the "stack and draw" technique that was developed initially for solid-core PCF [21]. The first reported HC-PCF, manufactured in 1999 at the University of Bath using this process, had a loss of about 100dB/m (Fig 1.7A) [14]. Incremental improvements to the fabrication methods (see Fig 1.7B and C) led to today's state-of-the-art HC-PCF based on the honeycomb structure (also called triangular lattice) with a high air-filling fraction cladding [22] and a record minimum loss of 1.2dB/km at 1550nm (Fig 1.8C, D and F) [23]. These fibres are now readily available commercially [24] and their unique properties exploited in an increasing number of scientific and engineering applications requiring air-guidance. Recent progress has also helped improve the Kagomé-lattice HC-PCF (Fig 1.7E and Chapter 7)

Because, in a HC-PCF, only a small fraction of the guided light travels in the glass, bulk material attenuation processes, such as the Rayleigh scattering at short wavelength ($<$450nm) and multi-phonon absorption at long wavelength ($>$2000nm), are dramatically reduced. As a result, one could expect the attenuation of the fibre to be ultimately limited by the Rayleigh scattering of air, well below the current attenuation figures for conventional index-guiding fibre (0.15dB/km, [25]) and solid-core PCF (0.18dB/km [26]). Nevertheless, problems arising from the design and fabrication of these fibres increase considerably this attenuation figure.

For instance, the HC-PCF's cladding needs to be designed with enough rings of holes in the cladding to avoid direct leakage from the core mode. Also, a high air-filling fraction ($>$90%) and the correct aspect ratio between the size of the silica interstitials and the joining struts (Fig 1.7D) [7] will dramatically reduce the portion of air-core fundamental mode field "seeing" the glass and decrease the optical loss of the fibre. Further reduction of this light-in-glass fraction can be achieved by designing a fibre with a large, 19cell defect core instead of the usual 7cells defect [23], and with thick, anti-resonant core boundaries (Fig 1.8D) [27,28]. Unfortunately, a large defect core also accommodate unwanted higher order modes, increasing the micro- and macro-bending loss and the number of surface

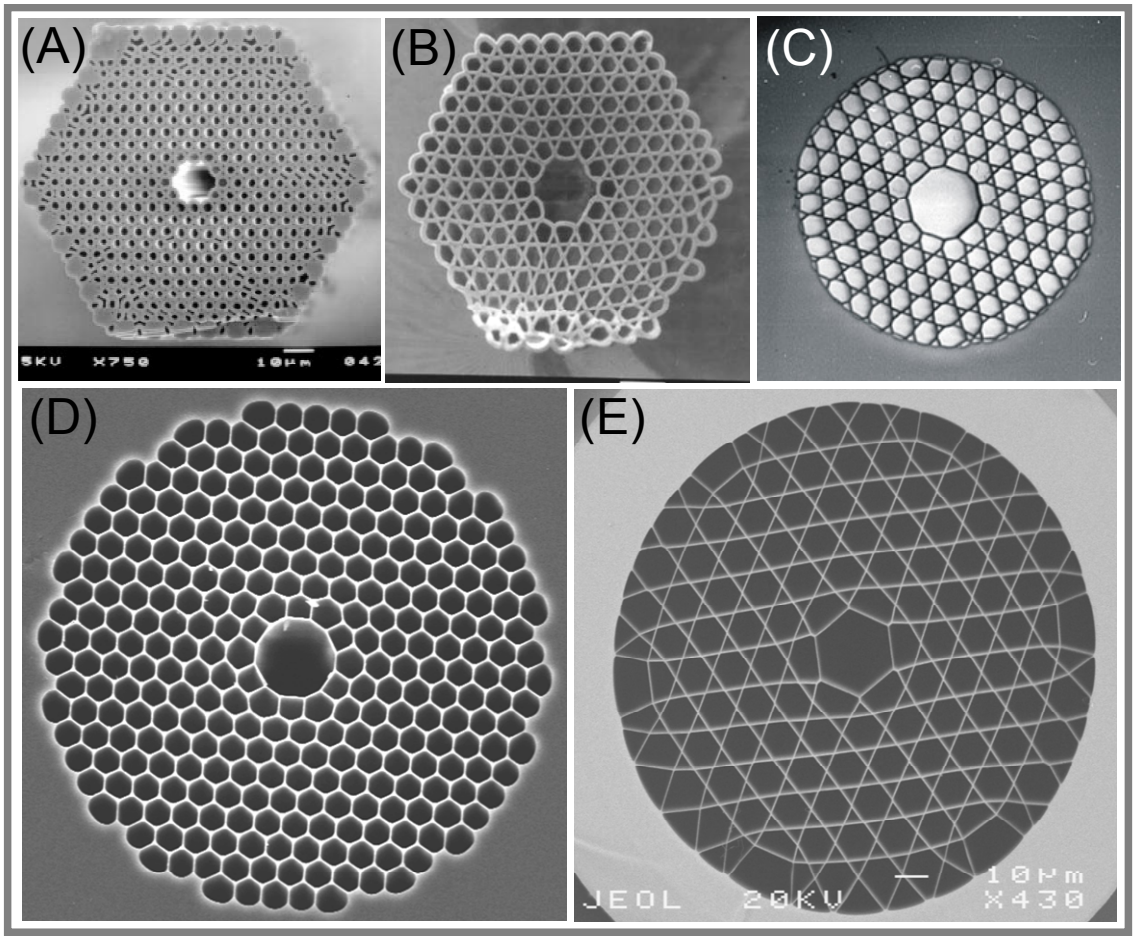

Fig. 1.7 Scanning electron micrographs of (A) the first fibre guiding in a hollow core [14], Improvements to the fabrication technique yield high air-filling fraction fibres such as the Kagomé structured HC-PCF in (B) and (C); (D) State-of-the-art 7-cells photonic band gap HC-PCF guiding at 1550nm (commercially available) and (E) large pitch Kagomé fibre.

modes supported inside the PBG, leading to closely packed "anti-crossing" events within the transmission bandwidth and further limiting the range of low loss guidance (Fig 1.8F). The position of these anti-crossings can however be managed by controlling the shape of the core so that they occur near the edges of the transmission spectrum [28,29].

The main loss mechanism of the low loss regions of the spectrum of the state-of-the-art HC-PCF then arises mainly from the coupling from the air-guided fundamental mode to other, non-guided modes induced by the surface roughness of the air-glass interfaces of the photonic structure. This roughness has its origin in thermally excited surface capillary waves frozen in the fibre during the fabrication process when the glass solidifies [30,31]. The attenuation due to this process evolves as the inverse cube of the operating wavelength (Fig 1.9) instead of the conventional $1/\lambda^4$ Rayleigh scattering dependence found for index-guiding fibres [23] and one would consequently expect that ultra-low loss could be achieved for a fibre operating at a very long wavelength. Unfortunately, due to

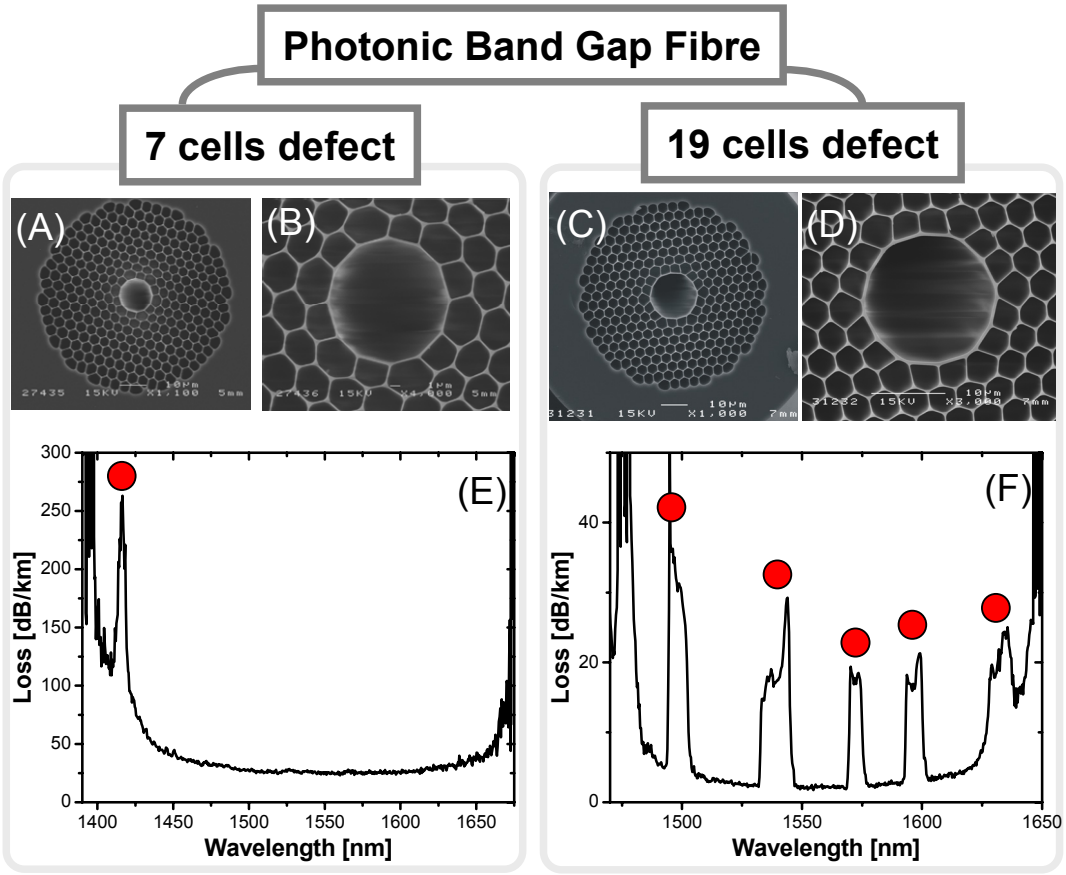

Fig. 1.8 Scanning electron micrographs of the state-of-the-art (A,B) 7-cells HC-PCF and (C,D) 19-cells HC-PCF both guiding at 1550nm. Note the thick, anti-resonant core surround in the 19cells-HC-PCF for a further reduction of the loss. (E) Loss spectrum of the 7cells HC-PCF and (F) of the 19cells HC-PCF showing the limited bandwidth of the fibre's spectrum, further reduced by anti-crossing events, indicated as red dots and creating high loss peaks.

the small but yet significant fraction of the fundamental mode field still propagating in silica, the infra-red absorption loss mechanism will increase the total attenuation in this region of the spectrum.

The current loss record of 1.2dB/km* is very close to the attenuation limit imposed by this surface roughness in this particular type of structure (Fig 1.8F). Such a low loss is ideal for non-linear processes requiring a long interaction length and a small effective area over a narrow bandwidth, like stimulated Raman scattering (see Chapters 4 to 6). It has been suggested that a loss of 0.13dB/km could be achieved at a wavelength of 1900nm [23]. However, this type of fibre would suffer from the same bandwidth limitations as the current low loss HC-PCF, restricted even further by anti-crossing events. As a result, 7cell

* At the time of writing

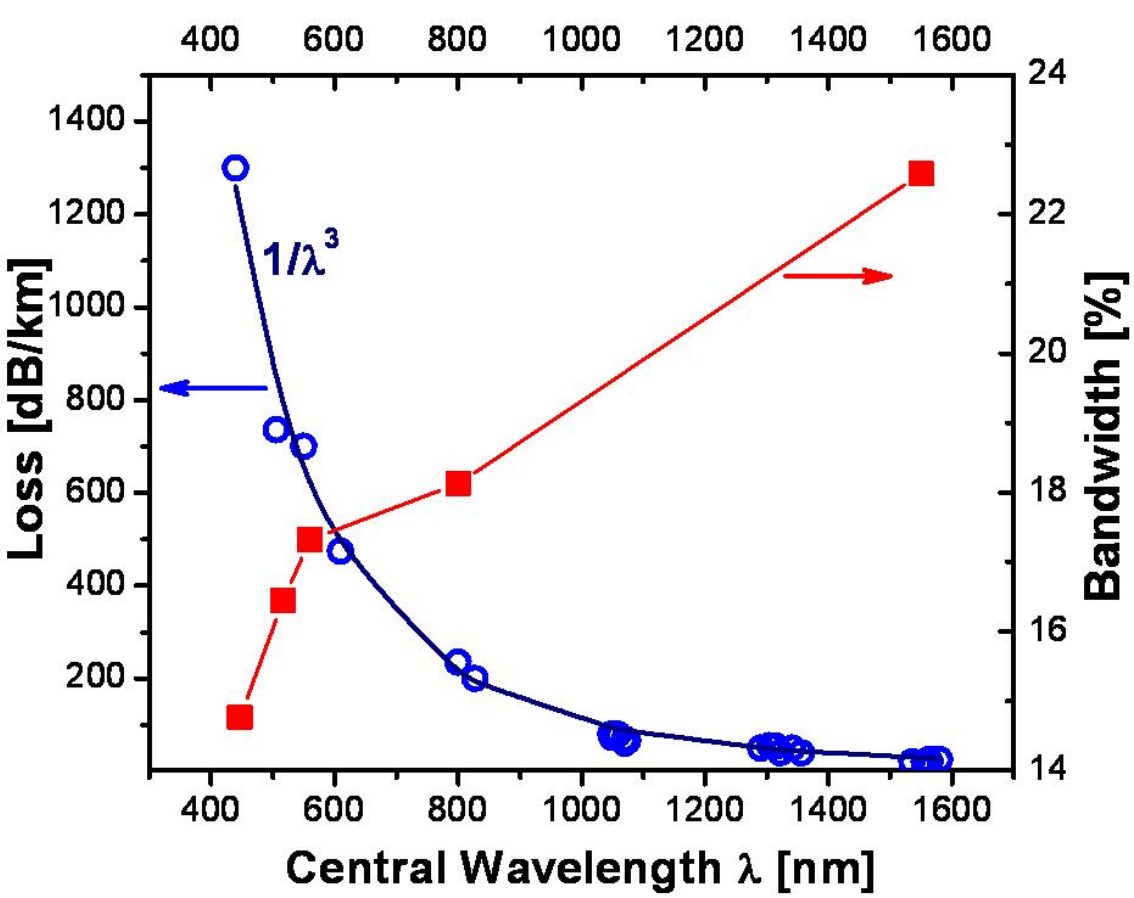

Fig. 1.9 Fibre attenuation (blue circles) and operating bandwidth (red squares) of fabricated HC-PCF as a function of their central operating wavelength. The loss follows a $1/\lambda^3$ evolution (dark blue) instead of the usual Rayleigh scattering ($1/\lambda^4$).

defect core HC-PCF (Fig 1.8A), exhibiting fewer anti-crossings at the expense of an increased attenuation figure, is preferred for the applications presented throughout this thesis.

1.1.3 Gas-laser interactions enhancement with HC-PCF

The key benefit of a gas-filled HC-PCF is that it guides predominantly in its hollow core, thus reducing any detrimental non-linear effects due to silica in favour of an enhancement of the non-linear properties of the gas phase medium. The small effective area and long interaction length of these fibres make them the ideal candidate for the observation of efficient gas-laser interactions.

Figure of merit

Efficient gas-laser interactions require long interaction lengths L_{int} and large laser intensity (energy/cm^2), generally achieved by focusing high power lasers onto a small effective area A_{eff}. A figure of merit (*fom*) of the efficiency of interaction can then be written:

$$fom = \frac{L_{\text{int}}\lambda}{A_{eff}} \tag{1.2}$$

where λ is the optical wavelength of operation and where a high figure of merit corresponds to a strong interaction. A high *fom* is however difficult to realise in free-space (Fig 1.10A) as the effective area A_{eff} cannot be smaller than the beam waist diameter $2\omega_0$, whilst the interaction length $L_{int,beam}$ is limited by the divergence of the focused laser beam, expressed as twice the Rayleigh length:

$$L_{\text{int},beam} = \frac{2\pi\omega_0^{\,2}}{\lambda} \tag{1.3}$$

Additionally, the intensity of the laser is restricted so as to avoid high power non-linearity [32]. The *fom* in this configuration is therefore ~2. Several techniques have been developed to improve this figure of merit. The most efficient so far has been the use of a capillary, also called "hollow fibre" (Fig 1.10B). Not to be confused with the HC-PCF, it is a single silica capillary of diameter a and refractive index n ~1.5 filled with the appropriate gas. The interaction length becomes longer and the *fom* takes the form [18]:

$$fom_{capillary} = \frac{6.8a\sqrt{n^2+1}}{\pi\lambda(n^2-1)} \tag{1.4}$$

The *fom* value is larger than the focused laser beam configuration only for large core diameter and is still limited to being 10 times more efficient than its free-space counterpart (for a 10μm bore radius).

To remedy this problem, and to be able to have small capillary diameters and a long interaction length, one needs to turn to the hollow core PCF technology. As these fibres guide with an attenuation α (in dB/m), their *fom* takes the simple form:

$$fom_{HCPCF} = \frac{\lambda}{a^2\alpha\pi} \tag{1.5}$$

A comparison of the efficiency of the HC-PCF to other systems is given in Fig 1.10C, showing the *fom* versus the bore radius a of the waveguide. The Y-axis gives the $\log[fom/fom_{beam}]$ for a direct comparison of the order of magnitude of the *fom* relative to that of the free-space propagation. A small core HC-PCF yields stronger, more efficient interactions. For example, a HC-PCF with 2dB/km attenuation and a core diameter of 5μm could be 10^6 times more efficient than the free-space focused beam. This fibre creates a new configuration in which non linear optics applications such as Raman scattering are achieved with laser power threshold dramatically lower than conventional techniques [18] and where further study of the regimes of light/matter interaction is possible [33].

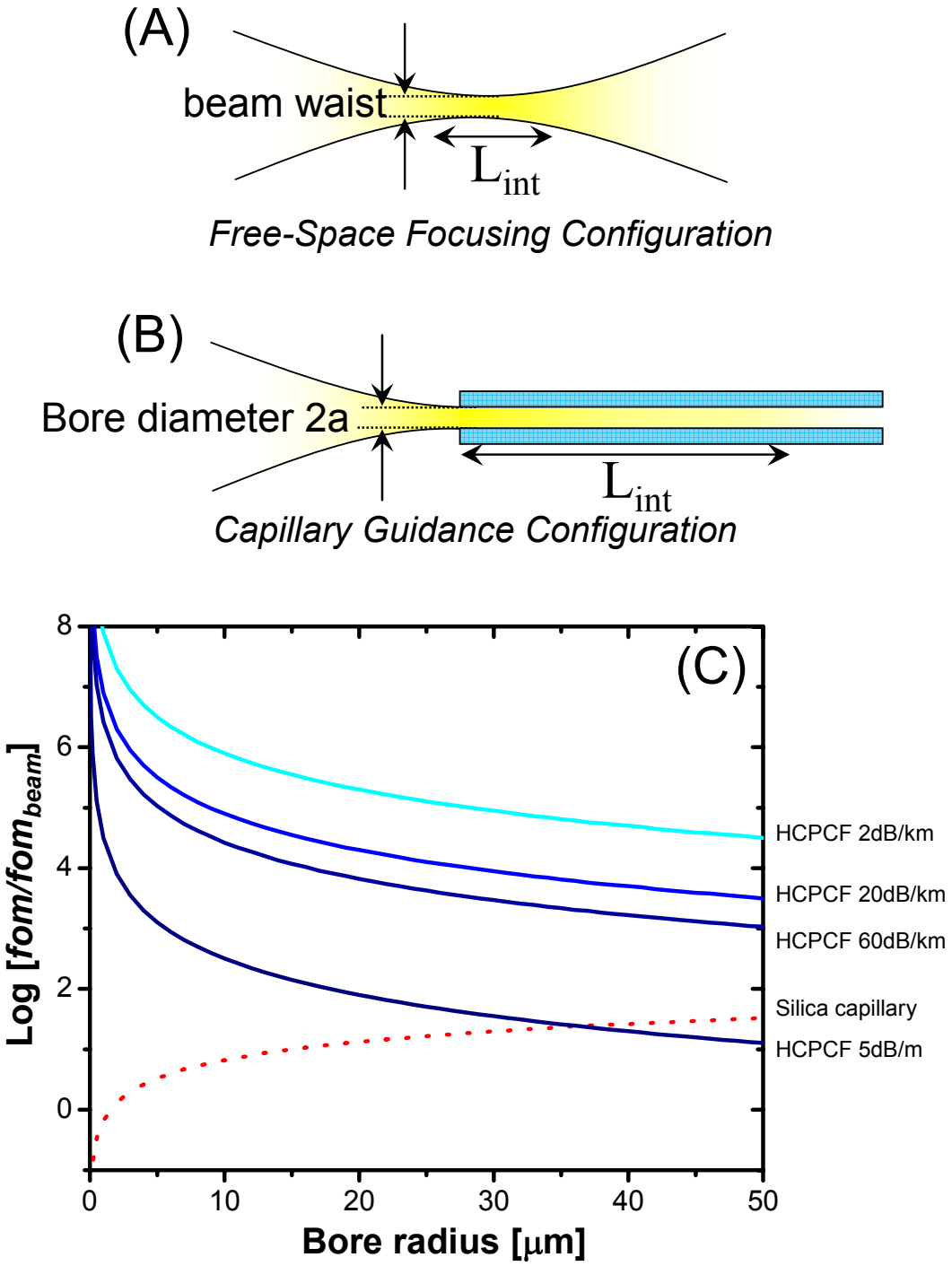

Fig. 1.10 (A) Focused laser beam in free-space configuration and (B) capillary guidance configuration. (C) Figure of merit (*fom*) of capillary guidance (dotted line) and HC-PCF guidance (solid lines) compared to that of the free-space propagation fom_{beam}.

1.2 Stimulated Raman Scattering in HC-PCF

Stimulated Raman scattering (SRS) is the two-photon inelastic scattering of an incident laser beam by the molecular excitation of the Raman medium, resulting in a frequency down-converted (Stokes line), or up-converted (anti-Stokes line) photon shifted from the pump frequency by the Raman transition frequency Ω_R (Fig 1.11) [34,35]. This highly efficient frequency conversion process is now a familiar phenomenon, used for a wealth of applications, including Raman gas lasers [36] and high-resolution spectroscopy [37], or Raman microscopy [38]. A renewed interest in SRS has sprung from the fast optics community motivated by the possibility, under appropriate driving conditions of the medium, of obtaining a large number of mutually coherent high-order Stokes and anti-Stokes fields over a very large frequency span with high efficiency [39]. The coherence and the broadband nature of the spectrum mean that it should be possible to synthesize sub-femtosecond optical pulses.

Stimulated Raman scattering can greatly benefit from the newly developed HC-PCF technology. Firstly, the fibre's high *fom* offers a reduction of the required laser power accompanied by an increase in the conversion efficiency of the Raman system allowing the realisation of compact continuous-wave (CW) Raman gas fibre-lasers (Chapter 6). Secondly, the unusually long interaction length of the fibre offers new excitation conditions for SRS (Chapter 5) ideal for generating broadband frequency coherent combs (Chapter 8). By combining these two properties, HC-PCF could give access to the generation of Raman sidebands in the CW regime.

1.2.1 Regimes of Raman amplification

Historically, the first regime of Raman amplification identified was the spontaneous Raman scattering [40]. It consists of the incoherent and independent scattering of incident photons by the medium and therefore, does not provide an efficient conversion from the pump to the Stokes radiation. When, however, the number of incident and scattered (Stokes) photons becomes large enough, stimulated Raman amplification arises [41]. Depending on the timescale of the interaction, i.e. laser pulse width, and the Raman gain of the medium, the stimulated regime can either be transient or in a steady state of amplification.

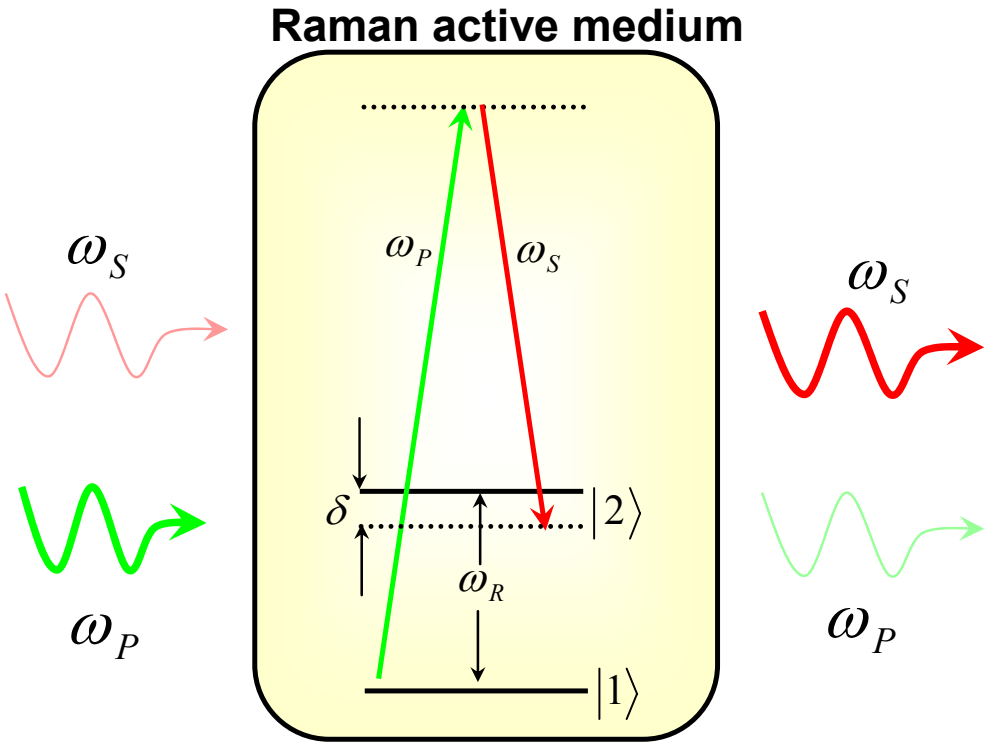

Fig. 1.11 Energy levels diagram for Stokes amplification via stimulated Raman scattering.

Raman scattering in steady-state regime

The stimulated Raman scattering is generally described in a simplified form, as an exponential build-up of the Stokes intensity given by $I_S \propto I_{S0} e^{gz}$ where I_{S0} is the incident Stokes power, z is the propagation length and the net Raman gain g can be expressed as a function of the Raman gain of the medium g_{SS} (in cm/GW) and the pump intensity I_P as $g = g_{SS} I_P$. However, this expression is valid only for laser pulses longer than the characteristic time $\tau_2 \approx T_2 g_{SS} I_P z$ where T_2 is the collisional dephasing time (typically ~100ps) of the medium, where the regime of amplification is in a steady-state [42]. The source of Stokes photons contributing to I_{S0} comes either from an incident laser radiation tuned to the Stokes frequency or from a sufficient number of Stokes photons generated by quantum noise through spontaneous emission. Maximum conversion to the Stokes radiation will therefore be achieved by choosing a Raman medium where both interaction length z and pump laser intensity I_P are as large as possible.

Thanks to its high interaction efficiency, a HC-PCF filled with a Raman active gas will reduce the pump power Raman threshold dramatically. For example, a 1W CW laser propagating through 10m of HC-PCF with a 10µm air-core filled with molecular hydrogen would provide the same amplification as a 10.000W laser in a 10cm long and 100µm large

gas-cell. Under these conditions, the conversion from pump to Stokes radiation can be highly efficient. The HC-PCF-based Raman laser represents an attractive alternative to the technique based on high finesse optical cavity to reduce the Raman threshold [43]. Indeed, the HC-PCF eliminates the engineering inconveniences of such multi-pass devices (poor conversion, cavity locking of the pump laser, limitation on the tenability of the Raman conversion, etc...). A demonstration of this approach is detailed in Chapter 6, where the first CW Raman laser based on an H_2-filled HC-PCF in a single pass configuration is presented.

Furthermore, if it is powerful enough, the converted Stokes radiation can itself serve as a pump for the generation of a second Stokes radiation, shifted further to the red. This can in turn serve for the generation of higher order Stokes lines. In addition, anti-Stokes radiation can be generated via a four wave mixing (FWM) process between two pump photon and one Stokes with $\omega_{AS} = \omega_P + \omega_P - \omega_S$ in case of high pump and Stokes power. Cascaded blue shifted anti-Stokes lines can be produced by further FWM between various components of the spectrum (pump, Stokes and anti-Stokes). However, the cascaded Stokes lines do not share a deterministic phase relationship with the pump. Consequently, the resulting spectrum cannot be recombined for pulse compression or waveform synthesis.

Raman scattering in transient regime

The transient regime of Raman amplification occurs when the laser pulse duration τ is longer than the spontaneous emission time scale τ_1 given by $\tau_1 \approx T_2/g_{SS}I_P z$ and shorter than the steady-state temporal boundary τ_2 [42]. More importantly, it can be noted that the generated Stokes can be phase-locked to the pump laser, so that the higher-order Stokes and anti-Stokes generated in this regime are mutually coherent [44,45]. This spectrum could be qualitatively viewed as the result of the combination of the spontaneously seeded SRS process to produce the first Stokes line, followed by parametric four-wave Raman mixing to produce the higher-order anti-Stokes and Stokes Raman lines [46,47]. Alternatively, the spectral components of higher order SRS spectrum could be viewed as the resultant of a mutual modulation of the molecular coherence and the generated Raman side-band (Chapter 8).

It is demonstrated in chapter 4 and 5 that, thanks to the HC-PCF's unique properties, the transient regime of Raman amplification could be achieved even with long duration pump pulses* (Chapter 4 and 5). This excitation conditions contrast with previously reported results regarding transient Raman amplification, obtained with Giga-Watt power

* Several times longer than T_2

transform-limited laser pulses with pulse width τ smaller than T_2 [44-46]. In chapter 8, a single nanosecond-pulsed laser coupled to a short length of Kagomé lattice HC-PCF is used to generate a broadband coherent spectrum using this new excitation conditions.

This frequency comb generation technique offers an excellent alternative to the state-of-the-art process of high-harmonic generation (HHG) in inert gases, at the heart of the emerging field of attoscience [48] (generating and utilising pulses that last 10^{-18}s). However, in order to create an optical waveform synthesiser with a similar degree of control to what can be achieved today in electronics with function generators; one must operate in the CW regime.

1.2.2 Coherent Raman scattering via molecular modulation

Although a large number of spectral components can be generated in the transient regime of Raman amplification, the method is intrinsically limited to pulsed lasers, even when using HC-PCF. However, the high molecular coherence at the origin of this frequency comb generation can also be achieved in the steady-state regime, opening the prospect of generating mutually coherent Raman sidebands in the CW regime.

Shortly after the discovery of the SRS in masers [49], it was noted by Garmine in 1963 [50] that the cascaded process of multiple-orders Stokes generation could be improved if the molecular oscillations of the Raman medium, driven by the two-photon Rabi frequency Ω_{12} created by the presence of the electromagnetic fields, were coherent enough. It was indeed observed afterward that coherent preparation of the medium not only increased the Raman efficiency, but also the number of phase-locked Raman components [51]. Several methods have now been developed in order to achieve the high molecular coherence required for the generation of ultra-broad frequency combs.

The technique that surfaced as the most promising for achieving high conversion efficiency and ultra-broad spectrum is the one suggested and demonstrated by Harris and co-workers [39] (Fig 1.12). After preliminary work on electromagnetically induced transparency [52], Harris understood that the generation of Raman sidebands, like the transparency process, requires not only the preparation of a molecular medium coherent with the excitation, as suggested by Garmine, but also for the phase of this coherence to adiabatically follow the excitation; i.e. the molecular medium will remain in the same coherent eigenstate as the sidebands are generated. This coherent behaviour, adiabatically driven by two electromagnetic fields, modulates the refractive index of the material, which in turn, generates collinear and mutually coherent sidebands [39,53]. For Raman gases such as H_2 and D_2, the width of the generated frequency comb can be as large as ~2000 THz and can

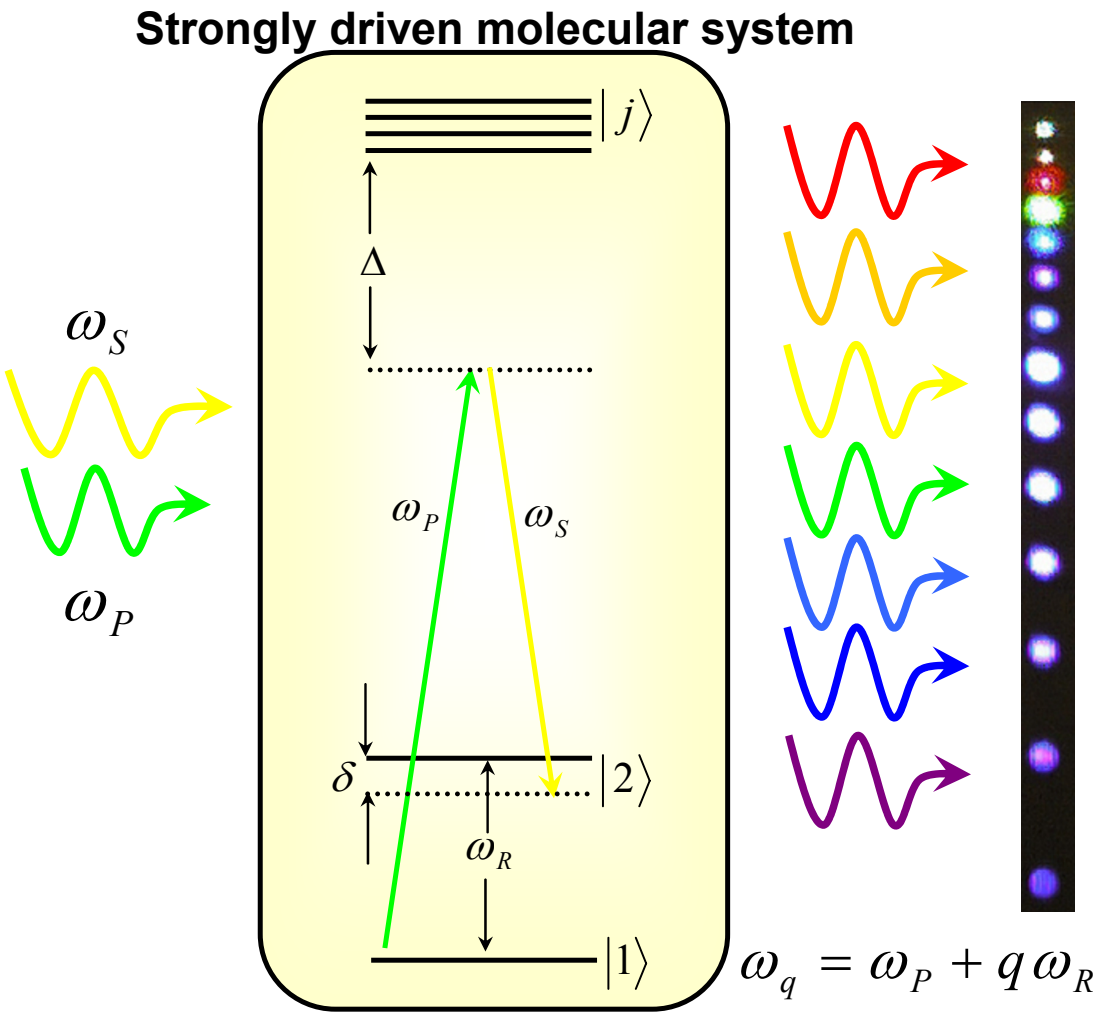

Fig. 1.12 Raman sidebands generation when conditions on coherence and adiabaticity are met. (Right) Typical resulting Raman sidebands in D_2 (from [53])

contain as many as ~200 strong rotational Raman sidebands or ~20 vibrational Raman sidebands. For example, Sokolov and Harris reported generating sidebands spanning from 195nm to 2.94µm of an initial 800nm/1064nm pulse in D_2 [54]. Furthermore, they suggest one could successfully recombine the frequency comb so as to obtain a compressed pulse below 0.7fs [55].

The generation of the coherent frequency comb by this molecular modulation method offer better prospects than the widespread HHG technique. Its most striking feature is its high conversion efficiency, several orders of magnitude higher than currently achieved by HHG [54]. Another interesting aspect of the Raman sideband generation process is that the frequency comb bandwidth and central wavelength are determined by the driving lasers and therefore, are not limited to the XUV/X-ray region of the electromagnetic spectrum as is the case with HHG. Finally and more importantly, even with thermal redistribution

due to population decay, relaxation and coherence dephasing, the mechanism of CW-driven molecular modulation remains efficient.

Interestingly, the conditions on adiabaticity and maximum coherence of the molecular system are fulfilled with a CW laser, providing the pump and Stokes lasers are strong enough to generate the oscillations in the first place. As a result, one could use the CW Raman laser presented in Chapter 6 to achieve efficient CW Raman sidebands generation and as a result, an efficient optical waveform synthesiser.

However, so far, the experimental realisation of such a synthesiser has been achieved either by HHG [56,57] or through molecular modulation [58-60] and limited to ultra-high power pulsed lasers. As a result, it bears more resemblance to pulse shaping (or compression) than to an optical version of the electronic function generator. This restriction could be lifted thanks to the combined small effective area and long interaction length offered by compact photonic micro-cells based on gas-filled HC-PCF. Such fibre-gas cells open the route for the generation of Raman sideband in the CW regime and, for the first time, realistic prospects towards the realisation of an optical waveform synthesiser *à la* electronics.

1.3 Towards an Optical Waveform Synthesiser

The advent of the "electronic era" is owing to the development of an electronic arsenal of compact function generators, transistors and switches, operating at their full potential in the GHz regime. The confluence of the breakthrough technologies of HC-PCF and molecular modulation technique, led Dr Fetah Benabid to propose that a stable and compact optical intensity waveform synthesiser could be created by generating a CW Raman sidebands frequency comb via the molecular modulation of H_2 inside a HC-PCF [61].

This last introductory section presents the principle of operation of the proposed optical synthesiser and the advantage of using HC-PCF for the realisation of the two-pump laser source required for the future generation of phase-locked Raman sidebands.

1.3.1 Principle of waveform synthesis

The principle of operation of an optical waveform synthesiser is similar to the way an electronic function generator operates; via Fourier synthesis. An arbitrary optical waveform can be generated by controlling the phase and amplitude of a set of sinusoidal

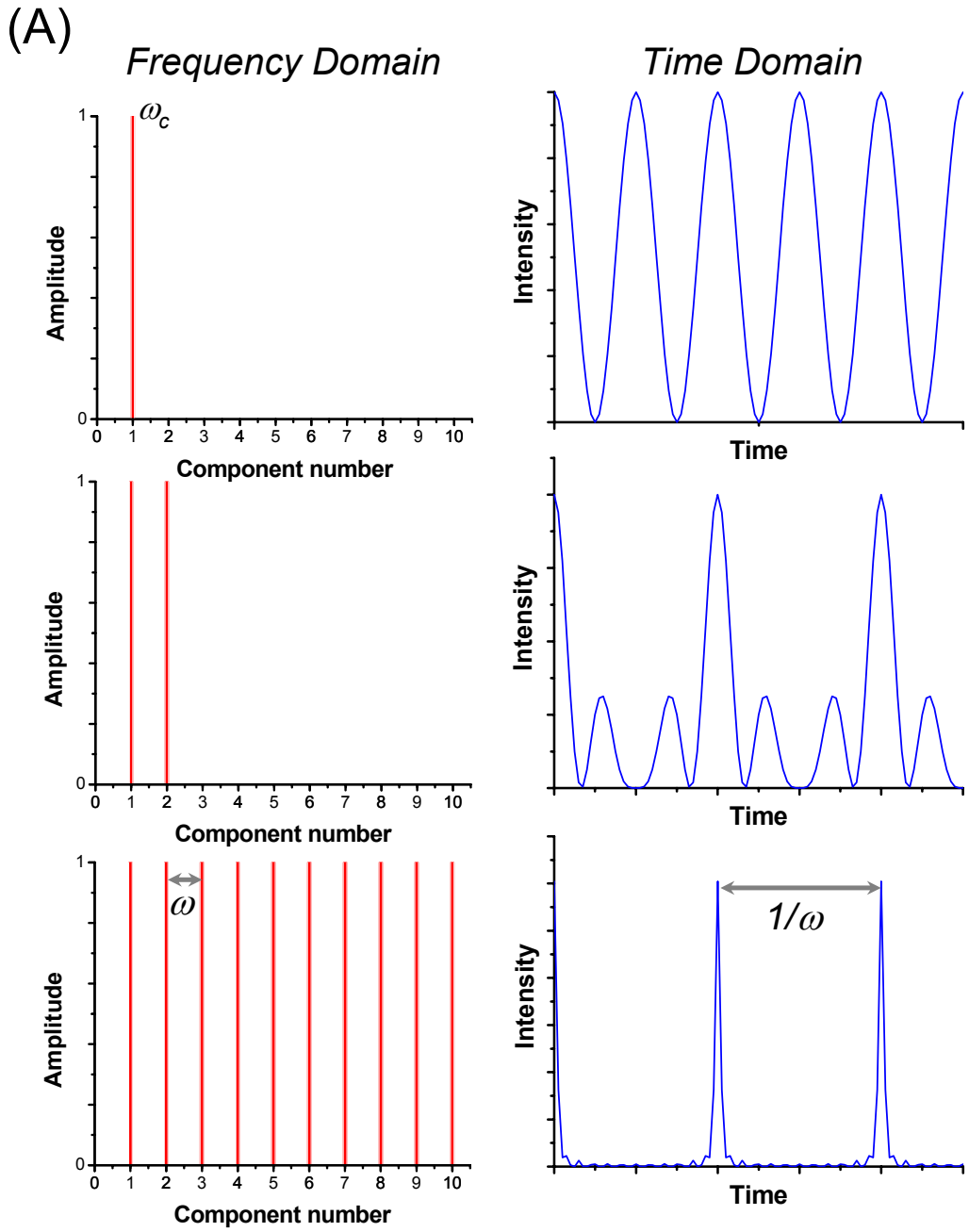

Fig. 1.13 (Left) Frequency and (right) temporal domain representation of a signal containing 1, 2 or 11 components.

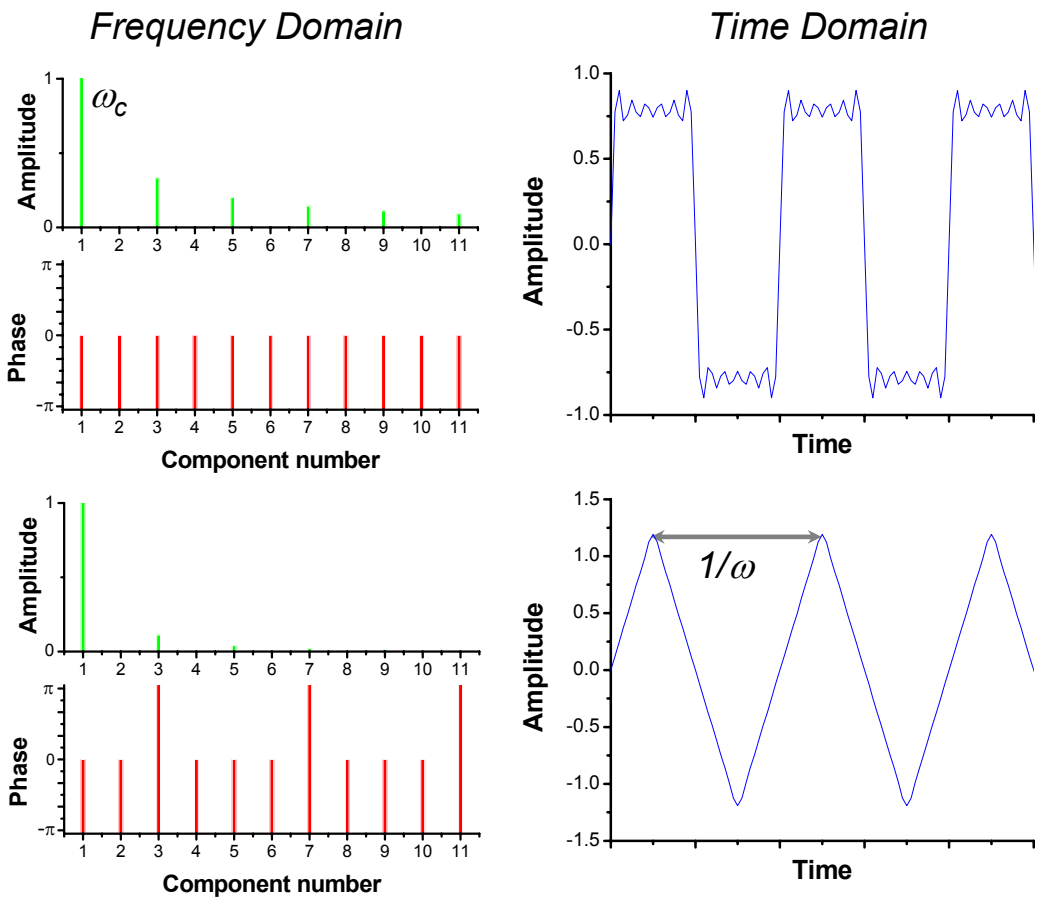

Fig. 1.14 (Left) Frequency and (right) temporal domain representation of (Top) square and (bottom) triangular functions generated from Fourier components with controlled amplitudes and mutual phase.

signals at the frequency $\omega_C \pm n\omega$, where n is an integer (Fig 1.13 and 1.14) with the modulation frequency ω larger than 10THz. The accuracy to which the waveform is reproduced depends on the number of spectral components (Fig 1.13) and on the relative phase relationship between these components (Fig 1.14).

The proposed experimental setup for the coherent Raman sidebands generator is represented schematically in Fig 1.15. The first part of the device combines a new generation of CW fibre-lasers with high power and narrow linewidth to the burgeoning technology of gas-filled HC-PCF to convert a fraction of the pump power into a strong Stokes radiation to be used as a driving laser. The second part of the device takes full advantage of the astonishing properties of the HC-PCF to generate the coherent frequency comb required to subsequently achieve waveform synthesis.

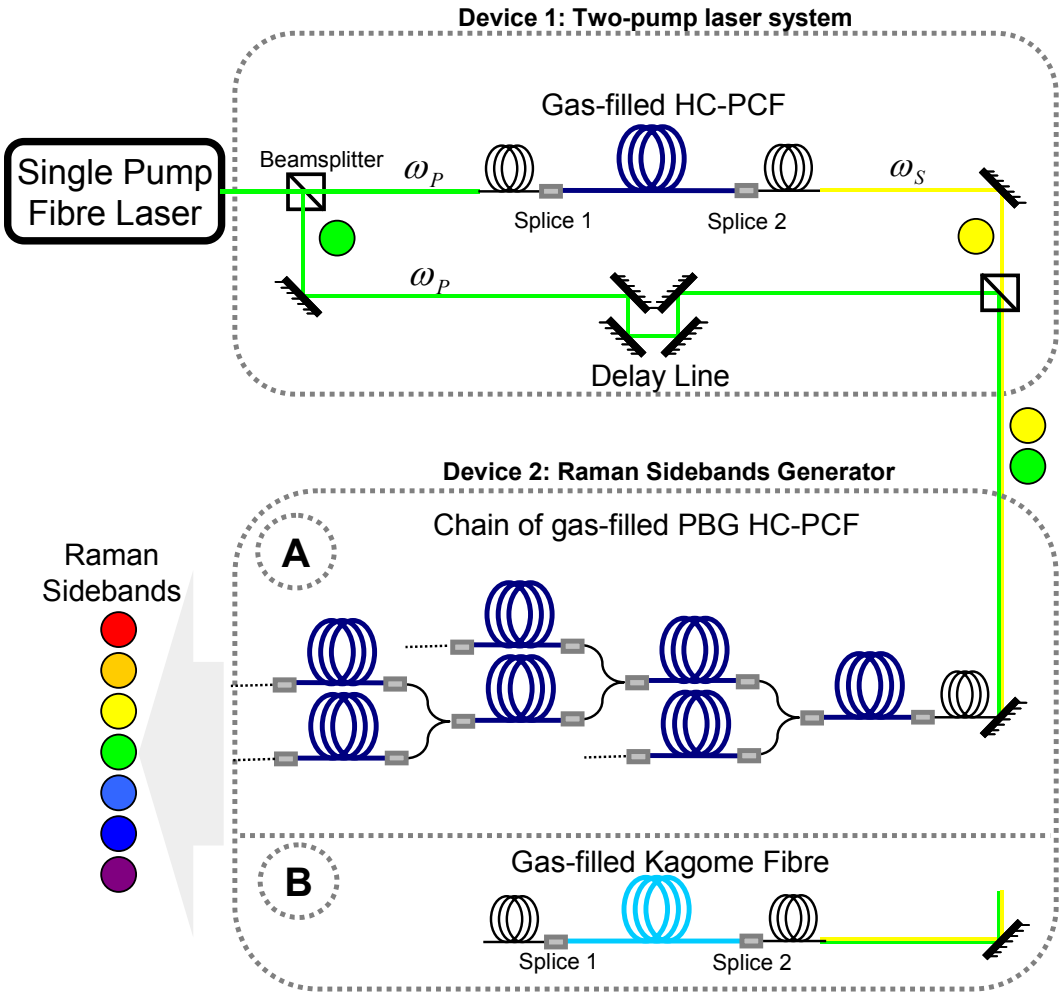

Fig. 1.15 Schematic of the proposed Raman sideband generator based on gas-filled HC-PCF. A single laser is coupled into Device 1 to generate the required Stokes radiation. The resulting two-pump laser system is then coupled onto Device 2 for the generation of the sidebands, either (A) via cascaded Raman sidebands generation using a chain of low pressure, low temperature HC-PCFs or (B) by using a single Kagomé-lattice HC-PCF.

1.3.2 Two-pump laser system based on HC-PCF

Two high power driving lasers, separated in frequency by the Raman transition Ω_R, are usually required to achieve efficient Raman sideband generation. The difficulty to find such a suitable pair has meant that only high power, pulsed Nd:YAG and Ti:Sapph can be used in deuterium-filled gas cells. Additionally, the common phase of the lasers needs to be locked so that maximum coherence is achieved.

This limitation can be lifted by converting part of a high-power narrow-linewidth CW pump fibre-laser into a Stokes laser source by rotational CW stimulated Raman scattering in hydrogen-filled HC-PCF (Device 1 in Fig 1.15). Because the conversion is done in the CW regime and the phase of the converted Stokes radiation is the same as that of the

pump radiation, we obtained the two necessary driving fields for the Raman sideband generation. Furthermore, this CW fibre-laser pair lifts the compromise between a strong adiabaticity and a strong coherence that surrounds the two-photon Rabi frequency [62]. The small detuning δ required for maximum coherence in the subsequent sidebands generation process is then managed by controlling both the temperature and the pressure of the gas trapped inside the HC-PCF fibre. Because of the low power operation possible in HC-PCF, a reduction of the AC Stark effect, usually observed in current Raman sideband generation setups, ensues, leading to the efficient generation of sidebands with sub-MHz detuning δ [60].

Overall, the combination of CW pumps and HC-PCF will make the technical implementation less challenging and the results more efficient.

1.3.3 Raman sidebands based on HC-PCF

The driving fields of the two-pump laser system are then coupled to the part of the device generating the Raman sideband spectrum that simply comprise a low-pressure, low-temperature HC-PCF filled with H_2 (Device 2 in figure 1.15). Due to the limitation imposed by the transmission bandwidth of the band gap fibre, the resulting system will generate a ~80 THz wide comb of Raman sidebands. This modest frequency comb could be dispersion compensated, amplitude controlled and recombined to achieve pulse shaping to the femtosecond level. However, the reduction of the pulse width to below the femtosecond would require the generation and guidance of a spectral bandwidth spanning over ~1000THz.

The necessary additional bandwidth could be obtained by using a chain of ~80 THz wide photonic band gap fibres with a different bandwidth location aligned in a branched tree-like arrangement (A in Fig 1.15), similar to the harmonic frequency chain in metrology which is the ancestor of the frequency comb [63]. An alternative to this cascaded Raman sidebands generation consists of using a single length of Kagomé fibre for the generation of all the sidebands simultaneously (B in Fig 1.15). As suggested by the results given in chapter 8, the achievable spectral bandwidth we can achieve spans from ~350 nm to ~2000 nm (containing ~45 Raman components from the ortho-hydrogen rotational Raman transition). This width would be enough to obtain pulses in the attosecond regime.

1.4 Thesis Outline

This thesis consists of three parts:

(i) Chapters 2 and 3 present the recent scientific developments in our understanding of guidance in photonic band gap fibres and the development of photonic micro-cells based on gas-filled HC-PCF aimed at maximising their gas-laser interaction efficiency.

(ii) Chapters 4 and 5 present a set of experiments on generating SRS in gas-filled HC-PCF leading to the first CW Raman gas-fibre laser reported in Chapter 6, based on the combination of a CW fibre-laser and the device developed in (i).

(iii) Chapters 7 and 8 validate that molecular modulation can be efficiently achieved inside a large pitch HC-PCF by the observation of a transient higher-order Raman scattering spectrum spanning nearly 3 octaves.

Chapter 9 provides a summary of the thesis and concludes on the feasibility of the optical waveform synthesiser in the near future.

References and Notes

[1] M. J. Renn and R. Pastel, *J. Vac. Sci. Technol. B* **16**, 3859 (1998).

[2] P. St. J. Russell, private papers (1991).

[3] E. Yablonovitch, *J. Opt. Soc. Am.* **10,** 283 (1993).

[4] S. John, *Phys. Rev. Lett.* **58**, 2486 (1987).

[5] A. A. Maradudin and A. R. McGurn, *J. Modern Opt.* **41,** 275 (1994).

[6] T. A. Birks, P. J. Roberts, P. St. J. Russell, D. M. Atkin, and T. J. Shepherd, *Electron. Lett.* **31**, 1941 (1995).

[7] J. Pottage, D. Bird, T. Hedley, J. Knight, T. Birks, P. Russell, and P. Roberts, *Opt. Express* **11**, 2854 (2003).

[8] K. Saitoh and M. Koshiba, *J. Quantum Electron.* **38**, 927(2002).

[9] JCMwave GmbH, www.jcmwave.com

[10] S. G. Johnson and J. D. Joannopoulos, *Opt. Express* **8**, 173 (2001).

[11] G. J. Pearce, T. D. Hedley and D. M. Bird, *Phys. Rev. B* **71**, 195108 (2005).

[12] N. W. Ashcroft and N. D. Mermin, *Solid State Physics,* Saunders College, Philadelphia, PA19105 (1976).

[13] T. A. Birks, G. J. Pearce, and D. M. Bird, *Opt. Express* **14**, 9483 (2006).

[14] R. F. Cregan, B. J. Mangan, J. C. Knight, T. A. Birks, P. St. J. Russell, P. J. Roberts and D. C. Allan, *Science* **285**, 1537 (1999).

[15] C. Kittel, *Introduction to solid state physics*, John Wiley & sons Ltd, USA (1995).

[16] C. M. Smith, N. Venkataraman, M. T. Gallagher, D. Muller, J. A. West, N. F. Borrelli, D. C. Allan, K. Koch, *Nature* **424**, 657 (2003).

[17] G. Humbert, J. C. Knight, G.Bouwmans, P. St. J. Russell, D. P. Williams, P. J. Roberts and B. J. Mangan, *Opt. Express* **12**, 1477 (2004).

[18] F. Benabid, J. C. Knight, G. Antonopoulos and P. St. J. Russell, *Science* **298**, 399 (2002).

[19] T. D. Hedley, D. M. Bird, F. Benabid, J. C. Knight and P. St. J. Russell, *Conference on lasers and electro-optics* (Baltimore) (2003).

[20] J. von Neumann and E. Wigner, *Physik. Zeitschr.* **30**, 465 (1929).

[21] J. C. Knight, T. A. Birks, P. St. J. Russell and D. M. Atkins, *Opt. Express* **21**, 1547 (1996).

[22] F. Benabid, *Philos. Trans. R. Soc. A-Math. Phys. Eng. Sci.* **364** 3439 (2006).

[23] P. Roberts, F. Couny, H. Sabert, B. Mangan, D. Williams, L. Farr, M. Mason, A. Tomlinson, T. Birks, J. Knight, and P. St. J. Russell, *Opt. Express* **13**, 236 (2005).

[24] Crystal Fibre A/S in Europe, Corning Inc. in the US and NTT in Asia.

[25] Held by Sumitomo Electric Ltd. (2002).

[26] Held by NTT Comm. (2007).

[27] N. M. Litchinitser, S. C. Dunn, B. Usner, B. J. Eggleton, T. P. White, R. C. McPhedran and C. M. de Sterke, *Opt. Express* **11**, 1243-1251 (2003).

[28] P. Roberts, D. Williams, B. Mangan, H. Sabert, F. Couny, W. Wadsworth, T. Birks, J. Knight, and P. Russell, *Opt. Express* **13**, 8277 (2005).

[29] R. Amezcua-Correa, N. G. Broderick, M. N. Petrovich, F. Poletti, and D. J. Richardson, *Opt. Express* **14**, 7974 (2006).

[30] M. K. Sanyal, S. K. Sinha, K. G. Huang and B. M. Ocko, *Phys. Rev. Lett.* **66**, 628 (1991).

[31] J. Jäckle and K. Kawasaki, *J. Phys.: Condens. Matter* **7**, 4351 (1995).

[32] G. Agrawal, *Nonlinear fibre optics*, Academic Press, London (2001).

[33] F. Benabid, G. Antonopoulos, J. C. Knight and P. St. J. Russell, *Phys. Rev. Lett.* **95**, 213903-1 (2005).

[34] Y.R. Shen, *The principles of nonlinear optics*, John Wiley & sons, USA (2002).

[35] R. Boyd, *Nonlinear optics*, Academic Press, London, (2000).

[36] L. S. Meng, P. A. Roos and J. L. Carlsten, *Opt. Lett.* **27**, 1226 (2002).

[37] M. D. Duncan, P. Osterlin and R. L. Byer, *Opt. Lett.* **6**, 90 (1981).

[38] J. X. Cheng, and X. S. Xie, *J. Phys. Chem. B* **108**, 827 (2004).

[39] S. E. Harris and A. V. Sokolov, *Phys. Rev. A* **55**, R4019 (1997).

[40] C. V. Raman and K. S. Krishnan, *Nature* **121**, 501 (1928).

[41] E. J. Woodbury and W. K. Ng, *Proc I. R. E.* **50**, 2367 (1962).

[42] M. G. Raymer, J. Mostowski, *Phys. Rev. A* **24**, 1980 (1981).

[43] J. K. Brasseur, K. S. Reparsky and J. L. Carlsten, *Opt. Lett.* **23**, 367 (1998).

[44] H. Kawano, Y. Hirakawa, and Totaro Imasaka, *Appl. Phys. B* **65** , 1 (1997).

[45] E. Sali, K. J. Mendham, J. W. G. Tisch, T. Halfmann and J. P. Marangos, *Opt. Lett.* **29**, 495 (2004).

[46] H. Kawano, Y. Hirakawa, and T. Imasaka, *J. Quantum Electron.* **34**, 260 (1998).

[47] R. L. Carman, F. Shimizu, C. S. Wang and N. Bloembergen, *Phys. Rev. A* **2**, 60 (1970).

[48] J. P. Marangos, *Nature* **446** 619 (2007).

[49] E.J. Woodbury and W. K. Ng, *Proc. I. R. E.* **50**, 2367 (1962).

[50] E. Garmine, F. Pandarese and C. H. Townes, *Phys. Rev. Lett.* **11**, 160 (1963).

[51] R.W. Minck, R.W. Terhune and W. G. Rado, *Appl. Phys. Lett.* **3**, 181 (1963).

[52] S. E. Harris, J. E. Field and A. Imamoglu, *Phys. Rev. Lett.* **64**, 1107 (1990).

[53] S. E. Harris and A. V. Sokolov, *Phys. Rev. Lett.* **81**, 2894 (1998).

[54] A.V. Sokolov, D. R. Walker, D.D. Yavuz, G.Y. Yin, and S. E. Harris, *Phys. Rev. Lett.* **85**, 562 (2000).

[55] A. V. Sokolov, D. D. Yavuz and S. E. Harris, *Opt. Lett.* **24**, 557 (1999).

[56] P. Antoine, A. L'Huillier and M. Lewenstein, *Phys. Rev. Lett.* **77**, 1234(1996).

[57] Y. Mairesse, A. de Bohan, L. J. Frasinski, H. Merdji, L. C. Dinu, P. Monchicourt, P. Breger, M. Kovačev, T. Auguste, B. Carré, H. G. Muller, P. Agostini, and P. Salières, *Phys. Rev. Lett.* **93**, 163901 (2004).

[58] V. Balic, D. A. Braje, P. Kolchin, G. Y. Yin, and S. E. Harris, *Phys. Rev. Lett.* **94**, 183601 (2005).

[59] M. Katsuragawa, K. Yokoyama, T. Onose and K. Misawa, *Opt. Express* **13**, 5628 (2005).

[60] A. V. Sokolov, M. Y. Shverdin, D. R. Walker, D. D. Yavuz, A. M. Burzo, G. Y. Yin and S. E. Harris , *J. Modern Opt.* **52**, 285 (2005).

[61] F. Benabid, Patent application GB 0615541.0 (2006)

[62] F. Le Kien, J. Q. Liang, M. Katsuragawa, K. Ohtsuki, K. Hakuta and A. V. Sokolov, *Phys. Rev. A* **60**, 1562 (1999).

[63] S.T. Cundiff, J. Ye, and J. L. Hall, *Rev. Sci. Instrum.* **72**, 3749 (2001).

Chapter 2

Photonic Metrology of Photonic Band Gap Fibres

This chapter presents two novel experimental approaches that probe the nature of the guidance in photonic band gap HC-PCF. The first consists of the direct visualisation of the photonic band gap while the second is based on imaging the cladding Bloch modes in order to identify the relevant resonant features of the fibre's structure. These experimental results provide a highly useful tool in the design of real fibres and in the improvement of their optical guidance. The numerical modeling in this chapter was performed by P.J. Roberts

2.1 Introduction

As discussed in chapter 1, the gas-laser interaction efficiency can be largely enhanced by using HC-PCF. In order to exploit this fibre to its maximum potential, a joint effort from theoretical modelling and experimental work was undertaken, building a clearer picture of the fibre's light trapping mechanism and paving the way for further improvement of its characteristics. The accurate modelling of the fibre, such as the characteristics of its cladding's DOPS, led to a better understanding of the experimentally observed linear properties of HC-PCF, including its modal attributes and the anti-crossing events

occurring between core-guided and surface-guided modes. This combination of theoretical models and experimental measurements accurately represent the *photonic metrology*[*] of such fibres and enabled the realisation of the state-of-the-art HC-PCF with ultra-low loss. Excellent examples of this joint effort are the scaling laws for the PBG in HC-PCF reported in [1], and the identification of air-glass surface roughness as a key loss mechanism [2].

However, the reliability of the theoretical side of the studies done on HC-PCF can be impeded by convergence problems at high frequency $k\Lambda$ and may also not correctly take into account all experimental parameters and their contribution to the total loss of the fibre. Furthermore, this numerical modelling lacks intuitive and predictive tools that would widen our understanding of out-of-plane PBG guidance. The work presented in this chapter aims to address the limitations mentioned above by developing experimental tools that (i) provide a direct measurement of the DOPS of a real fibre that can be compared with numerical modelling and (ii) validate a simple theoretical approach to explain how photonic band gap forms. The two complementary experiments provide us with a better understanding of how light propagates within the different constituent features of the HC-PCF and offer clues for the design of future HC-PCF optimized for gas-laser applications.

2.2 Visualization of the Photonic Band Gap in HC-PCF

The observation of light escaping a waveguide can yield as much information about the guidance mechanism as studying the light that is guided along it. As a matter of fact, angularly-resolved observations of escaping light have already helped to characterize planar waveguides [3], index-guiding fibre [4,5] and 3D photonic crystals [6], to only cite a few.

Similarly, the characteristic wavelength- and angular-dependence of the light scattered out of a HC-PCF could provide fruitful information about the fibre's photonic band gap properties. Indeed, a clear correlation appears between the theoretical and experimental

[*] This photonic metrology consists of any measurement that identifies and quantifies, theoretically or experimentally, the guidance properties of HC-PCF.

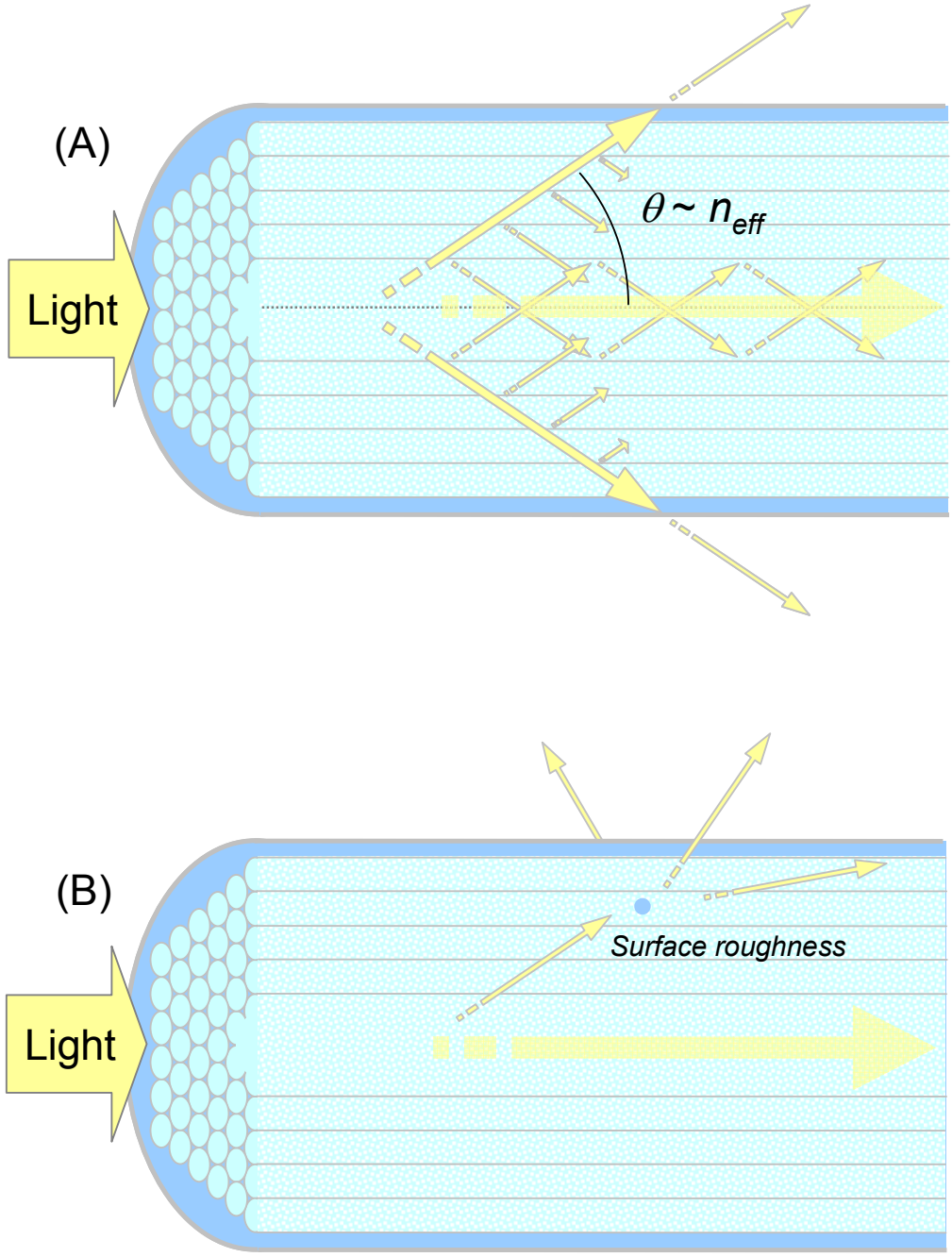

Fig. 2.1 Two possible light-escaping processes in HC-PCF. (A) Tunnelling of the air-guided mode through the cladding at an angle characteristic of the n_{eff} of the mode. This type of leakage is usually avoided by using enough rings of holes in the cladding. (B) Coupling from the air-guided mode to several non-guided cladding modes due to the surface roughness of the air/silica interface in the photonic crystal cladding.

Table 2.1: Correspondence between theory and experiment

Theoretical	↔	Experimental
Wavenumber k	↔	Wavelength λ
Effective refractive index n_{eff}	↔	Angle of propagation θ
Density of photonic states	↔	Escaping light power

characteristic parameters of the fibre (Table 2.1), so that the DOPS* diagram could be experimentally reconstructed. The experimental DOPS is linked to the leakage rate of light through the fibre either by "tunnelling" through the finite-thickness cladding, and continuing to propagate at a specific angle†, or by randomly scattering into and between other defect- or cladding-guided modes by the surface roughness at the silica/air interfaces (Fig 2.1). The recording of the intensity of light escaping from the side of the HC-PCF as a function of wavelength and angle of scattering can be represented as an "experimental DOPS" diagram that gives much information about the PBG characteristics. For example, the method can be used to determine the exact contribution of the surface roughness to the total loss of the fibre or to experimentally deduce the precise position of mode anti-crossings within the PBG.

2.2.1 Experimental Setup

The experimental setup for the wavelength- and angularly-resolved measurement of the light escaping from a piece of HC-PCF is presented in Fig 2.2. Light from a 7 mW tuneable external cavity semiconductor laser, covering the wavelength range from 1510 nm to 1630 nm, is coupled to a 50m-long HC-PCF guiding around 1550nm. A long piece of fibre is used here to ensure most of the power is in the fundamental mode so that a clearer DOPS diagram is obtained. The final few centimetres of the fibre are placed across the centre of a 32 mm diameter cylindrical immersion cell filled with index-matching fluid with a refractive index n_{MF} matches that of the silica jacket of the fibre. Only 5 millimetres of fibre are exposed; the rest of the fibre in the cell is surrounded by black tubing so that it does not contribute to the measured signal. Light escaping from the exposed region of fibre propagates through the cell and is detected by a cooled linear InGaAs photo-detector array. The array is placed approximately one focal length from the lens formed by the curved surface of the cell, so that light coming out of the fibre at a given angle arrives at a single point along the array, irrespective of its origin along the exposed fibre. To improve

* The DOPS calculated numerically are for infinite structures, whilst the experimental DOPS reported here is for a finite structure.

† Characteristic of the effective index n_{eff} of the guided mode

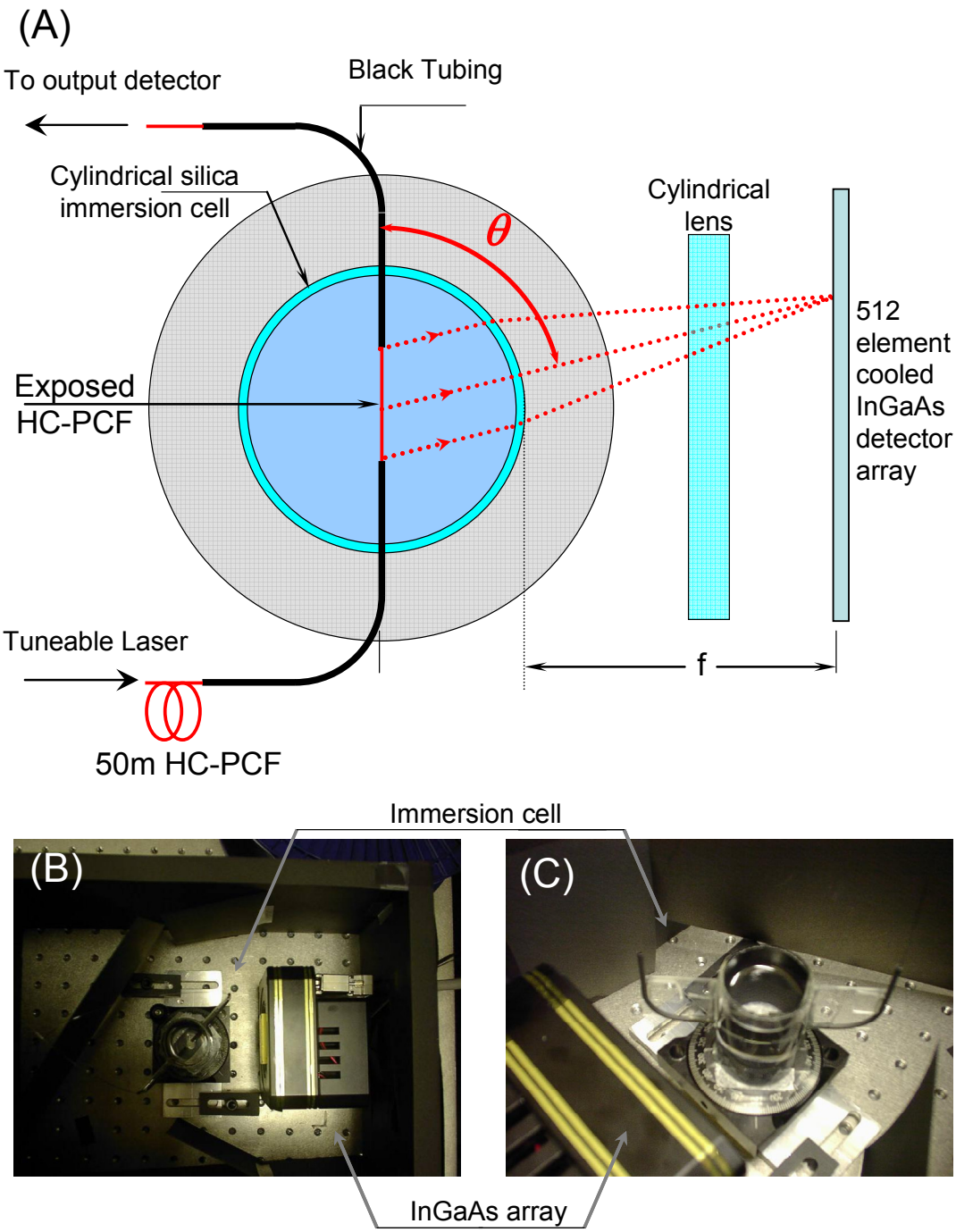

Fig. 2.2 (A) Experimental setup for the visualisation of the PBG in HC-PCF. The detector is separated from the surface of the immersion cell by roughly the focal length f of the cylindrical Fourier lens formed by the cell surface. An additional, orthogonally oriented cylindrical lens serves to increase the signal by covering a larger range of azimuthal angles. (B) and (C) Pictures of the immersion cell and the cooled InGaAs array detector used in the experiment.

the signal to noise ratio, an additional cylindrical lens focuses light from a range of azimuthal angles around the fibre. An angular range of ~12° can thus be imaged directly onto the array with an angular discrimination of 40 pixels per degree*. When used with an integration time on the order of a second, the InGaAs array collects sufficient light to analyze fibres with a loss around 1 dB/km at good signal to noise ratio.

2.2.2 Results and discussion

Escaping-light power diagram

Fig 2.3A shows the measured power of escaped light as a function of the wavelength and angle of scattering†. The corresponding wavenumber k and the effective index n_{eff} are calculated for the fibre's cladding pitch Λ=3.7µm. The data is normalised to the fibre's output power so that the resulting diagram can be directly compared to theoretical DOPS plots.

The band gap appears as a distinct dark wedge around n_{eff}=1, where a very low level of light is detected. This region is surrounded by bright horizontal stripes of high intensity above and below the band gap. The position of the PBG boundaries corresponds very closely to the location of the calculated band gap shown in Fig 2.3B.

HC-PCFs are designed with enough rings of holes to avoid direct leakage from the defect-guided modes, each ring providing ~10dB mode extinction. Therefore, the majority of the escaping light detected outside the PBG originates from the random, yet uniform, scattering of the defect-guided modes into high attenuation cladding modes caused by the surface roughness of the photonic crystal cladding (Fig 2.1A). As a consequence, the angular dependence of this scattered light gives direct information about the contribution of surface roughness to the total loss of the fibre [2].

Mode identification

As seen in chapter 1, air-guided modes exist only at particular values of n_{eff} within the PBG. Light escaping from these core-modes is therefore restricted to a very narrow range of angles. The direct observation of the light leaked out by these modes is made difficult by their low leakage rate inside the PBG region. However, as confinement becomes weaker at the band gap edges, light from these guided modes "tunnels" out and sharp lines appear in the intensity diagram. One such occurrence can be observed in Fig 2.3A and D for an

---

* Corresponding to a resolution in n_{eff} of Δn_{eff}~3 10^{-4} and therefore offering a good discrimination between modes

† An angle of 90° is normal to the fibre.

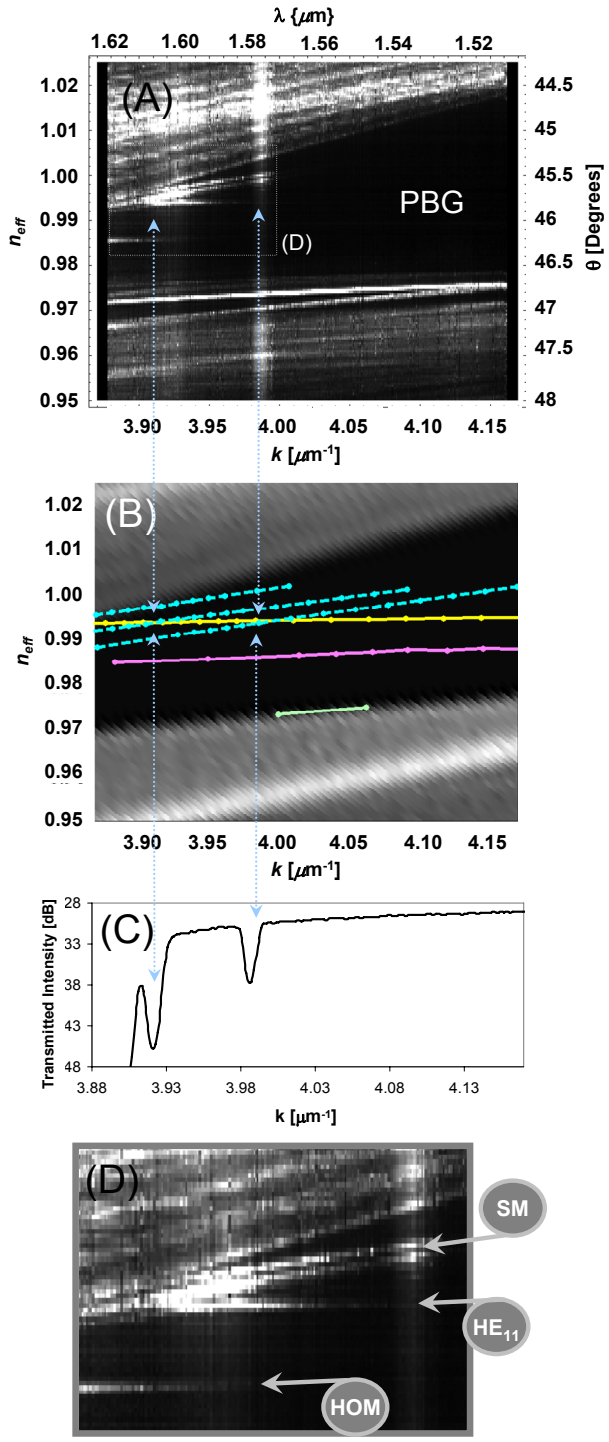

Fig. 2.3 (A) Scattered light signal as a function of n_{eff} and k, normalized to the output power of the fibre and plotted in dB. The band gap manifests itself as a dark wedge, corresponding to combinations of k and n_{eff} for which no scattering is observed. (B) Computed modal trajectories, with core modes marked as solid lines (yellow line: HE_{11}-like core mode) and surface modes with broken lines. Not all surface modes are shown and no anti-crossing events are represented (C) Transmitted spectrum of the fibre, showing that the vertical white bands in (A) correspond to loss peaks (identified as surface-mode anti-crossings) at specific wavelengths (D) Zoom of plot (A) pointing out the observed modes. HOM: Higher order modes, SM: Surface modes.

effective index of 0.993, corresponding theoretically to the fundamental HE_{11}-like mode in which the majority of the incident power resides (yellow line in Fig 2.3B). The increased leakage of this mode near the band edge is accompanied, as expected, by a drop in transmission at the output of the fibre, as seen in Fig 2.3C*. Other higher-order core-guided modes (HOM) can also be observed as sharp, near-horizontal lines in the experimental band gap region (Fig 2.3D) and identified via the theoretical plot (Fig 2.3B) as: TE_{01}, TM_{01} and HE_{21}-like modes as a single line at $n_{eff} = 0.986$, and the HE_{12}-like mode as a line along the bottom of the band gap around $n_{eff} = 0.975$. The fine lines of high intensity defining these core-guided modes in Fig 2.3A are almost parallel to the k axis, as expected from low-order core-guided modes predominantly guided in air.

The lines indexed *SM* in Fig 2.3D correspond to surface-guided modes also shown as dashed blue lines in the theoretical plot (Fig 2.3B). As expected from their high light-in-glass fraction, these modes are more dispersive than the core-guided modes and their trajectories are not parallel to the k-axis. Therefore, one can discriminate these modes from the core-guided modes by simply considering the slope of their trajectory in the DOPS diagram.

This direct and accurate measurement of the position of the guided core and surface modes inside the PBG allows the discrimination of their respective confinement loss as well as the verification of their theoretical location. It can also be used to predict mode anti-crossing events.

Modes anti-crossings

The experimental DOPS diagram in Fig 2.3A also shows bright vertical lines of scattered light around particular values of wavenumber k, extending over the full angular detection range. This is recognized as anti-crossings events between core-guided and surface modes (Fig 2.3B), and also confirmed in the measured transmission spectrum of the HC-PCF as sharp troughs in the fibre's transmission (Fig 2.3C). Indeed, close to an anti-crossing, the total scattered power greatly increases because a guided mode hybridizes with a surface mode that has far higher field strength at the air/silica boundaries, leading to enhanced surface roughness scattering.

The vertical line that appears at k=3.99 μm^{-1} corresponds to the local minima in the transmitted spectrum (Fig 2.3C) and is identified in the theoretical DOPS diagram (Fig 2.3B) as being due to anti-crossing of a surface-guided mode and the HE_{11}-like core mode.

* The other side of the PBG is not within wavelength range of the laser.

However, this actual crossing occurs too deeply within the band gap to be directly observed experimentally and can only be inferred by the increased leakage rate. As a matter of fact, only anti-crossing events located closer to the edge of the PBG, such as the one around k= 3.925 µm^{-1}, can be directly observed. Indeed, in this situation, the confinement loss of both surface and fundamental modes is increased and the mode trajectories become clearly evident in the experimental data.

2.2.3 DOPS of real HC-PCF

Using this experimental DOPS diagram, one could experimentally discriminate the surface roughness [2], the confinement loss of the guided modes and the position and strength of anti-crossing events participating in the total fibre's attenuation. Additionally, the method could be extended to measure the DOPS in frequency regions where the theoretical calculations fails to converge ($k\Lambda$>100).

One of the limitations of the technique is that the structured bands of high intensity contiguous to the PBG in the experimental diagram (Fig 2.3A) provide little information about the nature of the cladding modes and their origin. A more direct observation of these cladding modes, as presented in the following section, is required in order to identify the characteristic features responsible for the PBG guidance.

2.3 Identification of Cladding Bloch Modes in HC-PCF

The direct observation of the cladding modes from the high-DOPS bands surrounding the PBG is usually difficult due to the diffraction of high frequency spatial features of the modes. In this section, two experimental techniques are presented to circumvent this limitation. The first is based on the indirect identification of cladding modes by observing their Fresnel diffraction pattern evolution from the fibre's end surface. The second relies on a scanning near-field optical microscope (SNOM) to overcome the diffraction limitation and allow the direct measurement of the cladding modes and of their spatially-resolved optical spectrum. These two techniques clearly identify three resonators at the origin of the photonic band gap guidance: the apex, the strut and the air hole that form the photonic crystal cladding.

2.3.1 Theoretical concept of resonators in HC-PCF

Earlier work

Simple theoretical models in microstructures waveguides such as Bragg fibres have been developed around the concept of optical resonators since the 1970's [7-9]. These early reports found that modes in the Bragg cladding form a band composed of several constituent modes whose number is given by the number of microstructured layers. For higher frequencies and effective indices, this band shrinks to a set of degenerate modes confined in the high-index layers. This observation clearly indicates the role of the resonance properties of the high-index layer in the formation of the band gap [9].

This behaviour is amenable to a tight-binding description of band gap formation familiar from solid state physics. Fig 2.4 presents the similarities between the problem of electrons in a 1D crystalline lattice of N atoms [10], and photons in a photonic crystal arrangement of 1D high-index photonic crystal. In the solid-state tight binding model, electronic bands in the crystal are considered to be the result of bringing together isolated and identical atomic-like orbitals [10] so that a degree of spatial overlap is incurred. This model simply and accurately describes the behaviour of electrons in the crystal in solid state physics.

Similarly, in the photonic crystal problem, the atoms are replaced by high index waveguides and the electronic orbitals are replaced with the field extension of the waveguide mode* (Fig 2.4). In this case, however, the spatial overlap of the electromagnetic field can be obtained either by bringing the waveguides closer together (as in solid state), or by increasing the optical wavelength of the mode considered. When the spatial overlap becomes substantial, the modes split and spread, lifting the degeneracy (Fig 2.4).

The Anti-Resonant Reflective Optical Waveguides (ARROW) model [11], based on the coupled resonator picture, has been successfully applied to classes of photonic crystal fibres [12,13] with a structure made of a low-index background material with isolated high-index cylindrical rods. The frequencies of transmission bands are shown to be primarily determined by the geometry and the modal properties of the individual high-index inclusions irrespective of the lattice constant value. More recently, Birks et al [14] proposed a semi-analytical approach to understanding the formation of band gaps in all-solid band gap PCFs with a similar type of cladding structure. The authors modelled the out-of-plane mode structure of the fibre cladding by employing an approximate technique

* The electronic energy levels (ground or excited) are replaced by the modes (fundamental or HOM) of the high index waveguides.

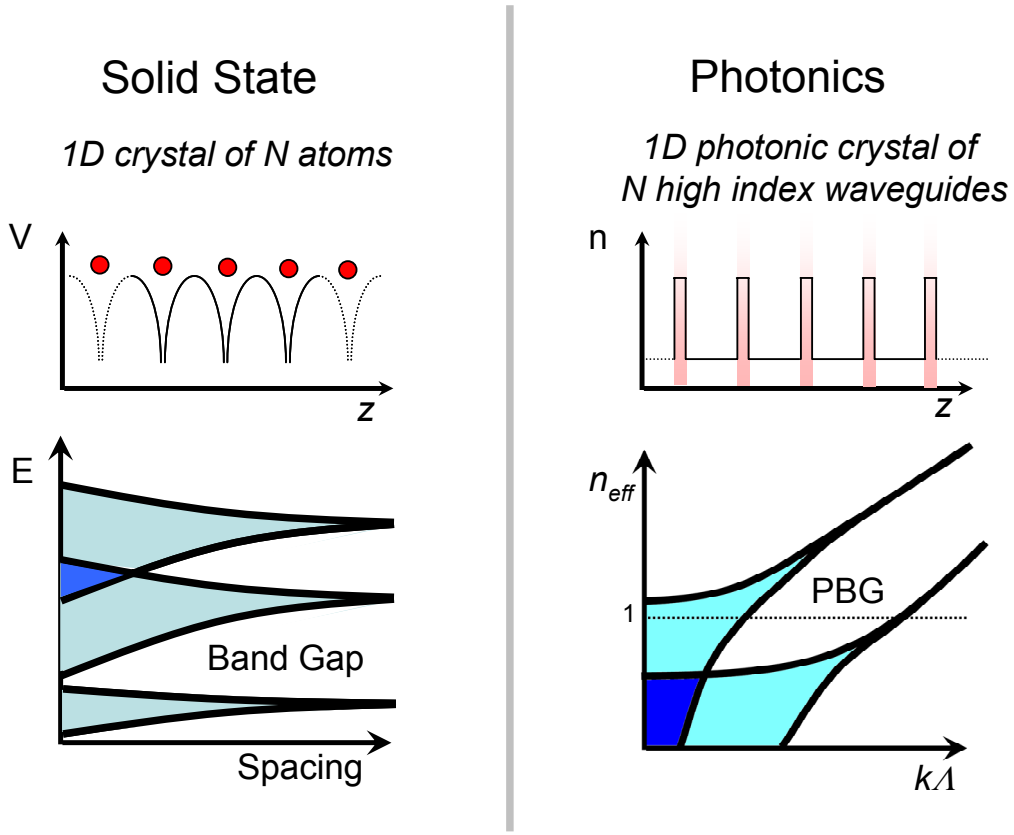

Fig. 2.4 Similarities between the tight binding model describing the formation of electronic band gap in solid sate physics (left) and the coupled resonator picture describing the formation of photonic band gap in photonic crystals (right).

related to the cellular method used in solid-state physics [10]. This method explicitly takes into account electromagnetic coupling between each high index cylinder within the cladding and, in contrast to the ARROW model, provides information on the width of the cladding pass-bands. The model also elucidates the hybridization which occurs between resonances associated with the localized high-index regions and the low-index regions which fit between them.

But these models are difficult to apply directly to an air/silica HC-PCF cladding because of its complex topological structure. Indeed, the interconnection of the high-index apices of such fibres calls into question the applicability of the picture of guidance and band gap formation based on the influence of a few constituent elementary resonator features. Consequently, in order to assess this view as an aid to designing realistic HC-PCF, it is useful to develop experimental or theoretical tools aimed at identifying any relevant cladding features which may be present.

Numerical modelling of the HC-PCF cladding modes

Fig 2.5 presents the DOPS diagram modelled using the plane wave approach [15] for an infinite cladding structure comprising a honeycomb lattice arrangement of hexagonal holes with rounded corners* (Inset in Fig 1.3 and [16]) corresponding to a good approximation to fabricated HC-PCFs. As expected from the tight binding model analogy, the cladding modes of the infinite cladding structure form a continuum.

For high normalized wavenumbers $k\Lambda$, light is well localized within the glass apices and the spatial overlap of a mode associated with an individual apex with equivalent modes of neighbouring apices, is minimised. As a consequence, the upper allowed-bands (Region 1 in Fig 2.5A) shrink to an extremely narrow region in the k-n_{eff} plane, similarly to what is expected from a tight-binding description of band formation. The overlap increases with increasing wavelength (due to the consequent reduction in confinement) or with a decrease in separation of neighbouring apices (driven by the fibre's pitch Λ). The effect of the overlap is to cause the mode-line associated with individual apex states to spread and form a band of finite width in the k-n_{eff} plane, and also to introduce a delocalized character to the cladding states [17]. This picture is well illustrated by the shape of region 1 in Fig 2.5A, and in Fig 2.5B which shows the DOPS over an extended frequency range.

Identification of the resonators forming the PBG

Figure 2.5A also shows a selected set of modes (coloured lines) in both regions. The solid and dotted lines correspond to modes found at the high symmetry points Γ and J of the Brillouin zone, respectively. Of particular interest is the anti-symmetric mode associated with the Γ-point of the Brillouin zone since it forms the upper edge of the out-of-plane photonic band gap of the cladding. The dispersion of this "apex mode" (red line in Fig 2.5B) and its near-field (Fig 2.6A) confirm that the light is predominantly guided in the interstitial apices. The apices are thus identified as the most important optical resonators associated with the upper band gap edge [18].

The symmetric form of the apex mode is characterized by the fields in all the apices being in-phase with one another, whereas the field changes sign between nearest neighbour apices for anti-symmetric modes. The symmetric apex mode is known as the fundamental space filling mode [12] and forms the upper boundary to Region 1, i.e. its mode-line (shown by the purple line in Fig 2.5B) designates the cladding cut-off index variation with wavenumber k.

---

* air filling fraction 91.9% and meniscus radius at the corners 0.24Λ.

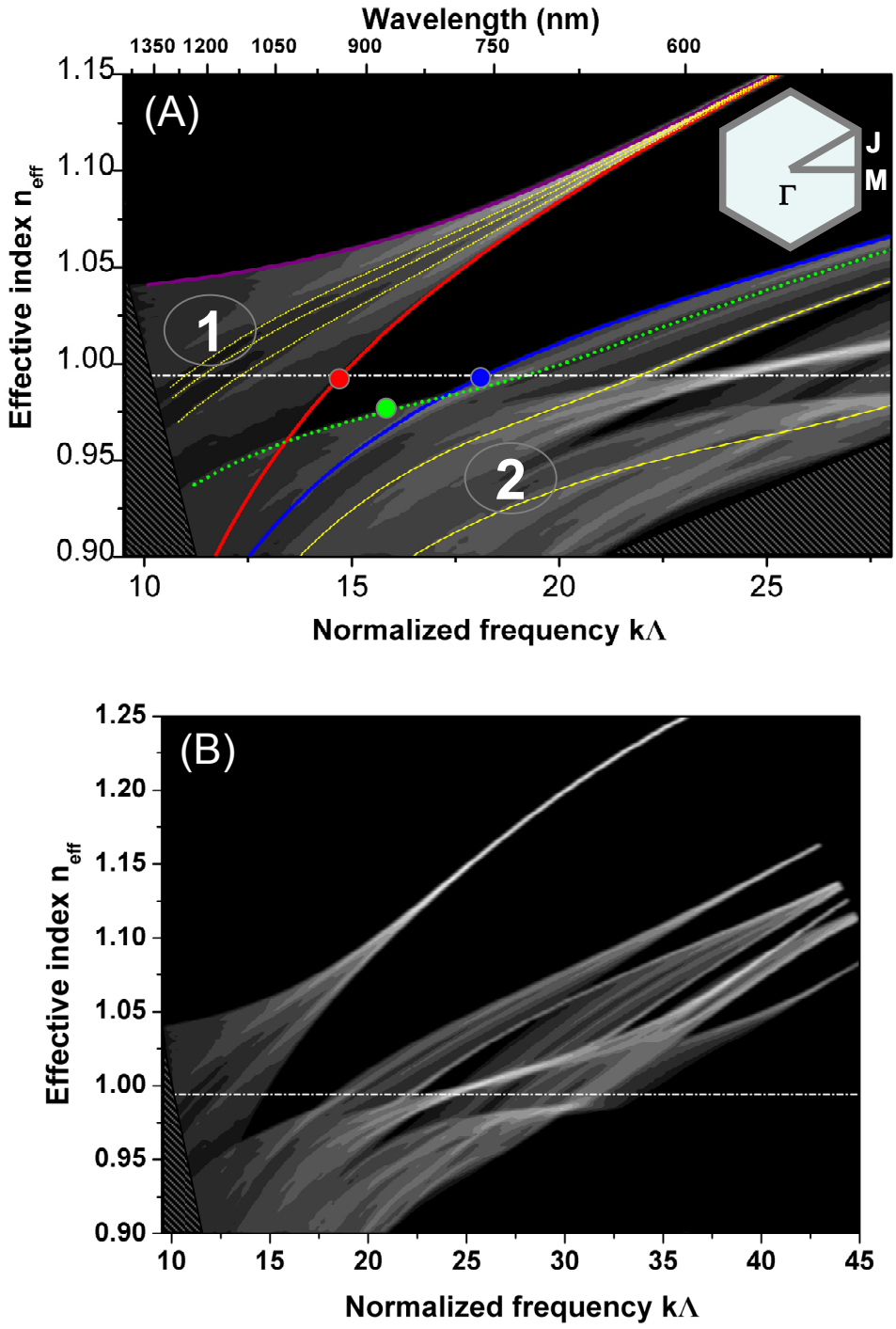

Fig. 2.5 (A) Calculated DOPS diagram for a triangular HC-PCF cladding lattice around the PBG region falling below the vacuum line. Black represents zero DOPS and white maximum DOPS. The upper X-axis shows the corresponding wavelengths for a HC-PCF guiding at 800 nm (Λ=2.15μm). The trajectory of the cladding modes on the edges of the PBG are represented in red for the interstitial apices mode, blue for the silica strut mode and green for the air hole mode. The solid lines show the Γ-point mode trajectories and the dotted lines the J-point mode trajectories. Inset: Brillouin zone definition. (B) Extended DOPS diagram up to $k\Lambda$=45.

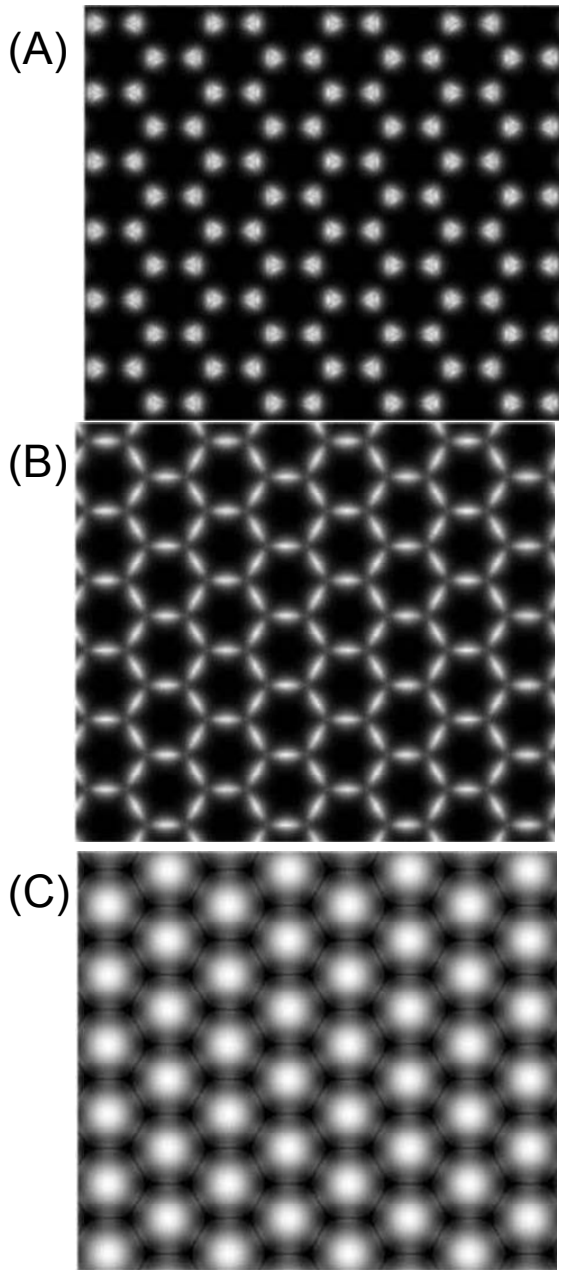

Fig. 2.6 Near-fields of the (A) "apex" mode, (B) "strut" mode and (C) the "airy" mode calculated at the position of the red, blue and green dot in Fig 2.5A, respectively.

The nature of the modes at the lower edge of the PBG is more complicated than those at the upper edge because of the overlap of several cladding modes. Indeed, the lower edge is formed from the trajectories of two cladding modes of different symmetry. At frequencies below $k\Lambda$=16.9, the edge is due to modes associated with the J-point within the Brillouin zone, represented by the dotted green lines in Fig 2.5A, and above this frequency, the edge is due to a mode located at the Γ-point, represented by the continuous blue in Fig 2.5A. The J-point mode (Fig 2.6C) guides predominantly in the air-holes of the cladding lattice and will therefore be called the "airy mode", whereas the Γ-point mode (Fig 2.6B) guides

predominantly within and close to the silica struts which join neighbouring apices with little of the field penetrating into the apices and will therefore be called the "strut mode". From this observation, it becomes clear that the silica struts affect the performance of the HC-PCF by limiting the upper-frequency boundary of the fibre transmission band. Moreover, the curve of the J-point "airy mode" suffers from anti-crossing events with modes associated with these glass features, thus limiting the PBG depth. One such event, occurring around $k\Lambda$=18, is responsible for the point of inflection in the mode trajectory of the airy mode (green line) observed near this frequency value, introducing a field component within and near the glass struts to the airy mode. Similar anti-crossing events are commonplace within region 2 in Fig 2.5A and result in cladding modes which typically show a high degree of hybridization between air-guided and silica-guided components. Such mode interactions also cause higher-order cladding band gaps to close up (e.g. Fig 2.5B at $k\Lambda$=26). As a consequence, the intuitive resonator-based picture of cladding states becomes of less use in this region. Near the band gap, which is the region of most relevance to HC-PCF guidance, sufficiently few resonators are involved in forming the cladding modes for the resonator picture to be a useful conceptual framework.

2.3.2 Fresnel zone imaging of HC-PCF cladding modes

In order to experimentally confirm the theoretical findings from above, accurate optical imaging of the cladding modes of the HC-PCF is required. However, a key issue with the imaging of these modes is associated with the rapid evolution of the field pattern from the end of the fibre. Indeed, the pattern can change appreciably after propagation of distances less than 1µm. This often precludes a direct observation of the near-field. In order to overcome this limitation, the field evolution through the Fresnel zone can be recorded and compared to the calculated evolution of candidate mode components.

Propagation and diffraction properties of HC-PCF cladding modes

Although the spatially delocalised nature of the cladding modes and their weak confinement makes their leakage decay too rapid for them to survive propagation along a few millimetres of fibre, some excitable cladding field components show a very low transverse group velocity $v_{g\perp}$ within the crystal plane and a consequent slow decay. These components correspond to stationary points of the dispersion surfaces associated with a high DOPS and generally occur at positions of high-symmetry within the Brillouin Zone.

If the optics at the input of the fibre excite cladding modes at wavenumber k over a small spread of n_{eff} values Δn_{eff}, the field within the cladding would initially evolve in a complex manner, due to the various cladding mode components acquiring different phases along the propagation length. Further along the fibre, however, only the modes with low $v_{g\perp}$ and

high DOPS within Δn_{eff} would remain, so that the surviving field has a much simpler structure with the same spatial dependence as a single (possibly degenerate) cladding mode and regains a high degree of spatial coherence. Consequently, the cladding field escaping from the output end of the fibre will show a self-interference pattern devoid of speckle and characteristic of the predominant surviving cladding mode.

Fig 2.6 shows the near-field of the three cladding modes (apex, strut and airy modes) defining the edges of the PBG, calculated at an effective index n_{eff} =0.995 representative of the HE_{11}-like guided mode within the band gap range (shown by a white dotted line in Fig 2.5A and 2.5B). It is interesting to note that all three modes satisfy the conditions above and could be observed after a relatively long propagation along the fibre. The evolution of the diffraction pattern of the apex and strut modes for indices close to that of the air-line is shown in Fig 2.7 as they propagate a short distance from the output end of the fibre (i.e. with the Fresnel zone).

In comparison to the strut modes (and the airy mode), the apex mode exhibits a much slower and simpler evolution of the diffracted field from the fibre end, due to the lower frequency of the mode which implies a lower spatial resolution of the glass features close to the air light-line. The easily distinguishable diffraction patterns and evolution within the Fresnel zone of these cladding modes indicate that a simple optical imaging of the patterns could be used to infer which cladding mode components are present in experimental observations.

Experimental Fresnel zone imaging

To optically image the HC-PCF cladding modes of interest, we excite a short length of HC-PCF at an effective index close to that of the air light-line. This is achieved by splicing a 3mm long HC-PCF (band gap centred at 800nm, pitch Λ=2.15µm) to one end of an SMF-980 fibre (using the technique described in Chapter 3); the mode field matching between the SMF mode and the fundamental mode of the HC-PCF is optimized for the frequencies lying in the fibre's transmission band. This ensures the excitation of cladding modes with an effective index close to that of the HE_{11}-like guided mode within a very narrow Δn_{eff} range. The remaining end of the SMF fibre is coupled to a super-continuum light source filtered to the desired wavelength using 3nm-bandwidth interference filters. The identification of the cladding Bloch-modes is then achieved by recording the diffraction pattern imaged onto a CCD camera using a microscope objective lens and its evolution as the fibre output end is moved along the optical axis of propagation, away from the output imaging lens, over a travel distance of ~100µm.

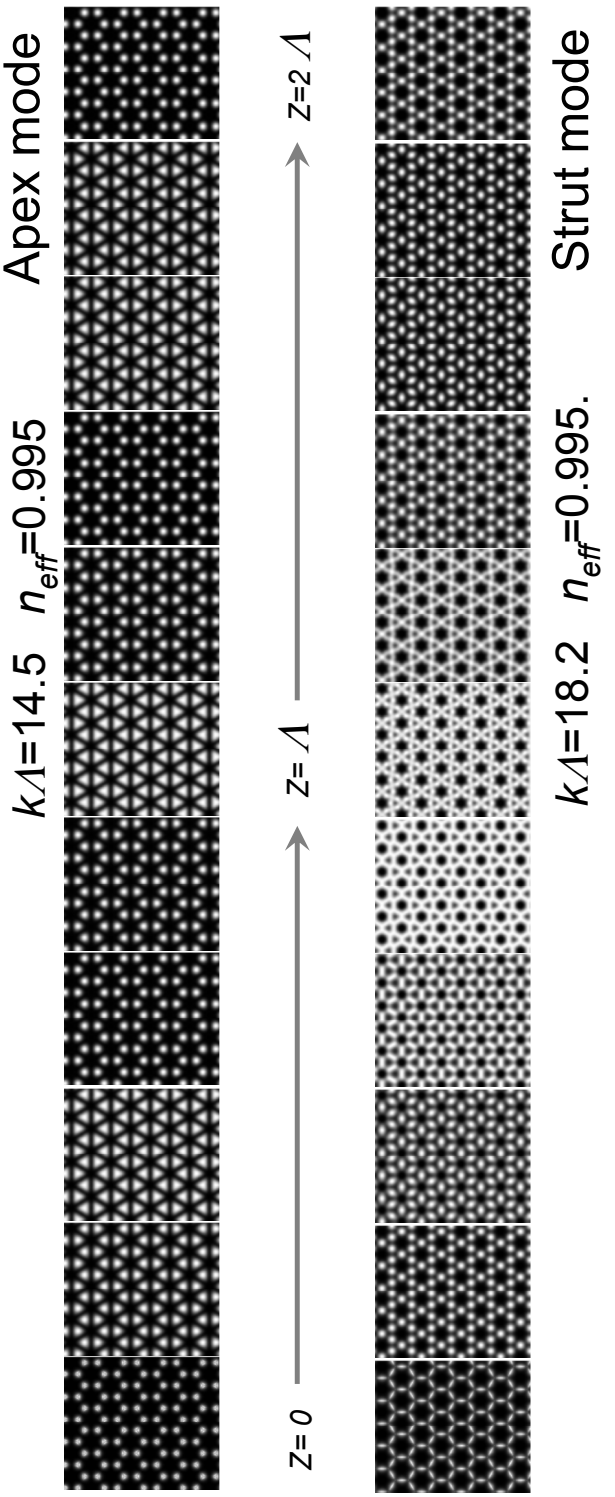

Fig. 2.7 Evolution of calculated Fresnel zone patterns of the apex mode and the strut mode as it propagates away from the fibre end (z=0). Two adjacent frames correspond to a spatial separation of 0.2Λ.

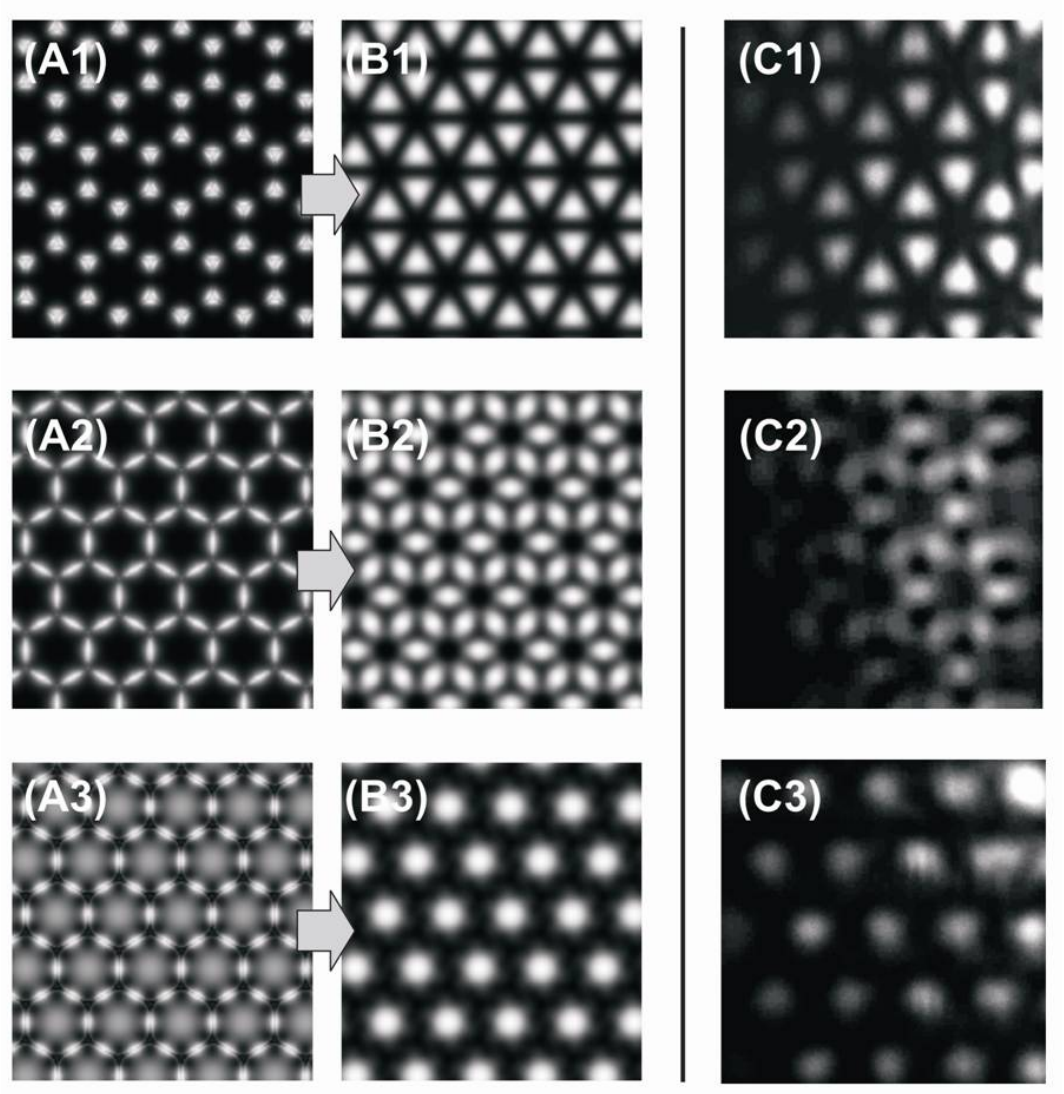

Fig. 2.8 (A) Calculated near-field profile for (A1) the apex mode, (A2) strut mode and (A3) airy mode. (B) Corresponding Fresnel zone mode patterns. The position of the diffraction pattern is 1.8Λ, 1.5Λ and 2.0Λ away from the fibre for the three modes, respectively. (C) Observed Fresnel zone mode patterns for a wavelength of 950nm, 750nm and 700nm in a HC-PCF guiding around 800nm. The pattern positions, relative to the end of the fibre, are in the range of 4-5μm.

Column C of Fig 2.8 shows the measured Fresnel zone patterns of the modes corresponding to wavelengths centred at 950nm, 750nm and 700nm, either side of the PBG (see Fig 2.5A for a wavelength scale of the PBG position for the fibre used here). The patterns correspond to an imaged cladding section covering ~9 air-holes and located 2-3 rings away for the fibre core. Although no direct imaging of the cladding modes near field is possible using this method, these recorded patterns match very well the calculated sequences (Column B of Fig 2.8) and makes this simple technique a rather powerful and accurate tool for identifying the propagating HC-PCF cladding modes responsible for the

formation of the PBG. Additionally, the system can be used to identify modes away from the PBG boundaries in order to experimentally probe the band structure. This is of particular interest around potential high-order PBG such as the one observed in Fig 2.5B at $k\Lambda$=22.5.

2.3.3 Mode imaging and spectral analysis by scanning near field optical microscopy

The Fresnel imaging technique's main limitation is the very strong diffraction of the high spatial frequency components of the cladding mode's field, leading to the incomplete imaging of the near-field. In order to overcome this restriction and directly measure the fibre's cladding near-field profile, the imaging process should consist of a detector directly probing the fibre's surface, as is the case in a SNOM. Additionally to the high spatial resolution of the near field images of HC-PCF's cladding available with this instrument, the technique offers the possibility to independently record the transmission spectrum of the cladding and core features, giving yet more insight into the PBG guidance mechanism.

SNOM observation of cladding modes

The principle of scanning near-field optical microscopy is the scanning of the sample with a nanometre-scale probe tip acting as a detector. In the experiment below, the sample under test is the HC-PCF output end; the tip consists of a gold coated, 150nm-core fibre taper used in collection mode.

A schematic of the experimental setup is shown in Fig 2.9. As in the Fresnel zone imaging experiment above, a few millimetres of HC-PCF are spliced to a length of conventional fibre coupled to a super-continuum source. Interference filters are used to select the operating wavelength. The near-field is obtained by scanning the tip with 0.15µm step, over an area covering a few unit cells of the HC-PCF cladding structure and collecting the spatially resolved data to recreate the near-field profile. The operation is repeated at various wavelengths of interest on both sides of the PBG transmission spectrum.

Figure 2.10 shows the typical measured near field profiles when the fibre is excited by light near the lower-frequency band gap edge and the upper-frequency edge (Fig 2.10A and 2.10B and 2.10C respectively). Figure 2.10A clearly shows that the imaged mode corresponds to that of the apex resonator whilst Fig 2.10B and 2.10C shows light confined predominantly in the struts and air, respectively. This measurement therefore directly corroborates what could only be inferred from the Fresnel technique.

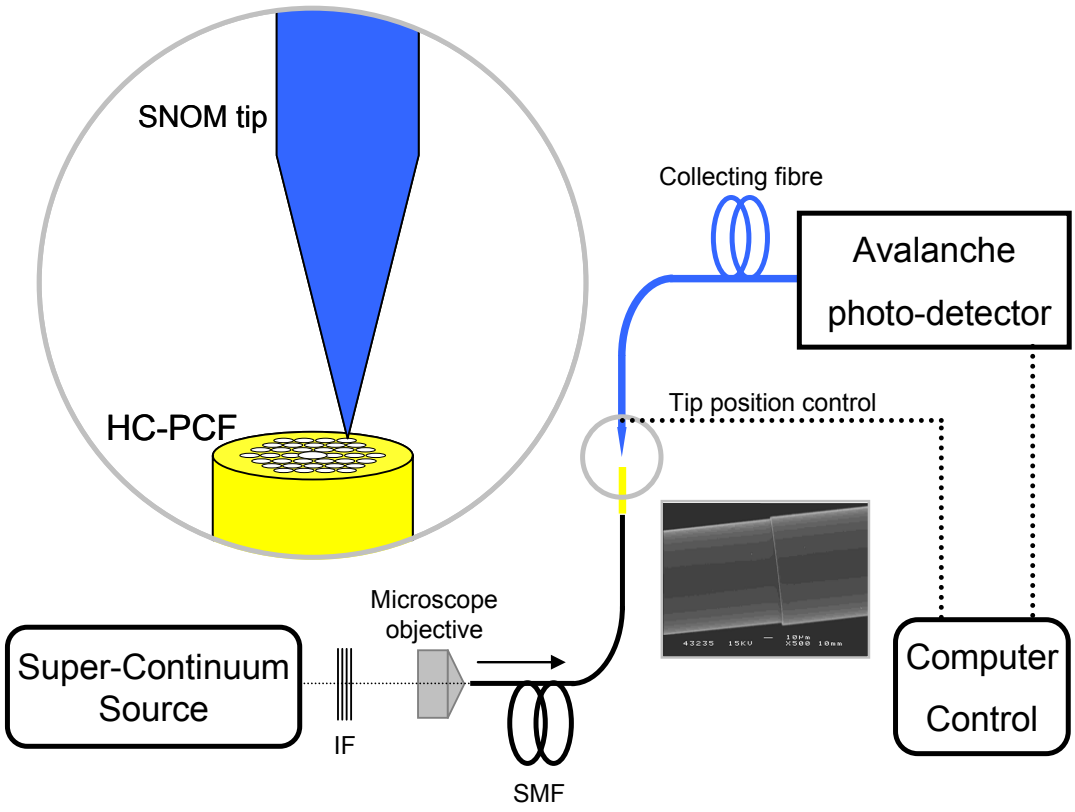

Fig. 2.9 Experimental setup for the near-field imaging of the HC-PCF's cladding using a SNOM tip in collection mode. IF: Interference filter.

Spatially resolved transmission spectrum of HC-PCF cladding

The advantage of a spatially resolved detection offered by the SNOM technique is that optical transmission spectra can be easily obtained for independent features of the fibre photonic crystal region and can therefore be used to verify that the relevant cladding and core modes show distinctive cut-offs relating to the fibre PBG location. An example of such discrimination between core and cladding spectrum is presented in Fig 2.11A for a HC-PCF guiding at 800nm and in Fig 2.11B and 2.11C for a HC-PCF guiding at 1064nm. As expected, the cladding's transmission cut-off corresponds closely to that of the core's PBG spectral boundaries, confirming that the DOPS decreases sharply inside the PBG region.

Thanks to its larger pitch, the 1064nm-guiding fibre offers a better separation between the constituent features of the cladding itself than the 800nm-guiding HC-PCF. When the tip is aligned with an interstitial apex, the transmission spectrum shows a cut-off around the same wavelength as that of the lower frequency edge of the PBG (solid black line in Fig 2.11C). This corresponds to the apex mode frequency cut-off near the air-line in accordance with the numerical simulation (Fig 2.5A). Similarly, for the strut and airy

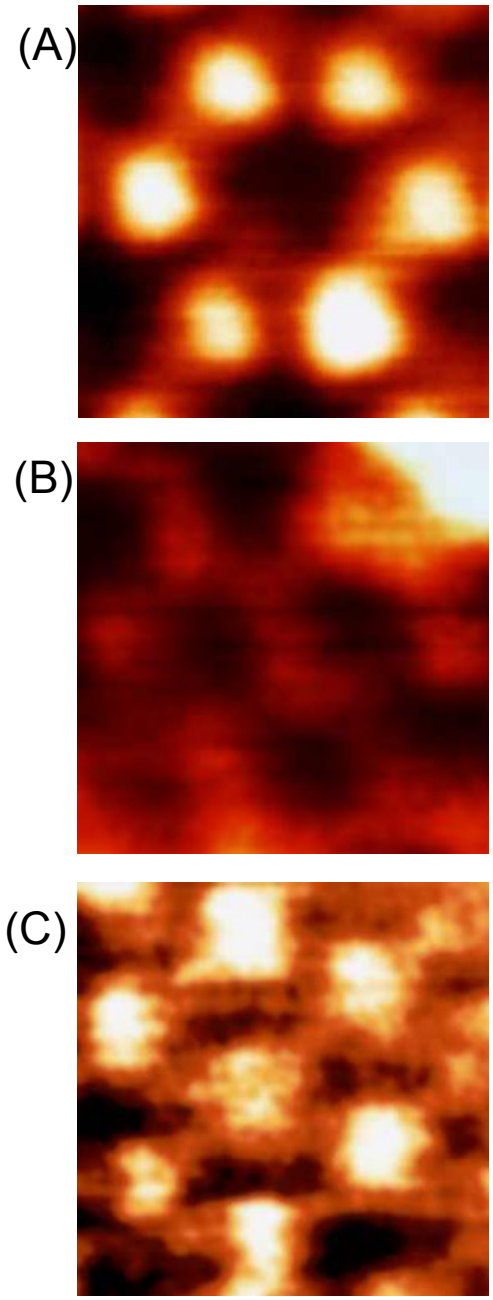

Fig. 2.10 SNOM images of the (A) "apex" mode (B) "strut" mode and (C) "airy" mode of the fibre cladding.

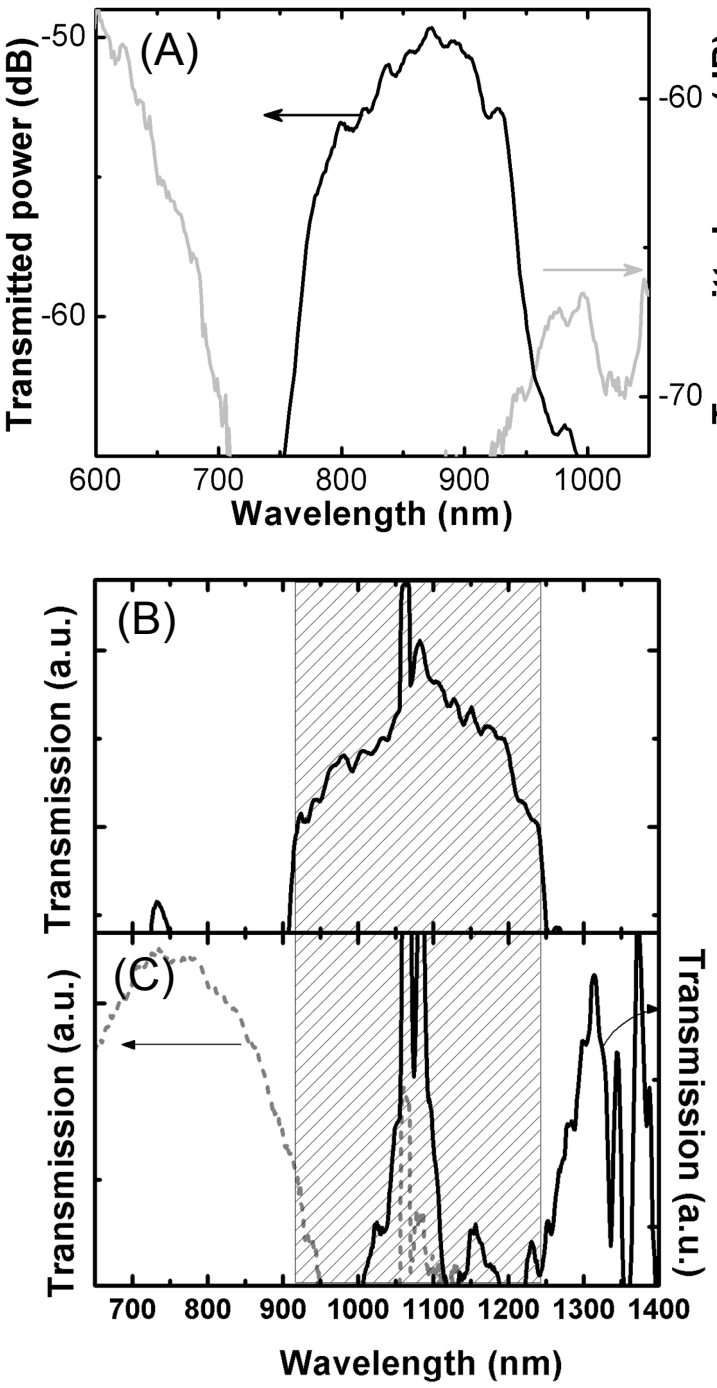

Fig. 2.11 (A) Optical spectrum of the HC-PCF guiding around 800nm taken with the SNOM tip aligned with the core (black line) and near an air-hole of the cladding (grey line), (B) Optical spectrum of the HC-PCF guiding around 1064nm taken with the SNOM tip aligned with the core, (C) with an interstitial apex (black solid line) and with an air hole of the cladding (grey doted line). The peaks around 1064nm are due to the residual super-continuum pump.

modes, the transmission spectrum shows a clear cut-off at the short wavelength side of the HC-PCF transmission bandwidth (grey line of Fig 2.11A and grey dotted line in Fig 2.11C). However, due to the limited spatial resolution of the SNOM and to the hybridization between the two constituent resonators, the transmission spectra collected when the tip was aligned on top of a strut or in an air hole do not show a measurable difference in their frequency cut-off.

2.4 Summary

Firstly, an experimental DOPS diagram was mapped by detecting light escaping from the side of a HC-PCF. Various guiding features such as cladding, core and surface modes or mode anti-crossing events were detected. The technique enables the optimisation of the transmission and more specifically the shift of the anti-crossings outside the PBG.

Secondly, the detection of the near-field profiles of cladding modes adjacent to the PBG region revealed the three relevant resonators responsible for the guidance: the apex, the strut and the air hole. It can be seen from this model that optimisation of the cladding structure could offer larger bandwidth. For example, thin struts would shift the resonant "strut" band to higher frequencies and increase the transmission span of the fibre.

The work reported in this chapter not only provides us with a better understanding of out-of-plane PBG formation in HC-PCF, it also offer routes to improve the optical attenuation and bandwidth of the fibre; two key characteristics required for non-linear experiments such as Raman scattering in H_2–filled HC-PCF, as reported in Chapters 4, 5 and 6.

References

[1] G. Antonopoulos, F. Benabid, T. A. Birks, D. M. Bird, J. C. Knight and P. St. J. Russell, *Opt. Express* **14**, 3000 (2006).

[2] P. Roberts, F. Couny, H. Sabert, B. Mangan, D. Williams, L. Farr, M. Mason, A. Tomlinson, T. Birks, J. Knight, and P. St. J. Russell, *Opt. Express* **13**, 236 (2005).

[3] H.-G. Unger, *Planar Optical Waveguides and Fibres*, Clarendon Press, Oxford, England (1977).

[4] M. E Lines, W. A. Reed, D. J. Di Giovanni and J. R. Hamblin, *Electron. Lett.* **35**, 1009 (1999).

[5] R. F. Cregan, J. C. Knight, P. St. J. Russell, P. J. Roberts, *J. Lightwave Technol.* **17**, 2138 (1999).

[6] A. F. Koenderink and W. L. Vos, *Phys. Rev. Lett.* **91**, 213902 (2003).

[7] P. Yeh and A. Yariv, "Bragg reflection waveguides," *Opt. Commun.* **19**, 427 (1976).

[8] P. Yeh, A. Yariv, and E. Marom, "Theory of Bragg fibre," *J. Opt. Soc. Am* **68**, 1196 (1978).

[9] P. Yeh, *Optical waves in layered media* (John Wiley and Sons, New York, 1988).

[10] N. W. Aschcroft and N. D. Mermin, *Solid state physics* (Saunders College, Philadelphia, PA19105, 1976).

[11] M. A. Duguay, Y. Kokubun, T. L. Koch and Loren Pfeiffer, *Appl. Phys. Lett.* **49**, 13 (1986).

[12] N. M. Litchinitser, A. K. Abeeluck, C. Headley and B. J. Eggleton, *Opt. Lett.* **27**, 1320 (2002).

[13] N. Litchinitser, S. Dunn, B. Usner, B. J. Eggleton, T. P. White, R. C. McPhedran and C. M. de Sterke, *Opt. Express* **11**, 1243 (2003).

[14] T. A. Birks, G. J. Pearce, and D. M. Bird, *Opt. Express* **14**, 9483 (2006).

[15] S. G. Johnson and J. D. Joannopoulos, *Opt. Express* **8**, 173 (2001).

[16] N. A. Mortensen and M. D. Nielsen, *Opt. Lett.* **29**, 349 (2004).

[17] J. Lægsgaard, *J. Opt. A: Pure Appl. Opt.* **6**, 798 (2004).

[18] F. Benabid and P. St. J. Russell, *Proceedings of SPIE:Photonic Crystal Materials and Devices III*, **5733**, 176, SPIE, San Jose (2005).

Chapter 3

Photonic Micro-Cells based on HC-PCF

This chapter presents the techniques adopted and equipment designed for loading gas into a HC-PCF and the realisation of a compact photonic micro-cell via fibre splicing. Specific methods have been developed for the fabrication of high pressure H_2 devices and low pressure gas-cells.

3.1 Introduction

Thanks to their low-loss photonic band gap guidance, HC-PCFs are up to a million times more efficient than glass capillaries at confining light into a small effective area over long distances, making it the ideal test-bed for gas-laser interaction in non-linear and quantum optics (Chapter 1). However, the realisation of all-fibre gas-laser devices based on gas-filled HC-PCF presents a series of challenges that need to be tackled before the fibre can be used in non-linear experiments such as Raman side bands generation.

The solutions adopted in this chapter for efficient gas loading in HC-PCF, at both high and low gas pressure and for the realisation of a photonic micro-cell based on gas-filled

HC-PCF are aimed at keeping the loss budget low in order to maintain the high gas-laser interaction efficiency offered by the fibre, as well as realising a compact and highly efficient all-fibre non-linear device.

3.2 Gas-Filled HC-PCF

Benabid et al. [1] first reported a HC-PCF filled with gas in a stimulated Raman scattering experiment in 2002, demonstrating a dramatic decrease in the power threshold required to achieve the non-linear effect. The realisation of the fibre gas-cell was done by applying a differential pressure between two gas control chambers, each containing one end of the fibre. Further SRS results confirmed the good conversion efficiency achieved in this configuration by reducing the power threshold by a factor of 10^6 (Section 5.2). However, the reliance on gas cells renders the system cumbersome and required careful laser alignment at the input of the fibre.

The stability and compactness of the device could be increased by hermetically splicing the HC-PCF to a piece of conventional solid core fibre* using a commercial fusion splicer, hence offering a compact, easy to use micro-cell solution utilising the full potential of the HC-PCF high gas-laser interaction efficiency.†

3.2.1 Differential pressure technique

The gas loading of HC-PCF is realised by applying a differential pressure between the two ends of the fibre (Fig 3.1). This is done by placing each fibre end in a gas control chamber that can be evacuated, or filled with the required gas.

The key advantage of the technique compared to simply placing the fibre inside a gas cell is that the fibre can be easily flushed of residual, unwanted gases that have accumulated inside its core and that an accurate monitoring of the gas loading process can be achieved simply by reading the pressure gauge of the gas control chambers.

---

* Generally, a solid core fibre that is single mode at the wavelength of operation (SMF)

† All improvements reported in this section have been developed jointly by Fetah Benabid, Philip Light and the author.

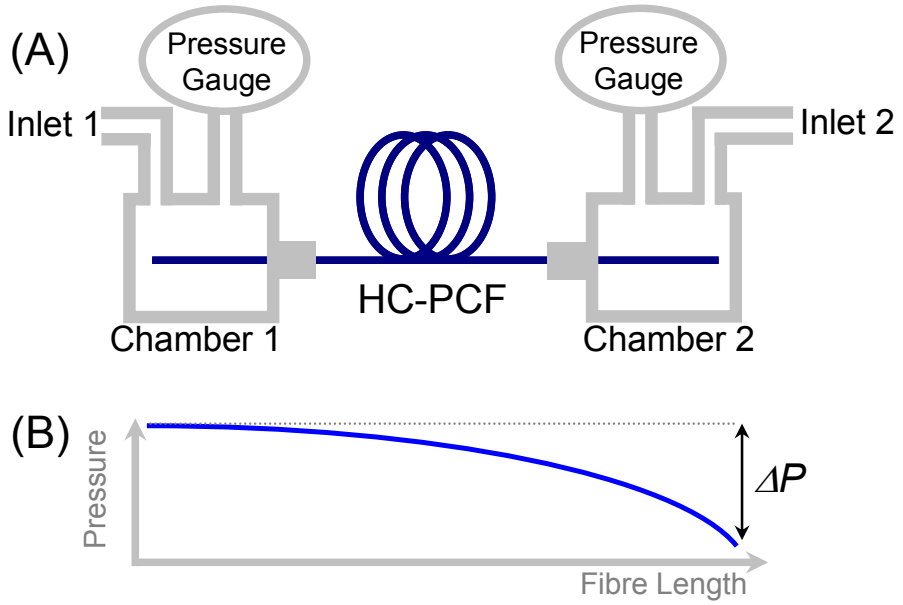

Fig 3.1 (A) Gas loading of HC-PCF using two pressure control chambers. (B) Schematic evolution of gas pressure distribution inside the HC-PCF as it is loaded. Filling one chamber with gas will induce a pressure differential along the HC-PCF.

Gas control chamber design

The gas control chambers consist of a ~1cm^3 cubic air-tight compartment with gas inlets on two of its sides (Fig 3.2). The back of the chamber is designed to feed the fibre through a metallic detachable gas-tight fibre holder. High-temperature resistant rubber throughputs compress against the fibre to avoid gas leakage. On the front side, a quartz window allows light to be coupled in and out of the fibre while it is inside the chamber. Anti-reflection (AR) coating on the window ensures the maximum coupling into the fibre, and avoids unwanted reflections. A metallic post is screwed onto the bottom side of the chamber for stability.

For high pressure applications, the chamber, similar to the one used in [1] (Fig 3.2A), is made of brass and operates at pressure up to 30bars. Gas can be introduced by one of the inlets (on the left of Fig 3.2A) while a mechanical pressure gauge is attached to the other side for pressure monitoring (on the right of Fig 3.2A). In this chamber, the interface between the fibre holder and the inner chamber compartment is made gas-tight by an O-ring, made of high-temperature resistant rubber.

For vacuum pressure applications (below 10^{-7}bars), however, this brass chamber is rendered useless by its high degassing rate. In order to avoid this problem, the chamber used at these low pressures is made of stainless steel (Fig 3.2B), which has a much lower degassing rate than brass. Similarly, a copper O-ring is used at the interface between the

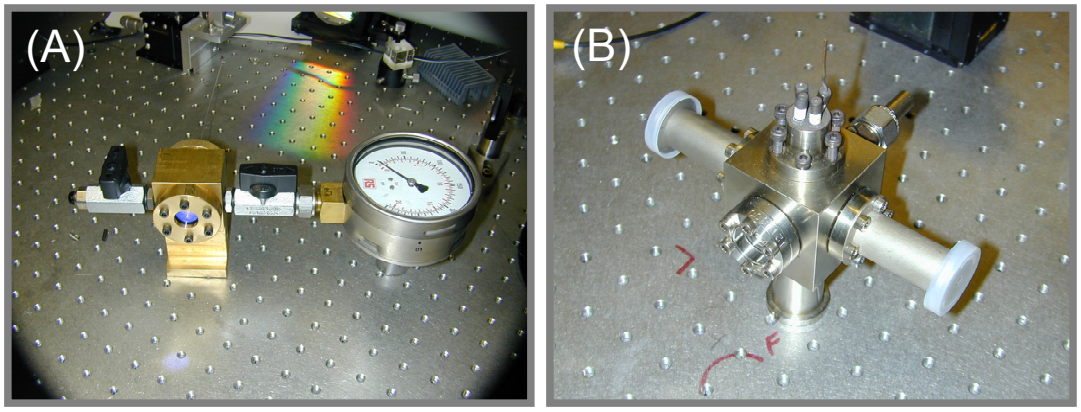

Fig. 3.2 (A) Brass gas control chamber for loading of high pressure gas and (B) stainless steel gas control chambers specially designed for vacuum applications

fibre holder and the inner chamber compartment to ensure excellent vacuum hermeticity. A Pirani or a Penning gauge replaces the mechanical pressure gauge for pressure monitoring and the gas inlets are fitted with vacuum grade tubing and valves. The top side of the chamber can potentially be used to insert additional equipment inside the chamber, like a Rubidium getter as seen in Fig 3.2B.

3.2.2 Fibre preparation for gas-filled HC-PCF

High pressure

Both ends of the HC-PCF are fed through a metallic holder, stripped of their protective coating and cleaved to ensure that no holes in the PCF structure are blocked by debris or dust. The fibre holders are then attached onto the chambers.

Fig 3.3 presents the high pressure gas loading process. The whole length of fibre is heated to 120°C on a hot plate for several hours. During this time, one chamber is filled with nitrogen gas (alternatively, helium) at a pressure above 5 bars whilst the other is evacuated using a mechanical pump (Fig 3.3A). This process removes any water or other vapour that could be trapped inside the fibre and avoids the fibre getting blocked by any residual material during the gas filling process. The first chamber is evacuated from any residual flushing gas and filled with the active gas (e.g. H_2) at pressure of up to 25 bars (Fig 3.3B). The fibre's internal pressure reaches equilibrium when the pressure gauge of both chambers reads the same value (Fig 3.3C). This is usually achieved after a few hours.

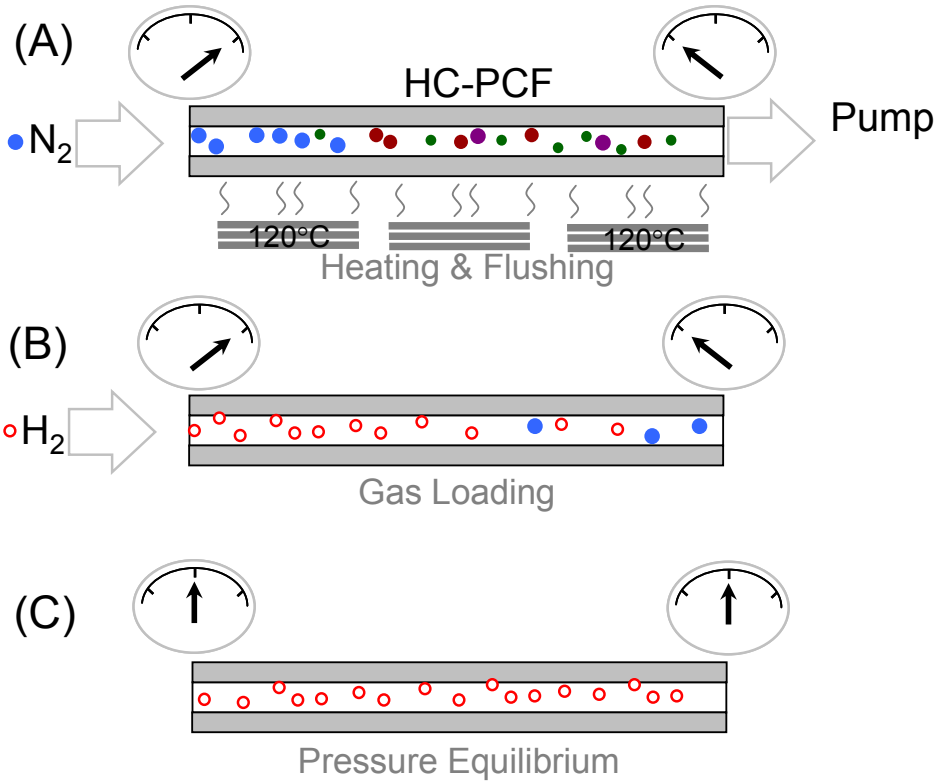

Fig. 3.3 Preparation of high pressure gas cells. (A) Heating and N_2 flushing of the fibre removes water and other impurities. (B) The gas loading process is done by differential pressure. (C) The gas cell is realised when the pressure is at the equilibrium, i.e. the pressure measured at the gauge of each chamber are identical.

Vacuum pressure

The preparation of low pressure gas cells only requires a few modifications to the high pressure gas filling process. In order to obtain low-contamination gas cells at such vacuum pressure, the second chamber is evacuated using a turbo pump or a high-vacuum mechanical pump below 10^{-4} mbar so that the flow of N_2 (or He) gas passing through the HC-PCF efficiently flushes impurity atoms or molecules out of the fibre. Next, both chambers are evacuated to a pressure of 10^{-7} mbar inside the HC-PCF. The fibre is then loaded with the required component such as the molecular gas acetylene (C_2H_2). The AR coated windows of the chambers allow for the actual gas pressure to be monitored via the linewidth of the component's absorption lines.

It is noteworthy that atomic vapours such as Rubidium (Rb) can also be loaded in polymer coated HC-PCF [2,3], opening new routes for the realisation of compact atomic clocks.

Advantages and limitations

The chambers allow excellent control over the pressure inside the fibre from 10^{-4} mbar to 30 bars, as well as the easy preparation of gas mixture. They are also crucial to the fabrication process of the all-fibre compact gas-laser devices presented in the following section.

Although an efficiency of up to 70% can be achieved in coupling a free-space laser beam into the chamber, the system is limited in the long term, by the mechanical stability of the alignment of the fibre with the laser beam. Additionally, potential thermal damage to the fibre end or the fibre holder can occur when using highly energetic lasers*. Lastly, the bulky design of the chambers, though needed to withstand the pressure imposed on the fibre, makes the system unwieldy.

To remedy these problems and render the system compact, easy to use and highly efficient, portable, all-fibre gas cells have been developed around the technique of HC-PCF splicing to conventional fibre.

3.2.3 Fusion splicing of HC-PCF to single mode fibre

The main issue when splicing any photonic crystal fibre is the deformation of the fine glass micro-structure (Fig 3.4). The problem is amplified when splicing HC-PCF due to their ultra-high air-filling fraction. Most fusion splicers commercially available rely on an electric arc between two electrodes in order to heat the fibres to be spliced and, although it is possible to gain control over the splicing parameters such as heating time and fibre-to-fibre pushing distance, the splicing temperature of these arc fusion splicers cannot be controlled as the arc is either on or off and cannot be set to a given temperature.

Although it has recently been proven to be possible [4], the splice loss incurred by using this technique is too high to create efficient gas cells. Another noteworthy method for splicing HC-PCF to conventional fibre consists of using a CO_2 laser to heat up the fibres [5] but yields even higher losses.

As a result, low-loss splices between PCF and conventional fibre are usually realised using a filament fusion splicer (fig 3.5A). The U-shaped tungsten filament that surrounds the fibres to be spliced (Fig 3.5B) allows accurate temperature control via the control of its electrical current. This large degree of freedom makes low-loss splicing HC-PCF to SMF possible [6].

---

* Such is the case with the 20W CW fibre laser used in Chapter 6

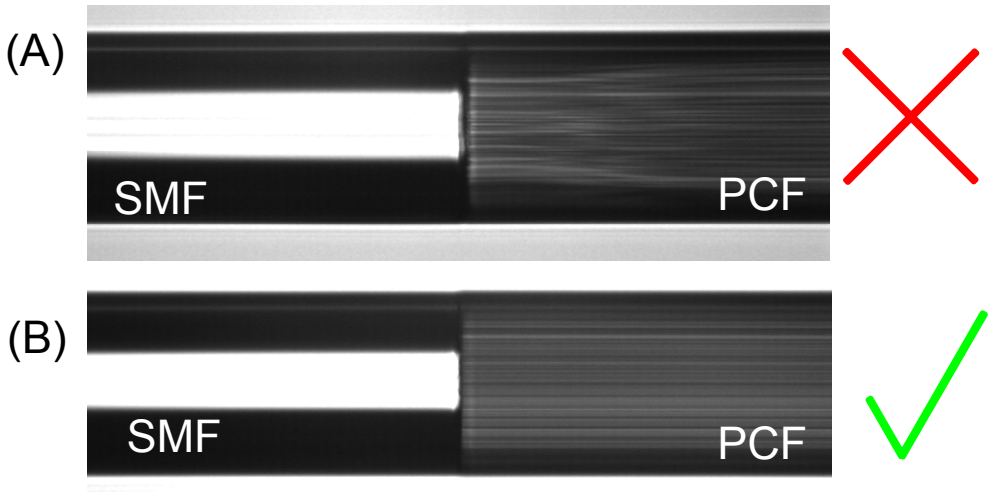

Fig. 3.4 (A) Deformation of PCF structure when splicing at high temperature, as in an arc fusion splicer. (B) Low-loss splice between PCF and SMF using a filament fusion splicer that allow control over the splice temperature

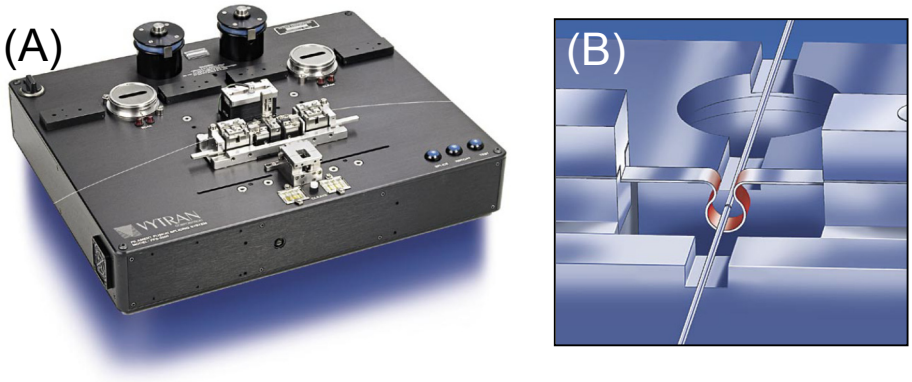

Fig. 3.5 (A) Filament fusion splicer (Vytran FFS2000). (B) Artistic view of the filament surrounding the two fibres to be spliced.

Low-loss HC-PCF/SMF splicing

Typical splice losses below 1dB have been reported for fibres guiding around 1550nm [6] (Fig 3.6A and B). A perfect splice would yield a loss of ~0.6-0.8 dB. Of this, 0.15 dB arises from the refractive index mismatch between the fibre cores (mainly, Fresnel reflection – Fig 3.7A). The modal field mismatch, which is estimated by the butt-joint approximation to be 0.4-0.6 dB in the case of 1550nm HC-PCF, is the principal source of loss at the splice (Fig 3.7B). Other microstructure deformations and fibre misalignment are estimated to contribute 0.1dB to the total splice loss (Fig 3.7C and 3.7D). The discrepancy between estimated and achieved splice losses is linked to the formation of a recess in the end-face of the HC-PCF when heated in the splicer (Fig 3.6C). The recess is believed to be the result of surface tension along the glass-air interfaces within the structure, the viscosity of which offers much less resistance to deformation than the solid glass in the outer-cladding of the fibre [6].

For HC-PCF operating at shorter wavelengths, the modal field mismatch becomes higher and consequently the splice loss increases. The typical values of 2dB/splice measured when splicing HC-PCF guiding at 1064nm is similar to what can be achieve by coupling in free-space, therefore maintaining the low loss budget of the system. However, the laser power stability, damage threshold, gas hermeticity and compactness offered by this technique means that these all-fibre devices can be used in portable, easy-to-use gas-laser systems.

3.3 All-Fibre Gas Devices Based on HC-PCF

Combining the process of gas loading in HC-PCF and the splicing technique presented above, a range of potential gas-phase photonic components such as gas lasers, sensors or reference etalons, becomes realisable. In this section, we present two examples of these photonic gas-phase devices. The first one is a high pressure micro-cell filled with H_2 reported by Fetah Benabid and the author in a Raman scattering experiment and was the object of a letter to Nature [7]. This gas-cell realisation technique is the object of a patent by Fetah Benabid and the author [8]. The second device consists of a vacuum pressure micro-cell reported to generate electromagnetically induced transparency (EIT) [9] and saturable absorption [10].

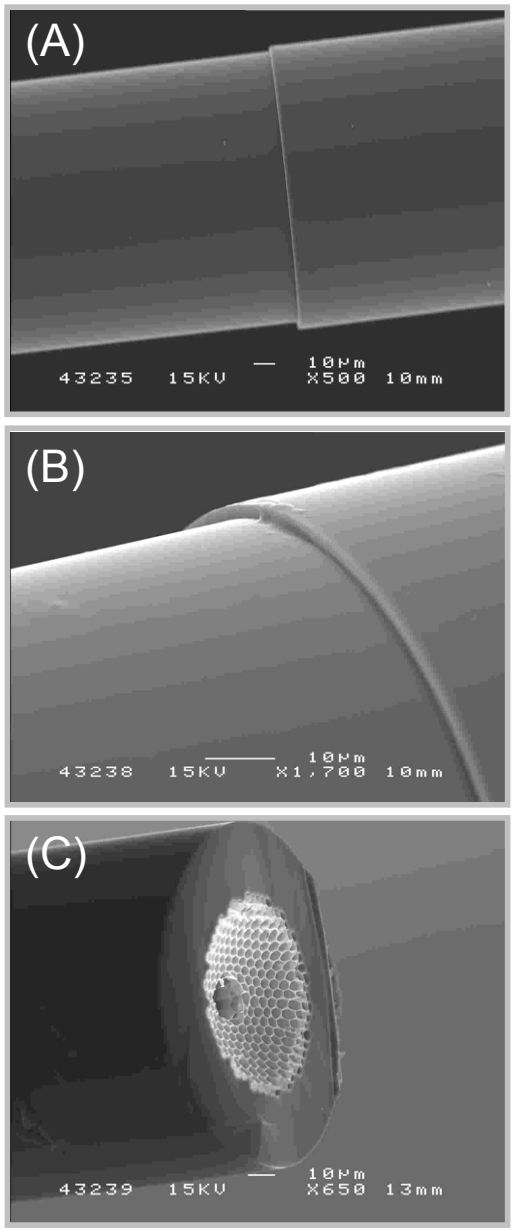

Fig. 3.6 (A) Scanning electron micrograph of the splice of HC-PCF to conventional single mode fibre. (B) Detail of the splice interface. (C) HC-PCF end face after splicing, showing the recess in the PCF region.

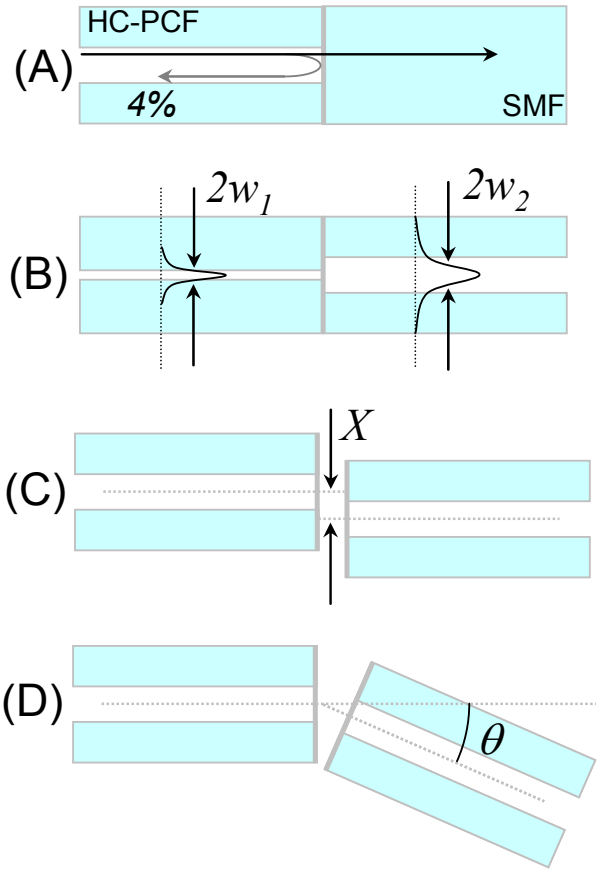

Fig. 3.7 HC-PCF/SMF splice loss can be broken down as (A) 0.15dB of Fresnel reflection, (B) 0.4dB due to mismatch between the modes supported by the two fibres and lastly, 0.1dB due to (C) fibre core misalignment and (D) angular mismatch between the fibres during the splice.

3.3.1 High pressure photonic micro-cell

Once the fibre is filled with the active gas at the required pressure following the process described in Section 3.2, each end of the HC-PCF is stripped of its acrylic coating, cleaved and spliced to SMF. Splice protectors are necessary to strengthen the splice as it is weaker than a conventional splice. As the pressure inside the HC-PCF is higher than the atmospheric pressure, there is no risk of contaminating the gas inside the fibre with air during the splicing process, although the splice does need to be quickly realised to limit the drop in pressure inside the fibre (Fig 3.8). The final device, compact and ready to use, is shown in Fig 3.9 in comparison to a match stick.

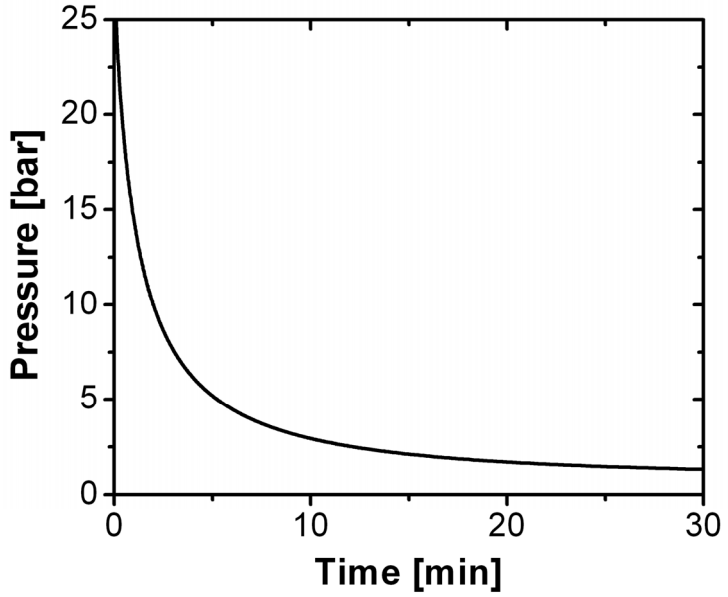

Fig. 3.8 Average pressure as a function of time for 10m of HC-PCF initially filled with 25bars of H_2 gas and with one end open to the atmosphere (the other end is spliced). It takes about a minute to perform the splice. During that time, the pressure inside the fibre will only have dropped by 25%. The calculation program was realised by Phil Light, using the gas flow equations found in [11].

Pressure limitation and gas diffusion

The pressure inside the HC-PCF is controlled whilst it is attached to the gas control chambers. The maximum experimental pressure tested on the fibre was 30bars, though this was limited only by the chamber's gauge maximum measurable pressure.

Although the splice shows strength equivalent to a gas pressure of 80 bars, of crucial importance for containing high pressure gases; when splicing the fibre to conventional solid core fibre, small leaks at pressure higher than 10bars have been observed at the splice interface. These can be avoided by applying glue to the splice, reducing the amount of gas leaked to the outside.

Long-term pressure stability problems arise when using gases (e.g. H_2 or He) that have a high permeation constant through fused silica. By considering the HC-PCF as a glass cylinder of outer and inner radii, r_{out} and r_{in}, equal to that of the silica jacket and the micro-structured cladding, respectively*, the pressure $P(t)$ inside the fibre at a time t after been spliced can then be written as:

* i.e. ignoring the presence of the thin silica webs of the fibre cladding.

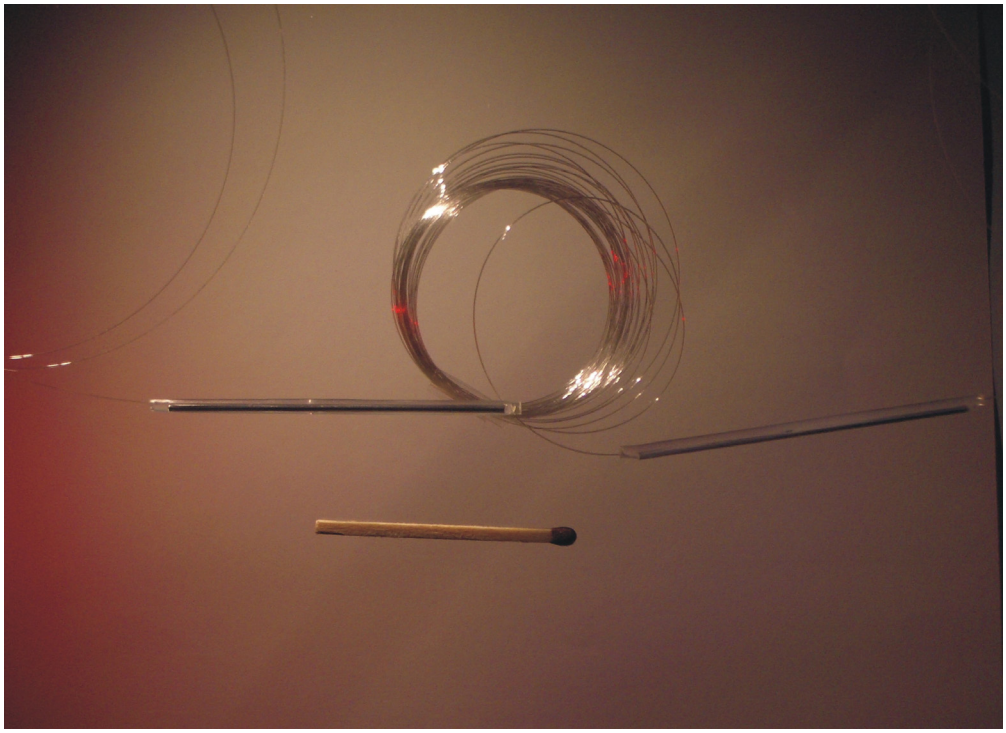

Fig. 3.9 HC-PCF based gas-cell compared to a match. The two metallic wires attached to the fibre are the splice protectors.

$$P(t) = P_0 e^{-Kt/\pi\left(r_{out}^2 - r_{in}^2\right)} \tag{3.1}$$

Here, K is the permeability of the molecule through silica* [12], P_0 is gas pressure at the time of the splice. This slow permeation of the gas through the fibre means that the device is not suitable for long term use. For example, a 10bar H_2 pressure gas-cell device, as shown in Fig 3.10, would be at atmospheric pressure after only 90 days.† This long-term pressure reduction will dramatically affect the performances of the gas cell in applications that require high pressure H_2 such as Raman scattering.

The high permeability of these molecules can, in some cases, be turned into an advantage, as in the following section, where Helium is used to fabricate low-loss, low-pressure gas cell devices.

3.3.2 Low pressure photonic micro-cell

Applications such as laser frequency stabilisation require monitoring of non-Doppler broadened absorption lines, usually achieved through saturable absorption [10] or electromagnetically induced transparency [9]. In the case of acetylene-filled HC-PCF, this

---

* K_{H2}=1.45 10^{-13} $cm^3.cm^{-2}.mm^{-1}.mmHg^{-1}$, K_{He}=1.25 10^{-10} $cm^3.cm^{-2}.mm^{-1}.mmHg^{-1}$.

† In good agreement with experimental observations

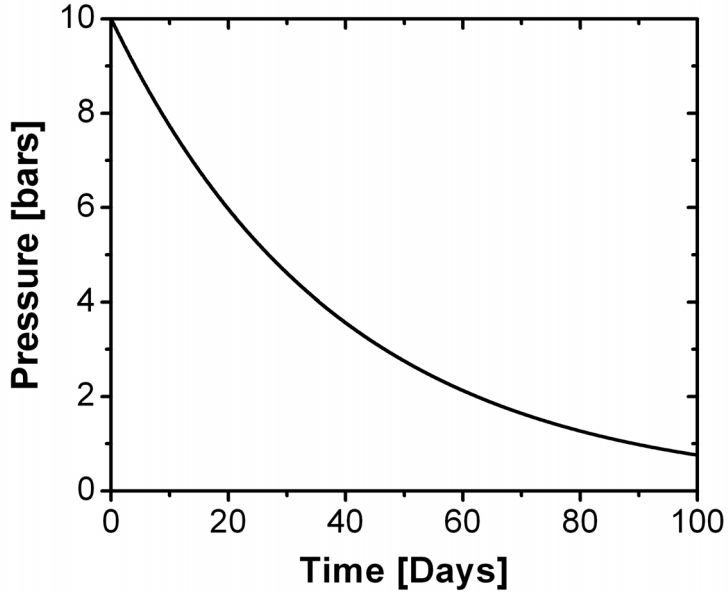

Fig. 3.10 Pressure inside a gas cell initially filled at 10bars as a function of time (at room temperature). Due to the H_2 permeation through a HC-PCF, the gas cell is unusable after 3 months.

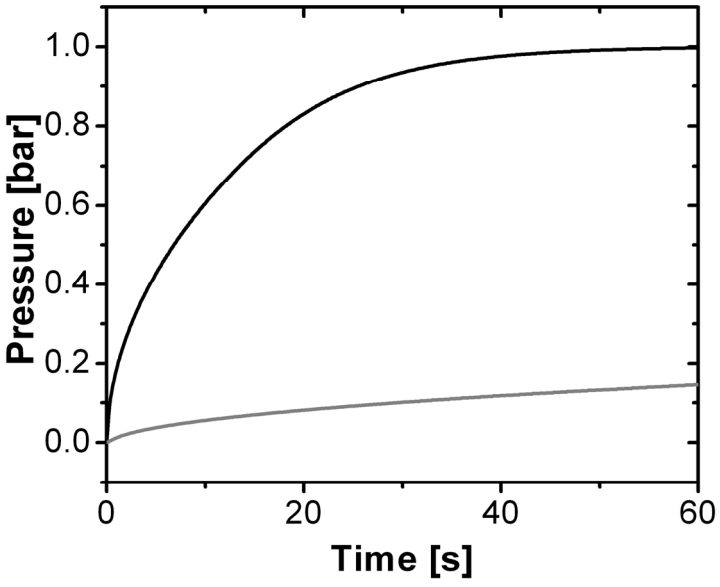

Fig 3.11 Average pressure as a function of time for a (black line) 1m-long and a (grey line) 10m-long HC-PCF filled with C_2H_2 at 1mbar. The calculation program was realised by Phil Light, using the gas flow equations found in [11].

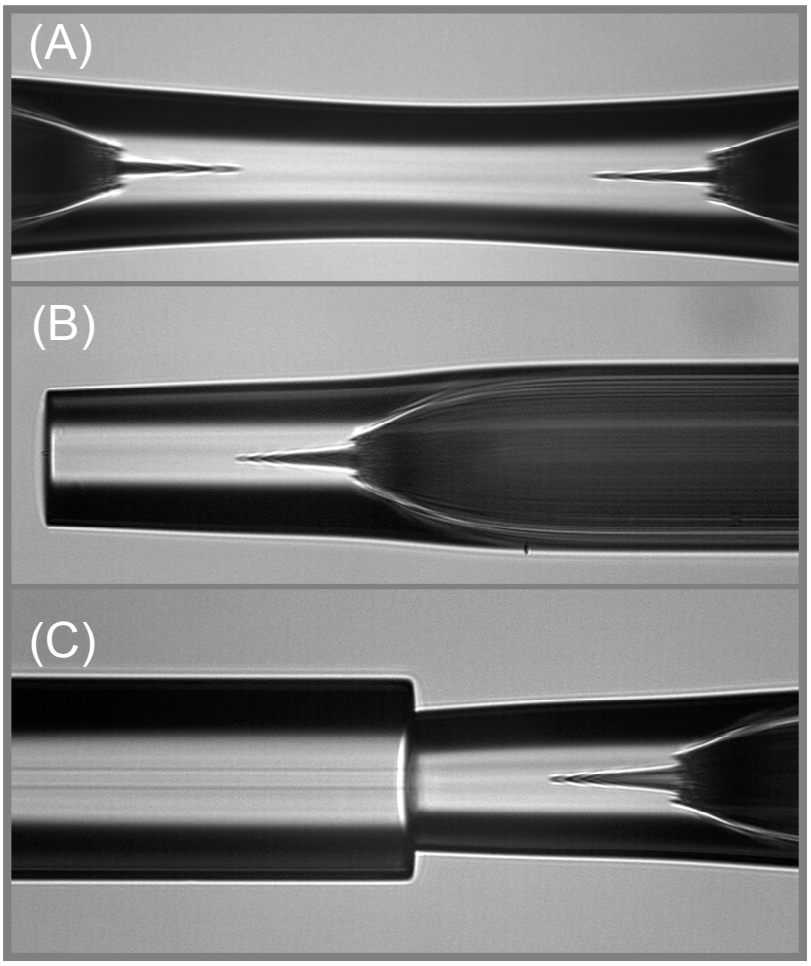

Fig. 3.12 (A) Side-view of the collapsed end of the HC-PCF. Due to its larger diameter, the core collapses slower than the cladding holes. (B) The fibre is then cleaved at the point of collapse and (C) spliced to single mode fibre.

means 1 to 10^{-4} mbars pressure inside the hollow core. The key issue when preparing an all-fibre low pressure all-fibre gas cell is the air contamination between the moment the fibre is cut off the gas control chamber and the moment it is spliced (Fig 3.11). Indeed, this preparation process takes up to a minute during which the internal pressure will increase, rendering the gas cell unusable. The following techniques have been developed to counter this drawback so that low pressure all-fibre gas cell with vacuum pressure and low insertion loss could be realised.

Collapsed end technique

Once the fibre has been flushed with high pressure nitrogen for a few hours, one end of the fibre is spliced to a conventional fibre; the other end remaining attached to the pressure chamber. The latter is evacuated using a mechanical pump, an adsorption vacuum pump, or a turbo vacuum pump before the active gas is introduced at the required pressure. Whilst keeping the fibre end hermetically attached to the pressure chamber, a section of

the fibre close to the open end is prepared and placed on the splicer to collapse the HC-PCF holes (Fig 3.12A). The fibre is then cleaved at the collapsed point (Fig 3.12B) and fusion-spliced to a conventional optical fibre (Fig 3.12C). The advantage of the technique is that no contamination is possible as the fibre crystalline structure is sealed and no impurity can penetrate the fibre. Both saturable absorption and EIT were observed in this device, making it an excellent candidate for frequency stabilisation applications [13]. However, the gas cell suffers from an insertion loss >10dB, mainly due to the splice loss at the collapsed end. Indeed, the slower collapse of the core hole compared to the rest of the structure results in a dramatic increase of the mode mismatch at the splice interface.

Diffusion technique based on Helium permeation

Another low pressure gas-cell preparation technique brings the loss figure down to the conventional 1-2 dB/splice. The novelty of the technique reported here resides in introducing helium gas inside the HC-PCF filled with vacuum pressure C_2H_2 in order to bring the total pressure inside the fibre to about 2 bars (Fig 3.13). This crucial step allows the remaining end of the HC-PCF to be fusion spliced to a conventional fibre under atmospheric conditions without contamination from outside gases. Furthermore, the high diffusion coefficient of helium through glass means that it will rapidly diffuse out through the fibre, leaving the initial low pressure acetylene inside the fibre. Thanks to the low loss splicing procedure at each end of the gas cell, the typical insertion loss has been measured to be typically 1.8 dB, corresponding, if one ignores the fibre transmission loss to a value of 0.9 dB per splice. Figure 3.14 show a typical sequence of how the transmission spectrum through the HC-PCF around the acetylene R15 absorption line evolves during the different steps of the fabrication process. The line is continuously compared to that of a commercial gas cell (Triad Co.) at a certified pressure value of 1 mbar. Figures 3.14A, 3.14B and 3.14C show the R15 line respectively (i) before loading the helium gas and splicing the second HC-PCF end (Fig 3.13A), (ii) ~2 hours after the gas-filled HC-PCF has been fully sealed showing the He induced broadening (Fig 3.13D) and (iii) ~7 hours after the second splice (Fig 3.13E). Figure 3.14(C) clearly shows the recovery of R15 absorption line and hence that the helium totally diffused out of the fibre in less than 7 hours. It is worth noting that the helium diffusion process can be sped up (~1 hour) by placing the HC-PCF gas cell in an evacuated chamber (10^{-2} mbar). Figure 3.14D shows the time evolution of the fibre's internal gas pressure, calculated from the Voigt fitting of the experimental absorption line [14] as the helium permeates through the fibre's silica jacket. The experimental pressure is observed to drop accordingly to the calculated He

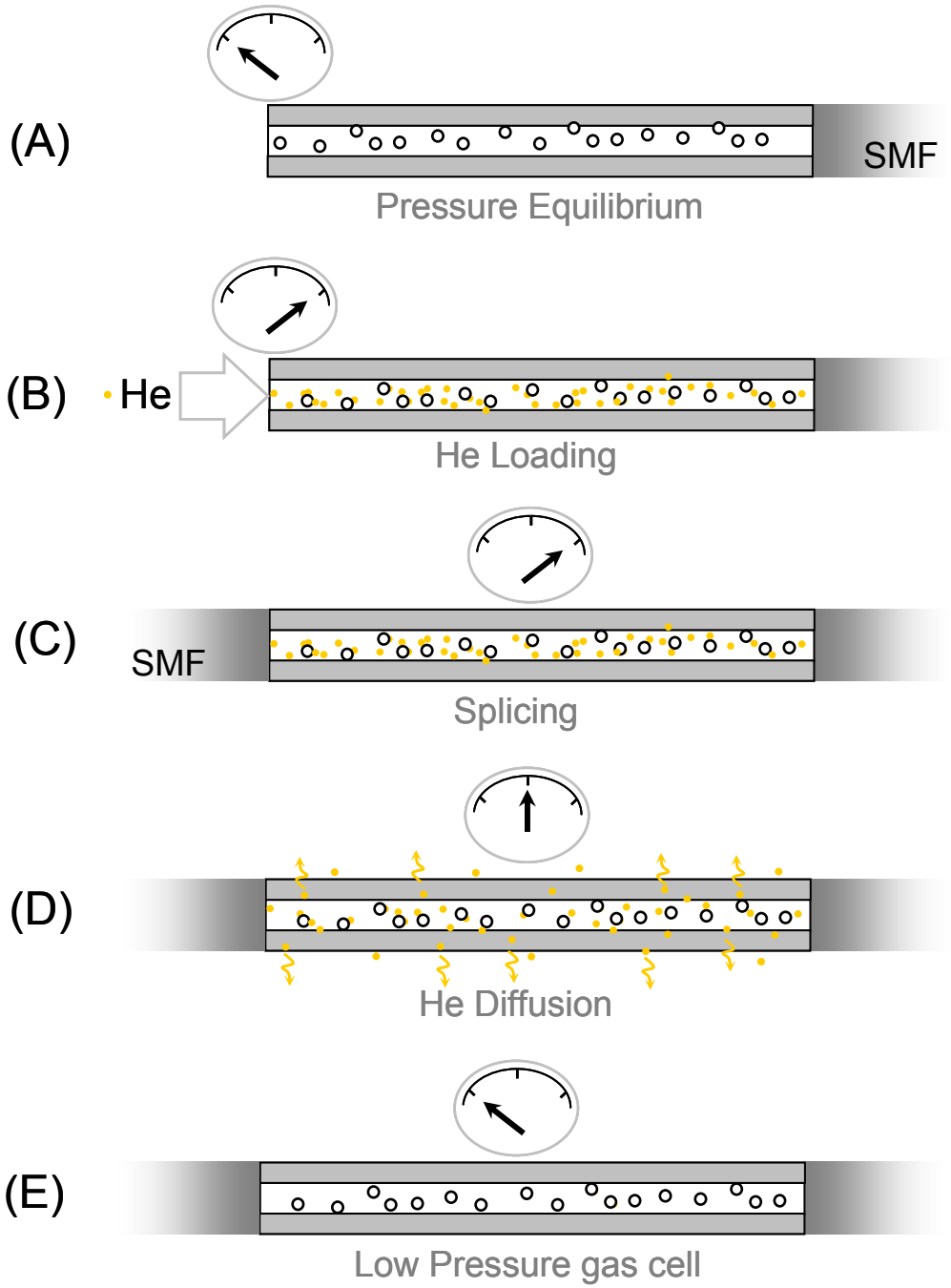

Fig. 3.13 Gas cell assembly procedure using Helium. (A) The HC-PCF with one end spliced to SMF is evacuated, baked and then loaded with acetylene at the desired filling pressure (B) The HC-PCF is loaded with helium at a pressure exceeding 1 atm and (C) its second end is spliced under atmospheric pressure. (D) The helium diffuses through the fibre (either in atmospheric or evacuated environment). (E) The end result is a gas cell with only the initial loaded acetylene.

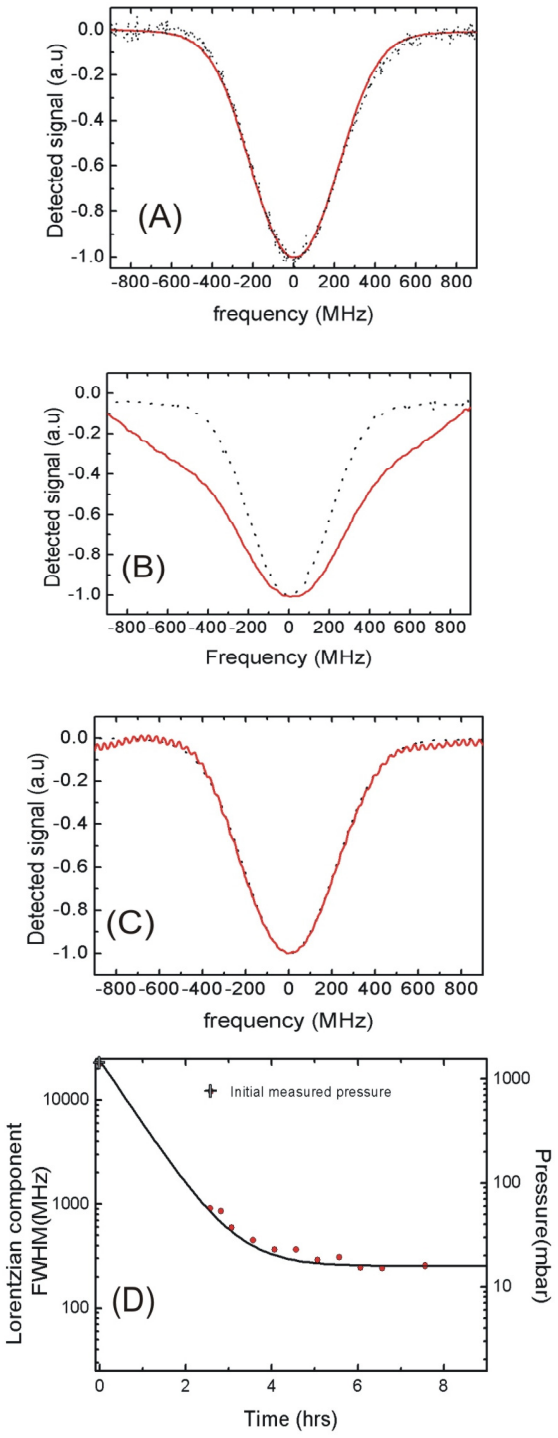

Fig. 3.14 Evolution of the shape of the acetylene R15 absorption line during the gas cell fabrication. The transmitted signal through a 1mbar commercial cell is given for reference (black dotted line). The red solid lines are the recorded transmitted signal through ~2 m HC-PCF when (A) one end of the fibre is still attached to a vacuum chamber, (B) during the helium permeation process and (C) after 7 hours, after total diffusion of He. The small oscillations are due to the etalon effect created between the two splices. (D) Experimental time evolution of the linewidth (FWHM) of the absorption line as the permeation takes place (filled circles and left hand vertical axis). The origin of time is taken at the time of splicing. The initial experimental point is deduced from the measured pressure. The solid line is the theoretical diffusion calculated from Eq. (3.1).

permeation rate, modelled using Eq. (3.1), before stabilising at a pressure of 12mbars, close to the initial C_2H_2 pressure of 10mbars.

Another effective method for accurately measuring the internal pressure of C_2H_2 in HC-PCF consists of realising EIT in the fibre and studying its pressure-dependent height and width. This method, described in details in [15], confirms that the technique allows the fabrication of µbar pressure gas cells with low insertion loss.

3.3.3 Advanced splicing for Fresnel reflection reduction

As described in Section 3.2, when a HC-PCF is spliced to conventional fibre, one is confronted with the problem of Fresnel reflection arising from the interface between the solid core of the conventional fibre and the air core of the HC-PCF, where ~4% of the incident laser power will be reflected back into the solid-core fibre. Optical feedback caused by this reflection can affect the stability of the laser source or even damage it, especially in case of a fibre laser. An example of such damage is the fibre fuse [16], as pictured in Fig 3.15, caused by a thermal shock wave travelling upstream from a normal splice to HC-PCF.

Moreover, these Fresnel reflections create etalon effects, highly parasitic in precision spectroscopy and laser metrology related applications such as saturable absorption in HC-PCF gas cells filled with a molecular gas or an atomic vapour [17-19] where a transmitted weak probe signal can interfere with the pump laser field reflected at the splice interface, making the observation of the saturation difficult.

This 4% reflection can, however, be reduced easily by altering the incident angle of the light on the interface, hence limiting the coupling of the reflected laser beam back into the silica fibre's core. Indeed, to avoid feedback by total internal reflection in the SMF, the incident angle has to be larger that the critical angle $\theta_c = sin(n_{cladding}/n_{core})$, where $n_{cladding}$ and n_{core} are the cladding and core refractive indexes of the SMF, respectively. A conventional fibre should therefore be cleaved at 8° angle so that the reflected light leaks out through the cladding to the outside. This solution has been implemented in the fibre optics industry as angled physical contact (APC) fibre connectors for high power laser delivery, with a typical return loss of -50dB. A similar result is expected from splicing a SMF28 and a HC-PCF guiding at 1550nm with an 8° angle, equivalent to having an APC connector coupled to the HC-PCF (Fig 3.16).

Angled cleave and splice

The angled cleave of both SMF and HC-PCF are realised using a cleaver (Oxford Fibre Ltd) that relies on shear stress to create the required angle. Special care is required in

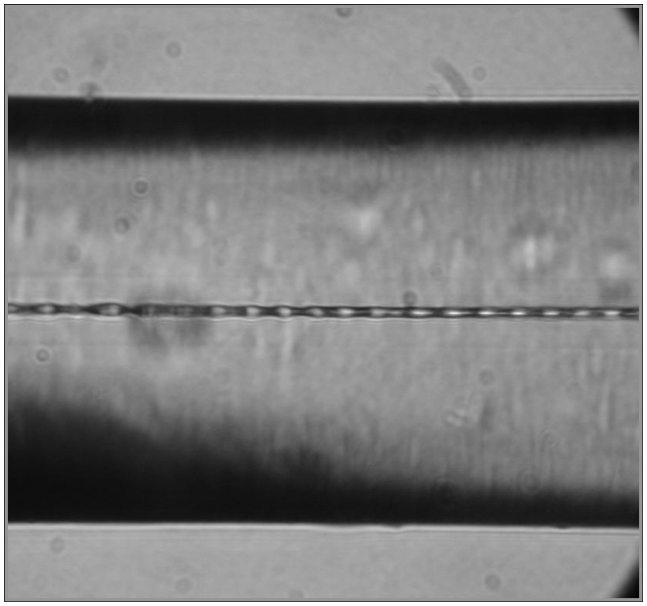

Fig. 3.15 Side view of a fibre fuse in the SMF28. The core has clearly been damaged by the fuse's thermal shock wave.

optimizing the tension exerted by the cleaver on the HC-PCF during the cleaving process to avoid crushing the fibre under shear stress.

The fibres are prepared at a complementary angle (Fig 3.17A), loaded onto the fusion filament splicer and are rotated so that the angled cleave of one fibre is parallel to that of the other. The optical transmission attenuation is monitored before (Fig 3.17B) and after the fibres are spliced together (Fig 3.17C and 3.17D), taking the end of the SMF28 as the reference for the loss measurement. The return loss is estimated from the ratio between the power detected at the output of a circulator placed at the input end of the monitoring setup and the input power (0dBm).

Splice Characterisation

Table 3.1 summarizes the optical transmission measurements of the fibre monitoring system when the fibres are butt-coupled before the splice, and after the fibre have been spliced, for a perpendicular cleave splice and for the angled cleave splice. The butt-coupling loss is comparable in both configurations. The small discrepancy could come from the difficulty in matching the angle exactly between the two fibres and therefore leaving a gap during the alignment process (Fig 3.17B). Once the angled fibres have been spliced, their transmission loss increases due to further misalignment of the fibres and to the alteration of the micro-structured cladding (see Fig 3.6C) during splicing. A typical splice loss of 3dB for the angled splice is achieved by improving the cleave angle repeatability and accurately controlling the splice angle. While the normal splice return loss of 16dB is

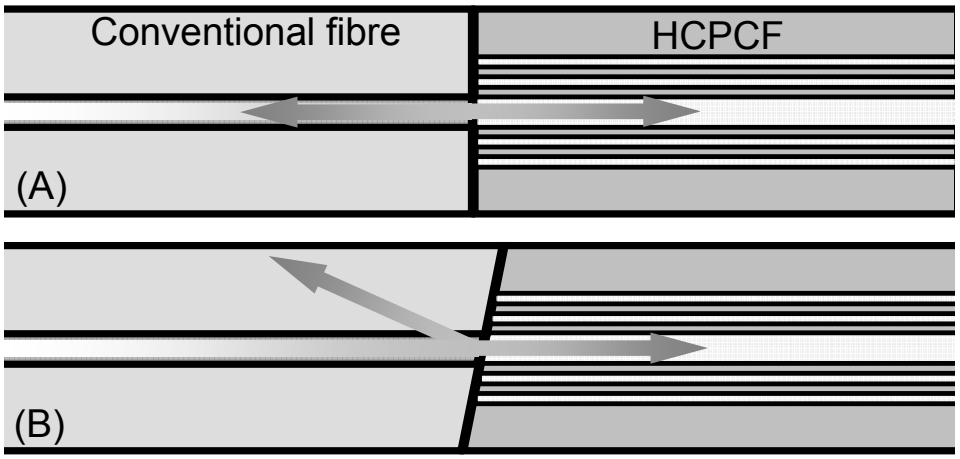

Fig. 3.16 Schematic (A) perpendicular and (B) angled splice between conventional fibre and HC-PCF. The Fresnel reflection is reduced thanks to the complementary angled cleaves of both fibres.

consistent with a 4% Fresnel reflection of the input laser power, the angled splice return loss is below the detector dynamic range (60dB). These loss values remain unchanged during the splicing process. This 44dB reflection reduction, combined with a transmission loss around 3dB, validates the method for low optical feedback HC-PCF gas cell devices, ideal for high power laser systems.

Table 3.1 Splice Optical Characteristics Comparison†

Splice Angle	Butt-Coupling Loss dB	Transmission Loss dB	Return Loss dB
0°	0.5	0.9	-16
8°	1.2	3.0	-60

† Typical value over 5 splices

Reduction of Fabry-Perot etalon effect in HC-PCF micro-cells

In order to corroborate the reflection reduction obtained with the splicing method described above, we fabricated two 1.7m-long C_2H_2-filled HC-PCF devices following the "Helium technique"; the first was prepared with a normal cleave, the other with an angled cleave. We used these gas cells in a counter propagating laser setup similar to the one use for saturable absorption in C_2H_2 in [17] (Fig 3.18). In this configuration, the Fresnel reflection from the normal splice of the fibre acts as a Fabry-Perot cavity that creates interferences when the laser frequency is scanned around an absorption line of acetylene (P13) as in Fig 3.19A. The calculated Fabry-Perot cavity length related to these interferences is 1.7m, close to the length of HC-PCF in the device. This confirms that

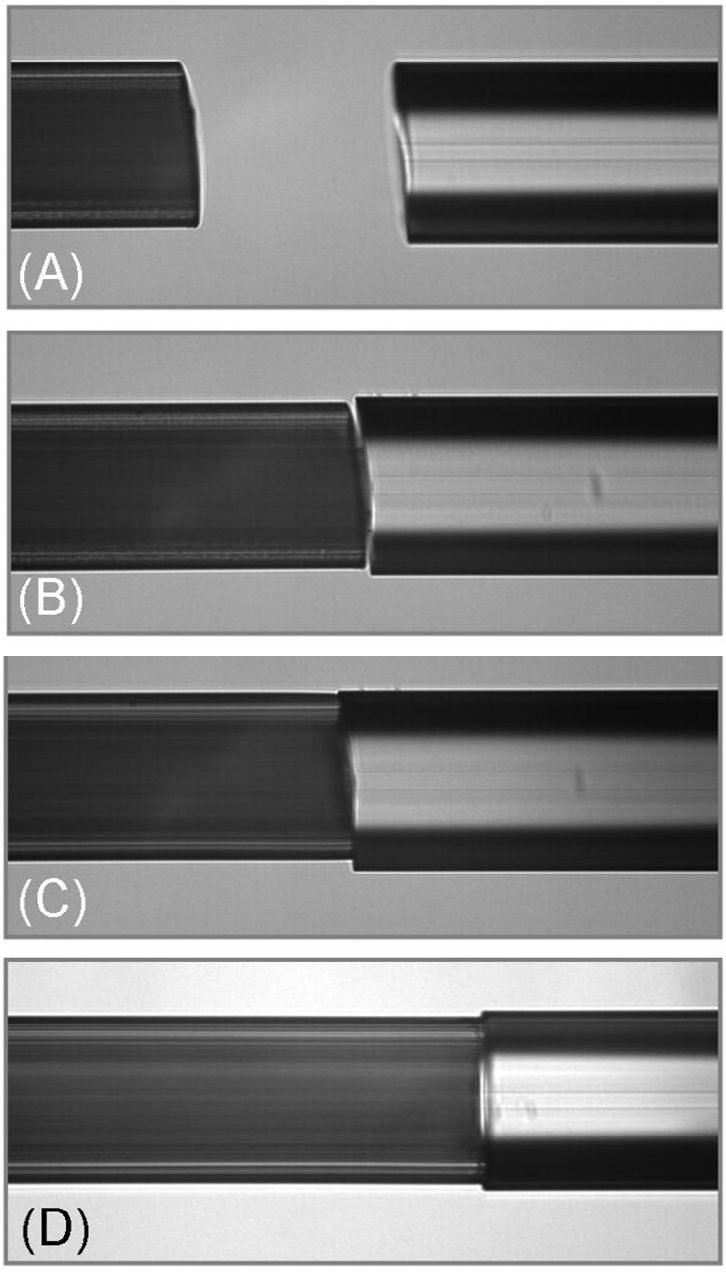

Fig. 3.17(A) Side view of the angle cleaved HC-PCF (left) and SMF28 (right). (B) Butt-coupling alignment of the fibres. (C) Side and (D) top view of the spliced fibres.

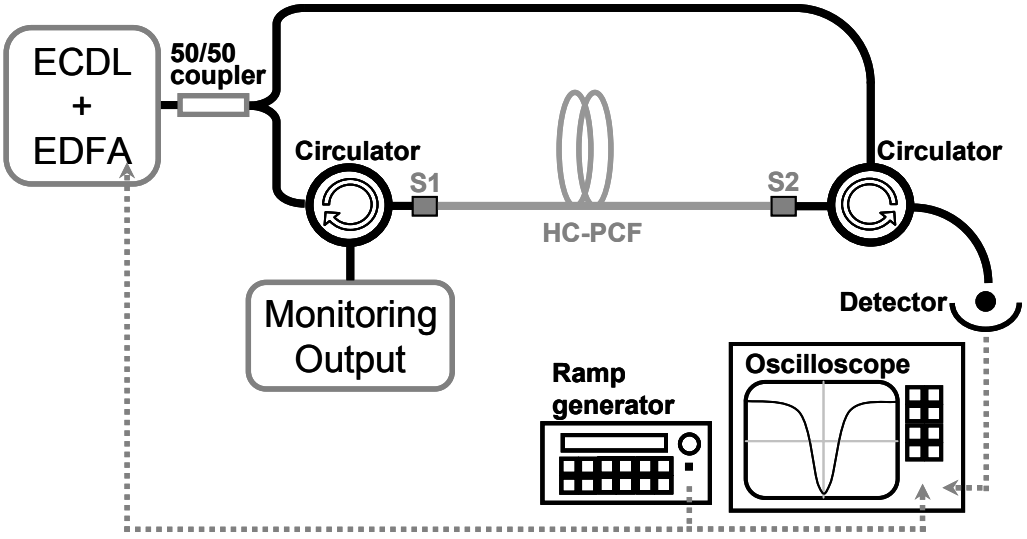

Fig. 3.18 Counter-propagating setup similar to the one used in saturable absorption [18]. A tuneable external cavity diode laser (ECDL) is coupled to an Erbium doped fibre amplifier (EDFA) and coupled to both sides of a HC-PCF gas cell via a 50/50 coupler. Circulators are used on both sides of the fibre to enable the detection of the absorption line on the oscilloscope.

these fringes appear from interferences between Fresnel reflections at the fibre's spliced ends. The detection of the absorption line is therefore made very difficult, as its linewidth (~500MHz) is very close to the frequency of the etalon (~200MHz). The only hint of the presence of the absorption line (black line in Fig 3.19A) is the reduction of the fringes amplitude around zero detuning.

Figure 3.19B presents a comparison of the back-reflected signal for the two fabricated gas cells in a part of the spectrum with no absorption line. Once again, large interference fringes are visible for the normal-cleave gas cell (in grey in Fig 3.19B). This interference pattern is dramatically reduced by the introduction of the angled cleave (in black in Fig 3.19B), together with the diminution of the average reflected power. This reduction is critical for the observation of faint non-linear gas-laser interaction effects.

3.4 Summary

All-fibre photonic micro-cells have been realised by combining the efficient loading of gas inside a HC-PCF thanks to the design of gas control chambers, and the splicing of the gas-filled HC-PCF to a conventional fibre with low loss. Specific techniques had to be developed for the realisation of low-loss, low-pressure gas cells for gas-laser applications interested in sub-Doppler features, such as EIT or saturable absorption. Additionally,

advances in the splicing process enabled a dramatic reduction in back-reflection and F-P etalon effects.

These photonic micro cells constitute a primary component in the realisation of the proposed optical waveform synthesiser (Section 1.3).

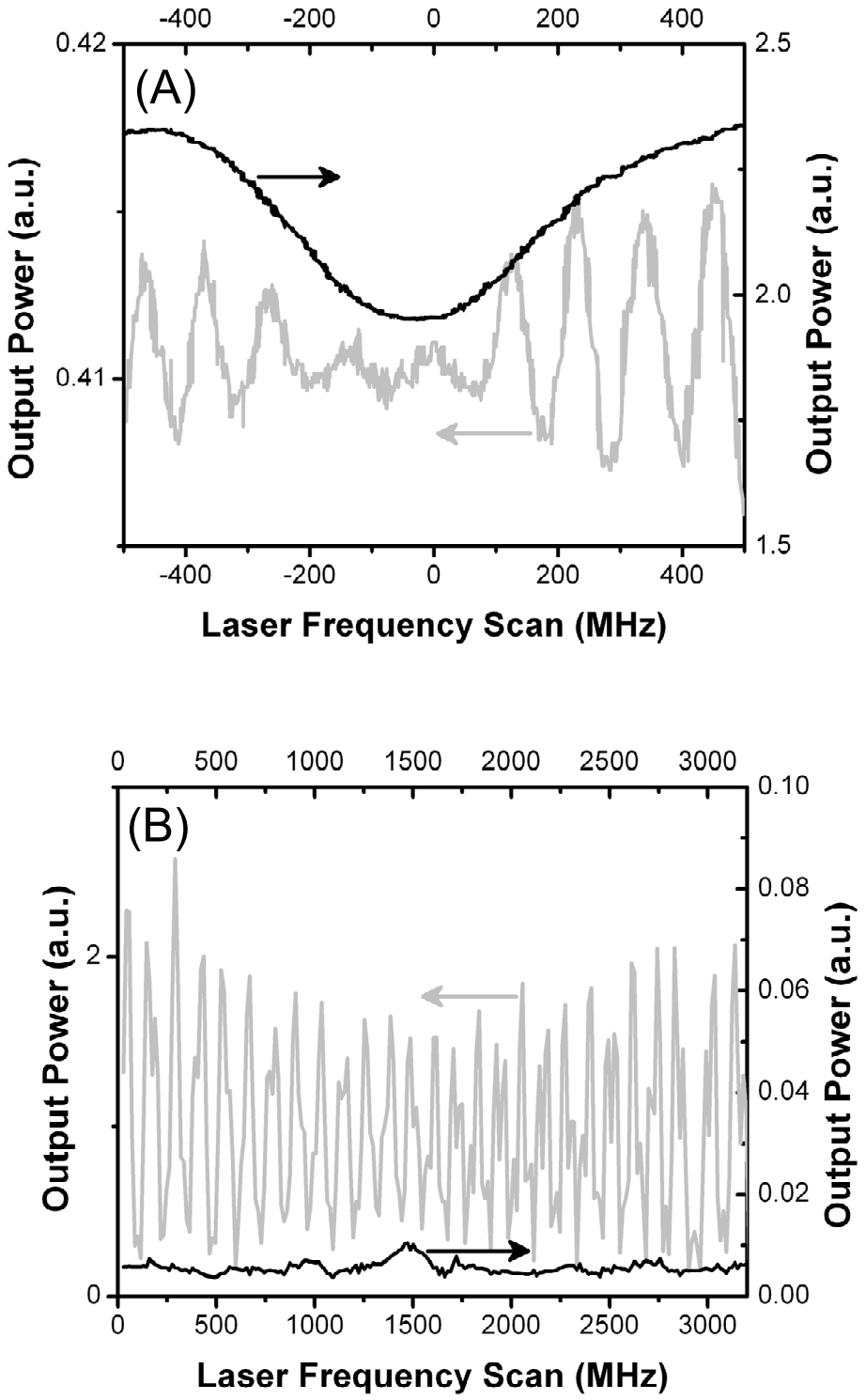

Fig. 3.19 (A) Reflected output power of a C_2H_2 gas-cell with perpendicular cleave versus laser detuning around the absorption line P13 of C_2H_2 (grey line). The interference pattern makes the detection of the line (black line) very difficult. (B) Output reflected power for the perpendicular (grey line) and the angle (black line) spliced HC-PCF gas cell. The fringes amplitude reduction is accompanied by a power reduction also due to the angle cleave.

References

[1] F. Benabid, J. C. Knight, G. Antonopoulos and P. St. J. Russell, *Science* **298**, 399 (2002).

[2] S. Ghosh, A. R. Bhagwat, C. K. Renshaw, S. Goh and A. L. Gaeta, *Phys. Rev. Lett.* **97** 023603 (2006).

[3] P. S. Light, F. Benabid, F. Couny, M. Maric, and A. N. Luiten, *Opt. Lett.* **32**, 1323-1325 (2007).

[4] R. Thapa, K. Knabe, K. L. Corwin, and B. R. Washburn, *Opt. Express* **14**, 9576-9583 (2006).

[5] J.H. Chong, M. K. Rao, Y. Zhu and P. Shum, *Photon. Tech. Lett.* **15** 942 (2003).

[6] L. Xiao, W. Jin, M. S. Demokan, H. L. Ho, Y. L. Hoo, and C. Zhao, *Opt. Express* **13** 9014 (2005).

[7] F. Benabid, F. Couny, J. C. Knight, T.A. Birks and P. St. J. Russell, *Nature* **434**, 488 (2005).

[8] F. Benabid, Patent N° WO 2006077437.

[9] K. J. Boller, A. Imamoglu and S. E. Harris, *Phys. Rev. Lett.* **66**, 2593 (1991).

[10] M. de Labachelerie, K. Nakagawa and M. Ohtsu, *Opt. Lett.* **19** 840 (1994).

[11] C.I Weng, W. L. Li and C. C. Hwang, *Nanotech.* **10** 373 (1999).

[12] S. Dushman and J. M. Lafferty, *Scientific Foundations of Vacuum Technique*, 2nd ed., Wiley (1962).

[13] F. Couny, P. S. Light, F. Benabid, and P. St. J. Russell, *Opt. Commun.* **253**, 28 (2006).

[14] W. C. Swann and S. L. Gilbert, *J. Opt. Soc. Am. B* **17**, 1263 (2000).

[15] P. S. Light, F. Couny and F. Benabid, *Opt. Lett.* **31**, 2538 (2006).

[16] D.P. Hand and P. St. J. Russell, *Opt. Lett.* **13**, 767 (1988).

[17] F. Couny, P.S. Light, and F. Benabid and P. St. J. Russell, *Opt. Comm.* **263**, 28 (2006)

[18] R. Thapa, K. Knabe, M. Faheem, A. Naweed, O. L. Weaver, and K. L. Corwin, *Opt. Lett.* **31**, 2489 (2006).

[19] P. S. Light, F. Couny, and F. Benabid, *Opt. Lett.* **31**, 2538 (2006).

Chapter 4

Stimulated Raman Scattering in Gas-Laser Devices based on HC-PCF: Theory

This chapter introduces the theoretical basics of stimulated Raman scattering (SRS) inside a H_2-filled HC-PCF and presents how the high confinement of the gas within the small core of the fibre affects amplification dynamics. Detailed theoretical predictions for pure rotational Raman amplification in a H_2-filled HC-PCF are obtained using these modified variables and a quantum mechanical approach.

4.1 Introduction

The realisation of the optical waveform synthesiser proposed in Chapter 1 relies on the efficient generation of Raman scattering in a HC-PCF filled with a Raman active gas, such as H_2. To give more insight into the experimental SRS results obtained in Chapter 5 and 6 using the photonic micro-cells described in Chapter 3, a reminder of the theoretical results for Raman amplification is given and applied to the present case of tightly confined Raman medium. Specific properties due to the unusually long interaction length achieved

in these micro-cells are emphasised, especially with regard to the generation of coherent SRS detailed in chapter 8.

Coupled-wave equations

The stimulated Raman scattering problem can be treated from different viewpoints: classically [1], semi-classically and quantum-mechanically [2-4]. All these models rely on coupled-wave equations linking the evolution of the pump and Stokes field to that of the excitation of the Raman medium. Within the quantum mechanic framework, these equations are based on the Maxwell-Bloch and Heisenberg equations*:

$$\frac{\partial \hat{E}_S}{\partial z} + \frac{1}{c}\frac{\partial \hat{E}_S}{\partial t} = -i\kappa_2 \hat{Q}^* E_L \tag{4.1a}$$

$$\frac{\partial \hat{Q}^*}{\partial t} = i\kappa_1 E_L^* \hat{E}_S - \Gamma \hat{Q}^* + \hat{F} \tag{4.1b}$$

Here, $\hat{E}_S$ is the (forward propagating) electric field operator for the continuum of radiation modes near the Stokes transition frequency† and $\hat{Q}$ is the slowly varying transition operator representing the field of molecules excitations and defined as the normal mode coordinate of the molecular motion. E_L is the laser field amplitude. The coupled constant κ_1 and κ_2 depend on the molecular polarisability of the medium and are linked to the Raman gain g_{SS} described in Chapter 1 by:

$$g_{SS} = \frac{2\kappa_1\kappa_2}{\Gamma} E_L^2 \tag{4.2}$$

Equation (4.1b) also includes the damping of the molecular oscillations due to collisions at the dephasing rate Γ and takes into account quantum fluctuations of the operator $\hat{Q}$ via the Langevin operator $\hat{F}$ [4].

These coupled equations show that the electric fields and the molecular motion couple together via the nonlinear term of the polarisability of the medium (i.e. κ_1 and κ_2). The interference between the molecular motion field $\hat{Q}$ and the electric pump field E_L drives the electric field E_S at the Stokes frequency. In turn, the interference of the two electric fields drives the molecular motion.

---

* The equations presented here are for a one dimensional system, limited to the Stokes generation and used with the slowly varying envelop approximation. A more complete, 3D theory is presented in [4].

† For long interaction length, only a single transverse spatial mode contributes to the emission.

Equations (4.1) are written in the limit of a single Stokes generation. Often, anti-Stokes emission arises from four-wave mixing process (Chapter 1.2); the intensity of which strongly depends on phase-matching conditions [5].

The aim of this chapter is to adapt this coupled-wave theory of SRS to the unusual case of a H_2-filled HC-PCF, where the gas-laser interaction length can exceed several metres and the gas is tightly confined inside a µm-sized hollow core. The theoretical Raman characteristics of such a system, like Raman linewidth, Raman gain and time-scale of the regimes of Raman amplification, help to understand the results obtained in Chapter 5 and 6 regarding the design of Raman gas fibre-lasers, and those obtained in Chapter 8 regarding coherent SRS in the transient regime of amplification.

4.2 Raman Characteristics of H_2-Filled HC-PCF

Molecular Hydrogen is the simplest molecule and has the largest Raman gain of all Raman active gases [6]. These two properties mean that the gas can be used for efficient Raman scattering applications (gas-laser [7,8], coherent Raman scattering [9-11]) and as a tool for the studies of the fundamental properties of Raman scattering process in gases [12,13]. In this section, the Raman characteristics of H_2 confined in a HC-PCF are presented, particularly the effect the molecular collisions with the fibre core walls have on the Raman linewidth and gain.

All calculations in Sections 4.2.2 and 4.2.3 are based on a 10µm core-diameter HC-PCF and a pump laser emitting at 1064nm (unless otherwise stated).

4.2.1 Raman transitions in Hydrogen

Three types of Raman molecular transitions are possible: vibrational, rotational and ro-vibrational. Vibrational energy levels are defined by their quantum number ν=0, 1, 2, 3... ν=0 being the ground state. The selection rule $\Delta\nu$= 0, ±1, ±2... applies for Raman transition between these energy levels. Each of these vibrational states have a fine structure of rotational states with quantum numbers J=0, 1, 2,... and the selection rule ΔJ= 0, ±2...* For molecular hydrogen at room temperature, most of the molecules are in the vibrational ground state ν=0 with ~75% in the rotational state J=1 (nuclear spin parallel, called ortho-H_2), and ~25% in J=0 (nuclear spin anti-parallel, called para-H_2).

* Two photon transition

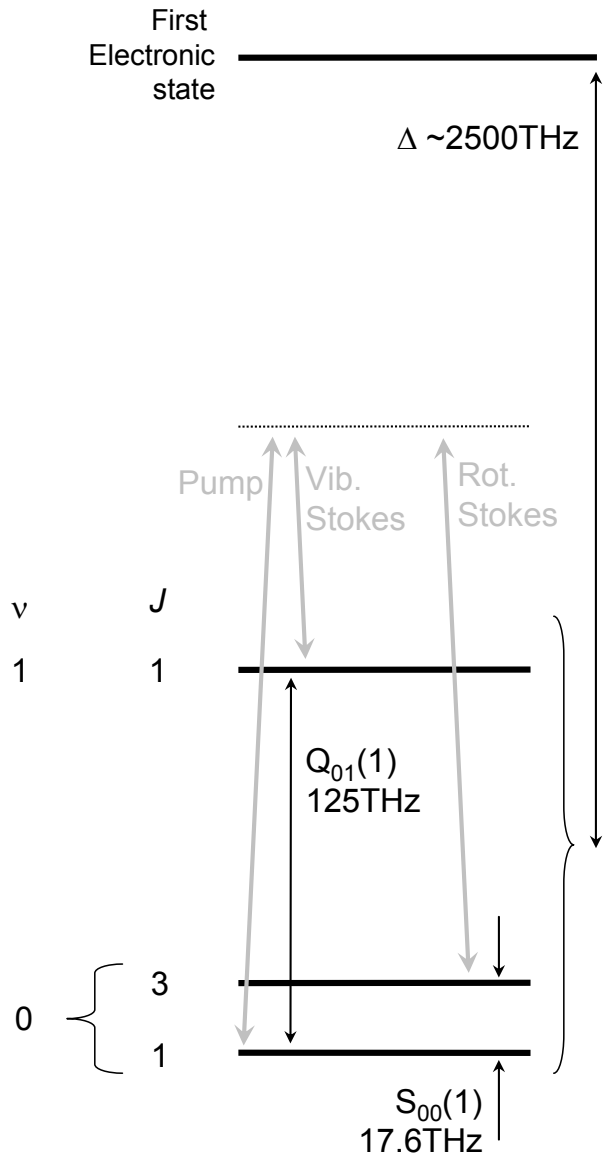

Fig. 4.1 Schematic representation of the energy level diagram for the vibrational and rotational transitions $Q_{01}(1)$ and $S_{00}(1)$ of molecular hydrogen in an off-resonance configuration.

Therefore, the most accessible Raman transitions*, written in the form $X_{\nu\nu'}(J)$ where ν (ν') is the initial (final) vibrational states and J is the quantum number of the initial rotational state, are the pure vibrational transition $Q_{01}(1)$ at a frequency of 4155 cm^{-1} (125THZ) and the pure rotational transition $S_{00}(1)$ of the ortho-H_2 at 587cm^{-1} (17.6THz) (Fig 4.1).

All Raman scattering experiments presented in this thesis are performed in an off-resonance configuration (away from the next electronic state; in H_2, Δ ~2500THz).

* At room temperature

Although the Raman gain g_{SS} in this situation is very small compared to what can be achieved in a near-resonance configuration, the frequency dependence of g_{SS} is reduced and accidental population of higher electronic energy levels does not come into play, making the Stokes conversion very efficient and easily frequency tuneable.

The Raman linewidth and gain of both vibrational and rotational Raman transitions in H_2 depend on pressure and temperature. In the unusual case of hydrogen trapped inside the air-core of a HC-PCF, these Raman characteristics are also modified by the molecular dephasing due to collisions with the core walls.

4.2.2 Hydrogen Raman linewidth in a confined medium

The role of the Raman transition linewidth Γ in the SRS process is two-fold. Not only does Γ strongly affect the Raman gain g_{SS}, it is also the limiting factor in applications requiring high molecular coherence, such as higher-order SRS and Raman sideband generation, and in gas-laser applications, where the Stokes line is to be used as a narrow-linewidth laser radiation. Consequently, one needs to establish the effect the confined geometry of a HC-PCF has on this Raman characteristic. The total Raman linewidth Γ of the system is composed of the natural Raman linewidth, Γ_R, additional pump laser linewidth (considered negligible in the following) and the linewidth γ_{wall} due to the collisions with the wall of the fibre's core. The latter comes into play at low pressure, when the mean-free-path of the gas molecules becomes as long as the core radius.

Wall collision linewidth

The dephasing rate (or linewidth) γ_{wall} due to the collisions with the hollow core wall can be considered as an escape rate [14,15] on the hard sphere model:

$$\gamma_{wall} = 2.405^2 \frac{D_0}{R^2\left(1 + C\frac{\lambda_{mfp}}{R}\right)} \tag{4.3}$$

R is the radius of the fibre core, λ_{mfp} is the mean free path of the molecule, C is a constant depending on the kind of collisional process (in the hard-sphere limit, C=6.8) and the value of 2.405 comes from the lowest zero of the 0^{th}-order Bessel function.

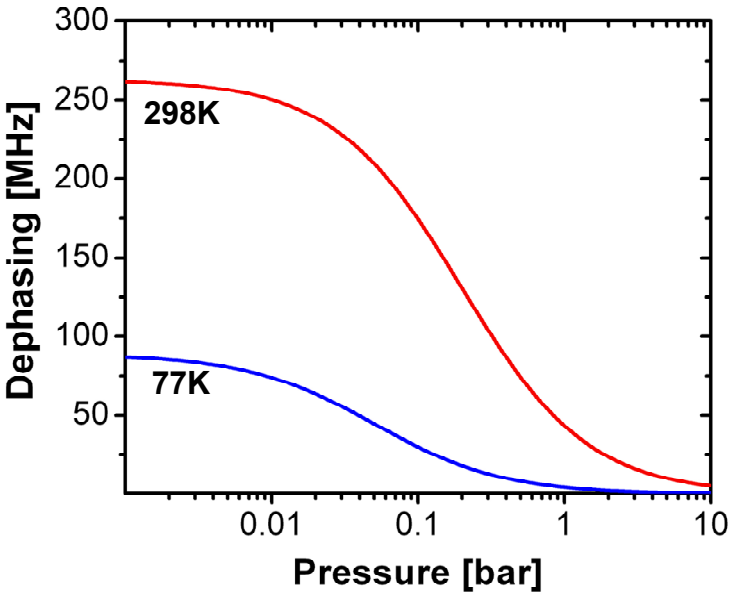

Fig. 4.2 Dephasing rate γ_{wall} due to collisions of gas molecules with the HC-PCF core wall as a function of pressure at (red line) room temperature (298K) and (blue line) liquid nitrogen temperature (77K).

The molecular self-diffusion coefficient D_0 is calculated from the Chapman-Enskog theory of diffusion and depends on the pressure P (in atmosphere) and temperature T (in Kelvin) [16] of the Raman medium:

$$D_0 = \frac{186.10^{-5} T^{3/2}}{1.273 P \sigma_{\text{Å}}^{\ 2}} \sqrt{\frac{2}{MW}} \tag{4.4}$$

The molecular cross section $\sigma_{\text{Å}}$ of H_2 is 2.827Å, and its molecular weight MW is 2.02amu. The mean free path of the molecule λ_{mfp} also depends on pressure and temperature and can be expressed as a function of the molecular cross section area of molecule $\pi\sigma_{\text{Å}}^{\ 2}$ and Boltzmann constant k_B as [16]:

$$\lambda_{mfp} = \frac{k_B T}{P} \frac{1}{\sqrt{2}} \frac{1}{\pi \sigma_A^2} \tag{4.5}$$

Figure 4.2 presents the linewidth γ_{wall} as a function of pressure at room temperature (298K) and liquid nitrogen temperature (77K). This collisional dephasing is below 100MHz at pressures above 1bar and only comes into play at low pressure, when the mean-free path λ_{mfp} of the molecule becomes larger than the fibre's core diameter R. It plateaus below 10mbars at a value of about 250MHz at room temperature and can therefore become the dominant dephasing process at such low pressure. However, the contribution

of this dephasing to the total linewidth can be considerably lessened by operating at low temperature, or by using a fibre with a larger core.

Natural Raman linewidth

The natural linewidth of a Raman transition depends on the type of transition considered. Based on experimental measurements, empirical expressions of the linewidth of the $Q_{01}(1)$ and $S_{00}(1)$ transitions of H_2 in free-space have been reported in 1986 by Bischel, Dyer and Herring [12,13] as a function of the temperature T and of the molecular density ρ of the gas*.

The temperature and density dependence of the Raman linewidth Γ_{vib} of the vibrational transition $Q_{01}(1)$ is fully described in the expression given in [12]:

$$\Gamma_{vib} = \frac{309}{(\rho + p)}\left(\frac{T}{298}\right)^{0.92} + \left[51.8 + 0.152(T-298) + 4.85\times10^{-4}(T-298)^2\right]\rho \qquad (4.6)$$

The parameter p was not added in [12] but is required to obtain the correct Doppler linewidth in the zero-pressure limit†:

$$\Gamma_{vib}^{\rho=0} = \Delta\nu_D = 7.15\times10^{-7}\nu_R\sqrt{\frac{T}{MW}} \qquad (4.7)$$

with ν_R the Raman frequency in MHz. It follows that p=0.286amg at 298K and p=0.163amg at 77K.

No direct expression is found, however, for the Raman linewidth Γ_{rot} of the rotational transition $S_{00}(1)$, though the empirical expression takes a similar form to that of the vibrational:

$$\Gamma_{rot} = \frac{A}{\rho + p} + B\rho \qquad (4.8)$$

B is a pressure broadening coefficient equal to 108MHz/amagat at 295K and 104MHz/amagat at 77K [12]. The parameter p in this rotational configuration is

---

* expressed in amagat (amg) as a function of pressure P and temperature T as

$$\rho(amagat) = \frac{T_0}{T}\frac{P}{P_0}$$

where T_0 and P_0 are the standard temperature (273.15K) and pressure (1atm), respectively. At room temperature (298.15K), a pressure of 1atm corresponds to 0.916amg, while at liquid nitrogen temperature (77K), it corresponds to 3.55amg.

† for densities lower that the cut-off ρ_C=3.33$A/\Delta\nu_D$ [12]

calculated to be p=3.8 10^{-2} amg at 295K and p=2.5 10^{-2} amg at 77K (from the condition imposed in Eq. 4.7). A is a coefficient related to the self diffusion coefficient D_0 by:

$$A = 4\pi k_R^2 D_0(\rho) \tag{4.9}$$

where k_R is the wave number of the Raman transition (k_R=586.90cm^{-1}). From Eq. 4.4, $D_0(\rho)$ is calculated to be 1.32 cm^2.amg.s^{-1} at room temperature and 0.44 cm^2.amg.s^{-1} at liquid nitrogen temperature.

Both vibrational and rotational Raman linewidth are plotted in Fig 4.3 as a function of pressure and at 295k and 77K. The linewidth of both Raman transitions is composed of three pressure ranges. At low pressure, the linewidth is dominated by Doppler broadening, leading to the vibrational linewidth being larger than the rotational one. As the pressure is increased, collisional narrowing (also called Dicke narrowing) is observed [17]. This occurs when the mean free path λ_{mfp} of the molecules is of the same order as the Raman wavelength. Finally, collisional broadening occurs at high pressure. In this regime, the rotational dephasing becomes larger than the vibrational Raman transition linewidth.

Total linewidth

The total Raman linewidths of H_2 confined in a HC-PCF is the sum of the natural linewidth (Γ_{vib} or Γ_{rot}) and the wall collision linewidth γ_{wall}. From the results above, one can see that the influence of γ_{wall} is negligible except in the Doppler-broadened pressure regime (below 100mbar), where the collisions with the fibre's core wall start to have an effect. As a matter of fact, γ_{wall} can even become the dominant dephasing process for the rotational Raman transition, as in the example presented in this section considering a fibre with a 10µm core diameter. Therefore, this could have detrimental effects in low pressure applications where a small linewidth is critical. One could, however, overcome this limitation by using a fibre with a larger core.

As well as its linewidth, the frequency of the Raman transition is also linearly dependent on pressure and temperature [18], offering some wavelength tuning control over the generated Stokes radiation.

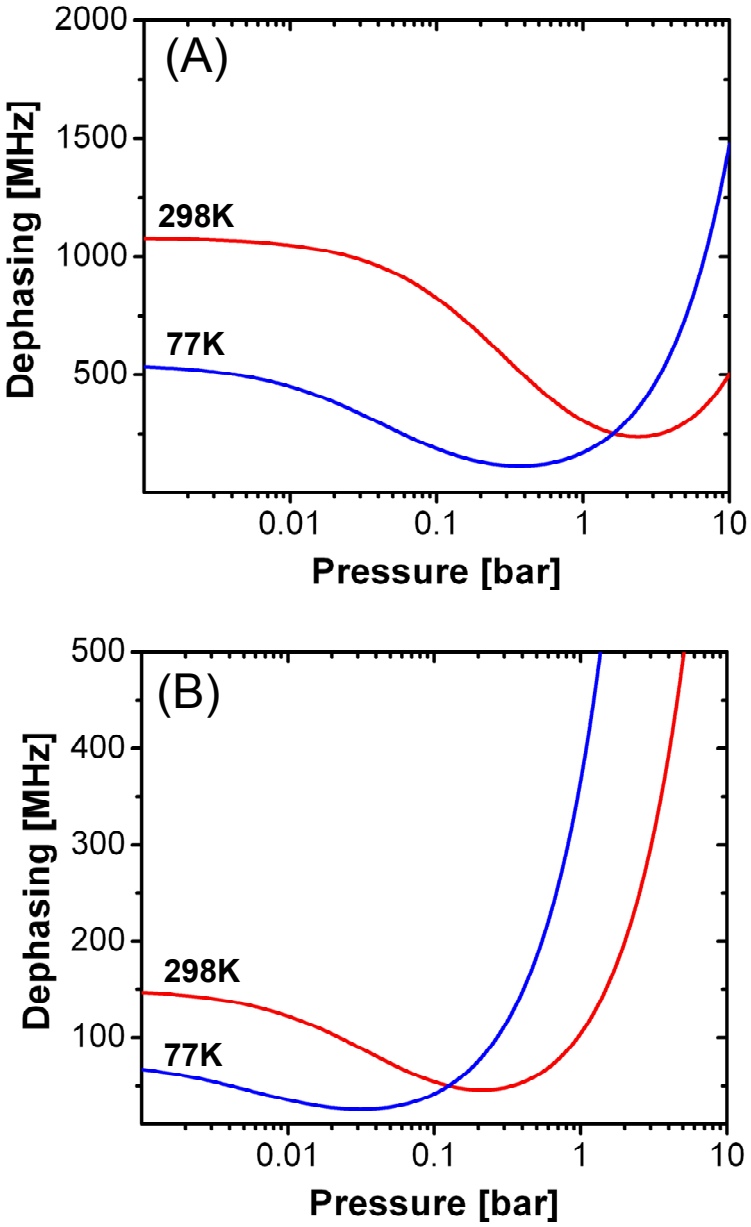

Fig. 4.3 (A) Vibrational and (B) rotational linewidth evolution with pressure at (red line) room temperature and (blue line) liquid nitrogen temperature.

4.2.3 Hydrogen Raman gain in a confined medium

Vibrational and rotational Raman gain

Thanks to the results obtained above for the modified Raman linewidth Γ in gas-filled HC-PCF, the Raman gain g_{SS} inside the fibre can be calculated. Due to the long interaction length of the system, the expression for the gain is taken to be approximately the plane-wave Raman gain α [18]. Bischel and Dyer give an expression of this gain for the vibrational transition in an off-resonant configuration [20]:

$$\alpha_{vib} = 9.37\times10^{6}\times\frac{52\rho}{\Gamma}\frac{K_B}{0.658}\left(\nu_P - 4155\right)\times\left(7.19\times10^{9} - {\nu_P}^2\right)^{-2} \tag{4.10}$$

where K_B is the Boltzmann population factor (0.658 at 295K) and ν_P is the pump laser frequency, in cm^{-1}. Once again, no such general expression is found for the rotational case. The rotational gain will therefore be deduced from the expression given by Carlsten [21]:

$$\alpha_{rot} = \frac{8}{5}\frac{\pi^2\omega_S}{c^2 n_S^2}\frac{(J+1)(J+2)}{(2J+1)(2J+3)}\frac{\gamma^2}{h\Gamma/2}\Delta N \tag{4.11}$$

where h is Planck's constant, c is the celerity of light, n_S is the refractive index of the gas at the Stokes wavelength and is close to unity 1, ω_S is the angular Stokes frequency and the parameter γ is the off-diagonal element of the molecular anisotropic polarisability. At 488nm, $\gamma^2 \sim 1\ 10^{-49}\ cm^6$ [22] scaling with optical frequency as $\nu_S/(\nu_i^2-\nu_P^2)^2$ where ν_S the Stokes frequency and ν_i the average transition frequency to other excited states ($8.48\ 10^4\ cm^{-1}$) [23]. The first rotational Stokes line of ortho-H_2 consists of a transition from level J to level J+2 with J=1. The number density difference ΔN between the initial state J and the final state J+2 takes the form:

$$\Delta N = N(J) - \frac{2J+1}{2(J+2)+1}N(J+2) \tag{4.12}$$

$N(J)$ and $N(J+2)$ are the population densities in the level J and $J+2$ respectively and can be calculated using the expression found in [21,24]. For J=1, we found ΔN=$1.699\ 10^{19}\ \rho\ cm^{-3}$ at 298K and ΔN=$1.32\ 10^{19}\ \rho\ cm^{-3}$ at 77K.

Dependence of Raman gain on pressure, temperature and pump wavelength

Figure 4.4A presents the evolution of the vibrational and rotational gains, α_{vib} and α_{rot} respectively, as a function of pressure at room temperature (298K). The ratio between the rotational and vibrational Stokes component of the Raman spectrum could be controlled via a wise choice of H_2 pressure. Indeed, at high pressure, α_{vib} is larger than α_{rot}, so that vibrational Stokes lines will be generated before the rotational ones. At low pressure, however, α_{vib} falls sharply for pressures below 1bar so that a pure rotational Raman

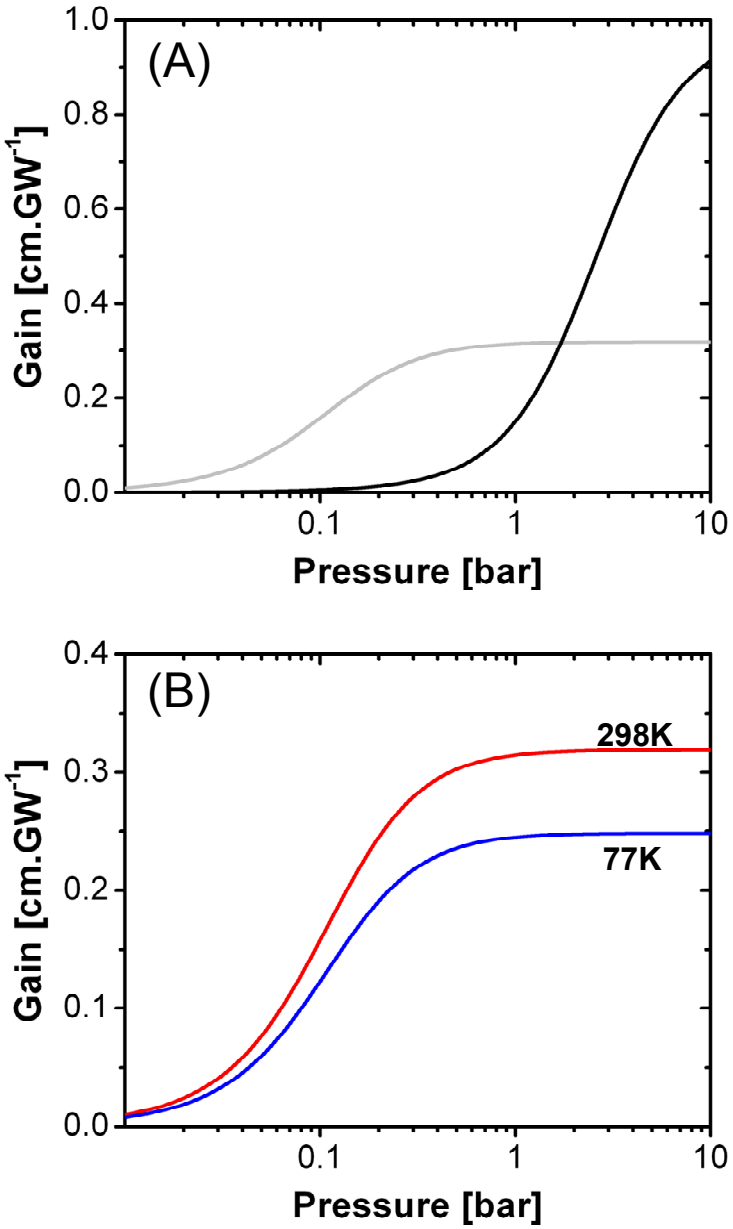

Fig. 4.4 (A) Raman gain of the (black line) vibrational transition $Q_{01}(1)$ and (grey line) rotational transition $S_{00}(1)$ at a function of pressure at room temperature. (B) Rotational gain α_{rot} as a function of pressure at (red line) room temperature and (blue line) liquid nitrogen temperature.

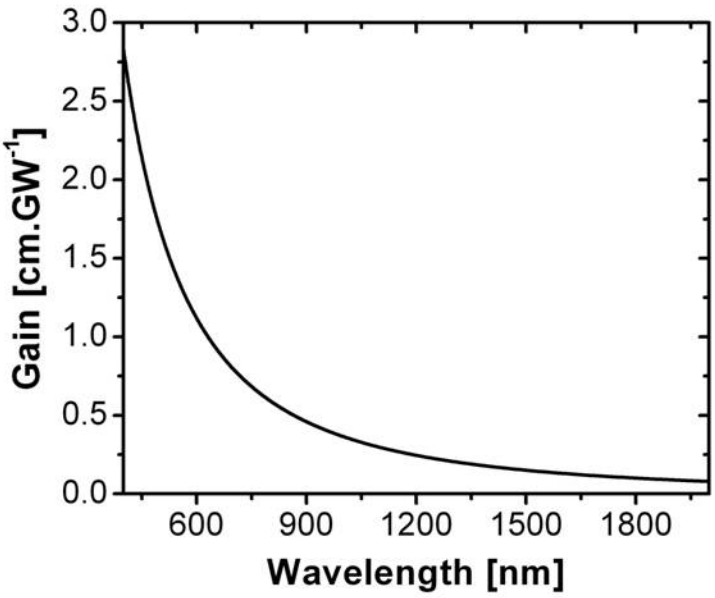

Fig. 4.5 Rotational Raman gain α_{rot} as a function of pump wavelength in an off-resonance configuration

spectrum could be realised. It is interesting to note that, in photonic band gap hollow-core fibres, the fibre's limited transmission bandwidth is usually too narrow to include the vibrational Stokes frequencies, leading to a preferential rotational Raman amplification regardless of gas pressure (Chapter 5 and 6). This is not the case for large pitch fibres, such as the Kagomé lattice fibre (Chapter 7) that possess a large enough bandwidth within which both vibrational and rotational Stokes lines can be generated (Chapter 8).

The Raman gain also depends on the temperature of the Raman medium as shown in Fig 4.4B for the Raman gain α_{rot}. At room temperature, the gain plateaus to a maximum α_{rot}=0.32cm/GW for pressures above 1bar while at liquid nitrogen temperature (77K), the gain is reduced to α_{rot}=0.25cm/GW. This reduction is mainly due to the thermal redistribution of the molecular populations between the two states J and J+2.

Additionally, the Raman gain strongly depends on the pump laser wavelength. For example, Fig 4.5 shows the wavelength dependence of α_{rot} at room temperature and for a pressure of 10bars. The steady reduction of the gain on the long wavelength side of the spectrum means that rotational SRS will be easier to achieve using high power lasers at short wavelength, especially in order to achieve CW Raman amplification in a single pass configuration.

Polarization dependence of Raman gain

Due to its isotropic polarisability, the vibrational Raman gain is essentially independent of the pump laser polarisation. On the other hand, the Raman gain of pure rotational Stokes lines will strongly depend on the polarisation of the laser system as it acts on the anisotropic non-linear polarisability γ of the medium [25]. Table 4.1 gives the relative Raman gains for various configurations of the Stokes and pump laser polarisation*. Equation 4.11 is calculated for the maximum rotational gain, obtained when using a circularly polarized pump laser and the rotational Stokes output counter-rotating circularly polarized.

Table 4.1 Polarisation dependence of rotational Raman gain α_{rot} [25]

Polarisation	Pump	Stokes	Raman Gain
Circular	↻	↺	α_{rot}
	↻	↻	$\alpha_{rot}/6$
Linear	↑	↑	$2\alpha_{rot}/3$
	↑	↓	$\alpha_{rot}/2$

As a matter of fact, the polarisation dependence of the rotational Raman process also extends to the coupling between Stokes and anti-Stokes radiation [2]. In Chapter 1, the generation of radiation at the Anti-Stokes frequency was described as a four-wave mixing process between two pump photons, a Stokes and an anti-Stokes photon with:

$$\omega_{AS} = 2\omega_P + \omega_S \tag{4.13}$$

In the circularly polarized case, Stokes and anti-Stokes are decoupled and their intensity is independent of the FWM phase-mismatch. In contrast, the Stokes/anti-Stokes coupling in the linearly polarised case will strongly depend on the FWM phase-mismatch. Indeed, if the phase matching condition is fulfilled (i.e. no chromatic dispersion and forward propagation of Stokes and anti-Stokes), a dramatic reduction of the Stokes and anti-Stokes amplitudes is observed [26] (see Chapter 5).

Such a strong dependence of the Stokes (and anti-Stokes) amplification on the polarisation and on phase-matching could therefore pose a problem when considering the generation and propagation of Stokes and anti-Stokes lines along a gas-filled HC-PCF.

* And away from phase-matching between Stokes and anti-Stokes that could dramatically reduce the gain.

Effect of HC-PCF group velocity dispersion and birefringence on Raman gain

The group velocity dispersion (or chromatic dispersion) of the Raman medium affects the relative phases of the pump, Stokes and anti-Stokes waves. Indeed, the propagation of these waves through a dispersion-less medium would yield maximum Raman gain as their phase relationship would survive along the length of the medium [27]. In HC-PCFs, however, the chromatic dispersion is of the order of 100ps/nm/km (Fig 4.6). Such dispersion would destroy the phase relationship between pump and Stokes radiation over a characteristic length L_{des}, defined as [27]:

$$L_{des} = \frac{\pi}{\left|v_P^{-1} - v_S^{-1}\right|\Delta\omega} \tag{4.14}$$

Where $\Delta\omega$ is the bandwidth of the pump laser and v_P (v_S) is the group velocity of the pump (Stokes) laser. As long as L_{des} is longer than the Raman length L_R, characteristic of the (dispersion-less) amplification of the Stokes field and expressed as:

$$L_R = \frac{1}{g_{SS} I_P} \tag{4.15}$$

, the pump-Stokes phase correlation will remain and no reduction of the Raman gain will be observed.

Additionally, the birefringence of the Raman medium could modify the state of polarisation of the propagating pump and Stokes radiation and, as a result, could strongly affect the Raman gain of the system. Due to deformations and non-uniformities of the HC-PCF's cladding and core during fabrication, the fibre is usually birefringent. Consequently, in order for the rotational Raman gain to be maximised, the Raman length L_R needs to be longer than the birefringence beat-length, L_B, of the fibre, defined as:

$$L_B = \frac{\lambda_P}{n_{slow} - n_{fast}} \tag{4.16}$$

where λ_P is the pump wavelength and n_{fast} and n_{slow} are the indices of the fast and slow birefringent axis of the fibre, respectively.

In HC-PCF, L_{des} is of the order of 100m, L_B of the order of 10mm*. L_R can therefore be easily controlled via the pump intensity I_P to be well between these two values.

* Away from anti-crossing and for a fibre guiding at 1064nm

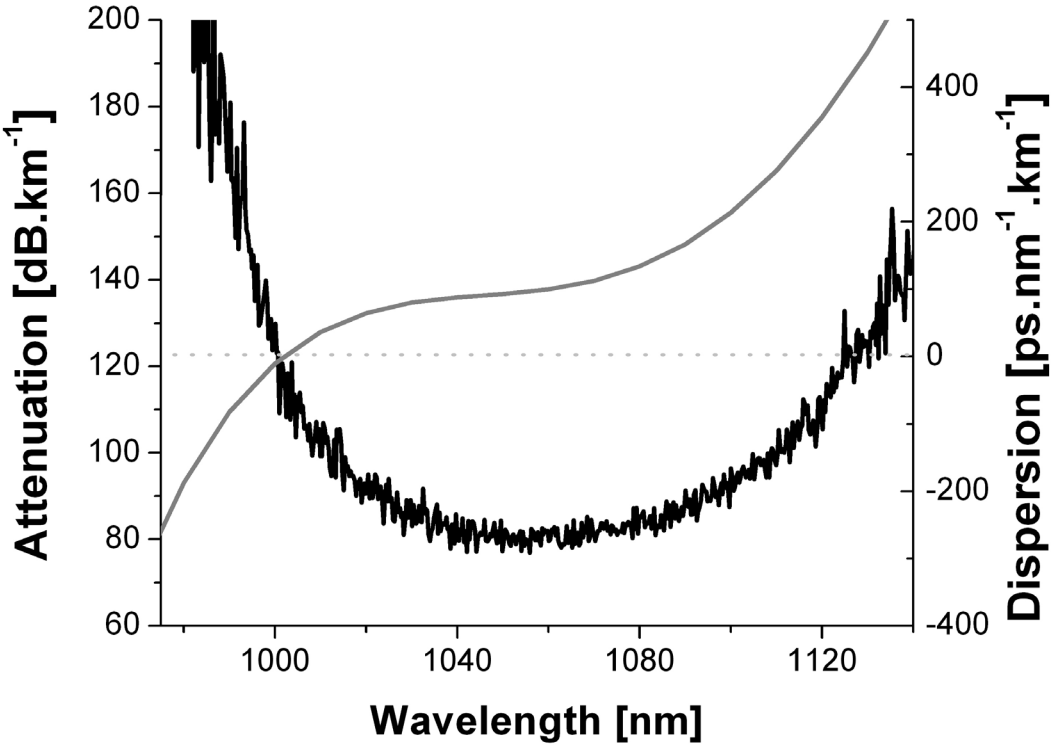

Fig. 4.6 Optical loss (black line) and chromatic dispersion (grey line) of a 7cells defect core HC-PCF guiding around 1064nm

4.3 Regimes of Stimulated Raman Scattering

The modified Raman gain and linewidth calculated above can be used for the resolution of the coupled wave equations (Eq. (4.1)). Raymer and Mostowski described the solutions to these equations in a situation where the Stokes is spontaneously initiated [4]. In this section, we apply these solutions to the case of rotational Raman scattering of ortho-H_2 in hydrogen-filled HC-PCF in a single-pump configuration*. The pump power Raman threshold is calculated for all regimes of Raman amplification and is shown to depend on the pump laser pulse width and on the Raman medium properties (i.e. length and gas pressure).

4.3.1 Spontaneously initiated Stokes intensity

As long as the propagation distance z and the interaction time τ are long enough, the Stokes radiation $I(z,\tau)$ will grow dramatically from the spontaneous Raman quantum

* i.e. without Stokes seed

fluctuations, represented by the Stokes noise intensity $I_S^n(0) = \Gamma h \nu_S / 2$, 2Γ being the Raman linewidth and ν_S the Stokes frequency [4]. Assuming a square pulse, this amplified Stokes intensity $I(z,\tau)$, deduced from the solution to the coupled wave equations, takes the form:

$$I(z,\tau) = \frac{h\nu_S \Gamma gz}{2}\left(e^{-2\Gamma\tau}\left[I_0^2(\sqrt{2gz\Gamma\tau}) - I_1^2(\sqrt{2gz\Gamma\tau})\right]\right) + h\nu_S \Gamma^2 gz\left(\int_0^\tau d\tau' e^{-2\Gamma\tau'}\left[I_0^2(\sqrt{2gz\Gamma\tau'}) - I_1^2(\sqrt{2gz\Gamma\tau'})\right]\right) \quad (4.17)$$

where I_0 and I_1 are modified Bessel functions. The net Raman gain coefficient g is defined in Section 1.2. A numerical evaluation of I_S from Eq. (4.17) is presented in Fig 4.7 as a function of the normalized interaction time $\tau\Gamma$ for various values of the net gain gz*. The three regimes of Raman amplification can be observed. For small net gain gz, or short time ($\tau \le 1/gz\Gamma$), spontaneous Raman scattering is observed. The Stokes amplification is very low, independent from the pulse duration τ and its intensity simplifies to:

$$I_S^{SP}(z,\tau) = \frac{\Gamma gz h\nu_S}{2} \quad (4.18)$$

For pump laser pulses longer than the molecular relaxation time T_2 ($\tau \ge gz/\Gamma$), the steady-state scattering is reached. As in the spontaneous regime, the Stokes intensity is also independent from the pulse duration τ, though the achievable Raman amplification can be much higher when working at large gz. In this regime, only the second term of Eq. (4.17) contributes to the amplification so that, with the upper integration limit taken to infinity, the Stokes expression reduces to:

$$I_S^{SS}(z,\tau) \approx h\nu_S \frac{\Gamma e^{gz}}{2\sqrt{\pi gz}} \quad (4.19)$$

, confirming that the net Raman gain g is the steady state Raman gain.For pulse duration between $\tau_1 = 1/gz\Gamma$ and $\tau_2 = gz/\Gamma$, the Stokes line strongly depends on the pump laser pulse width τ and the amplification regime is transient. Only the first term in Eq. (4.17) contributes and it is approximated to:

$$I_S^{tr}(z,\tau) \approx h\nu_S \frac{e^{2\sqrt{2gz\Gamma\tau} - 2\Gamma\tau}}{8\pi\tau} \quad (4.20)$$

This approximation is done by using the asymptotic form of the Bessel functions, with n=0 or 1 and $x = \sqrt{2gz\Gamma\tau}$:

---

* In gz, g is defined as $g = g_{SS} I_P$ (see chapter 1)

$$I_n(x) = \frac{e^x}{(2\pi x)^{1/2}}\left(1 - \frac{4n^2-1}{8x} + \ldots\right) \text{where } x >> 1 \quad (4.21)$$

Figure 4.8 present an example of the approximated Stokes intensities calculated using the equations above, compared to the analytical calculation given by Eq. (4.17).

The evolution of the characteristic times τ_1 and τ_2 with gz is also represented on Fig 4.7 in order to clearly identify the various regimes. The transient regime is generally limited to pulse width shorter or equal to the molecular dephasing time T_2 of the Raman medium, therefore maintaining a certain degree of molecular coherence during the Raman interaction that can be used to create enhanced Raman scattering resembling the Raman sidebands process achieved in the steady state regime [9,28,29]. However, this limitation to short pulses can be lifted by noting that the passage time $\tau_2 = gz/\Gamma$ is experimentally determined by the effective propagation length z and by the Raman gas pressure linked to the Raman half-width Γ. This means that one could extend the transient regime to longer pulses by operating at high net gain gz like in HC-PCF (Fig 4.7).

4.3.2 Pump energy threshold for steady-state and transient regimes

To experimentally identify the Raman amplification regimes, one could simply measure the Stokes intensity evolution with pulse width. However, this is made difficult by low amplification achieved in the transient state and the requirement to have a pump laser source with variable pulse length and stable peak power. It is simpler to study the evolution of the pump energy threshold for efficient Stokes conversion as a function of the pump pulse width in order to determine in which regime the system is in, as this doesn't impose any requirement on the laser stability.

In order to be experimentally detectable, the Stokes intensity has to build up to a level such that $\ln(I_S/I_S^{noise}) = G_{th}$, where the threshold net gain G_{th} is a constant between 15 and 30. This corresponds to a Stokes intensity I_S increase of up to 10^{13} times I_S^{noise}. By using the analytical approximations of the Stokes evolution in the steady-state regime (Eq. (4.19)), this threshold condition becomes:

$$\frac{g_{SS} z}{A_{eff}} P_{P,SS}^{threshold} - \frac{\ln\left(\pi \frac{g_{SS} z}{A_{eff}} P_{P,SS}^{threshold}\right)}{2} = G_{th} \quad (4.22)$$

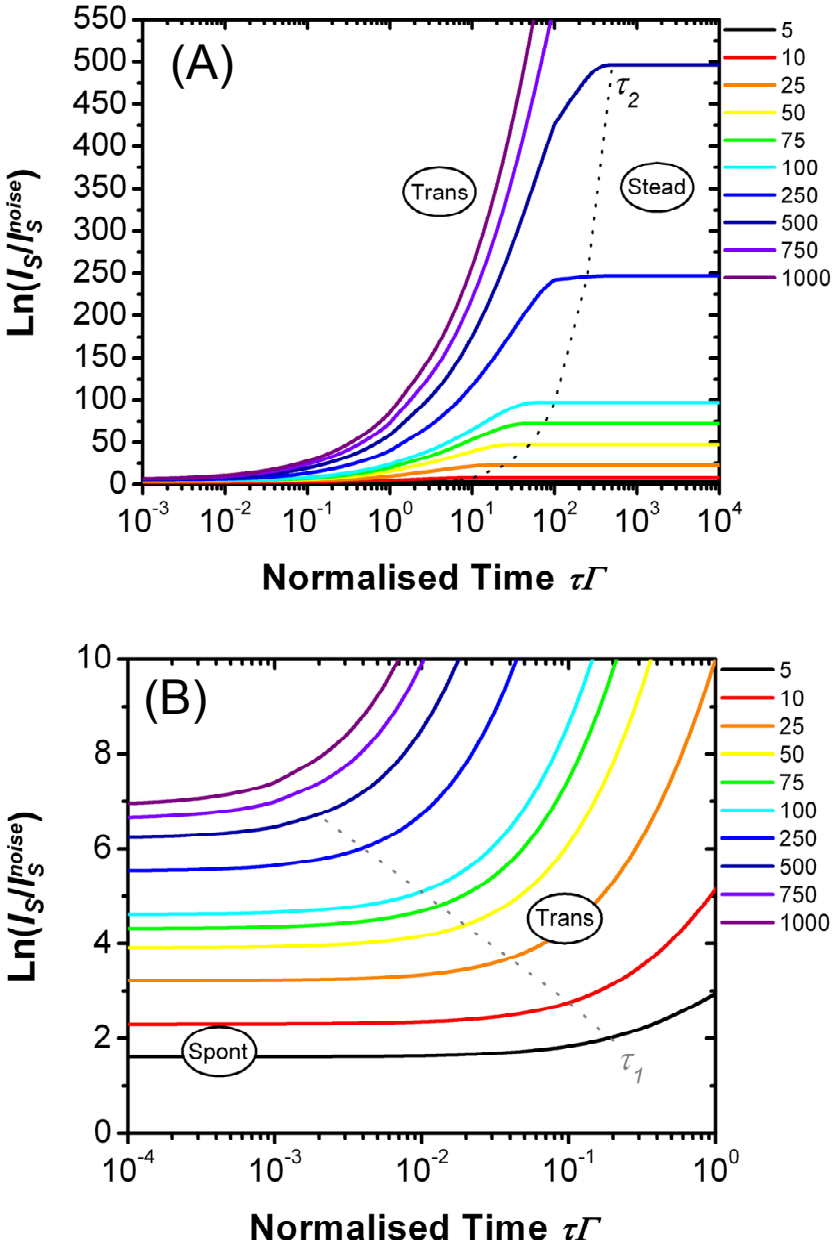

Fig. 4.7 Normalised Stokes intensity growth from quantum noise fluctuation I_S^{noise} as a function of normalised pump laser pulse width $\tau\Gamma$ for different values of gz (spanning from 5 to 1000) using equation 4.17 for (A) high values and (B) low values of $\ln(I_S/I_S^{noise})$ showing the three regimes of Raman amplification. The passage times τ_1 and τ_2 are identified as dotted lines in (A) and (B), respectively.

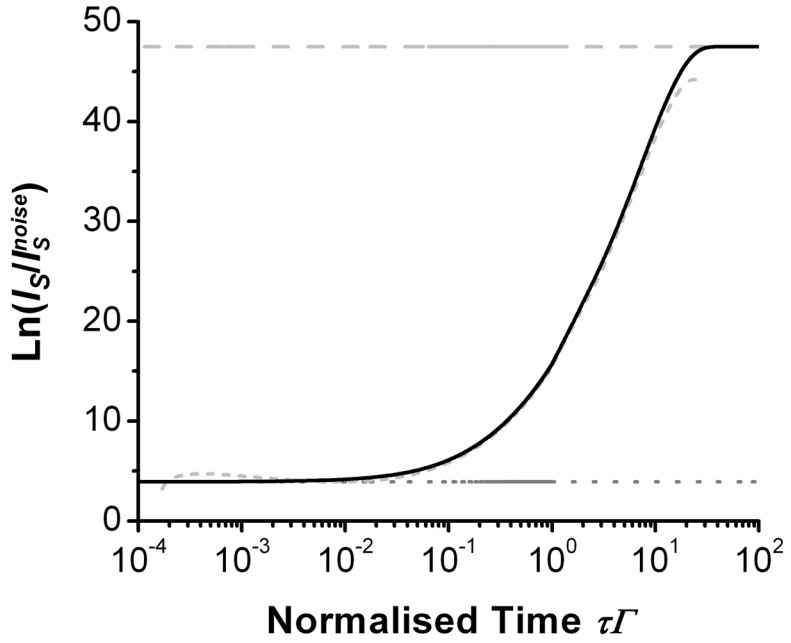

Fig. 4.8 Example of the approximation of Equation 4.17 for the Stokes growth at gz=50. Approximations in the spontaneous (grey dotted line), transient (grey dashed line) and steady-state regimes (light grey dashed line) have been calculated using Equations 4.18, 4.20 and 4.19, respectively.

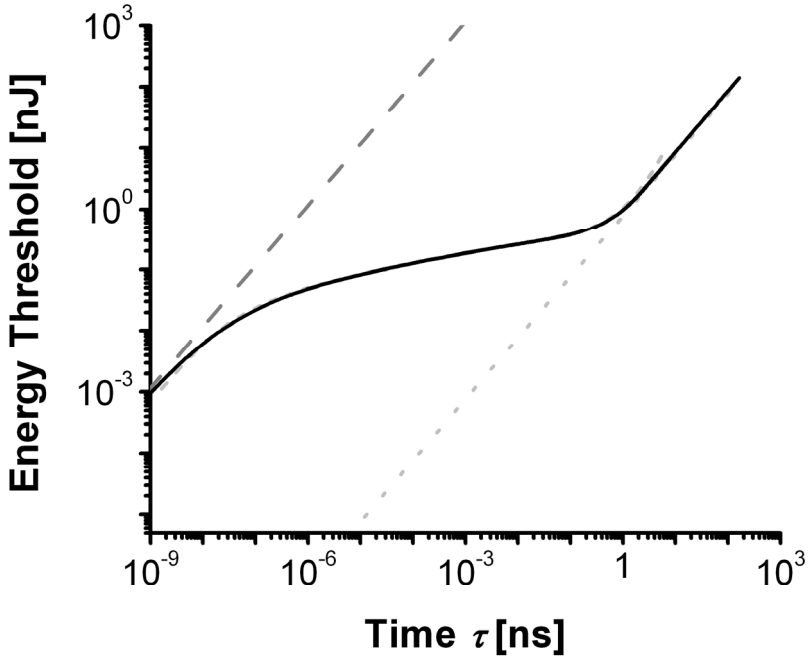

Fig. 4.9 Evolution of the Raman energy threshold with τ for a 15m long 1064nm HC-PCF filled with H_2 at 12 bars and with a loss of 60dB/km (solid black line). G_{th} is taken to be 17. Approximations of the energy threshold in spontaneous emission (dashed grey line), transient (dashed light grey line) and steady state (dotted light grey line) have been calculated using equations 4.23 to 4.25.

At high gain, the logarithmic term on the left hand side of the equation is small and the expression for the pump energy threshold* $E_{P,SS}^{threshold}(\tau) = P_{P,SS}^{threshold} \times \tau$ can be simplified to:

$$E_{P,SS}^{threshold}(\tau) \approx \frac{G_{th} A_{eff}}{g_{SS} L_{\text{int}}} \tau \tag{4.23}$$

where L_{int} is the effective length of interaction. Similarly, the transient energy threshold is found to be:

$$E_{P,tr}^{threshold}(\tau) \approx \frac{A_{eff}}{8\Gamma g_{SS} L_{\text{int}}} \left(G_{th} + \ln\left[4\pi\Gamma\tau\right] + 2\Gamma\tau\right)^2 \tag{4.24}$$

And in the spontaneous regime:

$$E_{P,SP}^{threshold}(\tau) \approx \frac{e^{G_{th}} A_{eff}}{g_{SS} L_{\text{int}}} \tau \tag{4.25}$$

Both the numerical evolution and the analytical approximations calculated here are plotted in Fig 4.9 for G_{th}=17. As presented experimentally in Chapter 5, the clear distinction that can be made between the evolution of $E^{threshold}(\tau)$ in those three regimes of amplification can be used to determine in which regime the system is in at a given pulse width.

Fibre Attenuation

The above calculations are obtained for a Raman medium with no attenuation at the pump or Stokes wavelength. The HC-PCF's optical loss at the pump frequency is introduced via the definition of the interaction length L_{int} that includes the attenuation of the fibre:

$$L_{\text{int}} = \int_0^L e^{-\alpha_P z} dz = \frac{\left(1 - \exp(-\alpha_P L)\right)}{\alpha_P} \tag{4.26}$$

where L is the fibre length (in m) and α_P is the attenuation fraction at the pump wavelength†. The fibre attenuation at the Stokes wavelength appears in the modified Stokes intensity:

$$I_S^{\alpha}(z,\tau) = I_S^0(z,\tau) \times e^{-\alpha_S z} \tag{4.27}$$

with $I_S^0(z,\tau)$ is the Stokes intensity without attenuation, as calculated in Eq. (4.17) and α_S is the attenuation fraction at the Stokes wavelength. The addition of the Stokes attenuation is also required on the net gain threshold condition: $\ln(I_S/I_S^{noise}) = (G_{th} + a_S z)$.

---

* in case of a square pulse of duration τ

† defined as $\alpha_P = 1 - 10^{\left(-\frac{a_P}{10}\right)}$ with a_P the pump optical attenuation expressed in dB/m

Figure 4.10 summarizes the theoretical results obtained for the energy threshold as a function of the fibre length in the steady-state and transient regime* for a fibre guiding at 1064nm, with 60dB/km attenuation at both pump and Stokes wavelength (Fig 4.10A), a comparison of the steady-state energy threshold for this fibre and a fibre guiding at 1550nm with 20dB/km attenuation and a core size of 10µm (Fig 4.10B) and a Kagomé fibre, with a loss of 1dB/m and a core diameter of 25µm (Fig 4.10C). As expected, the steady-state energy threshold is lower than that of the transient. It can be seen that the optimum fibre length, for which the energy threshold is the lowest, strongly depends on the fibre optical and physical characteristics. It is interesting that an ultra-low energy threshold can be achieved through long pieces of HC-PCF.

4.4 Summary

The evolution of the Raman linewidth and gain with pressure and temperature has been calculated for the atypical case of H_2 confined inside a HC-PCF. These parameters are shown to be similar to what can be obtained in free-space, to the exception of low pressure rotational Raman scattering. It was also established that the use of HC-PCF can open the transient regime of Raman amplification to nanosecond pulsed lasers and that the key limitation to low Raman energy threshold was the loss of the fibre. These theoretical findings serve as a base for the experimental work reported in Chapter 5, 6 and 8.

* Pump pulse width τ=1ns. As seen above, the fibre length defines in which regime the system is in.

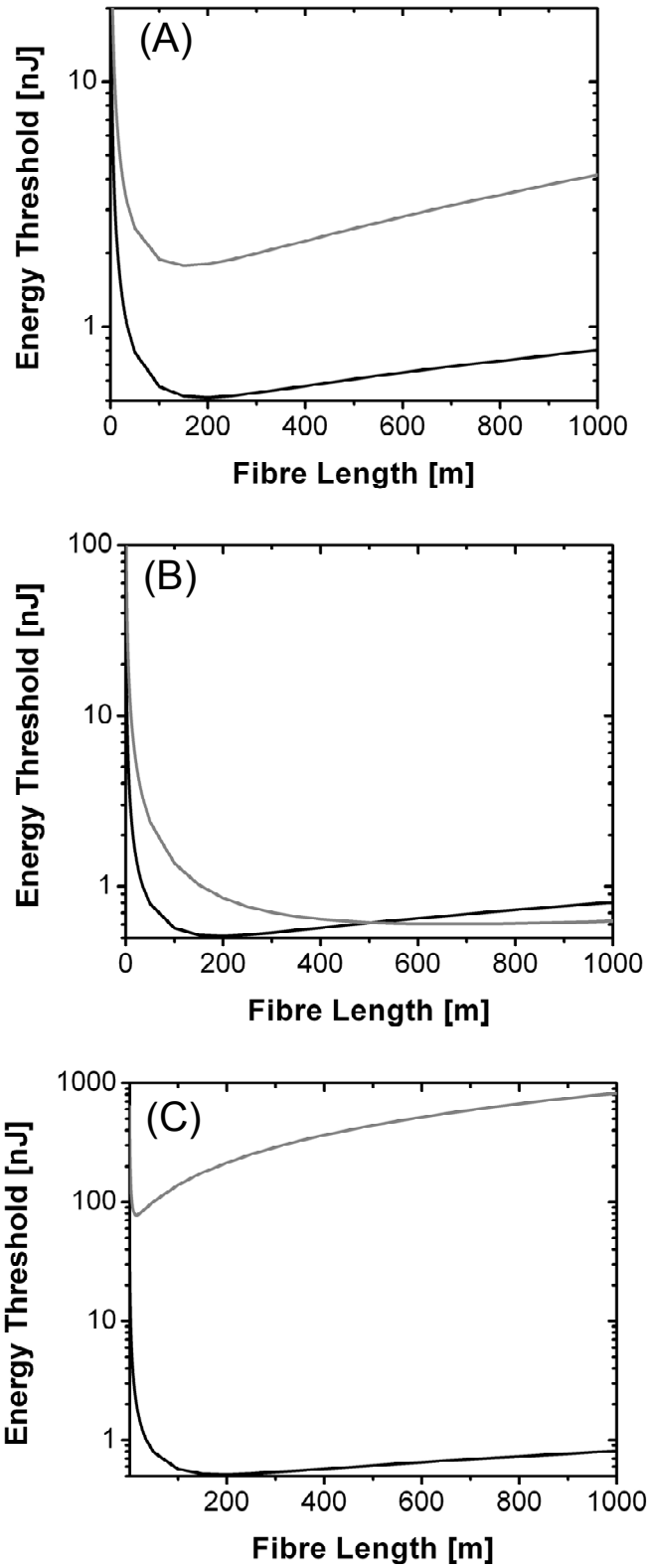

Fig. 4.10 (A) Energy threshold as a function of fibre length for the steady state (black line) and transient regime (grey line). (B) Steady state energy threshold as a function of fibre length for a HC-PCF guiding at 1064nm (black line) and one guiding at 1550nm (grey line). (C) Steady state energy threshold as a function of fibre length for the HC-PCF guiding at 1064nm (black line)and a Kagomé fibre (grey line). Details of the parameters used for the calculations are given in the text.

References

[1] R.W. Hellwarth, *Phys. Rev.* **130** 1850-1852 (1963).

[2] N. Bloembergen and Y. R. Shen, *Phys. Rev. Lett.* **12** 504 (1964).

[3] Y. R. Shen, *Phys. Rev.* **138** A1741 (1965).

[4] M. G. Raymer and J. Mostowski, *Phys Rev A* **24** 1980 (1981).

[5] S. Y. Kilin, *Europhys. Lett.* **5**, 419 (1988).

[6] R. W. Minck, R. W. Terhune and W. G. Rado, *Appl. Phys. Lett.* **3** 181 (1963).

[7] P. Rabinowitz, A. Kaldor, R. Brickman and W. Schmidt, *Appl. Opt.* **15** 2005 (1976).

[8] J. K. Brasseur, K. S. Repasky and J. L. Carlsten, *Opt. Lett.* **23** 367 (1998).

[9] H. Kawano, Y. Hirakawa and T. Imasaka, *Appl. Phys. B* **65** 1 (1997).

[10] M. Katsuragawa, K. Yokoyama, T. Onose and K. Misawa, *Opt. Express* **13** 5628 (2005).

[11] Y. Irie and T. Imasaka, *Opt. Lett.* **20** 2072 (1995).

[12] W. K. Bischel and M. J. Dyer, *Phys. Rev. A* **33** 3113 (1986).

[13] G. C. Herring, M. J. Dyer and W. K. Bischel, *Phys. Rev. A* **34** 1944 (1986).

[14] M. Graf, E. Arimondo, E. S. Fry, D. E. Nikonov, G. G. Padmabandu, M. O. Scully and S. Y. Zhu, *Phys. Rev. A* **51** 4030 (1995).

[15] E. Arimondo, *Chapter V in Progress in Optics XXXV*, Elsevier Science (1996).

[16] E. L. Cussler, *Diffusion: Mass Transfer in fluid systems*, Cambridge University Press (1984).

[17] R. H. Dicke, *Phys. Rev.* **89** 472 (1953).

[18] P. Lallemand, P. Simova and G. Brett, *Phys. Rev. Lett.* **17** 1239 (1966).

[19] M. G Raymer and I. A. Walmsley, *Progress in Optics* Elsevier, NY (1990).

[20] W. K. Bischel and M. J. Dyer, *J. Opt. Soc. Am. B* **3** 677 (1986).

[21] J. L. Carlsten and R. G. Wenzel, *J. Quant. Elect.* **QE-19** 1407 (1983).

[22] R. W. Carlson and W. R. Fenner, *Astr. J.* **178** 551 (1972).

[23] W. Bischel and G. Black, *AIP Conf. Proc.* **100**, 181 (1983).

[24] F. Hanson and P. Poirier, *J. Quant. Elect.* **29** 2342 (1993).

[25] R. W. Minck, E. E. Hagenlocker and W. G. Rado, *Phys. Rev. Lett.* **17** 229(1966).

[26] M. D. Duncan, R. Mahon, J. Reintjes and L. L. Tankersley, *Opt. Lett.* **11** 803 (1986).

[27] R. L . Carman, F. Shimizu, C. S. Wang and N. Bloembergen, *Phys. Rev. A* **2** 60 (1970).

[28] I. G. Koprinkov, A. Suda, P. Wang and K. Midorikawa, *Opt. Lett.* **24** 1308 (1999).

[29] E. Sali, K. J. Mendham, J. W. G. Tisch, T. Halfmann and J. P. Marangos, *Opt. Lett.* **29** 495 (2004).

Chapter 5

Rotational Stimulated Raman Scattering in Gas-Laser Devices based on HC-PCF: Experiments

The chapter presents several experimental milestones in the use of gas-filled HC-PCF for pure rotational stimulated Raman scattering. The efficient, low power-threshold Raman amplification and the control over the regime of amplification predicted in Chapter 4 are experimentally demonstrated. The second part of the chapter shows how an all-fibre gas-laser micro-cell such as the one presented in Section 3.3 can further improve the compactness and integration of the system.

5.1 Introduction

The original demonstration of stimulated Raman scattering in H_2-filled HC-PCF was reported in 2002 by Benabid et al. and consisted of the observation of vibrational first-order Stokes and anti-Stokes lines in a H_2-filled Kagomé-lattice fibre by use of a

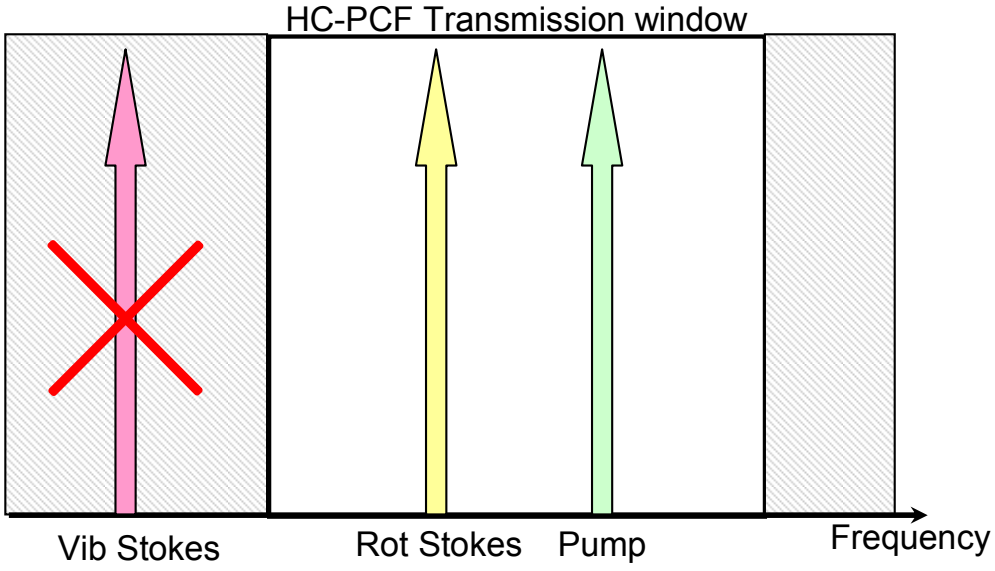

Fig. 5.1 The limited bandwidth of HC-PCF eliminates the vibrational Raman generation and promotes the Raman rotational conversion.

nanosecond pulsed frequency doubled Nd:YAG laser [1]. Although the general threshold of the effect was dramatically reduced compared to previously reported methods [2], it was still limited by the high attenuation of the fibre used.

The advent of the low-loss triangular-lattice HC-PCF (Chapter 1 and 2) and key improvements to the realisation of gas-laser devices based on gas-filled HC-PCF (Chapter 3) open new prospects for the generation of stimulated Raman scattering in HC-PCF at low power threshold and with a high conversion efficiency. By taking advantage of the limited bandwidth offered by the PBG hollow-core fibre, one can selectively obtain high conversion efficiency into pure rotational Stokes lines (Fig 5.1).

Molecular hydrogen is chosen as the Raman active gas in the following experiment because it has the highest Raman gain, a limited number of Raman transitions (Fig 4.1) and can be cooled to cryogenic temperatures whilst remaining in gas-phase. Efficient Raman scattering has also been observed in HC-PCF filled with gases with lower Raman gain, such as methane, though it is not discussed here.

The experiments reported in this chapter consist of (i) the first reported pure rotational stimulated Raman scattering in HC-PCF in the pulsed regime, with a Raman power threshold reduced by a factor of 10^6 compared to standard techniques and a photon conversion efficiency from pump to first Stokes of up to 92%, (ii) the study of the regime of Raman amplification as a function of pulse width, fibre length and gas pressure, to confirm the theoretical predictions of Chapter 4 regarding the observation of the transient

regime using a nanosecond pulsed laser and (iii) the realisation of a compact and highly efficient Raman converter based on the all-fibre micro-cell devices developed in Chapter 3.

The results obtained experimentally bear promising prospects for the realisation of a CW Raman converter using HC-PCF, the first photonic device of the proposed optical waveform synthesiser (Section 1.3).

5.2 Low Threshold SRS in H_2-Filled HC-PCF

5.2.1 Experimental procedure

The fibre used in this experiment is a 7-cell defect core triangular lattice HC-PCF with a bandwidth ranging from 1000nm-1150nm and a minimum attenuation 67dB/km at 1060nm. Each end of the fibre sample is attached to a gas control chamber and filled with H_2 at 7bars following the procedure described in Chapter 3. A schematic of the experimental setup is shown in Fig 5.2. The laser is a passively Q-switched Nd-YAG diode pumped solid state laser. The 0.8ns-long 1064nm pulses have a repetition rate of 6.3kHz and maximum energy of 1µJ. The laser power is controlled by a system of a rotating half-wave plate and polarizing beam splitter. The polarisation is controlled with a quarter-wave plate. In order to efficiently and selectively generate rotational SRS, a circularly polarized laser beam is preferable (see Section 4.2). The input and output pulsed signal is detected with photodetectors and/or on an optical spectrum analyser (OSA).

5.2.2 Low threshold and high conversion efficiency SRS

Figure 5.3 presents the transmitted power as a function of the coupled energy at the pump and Stokes frequencies for a long (35m) and a short (2.9m) piece of HC-PCF. Below threshold, no conversion is achieved and the output signal is at the pump frequency. Above a given threshold energy, the Stokes builds up dramatically while the pump is depleted. A larger conversion is obtained at higher power, when the Stokes saturated as most of the pump has been converted.

For the long piece of HC-PCF, the observed threshold for Raman emission is ~3nJ, a value 10^6 times lower than reported with conventional techniques [3,4,5]. This also corresponds to a peak power threshold of ~4W. This type of power is readily achievable using conventional CW lasers and, as shown in chapter 6, can be used to create a CW Raman converter in a single pass configuration. However, the conversion efficiency from the pump to the Stokes radiation is limited to below 40%.

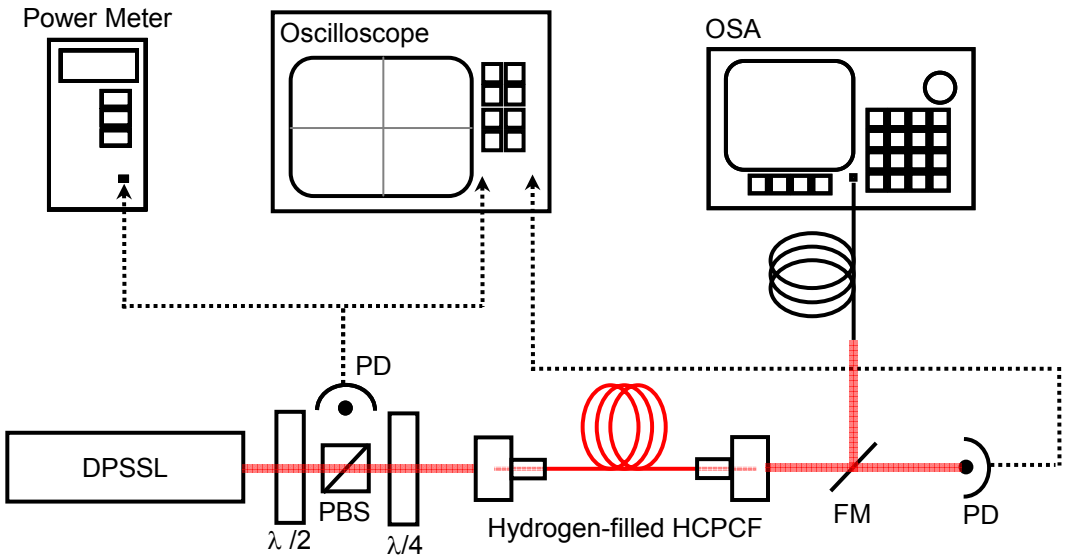

Fig. 5.2 Set-up for the rotational stimulated Raman scattering experiment. DPSSL: Diode-pumped solid state laser. PBS: Polarisation beam splitter. FM: Flip mirror. PD: Photodetector. OSA: Optical spectrum analyzer

Although it exhibits a higher pump energy threshold, the short fibre length displays a higher Stokes conversion efficiency of 86%, corresponding to 92% photon conversion efficiency; the highest reported in a H_2-gas Raman medium to date. The maximum conversion threshold is reached when every pump photon is converted into a Raman-shifted photon. Close to this threshold, the Stokes radiation is strong enough to take over the role of the pump radiation and generates a second Stokes emission (1216nm). While the HC-PCF exhibits high attenuation at this wavelength, conversion from the first to the second-order Stokes line was still experimentally observed and accounts for the drop in the first-Stokes power in the high coupled power region of Fig 5.3B. Through such an effect, a cascade of Raman frequency-shifted components can then be created. However, as each Stokes generation exhibits a large attenuation and because of the HC-PCF limited bandwidth, the number of Raman components generated in such a way is restricted to a few.

In accordance with the theory (Eq. (4.24)), the power threshold becomes lower as the fibre sample becomes longer. However, there is a trade-off between this parameter and the conversion efficiency, mainly governed by the linear optical attenuation of the HC-PCF.

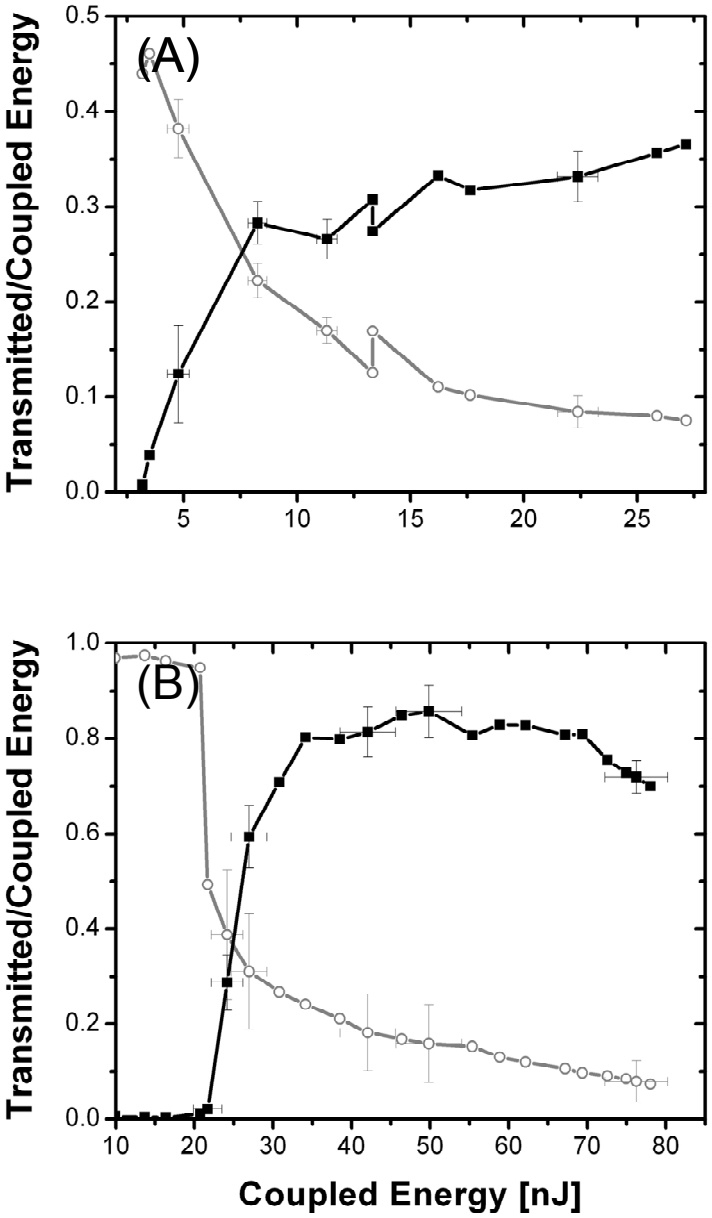

Fig. 5.3 Evolution of the ratio of transmitted average power over the coupled power as a function of the coupled pump energy for the (grey circles and line) pump and (black squares and line) Stokes in (A) 35m and (B) 2.9m of H_2-filled HC-PCF

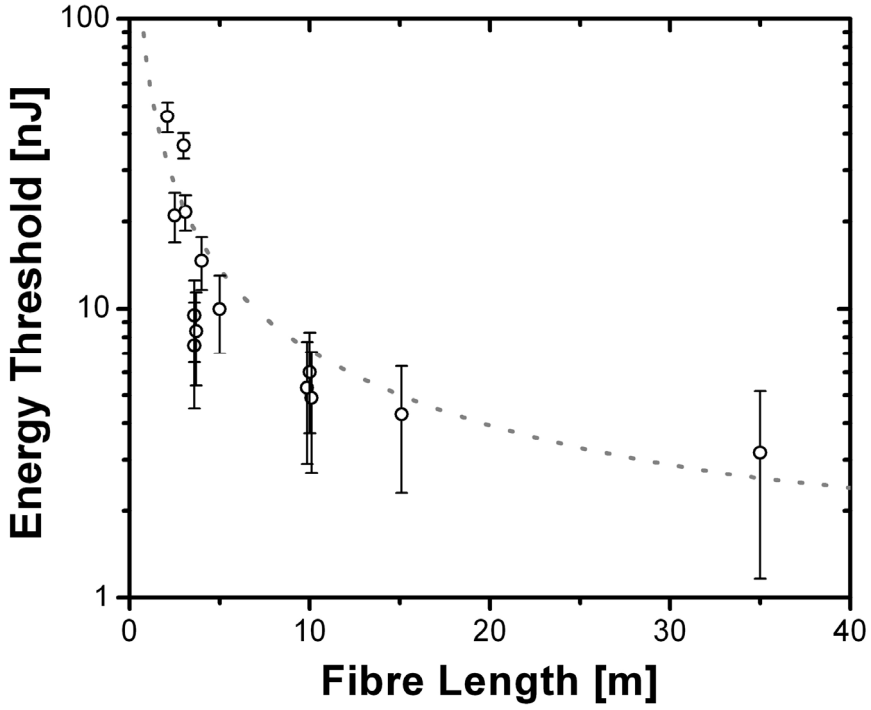

Fig. 5.4 Rotational Stokes threshold power as a function of length of H_2-filled HC-PCF. (Circle) Experimental data and (dashed line) theoretical fit using Eq. (5.1) with g_{SS}=0.32cm/GW.

5.2.3 Study of SRS with fibre length

Figure 5.4 presents a further study of the evolution of energy threshold with fibre length. The experimental energy threshold is plotted for various length of fibre, cut from the initial 35m to the 2.9m length from the fibre's output end, while maintaining the initial pressure inside the fibre to a constant 7bars, and the coupling conditions at the input end of the fibre are the same. As expected, a clear increase of the energy threshold is observed as the length of fibre becomes shorter. This is confirmed by the theoretical prediction:

$$E_{P,tr}^{threshold}(L) \approx \frac{A_{eff}}{8\Gamma g_{SS}} \frac{\alpha_P}{\left(1-e^{-\alpha_P L}\right)} \left(G_{th} + \alpha_S L + \ln\left[4\pi\Gamma\tau_P\right] + 2\Gamma\tau_P\right)^2 \qquad (5.1)$$

where τ_P is the pump pulse width (0.8ns). The threshold G_{th} is taken as a conversion fraction of 17. The Raman gain g_{SS} is taken to be 0.32cm/GW. Equation (5.1) is plotted in Fig 5.4 as a dotted line and agrees well with the experimental data.

5.2.4 Study of SRS with polarisation

As described in Chapter 4, the rotational Stokes and anti-Stokes lines are strongly affected by the polarisation of the input pump laser. The Stokes/anti-Stokes coupling remains strong as long as the Raman length is greater than the phase mismatch length. Under these conditions, the expected Stokes/anti-Stokes intensity ratio should vary as $\tan^{-2}(\psi$-

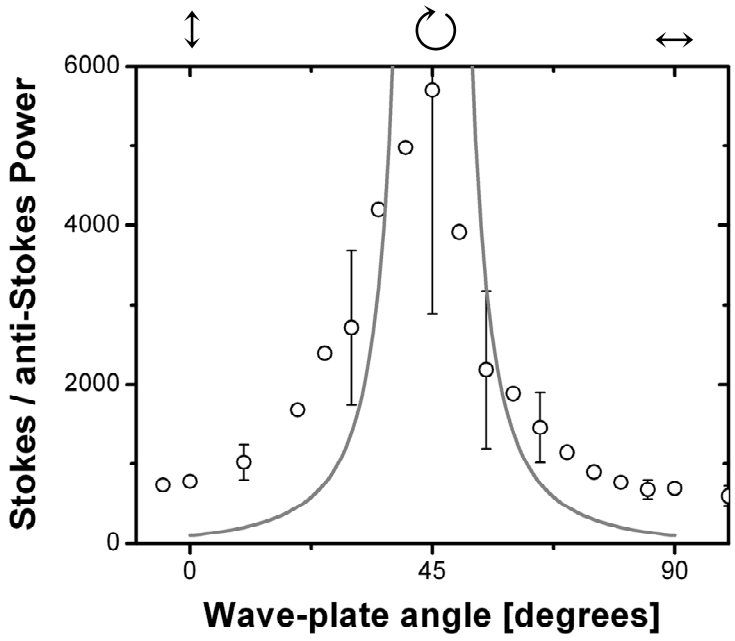

Fig. 5.5 Dependence of the Stokes/anti-Stokes ratio with the input polarisation. The experimental data (black circles) exhibit a behaviour expected by the theory (grey solid line)

$\pi/4$), where ψ is the polarisation angle [6.7]. Experimentally, the variation as a function of the angle of polarisation is verified (Fig 5.5), with the maximum anti-Stokes generation observed for circularly polarised pump light.

5.3 Control of Transient Regime of SRS in H_2-Filled HC-PCF

As indicated in chapter 4, the region of pump pulse width for which the transient regime of stimulated Raman scattering is achieved is temporally framed by the characteristic times τ_1 and τ_2 defining the temporal passage time from the transient regime to either the spontaneous or steady state regime, respectively. In the same chapter, it was also expected that the pump threshold energy would evolve differently in these various regimes, hence creating a tool for the study of Raman amplification related to various characteristics of the Raman medium or the laser pulse width. Benabid et al. reported such a study in PRL [8]. The experimental passage time τ_2 is shown to agree well with the theory and was experimentally measured to be 14ns for an 11m long fibre filled with 15bars hydrogen, 10

times larger than the Raman dephasing time T_2. The repercussions of transient SRS achieved with such long pulses include phase pulling between the Stokes and the pump, and low threshold Raman solitons with quasi-CW pulses.

The work described in this section proposes to complete this study of the evolution of the transient regime with the pump laser pulse width by looking at how the passage time τ_2 can be controlled through the fibre characteristics. Indeed, the theoretical expression $\tau_2=gz/\Gamma$ shows a linear dependence with the propagation length z and is inversely proportional to Γ~100MHz/atm [9] at high pressure*. A simple and accurate control over τ_2 and hence over the transient state is therefore possible through the fibre length and internal H_2 pressure.

5.3.1 Experimental procedure

The measurement of τ_2 is obtained on an experimental setup similar to Fig 5.2. The laser source is a Q-switch 1047 nm Nd:YVO_4 diode pumped solid state laser (DPSS) with adjustable nanoseconds pulse width τ (via the adjustment of the repetition rate). The 7-cell defect core HC-PCF, similar to the one used in the above low threshold Raman conversion experiment, guides around 1064nm with an average loss of 70dB/km. It is spliced at one extremity to conventional single mode fibre (SMF980) using the technique described in Chapter 3, while the other extremity of the fibre is linked to a pressure control chamber filled with H_2 at the required pressure. As in Section 5.2, laser power and polarisation control are achieved via a set of wave plates and a polarising beam splitter. The coupling efficiency of the input laser system into the spliced end of HC-PCF is ~30%, including the fibre splice loss. The output beam is collected onto an OSA. The pump peak power threshold is measured at the power meter when the first Stokes line (1115nm) is detected, corresponding to a G_{th}~15. The energy threshold is then deduced from this peak power measurement†. This is done for different pulse width values so as to estimate τ_2. In order to determine the evolution of this passage time with fibre parameters, measurements are repeated for 15 and 25 meters of HC-PCF, and for a set of pressure between 4 and 24 bars.

5.3.2 Evolution of pump energy threshold with pulse width

Figure 5.6 presents the evolution of pump energy threshold $E_{th}(\tau)$ obtained for the 15m-long fibre sample filled with 11.5 bars and 14.7 bars of H_2, respectively and shows a clear

---

* i.e. neglecting the effect of core wall collisions

† Considering square pulses

dependence of E_{th} with the pulse width. For long pulses, this dependence is quasi-linear, whilst it becomes more complex for short pulse widths. The inflection point between the two behaviours is seen around $\tau \sim 13.5$ns for the 11.5bars pressure fibre and $\tau \sim 11$ns for the 14.7bars pressure fibre. It is this inflection point that is taken to be the transition point τ_2 and is around 100 times longer than the typical pulse widths at which transient scattering is usually observed.

The theoretical evolution of the transient and steady state regime can be fitted to the experimental results by introducing the modified threshold equations:

$$E_{P,SS}^{threshold}(\tau_P, L, \Gamma) \approx \frac{\alpha_P (G_{th} + \alpha_S L) A_{eff}}{g_{SS}\left(1 - e^{-\alpha_P L}\right)} \tau_P + E_0 \tag{5.2a}$$

$$E_{P,tr}^{threshold}(\tau_P, L, \Gamma) \approx \frac{A_{eff}}{8\Gamma g_{SS}} \frac{\alpha_P}{\left(1 - e^{-\alpha_P L}\right)} \left(G_{th} + \alpha_S L + \ln\left[4\pi\Gamma\tau_P\right] + 2\Gamma\tau_P\right)^2 + E_1\tau_P \tag{5.2b}$$

E_0 is added empirically to fit the experimental data to account for the uncertainty in measuring G_{th} and the coarse approximation made in deducing the Stokes energy from the measured peak power. Indeed, instead of taking into account the pulse shape and duration dependence on the net gain and the pump pulse [10], the pulse width is taken constant and equal to that of the pump. Additionally, the quantum noise responsible for the spontaneous Raman emission is considered in the theory for a large tube and not a HC-PCF. As a result, E_1 is also added empirically and accounts for the modified spontaneous emission in the HC-PCF (number of photons with respect to free space). The theoretical expressions are evaluated for the experimental parameters and plotted in Fig 5.6.

It is noteworthy that, due to the low coupling efficiency, the energy threshold is higher than previously reported [8].

5.3.3 Evolution of τ_2 with fibre length and internal pressure

A summary of the experimental data regarding the evolution of τ_2 obtained for both length (25m and 15m) and a range of pressure is presented in Fig 5.7. On the same figure, the expected theoretical evolution $\tau_2 \sim gz/\Gamma$ is also given as solid and dotted lines for 25m and 15m interaction lengths, respectively. All experimental data fall within the theoretical prediction, considering the uncertainty on gas pressure (±0.2bars) and on the measurement of τ_2 (±0.5ns), confirming the high degree of control of the Raman transient regime for ultra-long pulses offered by the use of HC-PCF.

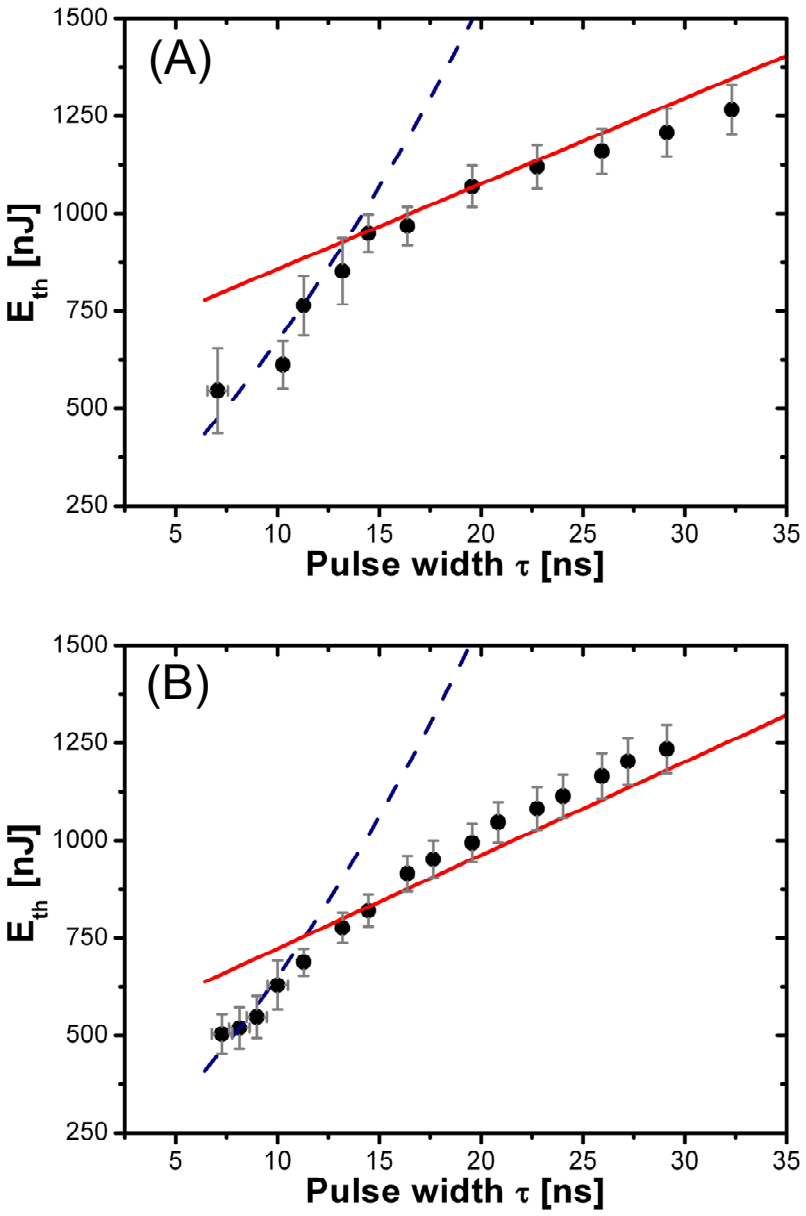

Fig. 5.6 Measured threshold energy E_{th} versus pulse width τ (black circles) for a hydrogen pressure of (A) 11.5bars and (B) 14.7bars and a HC-PCF length of 15m. Analytical results from Eq. (5.2) are shown in solid red and dotted blue lines, respectively.

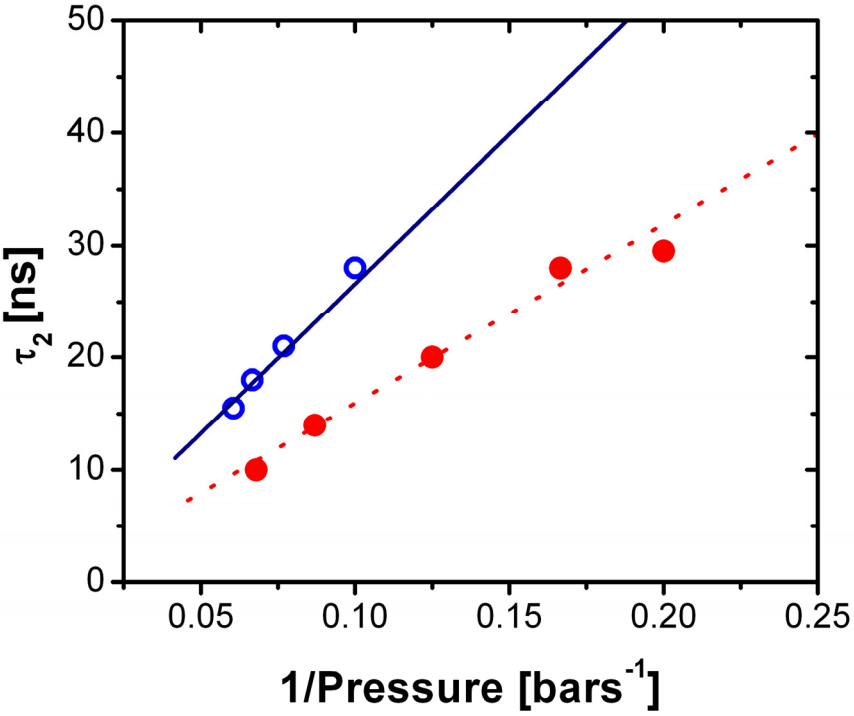

Fig. 5.7 Experimental τ_2 as a function of the inverse of the H_2 pressure for 15m (red dots) and 25m (blue circles). The theoretical evolution is represented in dotted red and solid blue lines, respectively.

Longer passage time τ_2 could be achieved by choosing a longer length of fibre and a lower gas pressure. For example, although our experiment was limited by the maximum pulse width available to the DPSS laser (~35ns), it is expected that τ_2~100ns could be achieved with a 50m long fibre filled with H_2 at 5bars. However, as shown in Section 5.2, the optimal interaction length limiting the process is imposed by the linear optical attenuation of the HC-PCF at the pump and Stokes wavelength, restricting the conversion efficiency. Also, there is a lower limit on the pressure of the Raman active gas as the rotational Raman gain g_{SS} dramatically decreases below ~3 bars, leading to an increase of the energy required to observe the amplification. However, these limitations should not impede transient amplification for pulses $<$ 500ns.

It is interesting to note that the characteristic passage time τ_1 from spontaneous regime to transient could also be controlled in such a way. However, its experimental demonstration would prove difficult as it would require the detection of low power spontaneous Raman scattering, and the use of high power ultra-short (femtosecond) pulsed lasers.

5.4 Compact Micro-Cell for Stimulated Raman Scattering

So far, stimulated Raman scattering has been obtained by filling HC-PCF with gas via pressure control chambers. In this section, the splicing technique described in Section 3.3 is used to create a compact, easy to use gas-laser device for high efficiency frequency conversion using SRS [11]. Different Stokes lines belonging to the rotational transitions $S_{00}(1)$ of ortho-hydrogen (17.6THz) or $S_{00}(0)$ of para-hydrogen (10.7THz), are observed and identified from the cascaded Raman process. The first Stokes line $S_{00}(1)$ is generated at extremely low input pump thresholds (<100W peak power). This is the first demonstration of a comb-like spectrum arising from multiple-order SRS in H_2 using such a low pump power. The device exhibits extremely good long term stability and thermal resilience, two parameters key to the success of Raman sideband generation in HC-PCF.

5.4.1 Experimental procedure

The H_2-filled HC-PCF used to create the photonic micro-cell is 5m long, guides at 1064nm with a loss of 60-70dB/km and has a bandwidth spanning from 950nm to 1200nm. Following the all-fibre gas-cell preparation procedure from Chapter 3, it is first spliced to a conventional single mode fibre at 1064nm (SMF980) with 1.6dB loss at the splice interface, taken to be the input end of the device. The internal gas pressure is then set to 6bar before the second splice is performed (2.0dB loss – output end of the device). The experimental set-up is similar to the one described in Section 5.3. The 1047nm Q-switched Nd:YVO_4 pump laser's pulse width is set to 13ns. Input power and polarisation are controlled via a set of wave plates and a polarising beam splitter. The laser is coupled into the input end of the gas-cell with ~50% efficiency. The output end is plugged directly into an optical spectrum analyser.

5.4.2 Results

Stokes generation

Figure 5.8 shows the typical measured spectra at 200W peak power. The richness of the generated spectrum at such low peak powers illustrates the extreme effectiveness of the gas cell as a Raman converter. Stimulated Raman scattering generates the first Stokes line $S_{00}(1)$ at 1115nm, while a four wave mixing process between the pump and the first Stokes is at the origin of the emergence of the second Stokes (1192nm) and first Anti-Stokes (986nm).

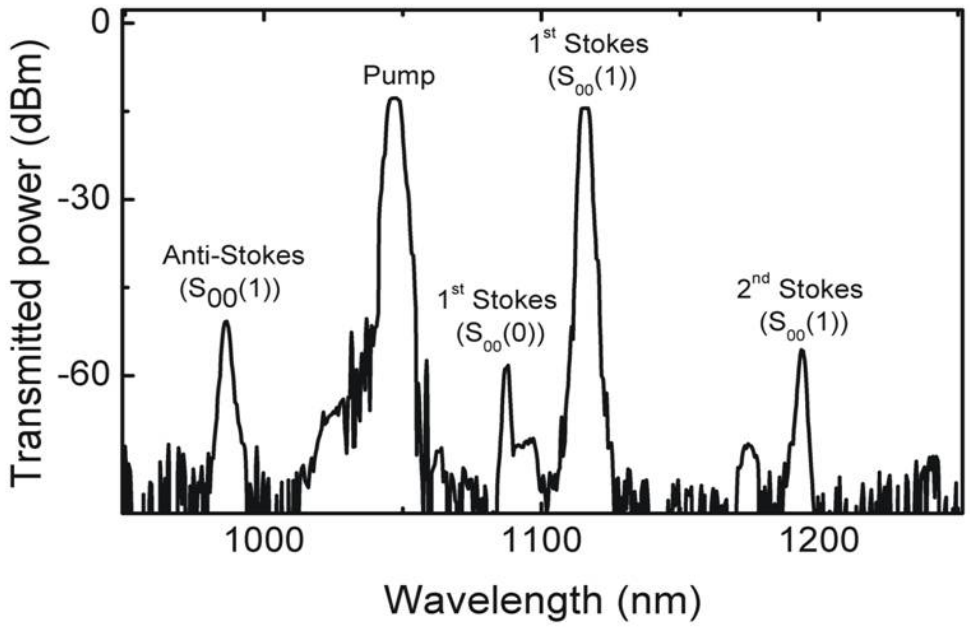

Fig. 5.8 Optical spectrum at the output of the HC-PCF based gas cell.

As hydrogen is a mix of 75% ortho-H_2 and 25% para-H_2 at room temperature, it is generally difficult to obtain rotational Raman amplification of the para-H_2 line $S_{00}(0)$. However, thanks to the long interaction length and suppression of the vibrational SRS achieved with the HC-PCF limited bandwidth, efficient para-H_2 rotational Raman scattering is routinely observed at 1085nm in the gas cell device.

Despite the long pulse duration of the pump laser, this compact Raman converter is operating in the transient regime (see Section 5.3). Thus, the four wave mixing process is helped by the high coherence of the Raman active medium. A further illustration of the role played by the molecular coherence in the transient regime is presented in Chapter 8, for the generation of broadband frequency combs.

Long term gas-cell stability

The high gas-permeation coefficient of H_2 through fused silica is a key problem when working with H_2-filled gas cell devices (Section 3.3). In order to verify the long term stability of the device, the power threshold of $S_{00}(1)$ is monitored for 40 days and is seen to increase steadily over this period (Fig 5.9). Indeed, the Raman gain will be reduced as the pressure inside the gas cell drops (Eq. (4.11)) due to the diffusion of the hydrogen molecules through the fibre cladding. From Eq. (3.1), the estimated pressure inside the fibre will have dropped to 2bar after 40 days, increasing the threshold peak power only by ~25%. This gas permeation effectively limits the life-time of the device. However, placing the gas cell inside an hermetic H_2-filled container would avoid this drawback.

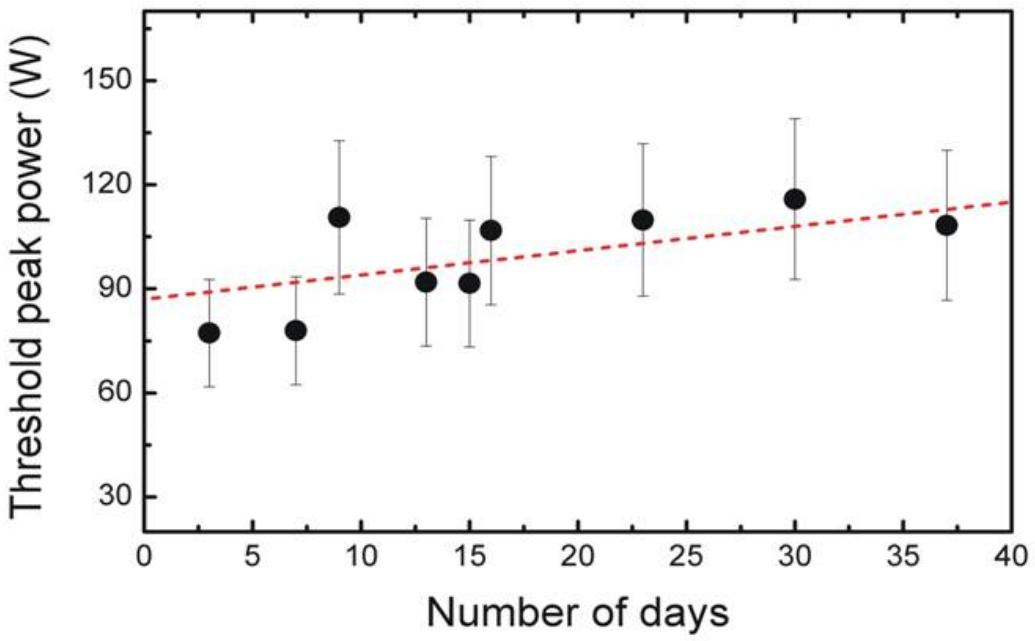

Fig. 5.9 Evolution of $S_{00}(1)$ peak power threshold as a function of time, showing the slow Raman threshold increase as the micro-cell ages. The origin of time corresponds to the day of fabrication of the cell.

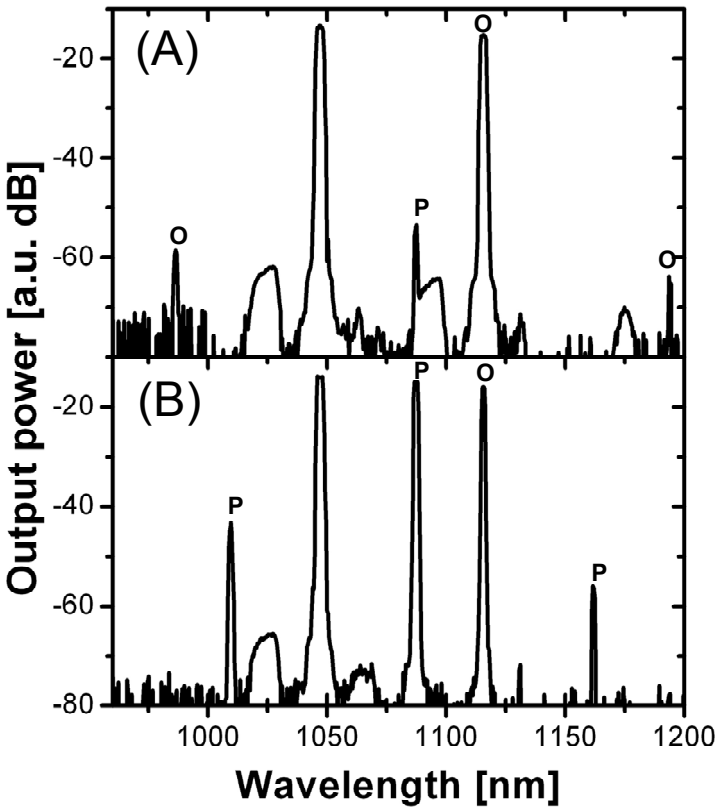

Fig. 5.10 Optical spectrum observed through a H_2-filled HC-PCF at (A) room temperature and (B) at 77K. The Raman lines are identified for the (O)rtho- or (P)ara-Hydrogen.

SRS at cryogenic temperatures

To illustrate the flexibility of the device and especially its resilience to low temperature, the gas-cell is simply immersed in a liquid nitrogen bath (77K). The optical spectrum is measured at room temperature and whilst the HC-PCF is cooled (Fig 5.10). Not only does the fibre still guide, but, due to the redistribution of the ground energy level populations of para- and ortho-H_2 at such temperature, a more pronounced conversion to several $S_{00}(0)$ lines is observed, together with the inhibition of the $S_{00}(1)$ lines.

5.5 All-Fibre Cavity Device using Fibre Bragg Gratings

It has been shown that the threshold required for SRS generation in hydrogen could be lowered by putting the Raman active medium in a high finesse Fabry-Perot cavity [12,13]. Following in these footsteps, this section presents the improvements made to the pump power threshold by the addition of a cavity to the Raman converter device reported above. The cavity is realised by splicing fibre Bragg gratings (FBG) on both sides of the gas-cell. Although these results are obtained for the pulsed regime, they are very promising for the diminution of the pump threshold in the CW regime, as reported in Chapter 6.

5.5.1 All-fibre cavity

When the cavity is resonant at pump and Stokes wavelengths, the power threshold P_{th} is related to the one in a single-pass configuration, $P_{th,sp}$ as follows:

$$P_{th} = \frac{\pi^2}{4} \frac{P_{th,sp}}{F_P F_S} \tag{5.3}$$

where F_P and F_S are the cavity finesse for the pump and Stokes wavelengths respectively.

In the present all-fibre configuration with FBG, the FBG at 1064nm acts only as a mirror to double the pump interaction length. The resonant cavity is realized at the first ortho-H_2 Stokes by two FBGs with equal reflectivity attached at each end of the gas cell. The finesse of the formed cavity is given by:

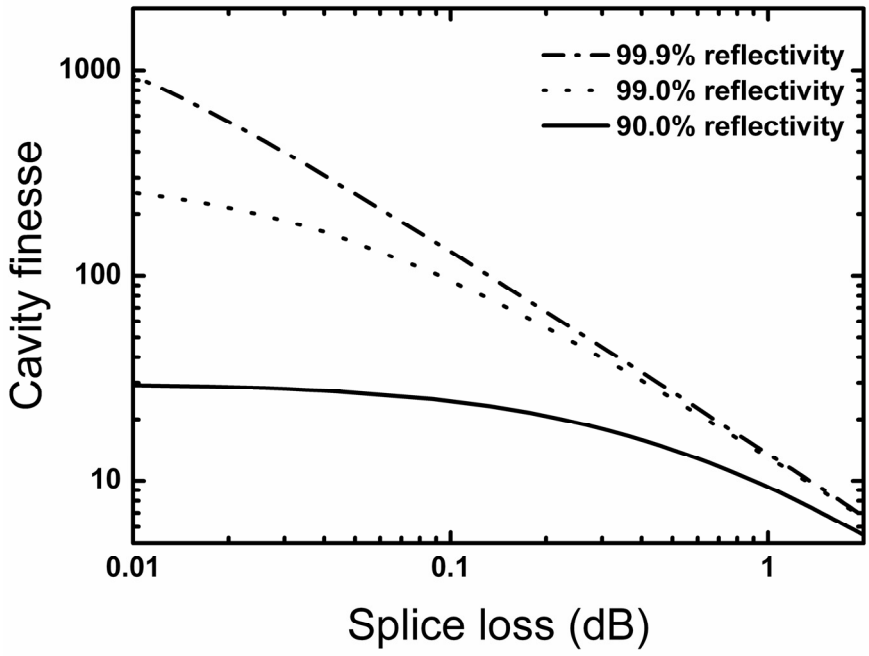

Fig. 5.11 Cavity Finesse *F* as a function of HC-PCF – SMF28 splice loss for a FBG reflectivity of (solid line) 99%, 99.9%(dotted line), 90%(dash-dotted line)

$$F = \frac{\pi\sqrt{R(1-\mathrm{A})}}{1-R(1-\mathrm{A})} \tag{5.4}$$

where R is the reflectivity of the FBGs. A is the power attenuation per round-trip. For a fibre length of ~10 m or less the linear loss of the HC-PCF is negligible in comparison with that of the splice loss. Consequently, A is taken to be equal to the splice loss. Figure 5.11 shows the evolution of the finesse F as a function of the splice loss, in dB per splice, for different FBG reflectivity. In the present experimental conditions, the reflectivity of the "Stokes" FBG is 99% and the loss per splice was slightly less than 2 dB. The calculated finesse F is therefore 6. From Eq. (5.3) and this finesse, one can expect to reduce the threshold by a factor of more than 10 in the current configuration. However, it can be seen from Fig 5.11 that improving the splice loss figure will improve this value more dramatically than by increasing the reflectivity of the FBG. A significant reduction of the optical loss inside the formed cavity (<0.01 dB) would require including the FBG inside the HC-PCF, but this solution constitutes a serious technological challenge.

Despite the fact that the results presented in the following section are obtained using a laser that is not CW and has a low repetition rate (limiting thus the influence of the FBG), they demonstrate the advantage of combining the HC-PCF based Raman converter

with FBG, and provide an insight as to what would happen with a CW pump laser (Chapter 6).

5.5.2 Experimental setup

Two photonic micro-cells are realized using a 6 m long HC-PCF filled with hydrogen at a pressure of 10 bars and spliced to conventional fibre using the technique described in Section 3.3. To provide a direct comparison, one device is prepared in a "single-pass" configuration (Fig 5.12A) while the other is in a "cavity" configuration (Fig 5.12B). In the latter, a FBG at the pump wavelength (1064nm) is placed at the output end of the gas-cell to maximize the effective length of the pump laser. The cavity is created by the addition, at each end of the gas cell, of FBGs at the first Stokes of ortho-H_2 (1135.6nm). The reflectivity of all gratings is 99% within a bandwidth of 1.5nm. Each splice to the HC-PCF (S1 and S2 in Fig 5.12) has a loss of less than 2dB.

In turn, both devices under test are coupled to a 1064.7nm diode pumped solid state microchip laser with a maximum average power of 50mW, a repetition rate of 10 kHz, and a pulse width of ~1ns. The coupling efficiency is 50 %. The input power and polarization is controlled by the usual set of wave-plates and a polarization beam splitter. The input average power is monitored via the second port of a beam-splitter (Power monitor 1 on Fig 5.12). In order to monitor the coupling efficiency and ensure it remains constant in both parts of the experiment, a 10/90 tap coupler is spliced at the input end of the device and plugged to a second power monitor (Power monitor 2 on Fig 5.12). Finally, the output spectrum of each device is recorded on an OSA as a function of the input average power. All measurements are made at room temperature.

5.5.3 Results

Figure 5.13 presents the transmitted optical spectrum for both configurations when the all-fibre devices are illuminated by the same laser input average-power of ~40mW. The single-pass configuration spectrum contains a strong ortho-H_2 first Stokes line, O-S1 at 1135.6nm, a first-order anti-Stokes, O-AS1 at 1002nm and a small peak of para-hydrogen first Stokes, P-S1. Even though no cavity is in place, the O-S1 line is already strong enough to act as a pump for the generation of the second Stokes, O-S2 at 1216nm and the para-H2 Stokes line at 1183nm. This spectrum is equivalent to the one presented in Section 5.4, yet with narrower Raman lines due to the narrower linewidth of the laser used in this experiment, and to the resolution of the OSA.

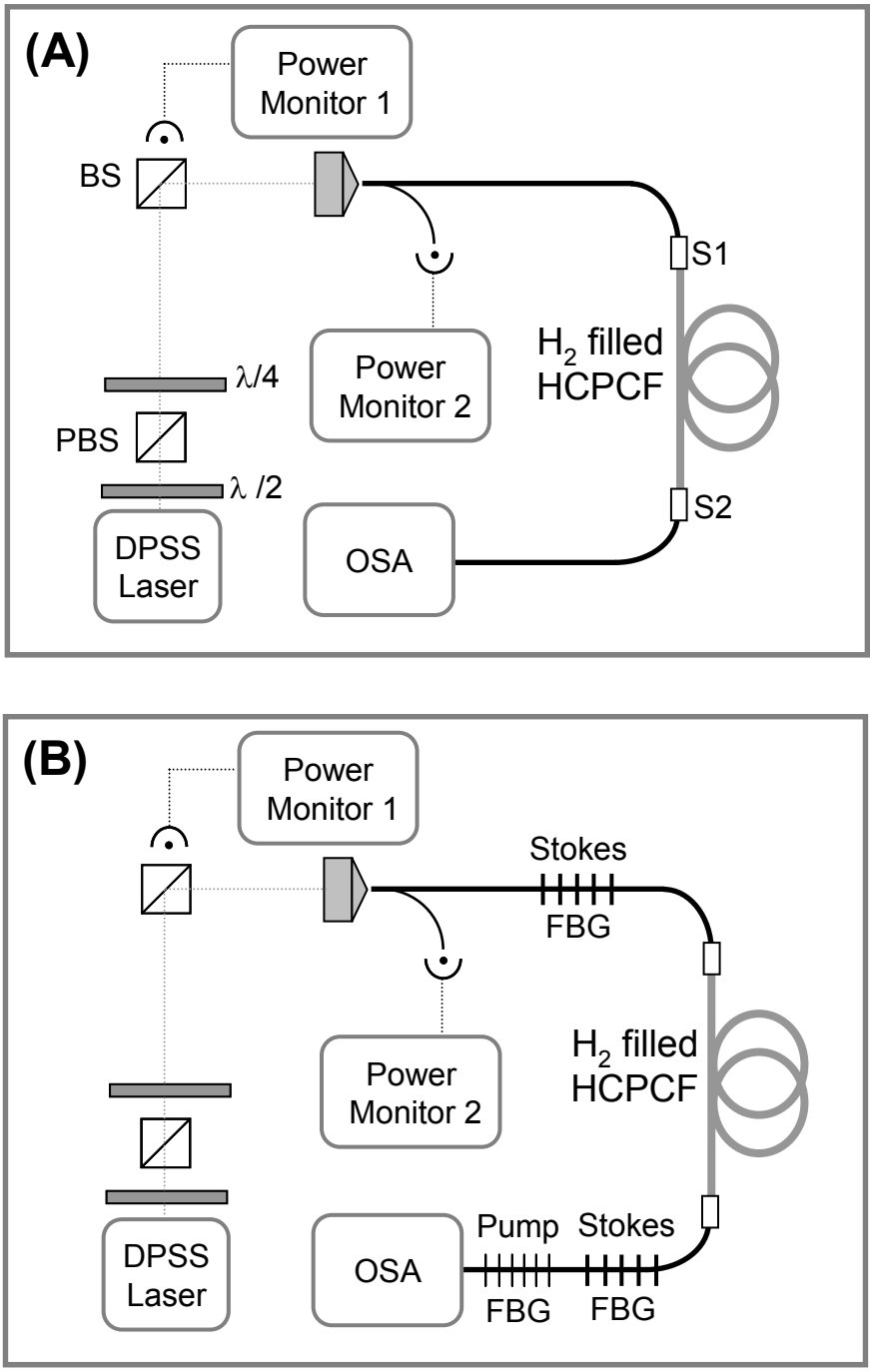

Fig. 5.12 Setup of experiment for SRS generation in (A) a single pass configuration and (B) using FBG to create the cavity. DPSS laser: Diode pumped solid state laser. PBS: Polarizing beam splitter. λ/4: Quarter wave plate. λ/2: Half wave plate. S1 and S2: Splices HC-PCF to SMF. FBG: Fibre Bragg grating. OSA: Optical spectrum analyzer.

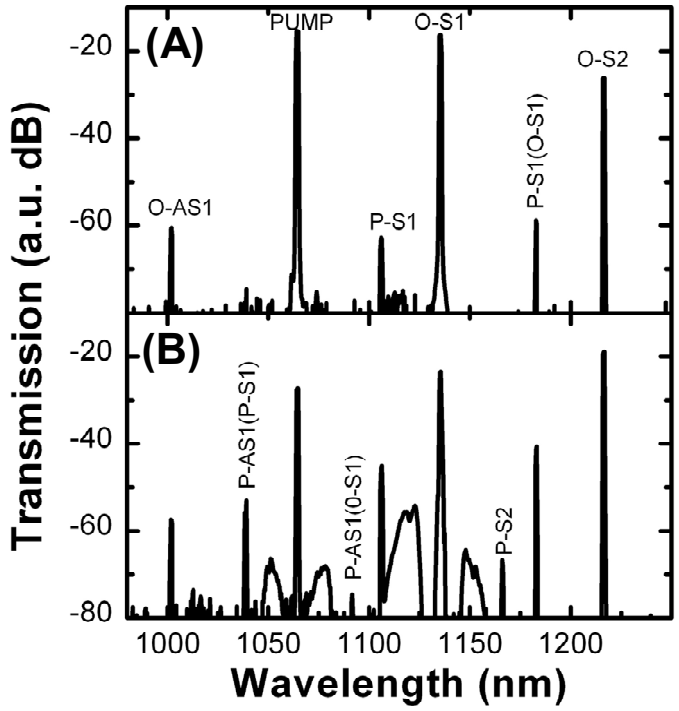

Fig. 5.13 SRS optical spectrum for (A) the single pass configuration and (B) with the FBG cavity attached to the gas cell. P: Para-H2. O: Ortho-H2. S: Stokes. AS: Anti-Stokes. Secondary pumps are in brackets.

Even though only 1% (-20dB) of the pump and first Stokes powers are transmitted due to the presence of the FBGs at the output end of the system, the enhancement of all the spectral Raman lines and the emergence of three supplementary lines compared to the single pass configuration confirms the efficiency of the cavity configuration (Fig 5.13B). Interestingly, both pump and first Stokes radiation are strong enough to generate a small spectral broadening due to the FBG silica fibre inside the cavity.

The effect of the 1064nm FBG can be assessed by the ~20dB enhancement of the transmitted first Stokes from para-hydrogen (P-S1 line). The power in the P-S1 line is in fact high enough to generate, via cascade, the second Stokes from the para-hydrogen (P-S2). More importantly, the 1064nm FBG decreases the Raman threshold for the ortho-hydrogen first Stokes (O-S1). This is illustrated in Fig 5.14A which shows the transmitted power of the O-S1 line as a function of the input average power. The average power threshold almost decreases by a factor of ~2, from 2mW to 1.2mW, corresponding to an input peak power threshold drop from 200W to 120W. The coupling efficiency being 50% and the splice loss being 2dB, we can estimate a peak power threshold reduction intra-cavity from 60W to 30W. On the other hand the saturation regime is also lowered

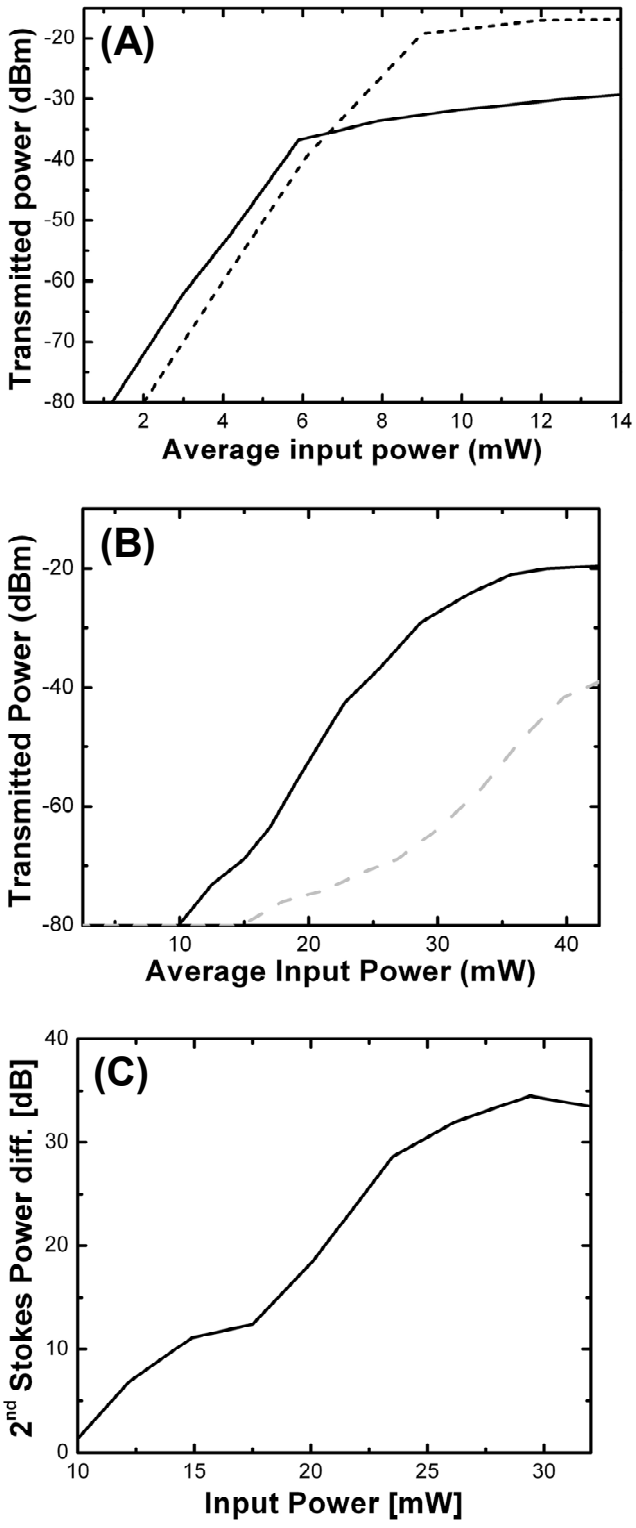

Fig. 5.14 (A) First Stokes and (B) second Stokes output power versus input average pump power, (solid line) for the cavity configuration and (dashed line) for the single pass configuration. (C) Second Stokes output power difference between the two configurations versus average pump power.

by the same factor; from 9mW to 5.9mW as less input power is required for the line to saturate and recombine with other lines.

Interestingly, at low power (before reaching saturation) the 1% transmitted power in the O-S1 exceeds that of the single pass configuration by ~10dB, indicating an enhancement by 30dB of the Stokes circulating power in the O-Stokes resonant cavity.

Secondly, the effect of this cavity on the build-up of O-S1 power is also apparent in the stronger second Stokes O-S2 line at 1216nm (Fig 5.14B). The threshold for the line is lowered from 15mW to 10mW by using the cavity. The difference in power between the two measurements (Fig 5.14C) reaches a maximum enhancement of 35dB at an input power of 30mW. Above this value, the line saturates. A similar effect, followed by a power decrease was observed in [8]. This is due to non-linear four-wave mixing (FWM) between the line of interest and other lines (in the case of [8], the Stokes and the pump lines; in the present case, the second Stokes and the first Stokes).

5.6 Summary

The low threshold and high efficiency Raman conversion and the control of the transient regime of amplification predicted in Chapter 4 have been experimentally observed in H_2-filled HC-PCF. The results indicate that the realisation of a low power threshold CW Raman laser based on these photonic micro-cells is possible (Chapter 6) and that frequency comb generation should be accessible via higher-order Raman scattering in the transient regime of amplification using a nanosecond pulsed pump laser (Chapter 8).

References

[1] F. Benabid, J. C. Knight, G. Antonopoulos and P. St. J. Russell, *Science* **298**, 399 (2002).

[2] For example: D. V. Guerra and R. B. Kay, *J. Phys. B: At. Mol. Phys* **26** 3975 (1993).

[3] M. R. Perrone, V. Piccinno, G. De Nunzio, and V. Nassisi, *J. Quant. Elect.* **33**, 938 (1997).

[4] F. De Tomasi D. Diso, M. R. Perrone and M. L. Protopapa, *Phys. Rev. A* **64**, 023812 (2001).

[5] R. J. Heeman and H. P. Godfried, *J. Quant. Elect.* **31**, 358 (1995).

[6] M. R. Hermann, D. H. Chambers, S. N. Dixit and T. J. Karr, *Phys. Rev. A* **43** 4079 (1991).

[7] G. V. Venkin, Y. A. Il'inskiĭ and G. M. Mikheev, *Sov. J. Quant. Elect.* **15**, 395 (1985).

[8] F. Benabid, G. Antonopoulos, J. C. Knight and P. St. J. Russell, *Phys. Rev. Lett.* **95** 213903 (2005).

[9] G. C. Herring, M. J. Dyer and W. K. Bischel, *Phys. Rev. A* **34** 1944 (1986).

[10] R. L. Carman, F. Shimizu, C. S. Wang and N. Bloembergen, *Phys. Rev. A* **2**, 60 (1970).

[11] F. Benabid, F. Couny, J. C. Knight, T. A. Birks and P. St. J. Russell, *Nature* **434** 488 (2005).

[12] J. K. Brasseur, K. S. Repasky, and J. L. Carlsten, *Opt. Lett.* **23** , 367 (1998).

[13] L. S. Meng, P. A. Roos, and J. L. Carlsten *Opt. Lett.* **27** , 1226 (2002).

Chapter 6

Continuous Wave Stimulated Raman Scattering in H_2-filled HC-PCF

In this chapter, the efficient Raman amplification achieved in HC-PCF (Chapter 5) is combined with a commercially available high-power, narrow-linewidth continuous-wave (CW) fibre laser to realize the first single frequency, CW pure rotational Raman laser based on H_2-filled HC-PCF [1]. The laser exhibits up to 99.99% of the output power at the first Stokes radiation, even at a pressure as low as 1 bar, with 50% quantum conversion efficiency of the coupled pump power, and a narrow linewidth. The observed coupled pump power threshold of 2.25W is further reduced to 600mW by use of fibre Bragg gratings to form a cavity.

6.1 Introduction

Off-resonance SRS in gas-phase materials is recognized as an efficient means to obtain spectrally narrow and widely tuneable laser sources. However, because of the low Raman gain in the near-infrared part of the optical spectrum and of the lack of narrow-linewidth high-power CW lasers at these frequencies, CW Raman lasers have been limited to visible wavelengths. To remedy this problem, experiments were undertaken to increase the

effective length of the Raman medium [2,3]. However, improvements to the Raman conversion efficiency were impeded by the laser beam diffraction. An alternative solution consisted of increasing the pump power inside the Raman medium by placing it in a high-finesse cavity resonant at both the pump and Stokes wavelength. Using such a setup, Carlsten and co-workers realised both vibrational and rotational CW Raman lasers using H_2 as the Raman active gas [4,5]. Despite the impressive ultra-low power threshold demonstrated by the technique, the conversion efficiency remained poor and the stringent simultaneous locking of the cavity to the pump and Stokes wavelength made its use limited.

The breakthroughs achieved in rotational Raman conversion using gas-filled HC-PCF (Chapter 5) hint not only that a CW Raman laser in a single pass configuration is achievable for the near-infrared, but that a high conversion efficiency and a quasi- single frequency output could concurrently be achieved.

Figure 6.1A shows the calculated photon conversion map of the system, giving the photon conversion to the first rotational Stokes signal as a function of two experimentally variable parameters: the fibre length and the input pump power. In the continuous regime, the photon conversion is simply calculated using the Raman photon rate equations* [6] where we limit the coupled equations to only the pump, the first and second Stokes and first anti-Stokes lines. The Raman gain is taken to be 0.32cm/GW at a pump wavelength of 1064nm (Section 4.2) for H_2 pressure inside the fibre of more than 5 bars. The fibre effective area is taken to be $20\mu m^2$ and its optical attenuations at the pump, first Stokes, second Stokes and first anti-Stokes wavelength have been measured to be 100dB/km, 140dB/km, 400dB/km and 140dB/km, respectively. Four wave mixing components can be added to the equations to corroborate previous experimental results (Chapter 5).

The results for the quantum conversion efficiency, given the parameters above, show that a Raman threshold as low as 1.4W is potentially achievable by using a 100 m long fibre sample (point 1 in Fig 6.1A). However, the conversion efficiency from the pump to the first Stokes is calculated to be only a few percent. In contrast, 90% of the pump input power could be converted into a Stokes radiation when using a fibre length shorter than 10m (point 2 in Fig 6.1A), though the threshold power to achieve this conversion is higher than 10W. In the present case, given the experimentally available power coupled into the fibre (up to 8.5W, represented by the dashed segment 3 of Fig 6.1A), the best photon

* The photon rate equation correctly represents the Raman amplification in the present case of continuous wave regime (equivalent to infinitely long pulses). It fails, however, in the transient regime of amplification [6].

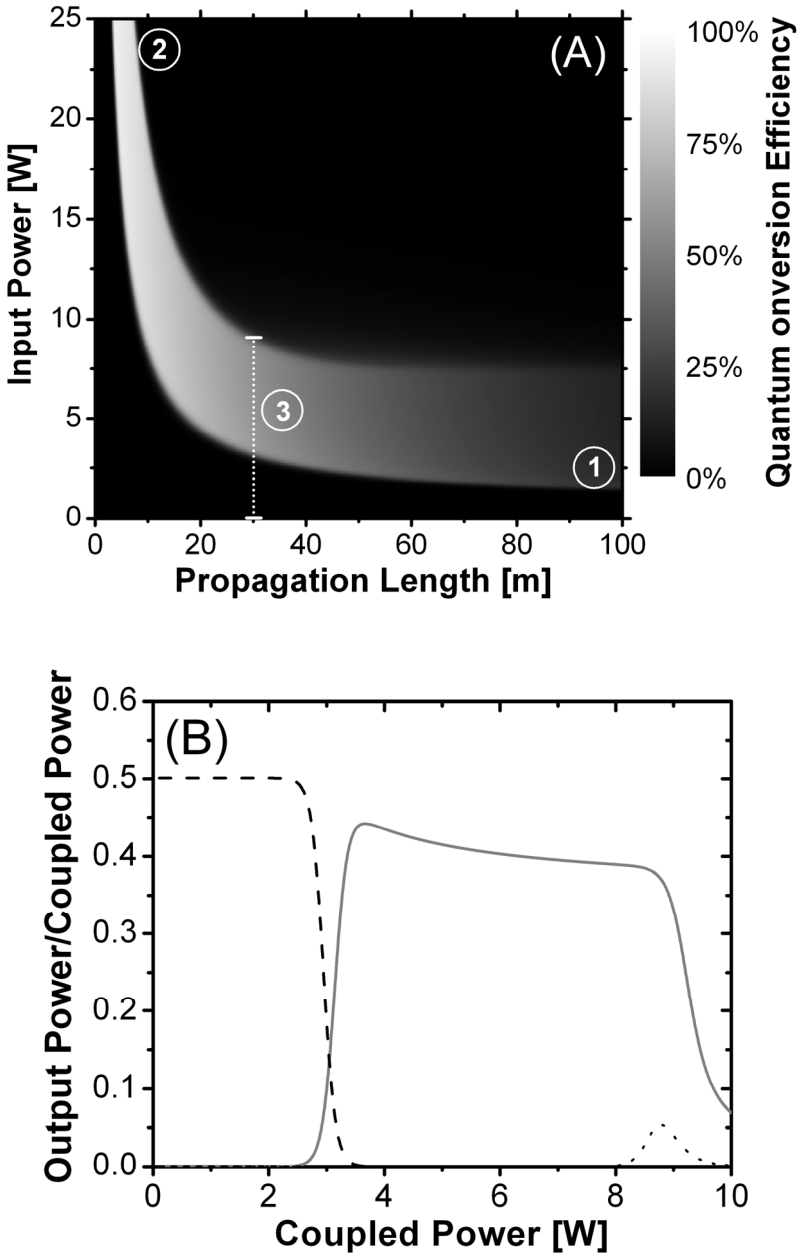

Fig. 6.1 (A) Theoretical conversion efficiency from the input pump power to the output power at the first rotational Stokes wavelength as a function of the propagation length and the input power. (B) Calculated output power ratio to the total input power at the pump (dashed line), first Stokes (solid grey line), second Stokes (dotted line) as a function of the coupled power for 30m of HC-PCF. The anti-Stokes output power is 10^{-6} weaker than the pump and Stokes lines and is not represented.

conversion efficiency one could hope for is ~50% at a HC-PCF length of 30m. The theoretical evolution of the power of all Raman lines as a function of the coupled input power, shown in Fig 6.1B for 30m of HC-PCF, illustrates the fact that the fibre length and pump power are the sole parameters required to achieve a single-frequency Raman laser operation. For input pump-powers less than ~2.5W, no strong Raman amplification is expected and 50% of the input pump power is lost by linear attenuation of the fibre. Above a pump power of ~3W, the pump power is dramatically depleted and more than 99% of the output light is expected to be converted into the first Stokes radiation at 1135nm. The output power at this wavelength is predicted to be ~45% of the total input power. Four-wave mixing between the pump and the Stokes radiation generates the anti-Stokes radiation at 1005nm, though, given the dispersion and the polarisation of the fibre, this only accounts for 10^{-6} of the total output power. Conversion into the second Stokes line, at 1215nm, starts above 8W. However due to the high attenuation of the fibre at this wavelength, most of the light is expected to be lost in the process.

6.2 Experimental Procedure

As shown in the schematic of the experimental setup in Fig 6.2, one fibre end is spliced to a few millimetres of SMF28 to ensure the maximum coupling efficiency into the HC-PCF, whilst also hermetically sealing the fibre's hollow core (Section 3.2). The other end of the fibre is placed into a gas control chamber filled with H_2 at the required pressure. A continuous-wave fibre laser operating at 1064nm, with a linewidth below 100 kHz and a variable power up to 25W [7] is coupled into the spliced fibre using a microscope objective and a system of $\lambda/2$ plate, polarization beam splitter and $\lambda/4$ plate for control of the polarization. The coupling efficiency into the HC-PCF is estimated to be 35% of the laser output power, including the loss due to the splice. The fibre output beam is collimated and dispersed onto a grating for direct observation of the Raman lines on a screen.

6.3 Results and Analysis

6.3.1 Efficient Raman conversion in HC-PCF

Figure 6.3 presents the profile of the dispersed output beam by a diffraction grating and its evolution with input pump power for a H_2 pressure of 5bars. For powers less than 2 W,

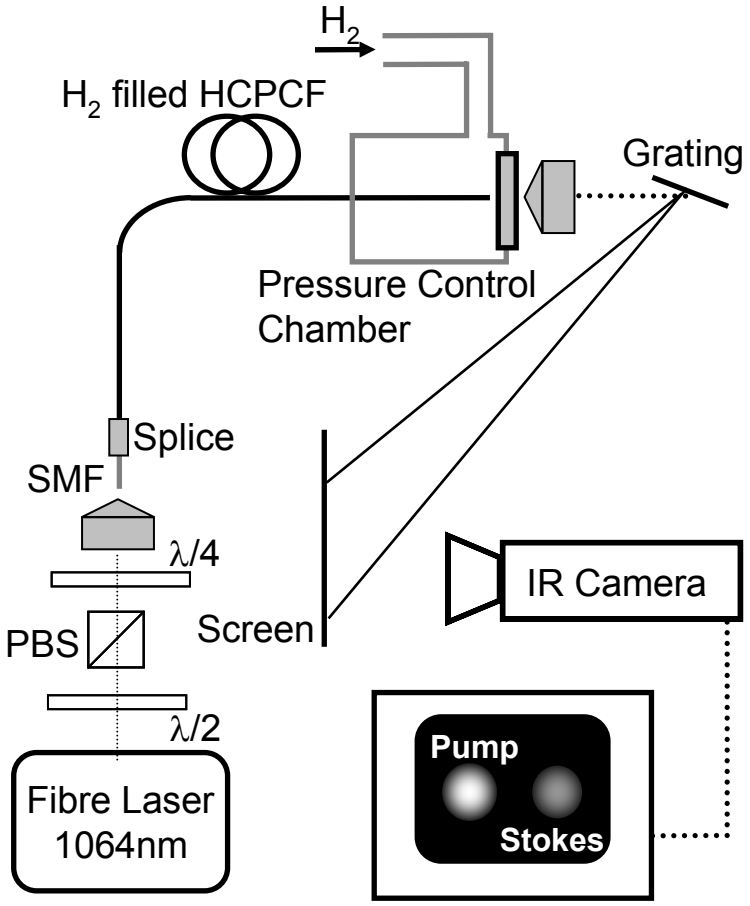

Fig. 6.2 Experimental setup, λ/2: Half-wave plate, λ/4: Quarter-wave plate, PBS: Polarization beam splitter, SMF: 980nm cut-off single mode fibre.

the profile consists of a single spot corresponding to the pump radiation (1064nm). At a coupled power of 3W, a large conversion from the pump into the first rotational Stokes line, $S_{00}(1)$ (1135nm) is observed. Above 5.2W, the pump is dramatically depleted and the majority of the output power is at the Stokes wavelength. No other Raman lines were observed using this technique.

This dramatically illustrates the quasi-full conversion to the Stokes wavelength. Furthermore, thanks to the long interaction length and the small effective area of the system, most of the Raman amplification happens in the forward direction, with only ~1% of the Raman light detected in the backward direction [8], believed to be a result of reflections at the fibre ends. To quantify the Raman conversion, the output light of the HC-PCF was collected onto a multi-mode fibre linked to an OSA. The optical spectrum at a coupled input power of 8.7W for a pressure of 5 bars is given in Fig 6.4B. A reference spectrum below threshold is shown for comparison (Fig 6.4A). The output $S_{00}(1)$ line is

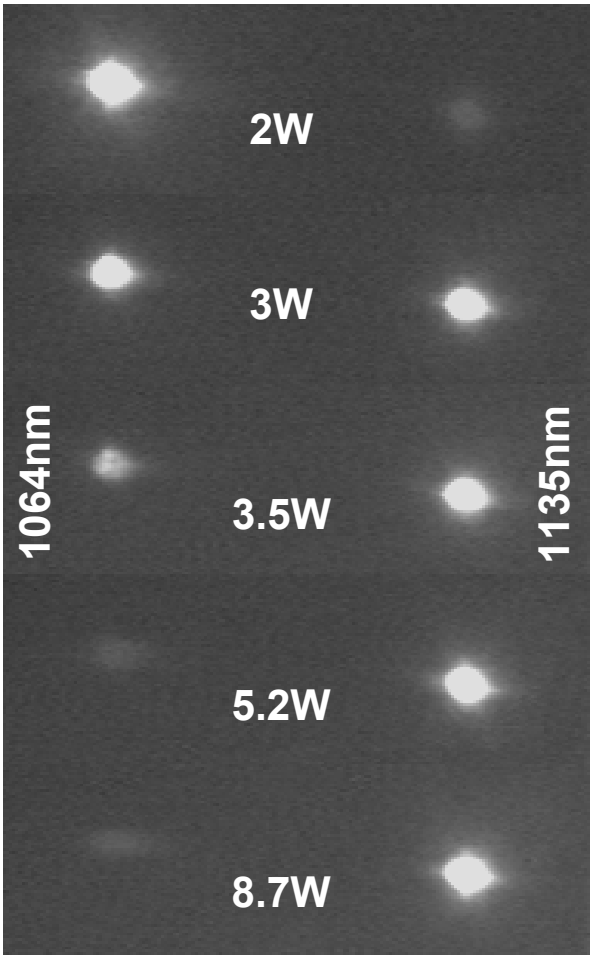

Fig. 6.3 Evolution of the dispersed output spectrum as a function of coupled input power: (Left) Pump and (right) $S_{00}(1)$ at 5bars H_2 pressure.

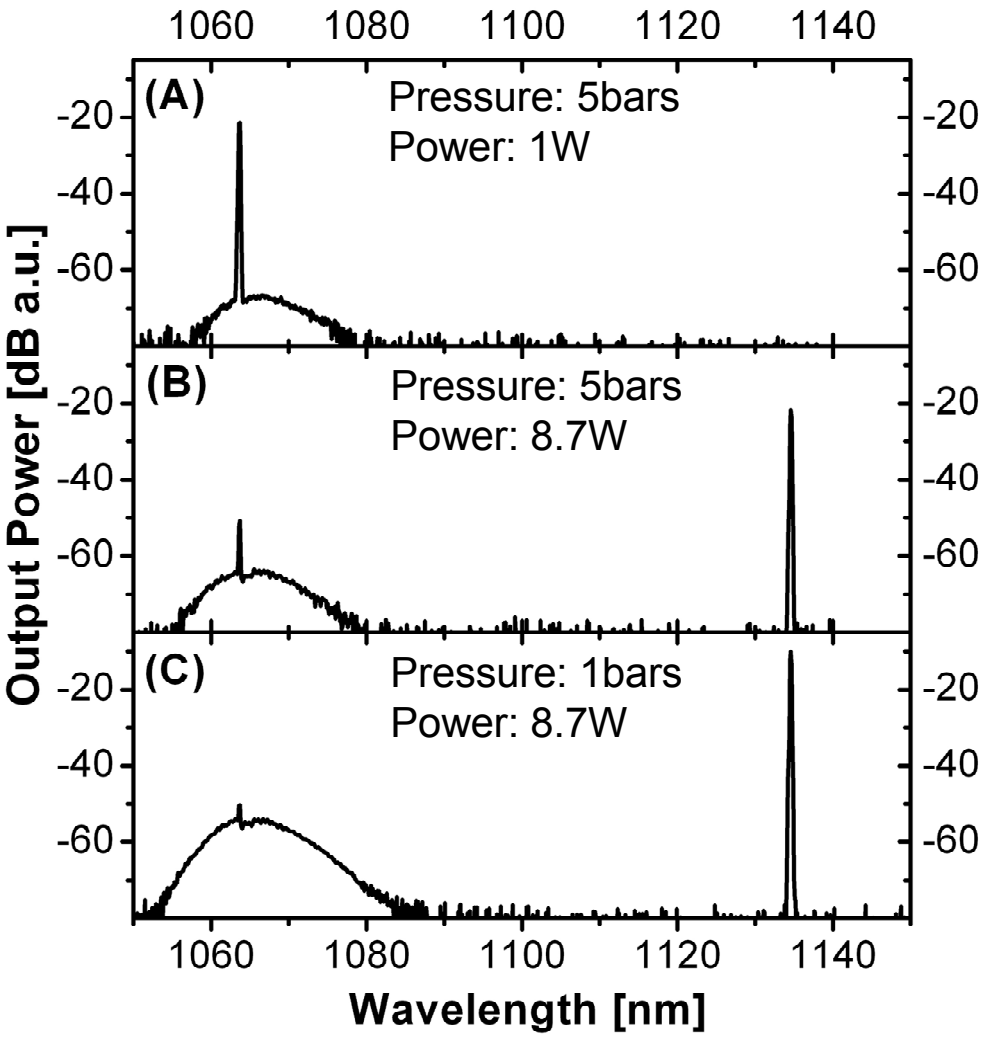

Fig. 6.4 Output optical spectrum for (A) 1W and (B) 8.7W coupled input power at 5bar H_2 pressure. (C) Higher conversion efficiency is achieved at 1bar pressure. The broad spectral feature around 1064nm is likely to be due to the residual fluorescence of the laser.

30dB stronger than the residual pump line, corresponding to 99.9% of the total output light. This trend of full pump power depletion in favour of near total conversion to Stokes radiation was observed for pressure as low as 1bar, as shown in Fig 6.4C. Moreover, in this configuration, the Stokes part of the total output power increases to 99.99%. This is the first report on the generation of SRS in hydrogen at this low pressure and with such high quantum conversion.

6.3.2 Comparison with theoretical predictions

To corroborate these results with the predicted evolution of Stokes radiation as a function of the input power (Fig 6.1B), optical spectrum measurements are used to deduce the ratio between the output power and the coupled input power at the pump and Stokes

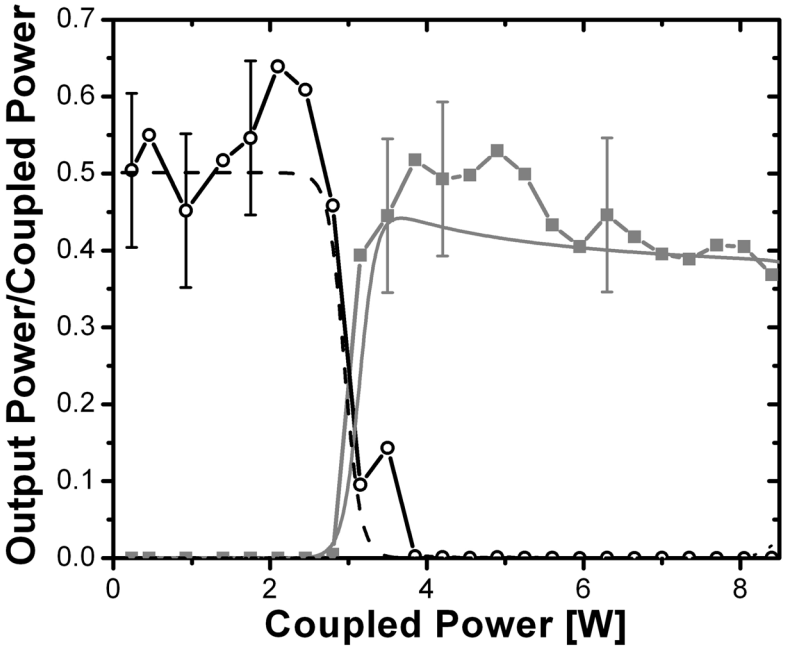

Fig. 6.5 Experimental output/input power ratio for the pump (circles and black line) and $S_{00}(1)$ (grey squares and line) at 5bars H_2 pressure. Theoretical calculations from Fig 6.1B are also repeated for the pump (dashed black line), the first (solid grey line) and the second Stokes (short dotted line). The anti-Stokes radiation is too weak to be represented.

wavelength. Figure 6.5 presents the results, together with the theoretical prediction calculated using the experimental parameters. As expected, 50% of the pump reaches the output of the fibre due to the 3dB linear loss along the HC-PCF. The measured threshold power of 2.25W and the ~50% conversion efficiency agree very well with the theoretical predictions. Also in line with the calculated model, no second Stokes is experimentally observed for the pump power range explored. A weak anti-Stokes line is detected at the limit of the dynamic range of the OSA and only accounting for 10^{-6} % of the total output power, so it is not represented on the graph. Due to the low birefringence and the long length of HC-PCF used in the experiment, no significant polarization dependence of the conversion threshold is observed.

6.3.3 Influence of gas pressure on performance

Similarly to the output Stokes/pump ratio, the power threshold is also expected to vary with pressure. Figure 6.6 presents the measured Stokes threshold power versus H_2 pressure, together with the theoretical value based on the pressure dependence of the Raman gain [9]. Although both experimental and theoretical results show a sharp power

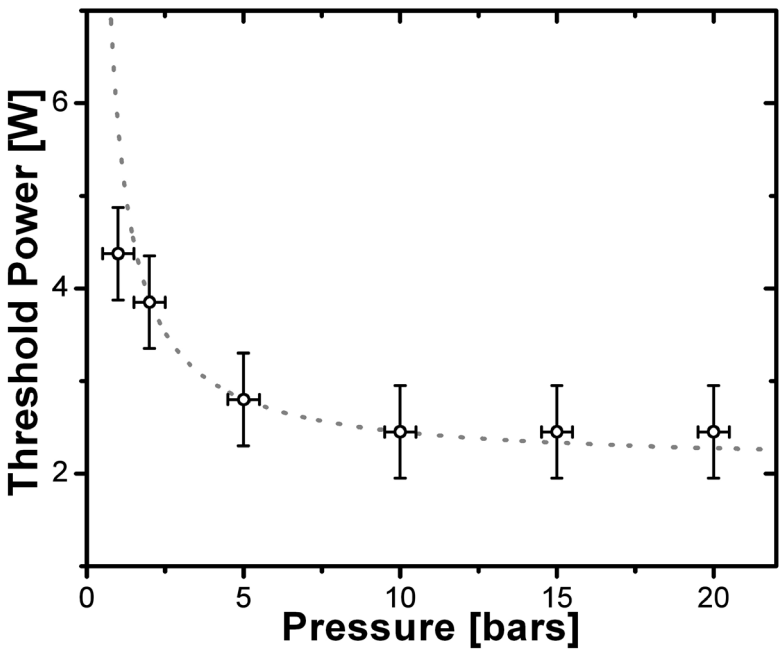

Fig. 6.6 Experimental (circles) and theoretical (dotted line) evolution of $S_{00}(1)$ threshold power with H_2 pressure.

threshold increase at low pressure, Raman amplification can still be observed at atmospheric pressure. The Stokes radiation linewidth was measured using a scanning Fabry-Perot spectrometer for a 4bars H_2 pressure inside the fibre. The expected Raman linewidth is of the order of 500MHz [10]. However, the measured spectral width of the Stokes line is below the 200MHz resolution of the spectrometer, indicating a strong gain spectral-narrowing [11].

6.3.4 Improvement to Raman threshold via FBG cavity

To improve the conversion efficiency and reduce the threshold power, FBGs are introduced in the experiment. This technique has already been shown in Section 5.5 to reduce the Raman threshold power of a HC-PCF gas-cell used with a pulsed laser. As shown schematically in Fig 6.7, a 99% reflective FBG at the pump wavelength (1064nm) is spliced at the output end of a 10bar gas-filled HC-PCF, while a cavity is formed at the Stokes wavelength by the addition of a 1135nm 99% reflective FBG on each side of the HC-PCF. Figure 6.8 shows the output power at the pump and Stokes wavelength as a function of the coupled input power. The measured threshold is reduced to 600mW, about 6 times less than the single pass corresponding qualitatively to the finesse of the formed cavity (similar to results in Section 5.5). A reduction of the HC-PCF/conventional fibre splice loss could produce high conversion efficiency Raman lasers below the 100mW barrier.

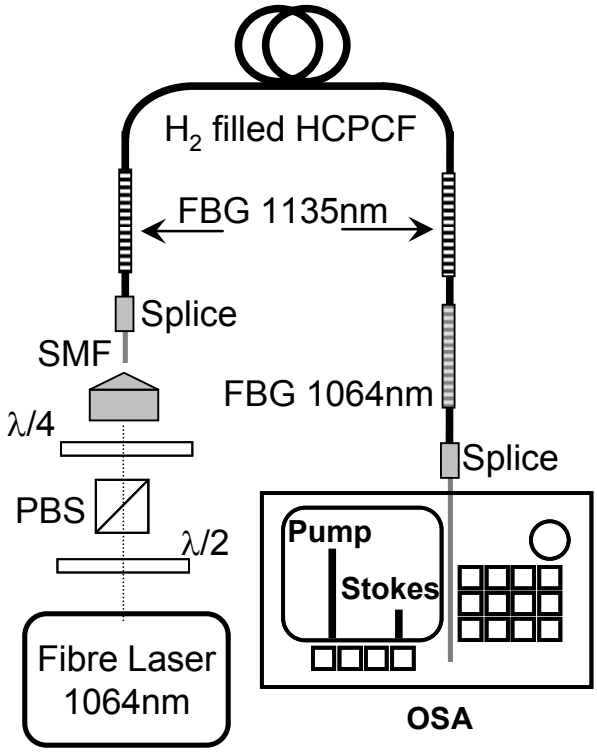

Fig. 6.7 Low threshold, all-fibre CW Raman laser experimental setup. FBG: Fibre Bragg Grating .

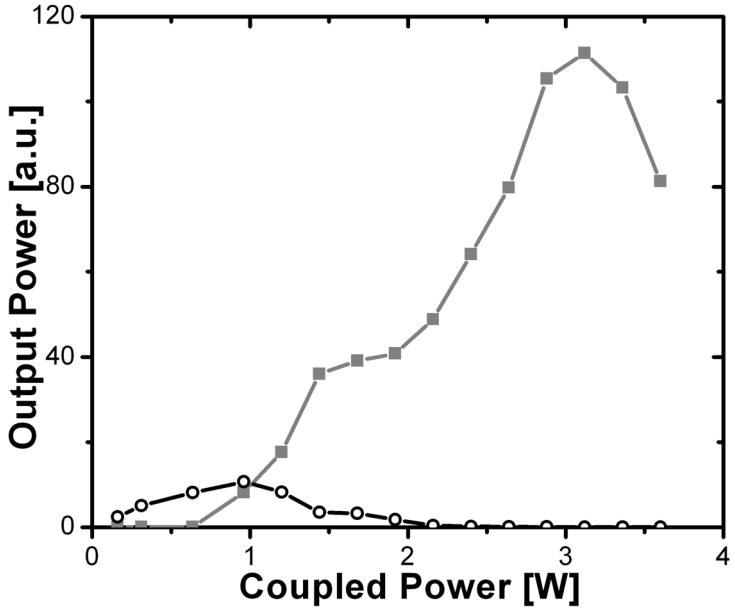

Fig. 6.8 Output power vs coupled input power for the pump (circles and black line)and $S_{00}(1)$ (grey squares and line) when using FBGs to form a cavity. The drop in Stokes intensity above 3W is due to conversion to second Stokes.

6.4 Summary

A single-pass CW Raman laser based on H_2-filled HC-PCF with 2.25W power threshold and 50% conversion efficiency into the Stokes line has been reported. The fibre proved an excellent Raman converter, with up to 99.99% of the output power at the Stokes wavelength, even at atmospheric pressure. A further reduction of the threshold to 600mW was made possible by the addition of FBG at the pump and Stokes wavelength. Further improvement on HC-PCF and splice loss would bring higher conversion efficiency and further reduce the threshold power.

The device is the first milestone toward the realisation of the proposed optical waveform synthesiser and reveals a prospective for a new type of compact Raman gas lasers based solely on photonic and optical fibre solutions. The low operating pressure of the laser and its narrow linewidth could also be of interest in coherent and quantum optics applications [8].

References and notes

[1] F. Couny, F. Benabid and P. S. Light, *Phys. Rev. Lett.* **99**, 143909 (2007).

[2] R. W. Minck, R. W. Terhune and W. G. Rado, *Appl. Phys. Lett.* **3**, 181 (1963).

[3] P. Rabinowitz, A. Kaldor, R. Brickman, and W. Schmidt, *Appl. Opt.* **15**, 2005 (1976).

[4] J. K. Brasseur, K. S. Repasky, and J. L. Carlsten, *Opt. Lett.* **23** , 367 (1998).

[5] L. S. Meng, P. A. Roos, and J. L. Carlsten *Opt. Lett.* **27** , 1226 (2002).

[6] Y. R. Shen and N. Bloembergen, *Phys. Rev.* **137**, A1787 (1965).

[7] IPG Photonics, www.ipgphotonics.com

[8] M. G. Raymer, *J. Mod. Opt.* **51**, 1739 (2004).

[9] J. L. Carlsten and R. G. Wenzel, *J. Quant. Elect.* **19**, 1407 (1983).

[10] R. J. Heeman and H. P. Godfried, *J. Quant. Elect.* **31**, 358 (1995).

[11] M. G. Raymer and J. Mostowski, *Phys. Rev. A* **24**, 1980 (1981).

Chapter 7

Ultra-broad Guidance in Large Pitch HC-PCF

This chapter introduces an alternative type of HC-PCF that guides over an ultra-large wavelength span thanks to a large-pitch photonic crystal cladding. The technique of fabrication, the optical characterisation and the identification of the novel guidance mechanism of the fibre are presented. This new type of fibre is the object of a patent by the author and Fetah Benabid [1].

7.1 Introduction

Thanks to the outstanding guidance properties of photonic band gap HC-PCF (based on a triangular lattice), a number of breakthroughs have been demonstrated in various applications such as efficient gas-laser fibre devices (Chapter 5 and Chapter 6), high power soliton delivery [2] and efficient electromagnetically induced transparency [3,4] to mention a few. However, drawbacks such as the intrinsically narrow transmission bandwidth of the fibre, the overlap between fundamental mode and interface modes [5], the high light-in-glass fraction of the air-guided modes and the challenges posed by fabricating these fibres with small pitches (<2 µm), excluded the implementation of photonic band gap HC-PCF from a large number of applications requiring broadband guidance or guidance in the visible or UV.

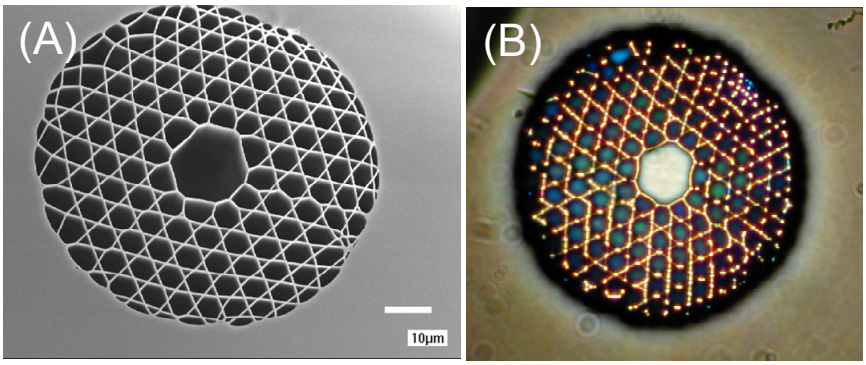

Fig. 7.1 (A) Scanning electron micrograph and (B) Optical micrograph of the Kagome fibre reported in [6]. Note the white light guided in the core, indicating a broadband guidance in the visible.

An alternative HC-PCF, based on a large pitch Kagomé lattice, has been reported to guide over extended frequency ranges [6] (Fig 7.1). As a matter of fact, this type of fibre was one of the first to be investigated experimentally as a possible candidate for photonic band gap guidance. But the lack of understanding of their guidance mechanism stood in the way of further improvement to the fibre loss and transmission bandwidth. Indeed, the unusual broadband guidance, illustrated in Fig 1B by the white light emerging from the fibre core, remained a mystery for some time as it was established later that the cladding photonic structure does not exhibit a photonic band gap; instead, it was recognized that, at the transmission wavelengths, the photonic structure of the Kagomé cladding exhibits a lower density of photonic state than that of the vacuum [7]. This apparent correlation between guidance and low DOPS raises more questions than it answers. Indeed, the presence of photonic states in the structure (i.e. cladding modes) implies, by virtue of mode interaction close to the phase-matching condition, that there should be a degree of mode-hybridization between the hollow-core mode and the cladding modes, similar to mode anti-crossing events observed in triangular lattice photonic band gap HC-PCF (Chapter 1). Consequently, this argument alone is insufficient when trying to explain the dramatic reduction in confinement loss compared to a simple hollow capillary with the same core diameter.

In this chapter, a more complete model of the guidance of this class of HC-PCF is built from fabrication and experimental characterisation results obtained for large-pitch Kagomé lattice fibre (Λ~12µm) by the author. A portfolio of fabricated large pitch fibres is presented. All the fibres exhibit broad transmission regions with relatively low loss covering the detection bandwidth of the optical spectrum analyser. They also show a low surface mode coupling, a high light-in-core fraction and a low chromatic dispersion. These

optical characteristics are confirmed with theoretical models of the fibre calculated by Dr P.J. Roberts.

From these studies, a new type of light guidance emerges where the core mode is thought of as a low interacting bound photonic state in a continuum of cladding modes akin to Von-Neumann Wigner bound states observed in quantum electronics [8]. The identification of this new guidance mechanism allows the optimization of the fibre bandwidth and loss for non-linear optics such as Raman side band generation or transient higher-order SRS (Chapter 8).

7.2 Fabrication of Large Pitch Kagomé HC-PCF

The fabrication technique for the Kagomé structured fibre is in many ways similar to that of triangular lattice photonic band gap (PBG) fibre. However, it is remarkable that only a few differences in the manufacturing process will transform the narrow bandwidth guidance of photonic band gap fibres to the ultra-broad bandwidth obtained with Kagomé fibres.

7.2.1 Stacking and cane drawing

The method used to create the Kagomé structure is the well-known "stack and draw" technique, similar to the one used for triangular lattice HC-PCF and solid core PCF [9] (Fig 7.2). Accordingly, thin circular capillaries are used as the air-filling fraction (AFF) of the stack corresponds roughly to that of the resulting fibre; the targeted air-filling fraction being between 80 and 90%. The stacks are fabricated without core tubes to avoid the presence of surface modes at the core vicinity. For stacks involving large core defect (7 and 19 cells defects), shorter capillaries are placed at either ends of the stack leaving a gap in the middle. Only canes from the centre of the stack will be usable for fibre drawing. Stacks for the single cell defect fibre are completed without defect and placed into a "jacketing" tube for robustness, before a single capillary is removed from the centre of the structure. The final outer diameter of the fibre, limited by the number of rings and the large pitch of the fibre, needs to be as small as possible (usually ~300μm) and therefore implies the use of a thin tube for the jacketing of the stack prior to drawing the canes (Fig 7.2B).

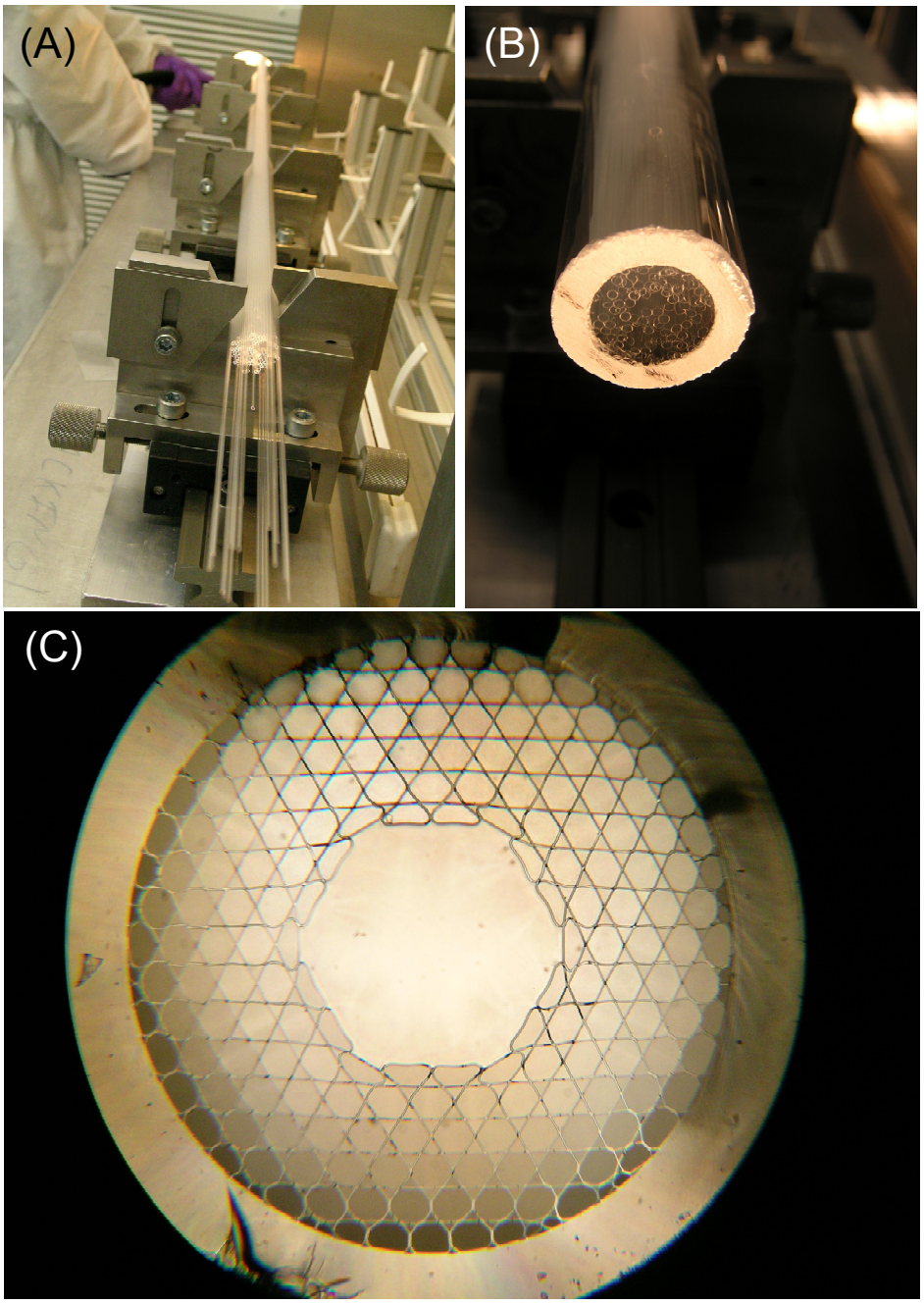

Fig. 7.2 (A) Stacking of capillaries on the stacking rig. (B) Jacketed stack. (C) An example of 19cell defect core Kagomé cane. Note the absence of the core tube, generally used in the fabrication of photonic band gap HC-PCF. The fabrication is done in a clean room to avoid contamination.

During the cane pulling process of conventional PBG fibre stacks, a vacuum is applied between the stack and the jacketing tube to collapse the interstitial, triangular holes and allow for the whole structure to fuse with the outer tube. In the case of the Kagomé fibre, no vacuum is used; the temperature is lowered until the structure is joined to the jacketing tube completely and a good, non-collapsed Star-of-David structure is obtained (Fig 7.2C). The resulting canes are 1m long and have an outer diameter of ~3.5mm.

7.2.2 Fibre drawing

The Kagomé cane is placed into an additional jacket tube and a vacuum is applied to the region between the cane and the tube so that the fibre can be drawn at high tension/low temperature without breaking. The integrity of the cladding and core structure of the large core defect fibres is preserved by applying a vacuum to the core. This is not necessary in the case of the single cell defect Kagomé as the core is small enough not to expand during the draw. The structure air filling fraction is maintained by pulling the fibre at low temperature, high preform feed rate and high drawing tension (in our case, typically <1950°C, >50mm/min and >400g respectively). Figure 7.3 shows scanning electron micrographs and optical micrographs of the 19, 7 and single cell defect core fibres when light is coupled through ~1cm of fibre.

Table 7.1 summarizes the fibres' dimensions. The smallest core, i.e. the single cell defect fibre core, is around 22µm in diameter and is already comparable in size to a 19cells defect triangular lattice HC-PCF core. The 19cells defect fibre core dimensions are truly enormous, reaching a diameter of ~65µm. The ellipticity of the 19cells defect core is due to the initial ovality of the jacketing tube used during the fibre drawing process. It is also remarkable that the "petal" shape of the core remains for this fibre, as it usually disappear during fibre drawing due to surface tension.

Table 7.1: Physical dimensions of Kagomé HC-PCFs[a]

Defect	Pitch Λ µm	Core size min/max µm	Strut width µm	AFF[b]
1 cell	11.8	22.3 / 26.1	0.67	0.82
7 cell	11.5	43.7 / 45.4	0.61	0.83
19 cell	10.9	47.8 / 68.3	0.51	0.85

a: Fibres' outer diameter 300µm, b: Air-Filling-Fraction

Small differences in pitch and strut thickness between the samples lead to different colours being guided through the cladding, as seen in Fig 7.3 (D-F). Interestingly, guided core-modes and cladding modes in Kagomé-lattice HC-PCF can co-exist even at the same wavelength (Fig 7.4). Although this causes a contradiction with the photonic band gap

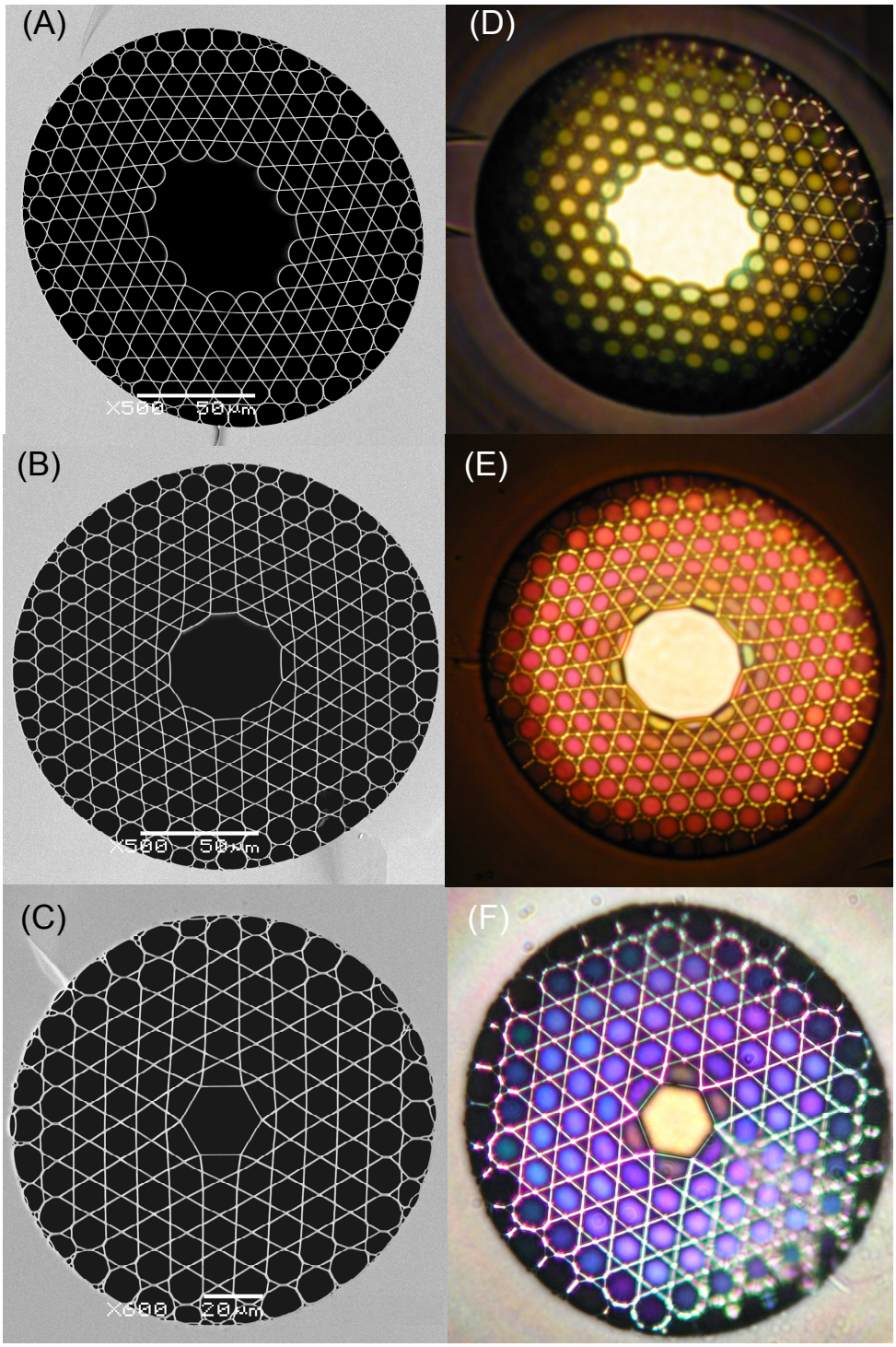

Fig. 7.3 (A - C) SEM and (D - F) optical micrographs of the single cell, 7 cell and 19 cell defect fibres. The samples are 2cm long and coupled in transmission to a tungsten lamp.

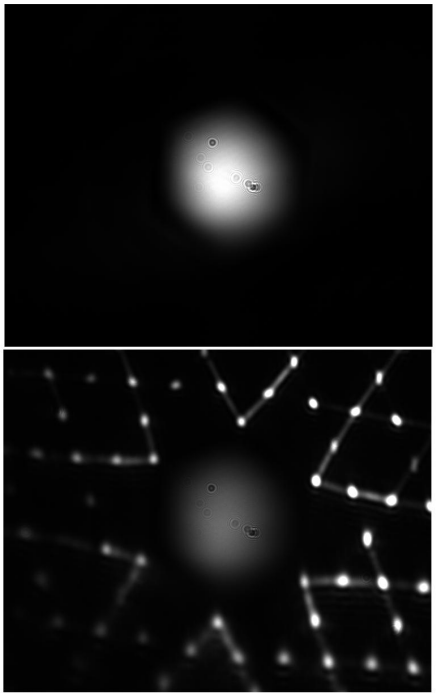

Fig. 7.4 Observation of near-field at 600nm with different coupling through core (top) and cladding (bottom).

guidance principle*, it does not seem to affect the light confining properties of the fibre. An example of this atypical guidance is the "white" light observed in the core in Fig 7.3 indicating a broad bandwidth transmitted in the visible region of the spectrum.

It is worth noting here that the fabrication of fibres with higher AFF is achievable by the post processing of the cane using hydrofluoric acid (HF) or using ultra-thin capillaries during the stacking process. Both methods have been tested and have effectively led to higher AFF. However, the resulting fibres had a higher optical attenuation and a narrower bandwidth than fibres fabricated using the "blowing up" technique (Section 7.5).

7.3 Optical Characterization

The fabricated Kagomé fibres are expected to transmit with low attenuation over a broader bandwidth than their photonic band gap counterparts. Critically for non-linear optics experiments, guided core-modes also exhibit low power-in-glass fraction, leading to a reduced chromatic dispersion, and a relative immunity to bend loss.

* i.e. no light can exist in the cladding within the PBG wavelength range (see Chapter 2)

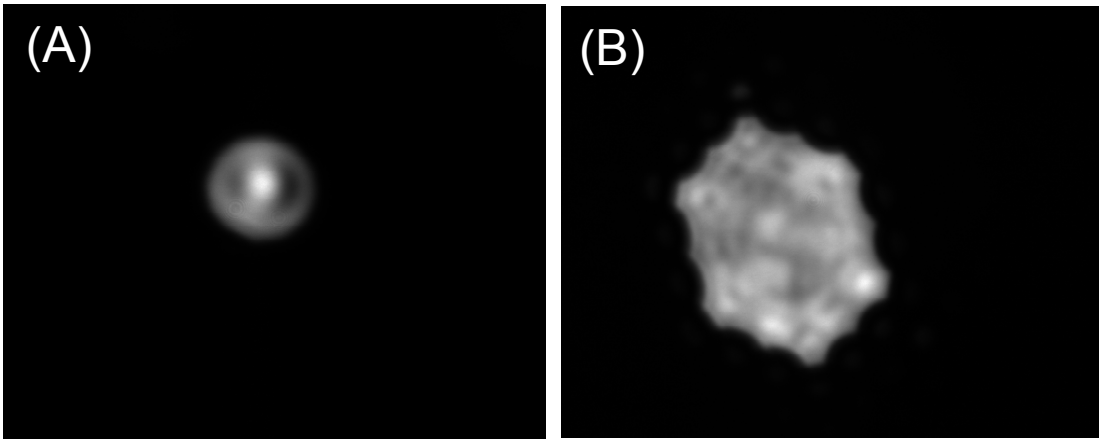

Fig. 7.5 Near-field profiles of (A) 7 and (B) 19cells defect core Kagomé HC-PCF. Note that, as opposed to large core PBG fibres, most of the guided light is within the core boundaries.

7.3.1 Near-field profile

As with conventional waveguides, a Kagomé fibre with a large core defect is expected to accommodate more modes than a fibre with a smaller core defect. This is illustrated in Fig 7.5, showing the near-field pattern at the output of the fibre at 700nm in case of the 19cells and 7cells defect core. Indeed, the near-field profile observed for the 19cells defect core fibre exhibits a non-homogeneous intensity profile and indicates that a large number of modes are guided, while the 7cells defect core fibre shows a more uniform mode pattern and guides fewer modes. It is therefore difficult to couple predominantly into the fundamental mode (HE_{11}) using these fibres as higher order modes are also easily coupled into.

Figure 7.6 shows the near-field profile of the single-cell defect core fibre that supports only the fundamental mode (Fig 7.6A) and two of the 4-fold degenerate higher order modes (Fig 7.6B and 7.6C). It is remarkable that such a limited number of modes are guided in such a large core (>20µm), facilitating the predominant coupling into the fundamental. The excited fundamental mode is also extremely well confined in the core as is shown in its radial profile in Fig 7.6D. Indeed, most of the mode intensity is within the core boundary with no light detected in the silica surround or in the cladding holes, indicating an extinction ratio >20dB in the first ring of holes. The measured NA of this fundamental mode at 700nm is measured to be 0.035.

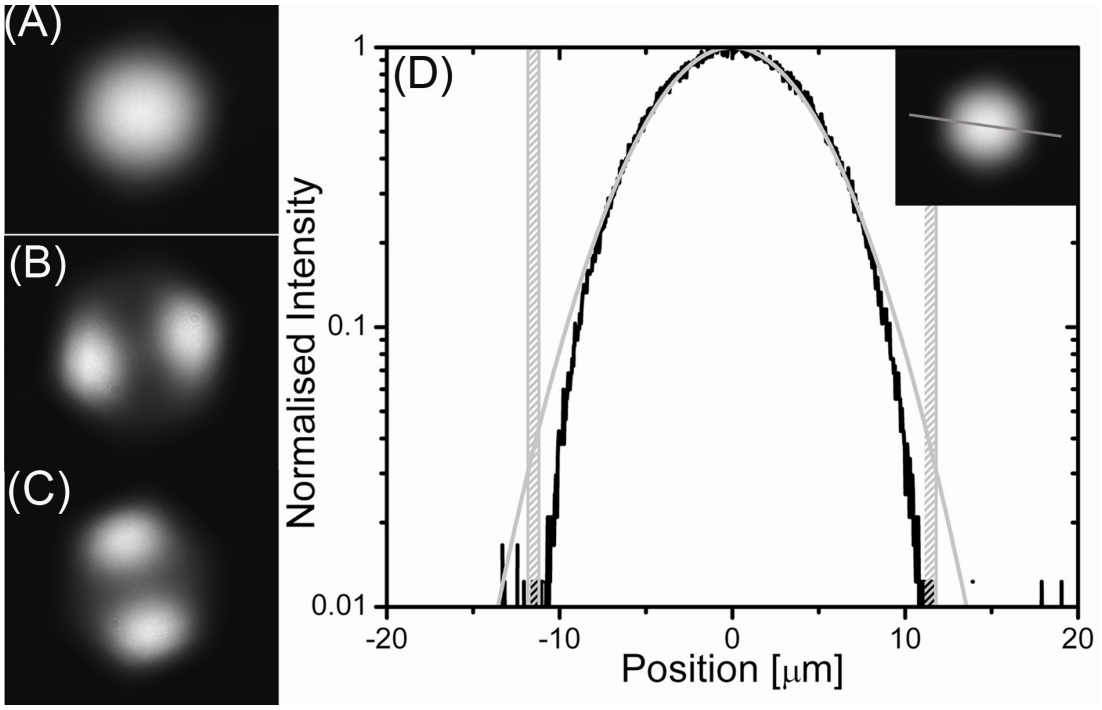

Fig. 7.6 Experimentally imaged near field profiles of the selectively excited (A) fundamental-like and (B, C) higher order core modes for the single cell defect Kagomé fibre. (D) Log-scale intensity cross-section of the fundamental mode (black line). Best Gaussian fit (grey line). The hashed grey regions indicate the position of the core walls. Inset: Cross-section position.

7.3.2 Transmission properties

The transmission spectra of the fibres are recorded by butt-coupling the fibre source to a few-meter long Kagomé fibre so that only the core modes are excited. In order to verify that no light is coupled into cladding modes, the near-field profile is also checked on a suitable camera, using a 3nm-bandwidth monochromator to select the wavelength of interest.

Figure 7.7A shows the transmission spectrum for the 19cells fibre sample with two high transmission regions; one in the visible spanning over 250nm* and the other one in the IR, as large as 700nm. Low levels of core guidance were also measured in the low transmission region (800nm-1025nm). Figure 7.7B presents the cut-back loss measurement for this fibre with a flat attenuation of 0.75dB/m on average for the near IR band and reaching a

* Nearly twice as large as the transmission bandwidth of a photonic band gap HC-PCF guiding in the visible

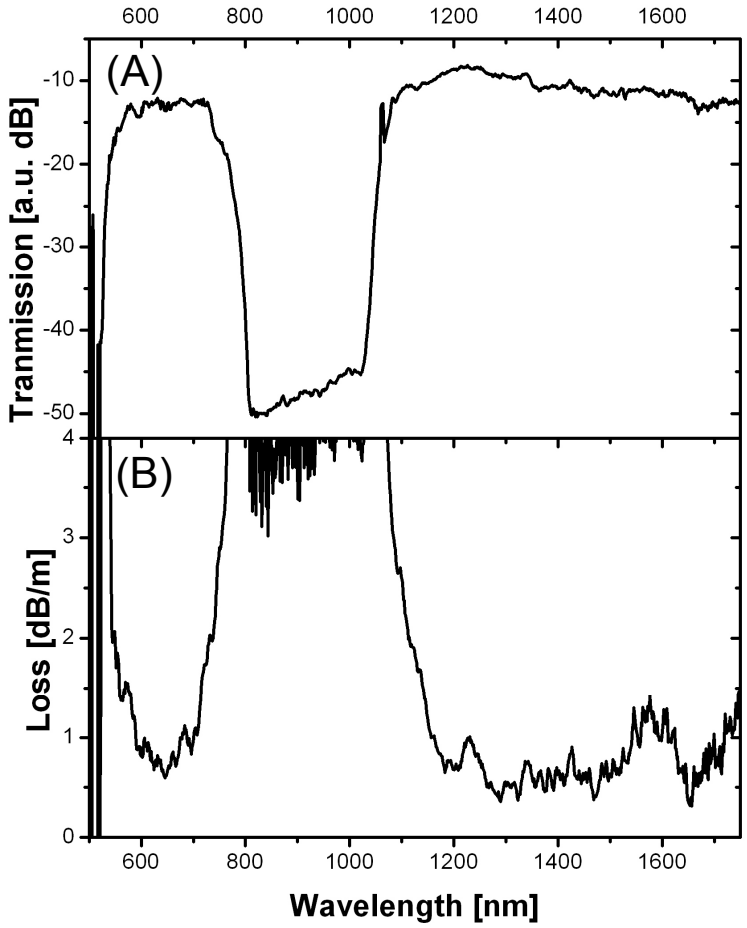

Fig. 7.7 (A) Transmission and (B) attenuation spectrum for the 19cells defect core Kagomé fibre.

minimum of 0.3dB/m. The loss is also below 2dB/m for most of the visible band, close to that of the photonic band gap HC-PCF guiding at this spectral range.

Figure 7.8 presents the transmission spectrum of the single cell fibre when the fundamental mode is predominantly coupled into. Once again, the measured transmission spectrum over a few meters exhibits two wide bands with high transmission. As for the 19cells defect core fibre, these bands sandwich a low transmission band where light is still guided in the fundamental mode, though with increased optical attenuation.

Similarly to PBG fibres, the two high transmission bands can be shifted to longer (shorter) wavelength as the fibre's pitch is increased (decreased) during the drawing process. This shifting mechanism can be thought of, in the case of PBG HC-PCF, as a zero DOPS region (PBG) shifting on a high DOPS background (no transmission). However, in Kagomé fibre, it is better described as a high DOPS band (low transmission) shifting over a low DOPS background (high transmission).

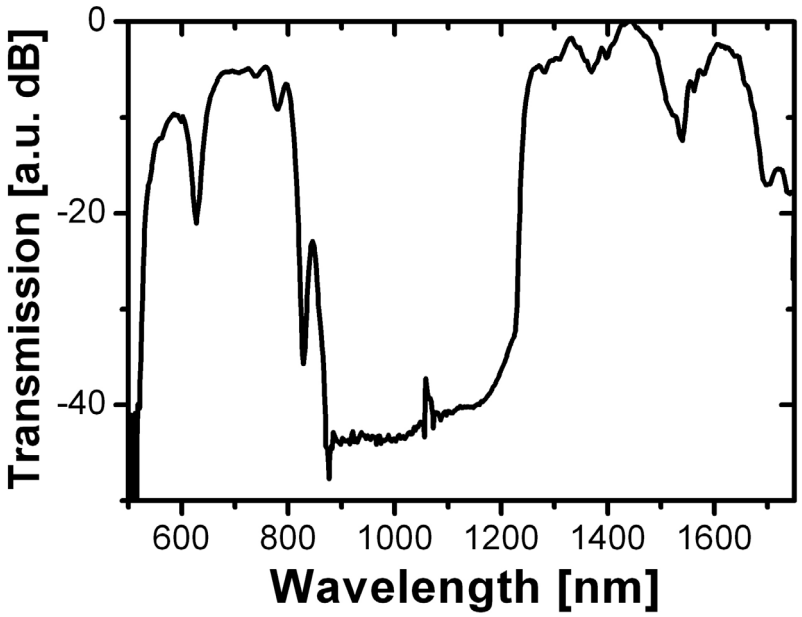

Fig. 7.8 Single cell defect core Kagomé fibre transmission spectrum.

7.3.3 Chromatic dispersion

A low chromatic dispersion is paramount to achieving efficient non-linear processes such as Raman scattering or Raman sidebands, especially when working with ultra-short laser pulses. Thanks to its low light-in-glass fraction, one would expect the Kagomé fibre to possess a very low dispersion, which, combined with the already identified broadband transmission, makes it the ideal candidate for the generation of Raman sidebands or other broadband non-linear effects.

The method chosen for measuring the chromatic dispersion of the fundamental mode of the single cell defect core Kagomé HC-PCF is based on interferometry (Fig 7.9). A broadband light source (tungsten lamp or supercontinuum source filtered at the wavelength of interest) is coupled into the fibre under test placed on one arm of the interferometer; whilst, on the other arm, light is allowed to propagate in free-space. The interferometric pattern created by the recombination of both arms is recorded thanks to the computer synchronized motion of the mirror on the fibre-free arm. The interference fringes shift in position as the wavelength is changed, indicating that the light incurs a wavelength-dependent delay as it travels through the fibre. The group velocity dispersion is then calculated as the derivative of the measured group delay.

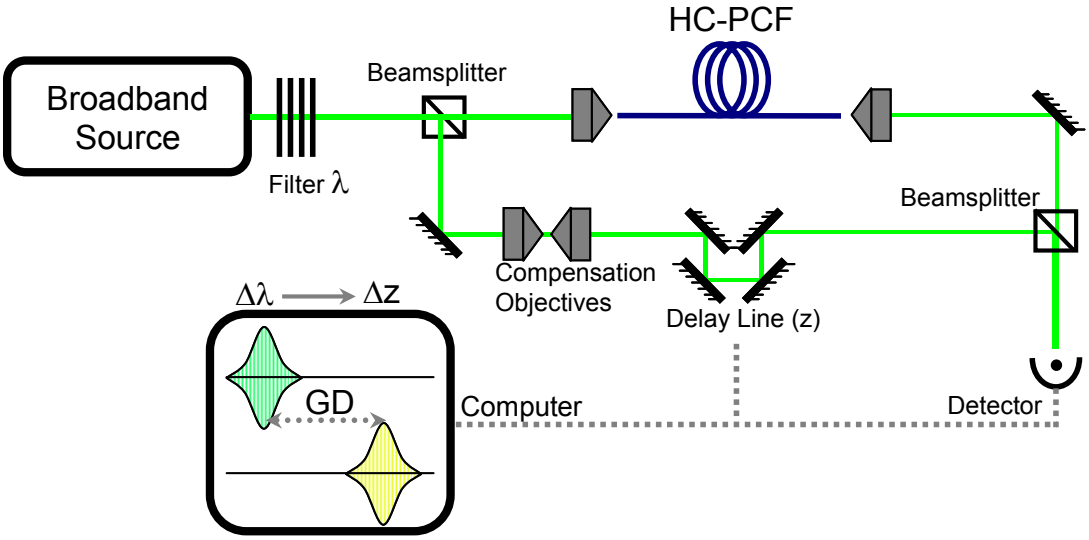

Fig. 7.9 Interferometric setup for the measurement of chromatic dispersion in HC-PCF. A change in wavelength (Δλ) leads to the displacement of the fringes (Δz) equal to the group delay (GD). A set of two microscope objectives are placed in the free-space arm of the interferometer to compensate the group delay of the coupling microscope objectives in the fibre arm.

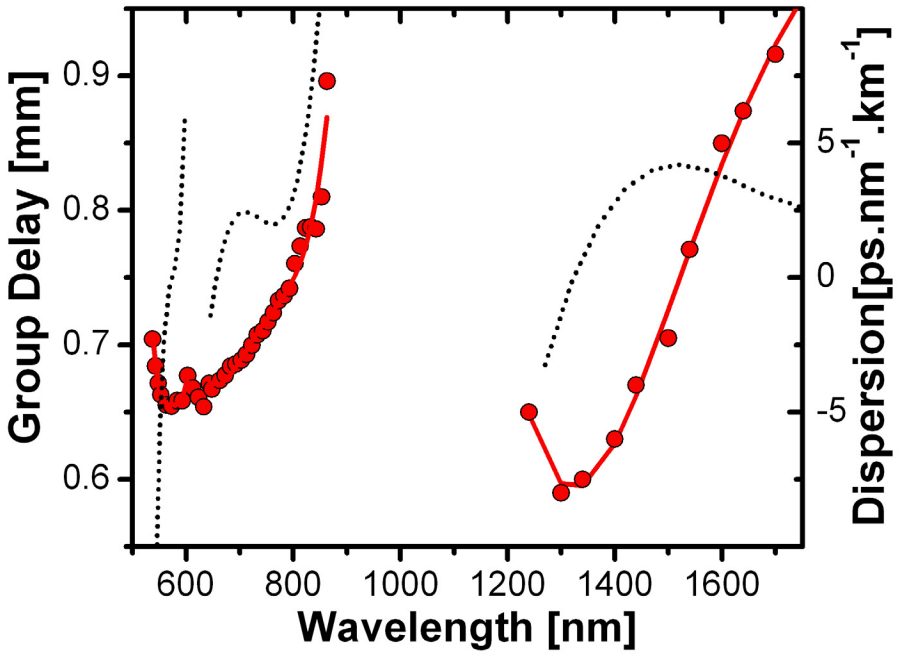

Fig. 7.10 Measured group delay (red dots), polynomial fit (red solid line) and dispersion fit (black dotted line) of a 90cm-long single cell defect Kagomé fibre. The group delay data for the IR band are up-shifted by 0.5mm for clarity.

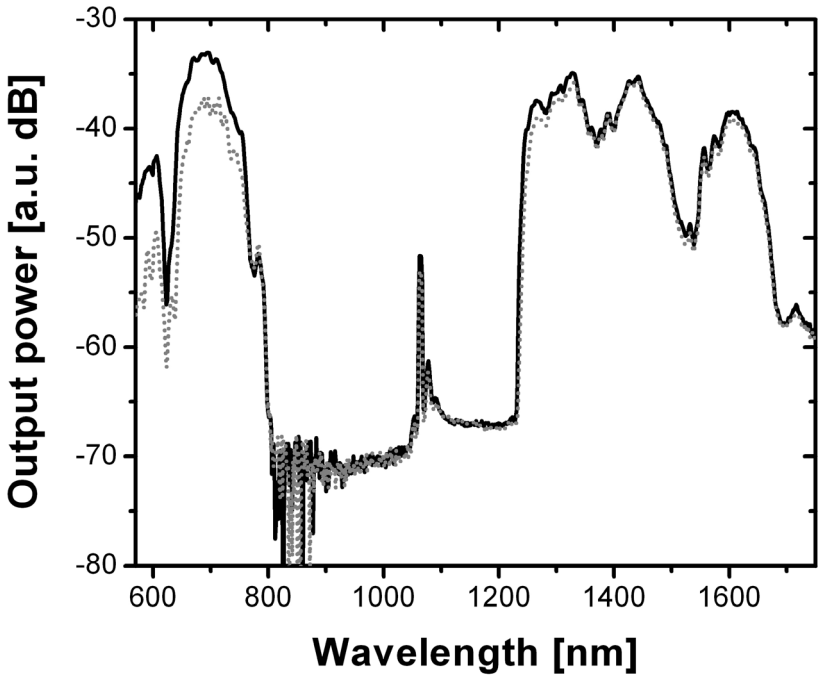

Fig. 7.11 Transmission spectrum of a straight, 2m-long sample of single cell defect core Kagomé fibre (black solid line) and when a 1cm radius bend is applied somewhere along the fibre (grey dotted line).

Figure 7.10 presents the measured group delay and the inferred chromatic dispersion of the fundamental mode of a 90cm-long single cell fibre. The dispersion has the typical tilted, flattened S-shape of a photonic band gap fibre (Fig 4.6); though the average figure throughout the whole transmission region of 2ps/nm/km is about 25 times lower than photonic band gap HC-PCF's dispersion, except near the low transmission regions. The measured dispersion further confirms the very low light-in-glass fraction of the fundamental mode and its exceptionally low coupling interaction with other cladding modes.

7.3.4 Effect of bending on transmission

Figure 7.11 shows the transmission of a straight section of Kagomé fibre compared to the same section with a 1cm radius bend. It can be seen that bending the fibre has little effect on the guidance properties of the fibre. Once again, this illustrates the limited coupling between the fundamental core-guided modes and the cladding modes that exist at the same frequencies.

7.4 Principle of Guidance

The numerical results presented here have been calculated by P.J. Roberts. The modelled structure is a Kagomé lattice closely matching the photonic crystal cladding obtained in fabricated fibres (Fig 7.12). Similar results have been obtained with other designs (large pitch triangular lattice and square lattice fibres) and are under investigation.

7.4.1 Kagomé lattice Density of states

Figure 7.13 presents the DOPS diagram of a periodic and infinite Kagomé structure as a function of the normalized wavenumber $k\Lambda$ and the real part of the effective index n_{eff} (a primitive unit cell is shown in the inset of Fig 7.13). The fabricated fibre (Fig 7.12A) has a pitch Λ~12µm corresponding to unusually high normalized wavenumbers, $k\Lambda$, ranging up to 200. As a result, calculations are conducted using a finite element (FE) solver [10], converging more rapidly at high $k\Lambda$ than other methods.

No photonic band gap is observed in the diagram. Instead, a relatively low DOPS is observed over two regions of the spectrum (region I and III) where the optical transmission is expected to be high.

Understanding the structure of the DOPS map requires the identification of the fibre's cladding resonators, similarly to the work done experimentally for the triangular lattice HC-PCF in Chapter 2. Narrow high-DOPS bands, represented in deep red in Fig 7.12, have slopes that decrease with increasing $k\Lambda$ and are associated with resonances of the cladding holes. The steeper and less well pronounced turquoise bands (such as region II) are associated with resonances of the connected network of glass struts.

Figure 7.14 compares the high and low bands of transmission measured in the single cell defect core Kagomé fibre (Fig 7.8). The frequency edges of the transmission bands match well with those inferred from the imaginary part of the effective index of the "fundamental" HE_{11}-like guided mode calculated using the structure in Fig 7.12B.

From these observations, it would seem that guided core-modes and cladding modes in Kagomé-lattice HC-PCF can co-exist even at the same ($k\Lambda$,n_{eff}). This situation is illustrated experimentally by the near-field of the transmitted white light through a few centimeters of fibre in Fig 7.3 and the example of experimental near-field profile at 600nm in the experimental fibre (Fig 7.4). This, then, appears to indicate the presence of bound or quasi-bound states (here, core modes) within a continuum (here, cladding modes), analogous to the problem of electronic bound states at energies above the potential

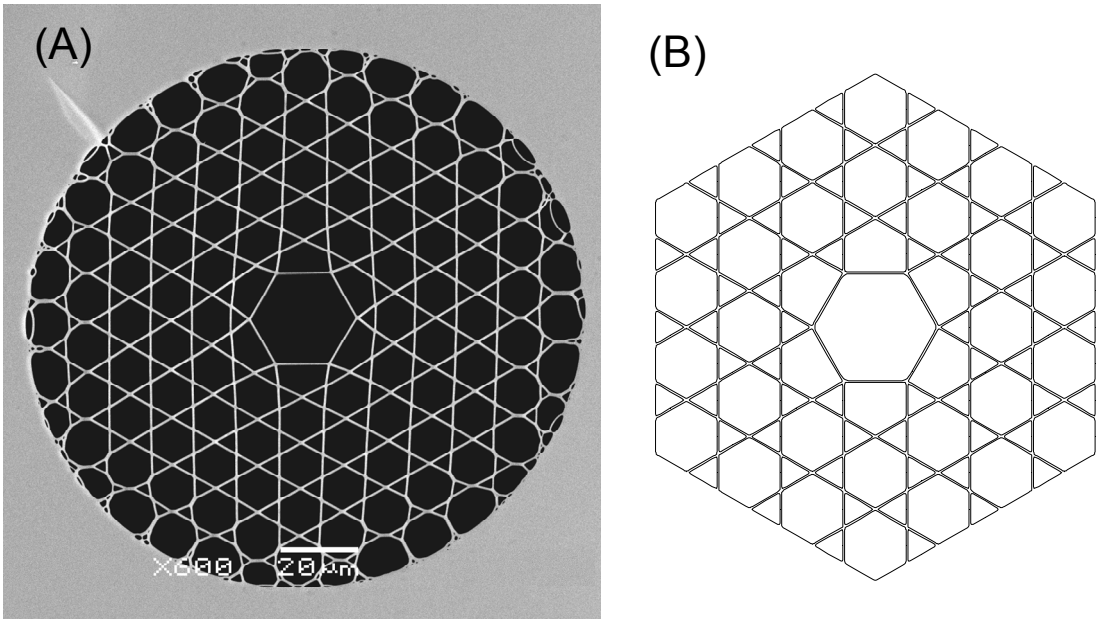

Fig. 7.12 (A) Scanning electron micrograph of the fabricated fibre. (B) Kagomé model used in the calculations.

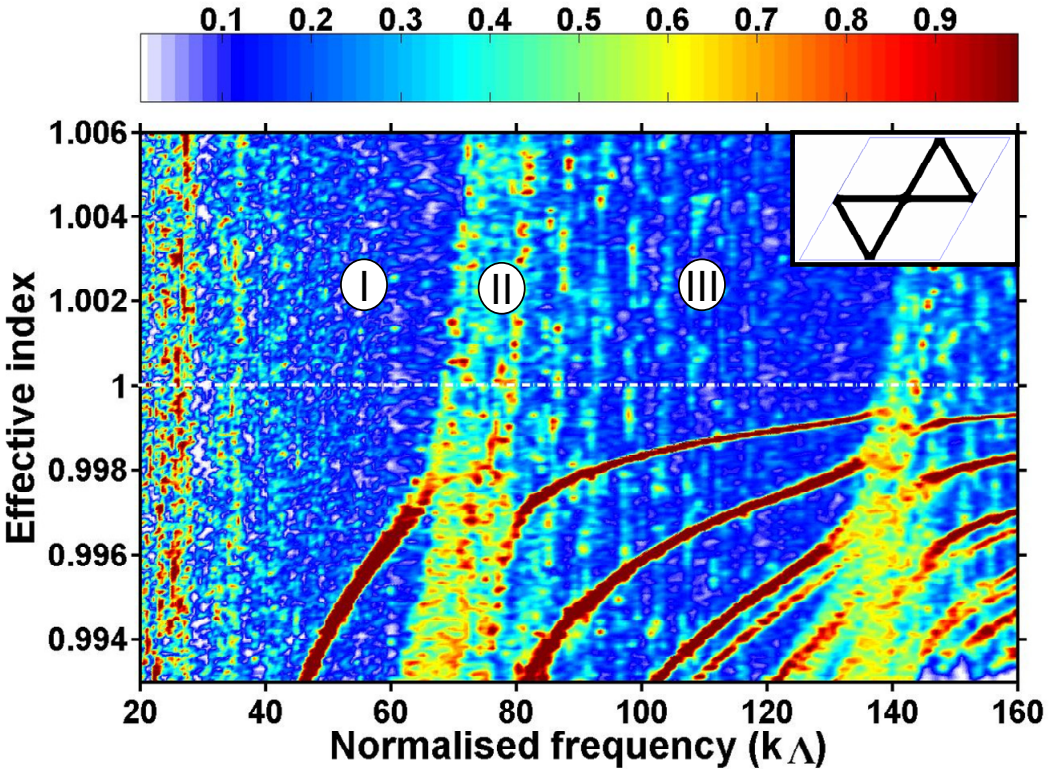

Fig. 7.13 Calculated normalized DOPS diagram as a function of the real part of the effective index and normalized wavenumber. Inset: Primitive unit cell of the Kagomé lattice.

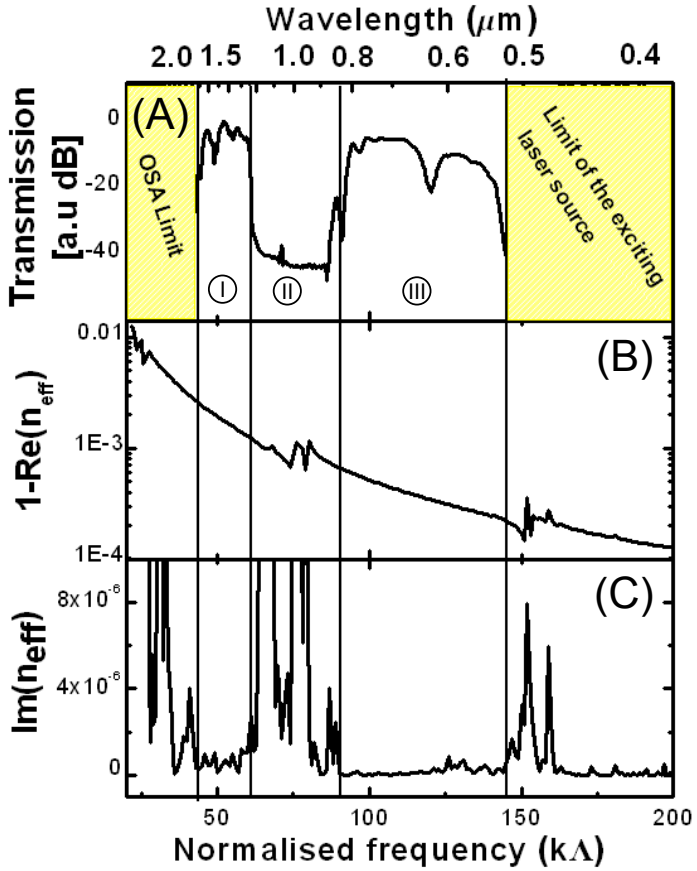

Fig. 7.14 (A) Single cell Kagomé fibre transmission plotted as a function of normalised frequency $k\Lambda$. The yellow regions indicate the spectral bounds imposed by the detection and the excitation systems. The vertical grey lines separate the different transmission bands. (B) Calculated real and (C) imaginary part of the effective index n_{eff} of the HE_{11}-like core mode ($Im(n_{eff})$ relates to transmission loss). At the edges of the high transmission band (i.e. Band (I) and (III), the index exhibits strong and rapid variations and a higher loss figure for band (II) due to strong inter-mode interactions.

barriers (i.e. spatially confined within the continuum), predicted by Von Neumann and Wigner as far back as the infancy of quantum mechanics [8,11]. The origin of this photonic paradigm can be explained by study of the interaction (or absence of interaction) between core and cladding modes.

7.4.2 Modal study

Figure 7.15 show calculated core and cladding modes at representative frequencies of the two high transmission bands (i.e. band I and III). In these regions, cladding photonic modes with effective index values close to the core mode are mainly localized at silica struts with rapid field decay into the air regions and a very steep dispersion (n_{eff} variation with $k\Lambda$). More significantly, they also exhibit fast phase oscillations of the field in glass, a

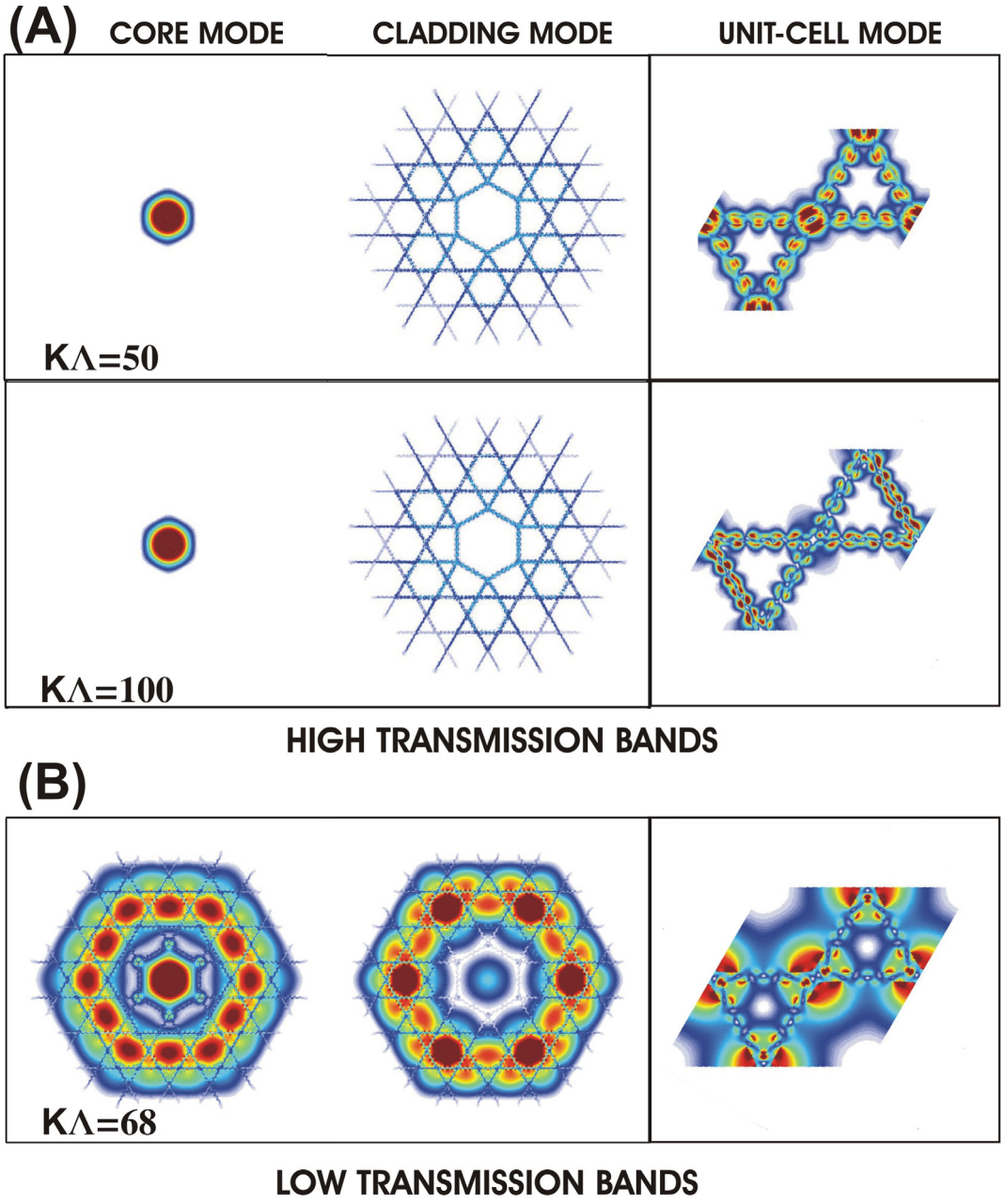

Fig. 7.15 Nature of the Kagomé-lattice HC-PCF cladding modes. (A) The first two columns show the core mode and a cladding mode for a frequency $k\Lambda$=50 in band (I) (top), and for a frequency $k\Lambda$=100 in band (III) (bottom). At each frequency, the effective indices of the core and cladding mode differ by less than 10^{-5}. The third column shows the mode of an infinite Kagomé lattice which corresponds to the cladding mode in column 2, calculated for the same frequencies at the Γ-point of the Brillouin zone. (B) Same as in (A) for $k\Lambda$=68 (in band (II).

manifestation of the large transverse wavevector components associated with such waveguide-modes at low indices ($n_{eff} \leq 1$) and high $k\Lambda$ (i.e. higher order modes). This behaviour is observed whether the calculation is based on a finite structure in which a core is included (second column in Fig 7.15) or on an infinite structure without a core being present (third column in Fig 7.15). The fast field oscillations of the cladding mode support the case for a strong transverse-field mismatch leading to a "washing-out" of the overlap with the slowly varying core-field distribution.

A further corroboration of this "inhibited coupling" between core and cladding modes is given by the strong confinement of the fundamental core-mode field intensity within the core observed experimentally in Fig 7.6 and confirmed theoretically in Fig 7.16. The calculated near-field profile shows that the field has decayed by ~30dB before the silica surround is reached. This figure is below the typical values, ~20dB, calculated and observed for band gap fibres with approximately the same mode size. Since so little field penetrates into the cladding, the core-mode shows low propagation loss as well as low interaction with the glass-confined cladding modes (Fig 7.16A). This rapid cladding decay of the fundamental core mode also indicated that only a limited number of cladding layers are required for the guidance to be efficient. Hence, an estimate of three rings of holes are required for the guidance to be efficient in this new guidance mechanism, while up to 8 rings are needed to achieve a good confinement loss in PBG fibre.

Crucially, these highly-dispersive fast-oscillating and silica-guiding properties are observed even for cladding modes of the same symmetry class as a core mode and that have effective index values which differ by only $\Delta n \sim 10^{-5}$ or less from the core-mode index. Despite this high degree of longitudinal phase-matching, the hybridization is observed to be extremely weak. Such an occurrence extends over the broad frequency range of both bands (I) and (III), and is illustrated in Fig 7.16A by the low value of the power-in-glass fraction over these frequency ranges. It is worth noting that this "non-interaction" between states with the same symmetry superficially might appear to violate the "non crossing rule", but in fact, as was pointed out by Von Neumann and Wigner [8], this rule ceases to hold where dense continua are involved.

The fast-oscillating nature of these modes also elucidates the immunity of the Kagomé HC-PCF to bend loss observed in Fig 7.11. In analogy with fibers which have a cylindrical symmetry (e.g. Bragg fibres), these modes are associated with a very high effective "*m*" number which governs the azimuthal field dependence. A perturbation which may induce coupling between the core mode and such cladding modes necessarily requires a fast

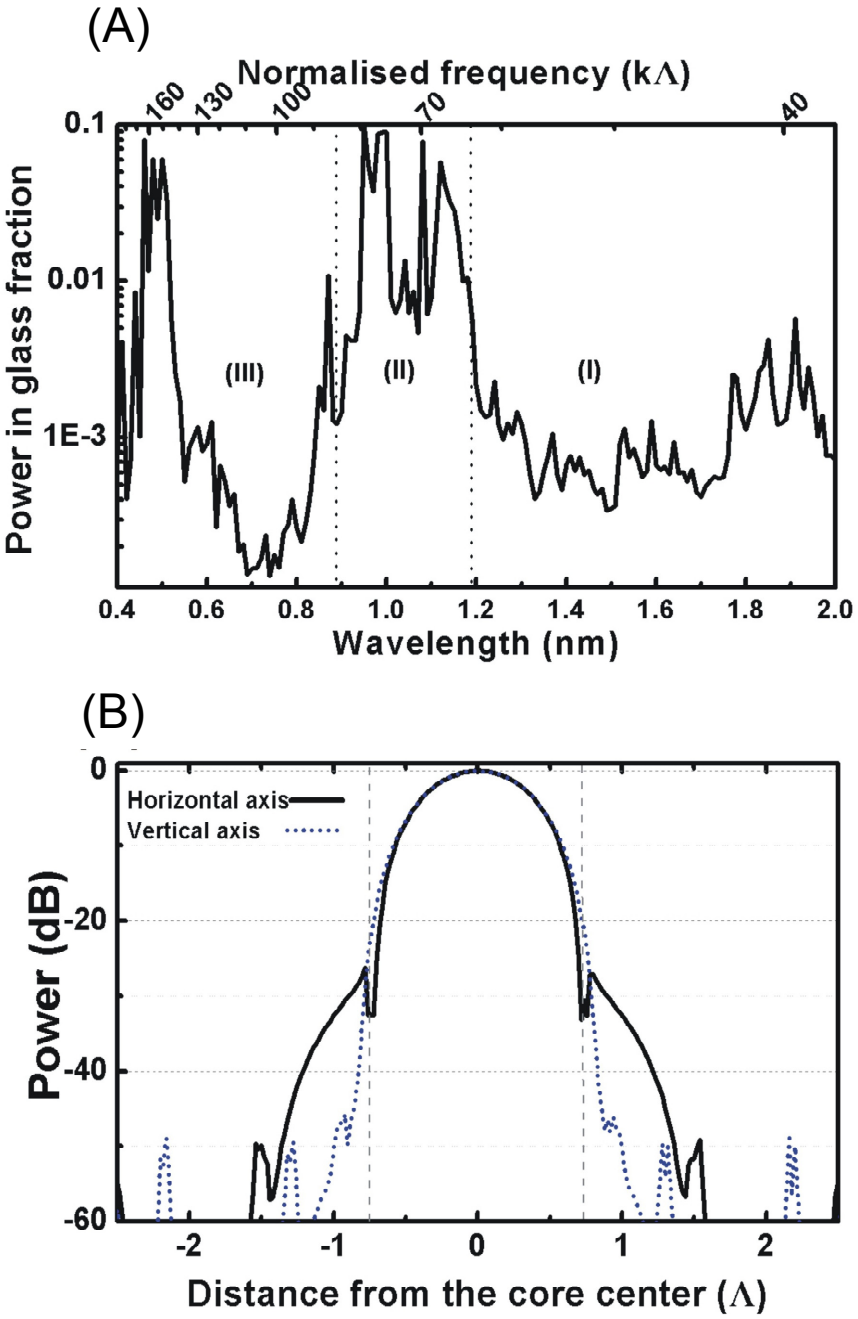

Fig. 7.16 (A) Power in the glass fraction plotted as a function of kΛ. (B) Intensity profile of HE_{11}-like mode along the horizontal and vertical cross-section respectively, the orientation is same as in A and B. The vertical grey dashed-lines show the silica core-wall positions for the horizontal axis.

azimuthal variation (in order to produce a large Δm). A fiber bend, however, is primarily associated with a change in m of just 1, thus providing the fibers with good resilience to bend induced coupling from core mode to these cladding modes despite the small detuning. The coupling induced by such perturbations is also weakened due to the small overlap between the core mode and cladding mode intensity distributions.

The Kagomé cladding can be thought of as a set of concentric rings of struts, similar in structure to Bragg hollow core fibres (Fig 7.17) [13,14]. Strong interactions can, therefore, result for glass resonances which involve slow variation of the phase around each hole periphery. Figure 7.15B shows a representative mode (kΛ=68) of the low transmission band (band (II)). The modes of this band belong to a family of cladding modes for which the inhibited coupling with the core no longer holds. This is caused by the interaction between the cladding hole-modes and glass strut-modes which becomes stronger nearer to the lowest-order resonance wavelength that can be estimated from $k\Lambda = \pi\, j\left(t/\Lambda\right)\Big/\sqrt{n_{gl}^2 - 1}$ (j=1,2,3...), where t is the strut thickness and n_{gl} the refractive index of the glass. For the strut thickness t=0.044, this corresponds to $k\Lambda$=68, 136, etc... which coincides with normalised wavenumber values around which strong mode interaction is evident in the figure. The interaction increases the effective index of some of the air-dominated modes so that they may phase-match with the HE_{11}-like resonance of the core. The consequent hybridization of the compatible modes leads to the enhanced leakage from the core around the same wavenumber values in a similar way to that of mode anti-crossings in photonic band gap HC-PCF.

This new generation of HC-PCF holds the promise of low optical attenuation over ultra-broad bandwidth spanning the UV and the visible part of the spectrum. The guidance mechanism identified here is under investigation in other large-pitch structures such as triangular and square lattice HC-PCF (Fig 7.18). Preliminary results show the exceptional characteristics of the Kagomé fibre are not limited to this lattice and can be observed in these alternative designs.

More importantly, the results obtained above enable the design of an optimised Kagomé HC-PCF offering an improved frequency bandwidth and optical loss.

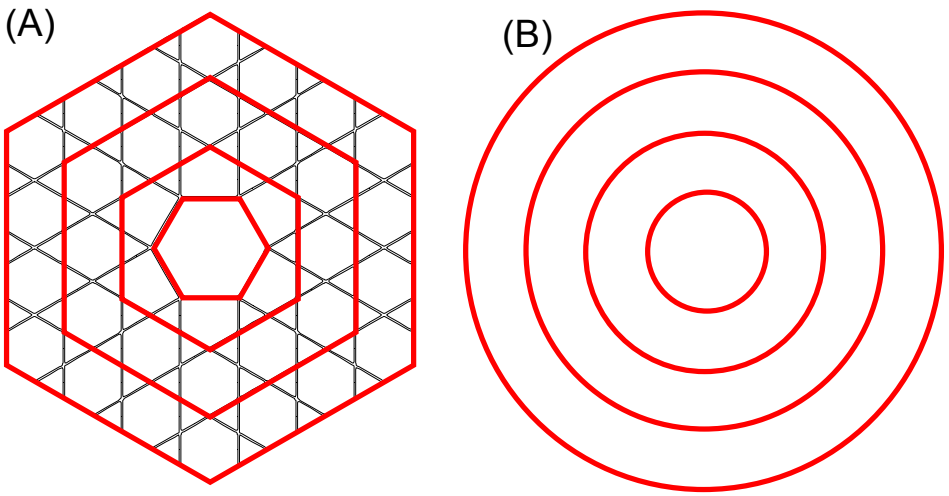

Fig. 7.17 Comparison between (A) the Kagomé lattice and (B) a Bragg fibre.

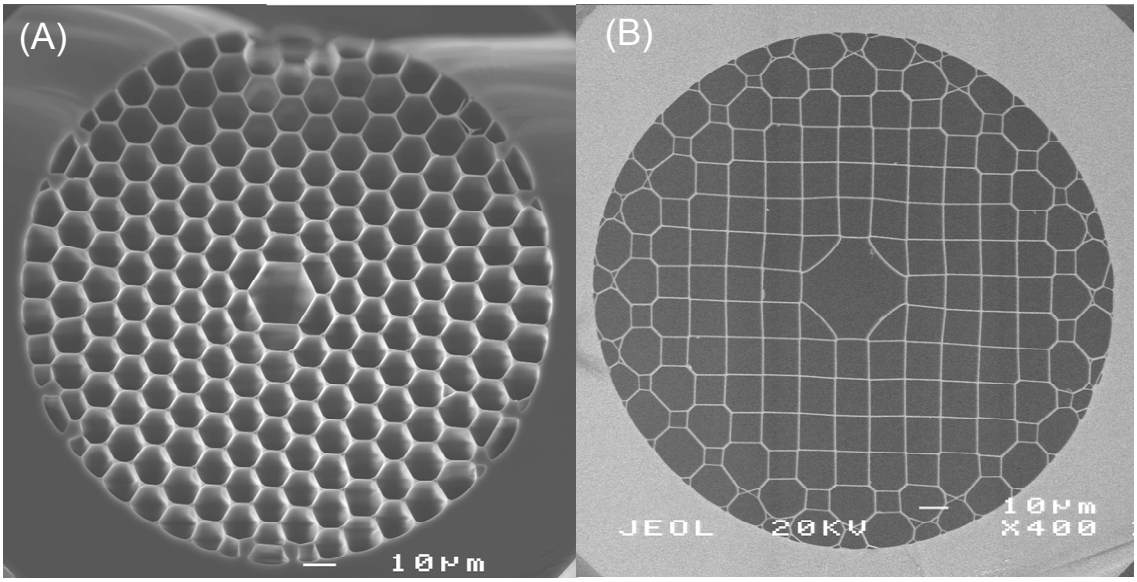

Fig. 7.18 Scanning electron micrograph of (A) a triangular and (B) square lattice large-pitch HC-PCF

7.5 Optimization of Bandwidth

The experimental characteristics reported in Section 7.3 confirm that the guidance mechanism reported in Section 7.4 has been rightly identified and open a new route to designing and fabricating a new Kagomé-lattice fibre in which the struts resonances causing the strong interaction with the core mode are all pushed to short wavelength. This is achieved by thinning the glass struts during the fabrication of the fibre. This also has the benefit of weakening the interaction and narrowing the wavelength range over which significant interaction occurs, widening the high transmission bands, thus maximizing the optical bandwidth and further reducing the dispersion. However, the struts must not be too thin as it would compromise the long wavelength guiding ability of the fibre.

Figure 7.19 shows scanning electron micrographs and physical characteristics of three Kagomé fibres fabricated with a view to optimizing the transmission bands. The thinning of the cladding struts is achieved by increasing the applied gas pressure within the cladding and core during the fibre drawing process. As the fibre is drawn at high tension (low temperature), a pressure of about 50kPa is required to significantly reduce the strut thickness. This cladding and core pressure is twice as high as the pressure used in the fabrication of "conventional" HC-PCF, where the air-filling fraction is increased by blowing up the cladding holes.

The thickness reduction obtained for fibres B and C compared to fibre A results in a dramatic enhancement of the transmission bandwidth accompanied by a shift of the bands to shorter wavelength (Fig 7.19). The expansion of the cladding region also causes the pitch to slightly increase in size (Table 7.2), and consequently one might expect a shift of the spectral features to longer wavelengths as is the case for PBG fibre. However, this does not occur since the spectral positions of the low transmission bands are driven by resonances of the constituent glass struts which are dictated by the strut width (Table 7.2).

Table 7.2: Physical characteristics of "blown-up" Kagomé fibres

Fibre	Cladding/Core Pressure kPa	Pitch Λ µm	Strut width µm
A	0	11.18	0.39
B	20	12.12	0.36
C	50	12.69	0.29

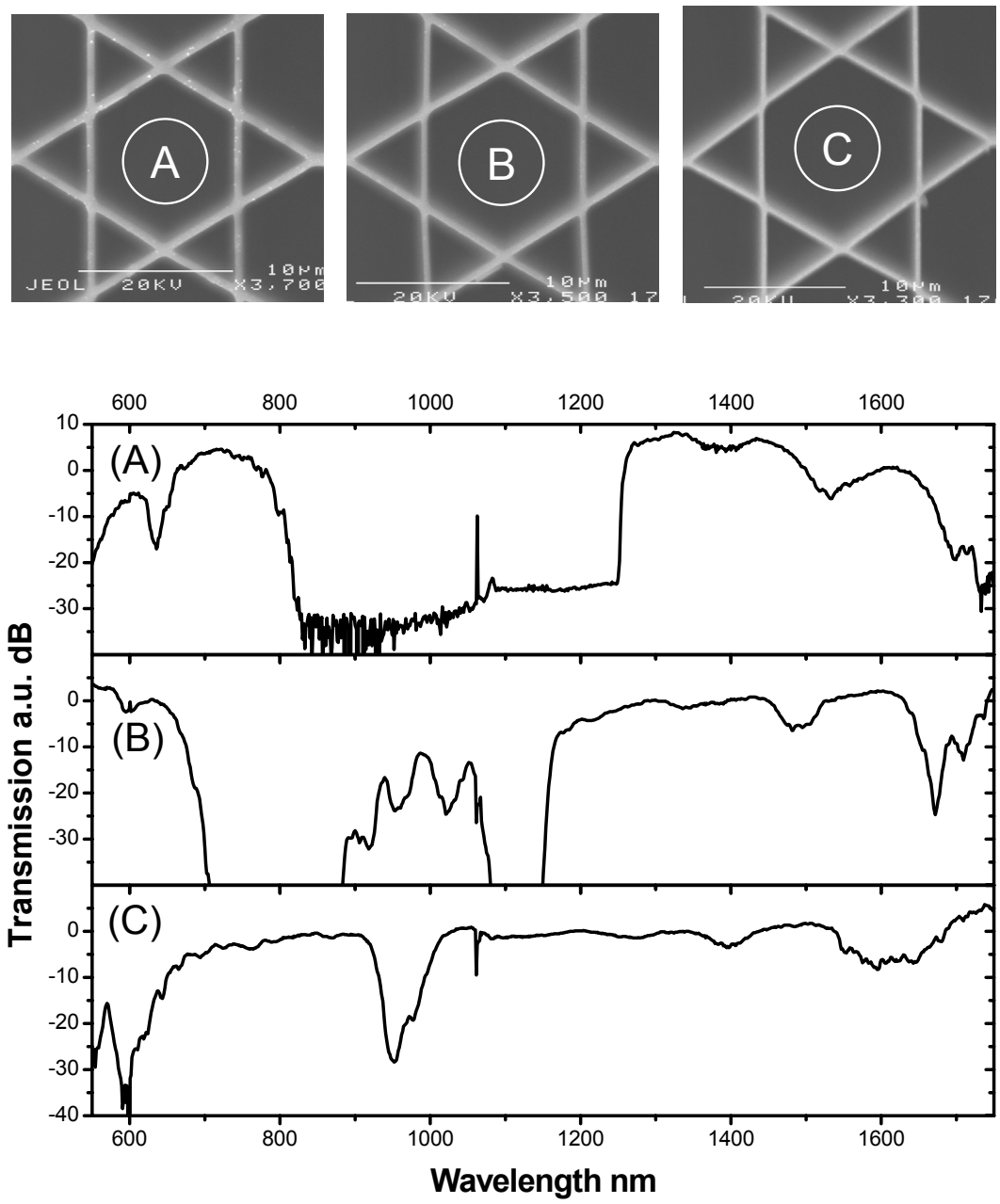

Fig. 7.19 (Top) Scanning electron micrographs of the cladding of a Kagomé fibre fabricated at (A) 0 kPa, (B) 20 kPa and (C) 50 kPa gas pressure applied to both cladding and core. (Bottom) Optical spectrum of the corresponding fibre.

Fibre C in Fig 7.19 has struts thinned to approximately 290 nm. The lowest strong strut resonance is pushed to near 600 nm. Although the struts are very thin (only ~2% of the pitch size), it is sufficient to confine light with a low leakage loss up to an estimated wavelength of 2500 nm.

As for the struts, resonances can also be identified at the glass nodes where the glass struts join. The less pronounced transmission dip near 950 nm observed for fibre C in Fig 7.18 can be identified theoretically to these glass nodes resonances. Once again, a careful design of the fibre shall push these resonances away from the wavelengths of interest.

7.6 Summary

Fabrication and characterisation of large pitch Kagomé fibres have been presented. This unusual type of fibre guides by inhibited-coupling between core and cladding modes, similar to what can be observed in Von Neumann-Wigner bound states. The identification of this new type of hollow core guidance will lead to the development of the next generation of HC-PCFs with even broader bandwidth and lower transmission loss.

The relatively large core-size of this fibre simplifies the gas filling process and reduce the wall-induced decoherence in quantum optics applications [3,4]. Furthermore, it represents an excellent and unique host for atomic-vapour based applications. The very large core of the 19 cell defect Kagomé fibre makes it the perfect candidate for gas sensing applications. The ultra-flat chromatic dispersion properties and low light-in-silica fraction of the single cell fibre creates new prospects for non-linear optics in gaseous media over a large optical bandwidth. More importantly, it can be used to synthesise ultra-broad frequency combs, the second main device in the proposed optical waveform synthesiser.

References and notes

[1] Patent application N° KS.P42029GB

[2] D. G. Ouzounov, F. R. Ahmad, D. Muller, N. Venkataraman, M. T. Gallagher, M. G. Thomas, J. Silcox, K. W. Koch, and A. L. Gaeta, *Science* **301,** 1702 (2003).

[3] S. Ghosh, J. Sharping, D. G. Ouzounov and A. L. Gaeta, *Phys. Rev. Lett.* **94**, 093902 (2005).

[4] F. Benabid, P.S. Light, F. Couny, and P. St. J. Russell, *Opt. Exp.* **13**, 5694 (2005).

[5] C. M. Smith, N. Venkataraman, M. T. Gallagher, D. Muller, J. A. West, N. F. Borrelli, D. C. Allan, K. Koch, *Nature* **424**, 657 (2003).

[6] F. Benabid, J.C. Knight, G. Antonopoulos and P. St. J. Russell, *Science* **298**, 399 (2002).

[7] T. D. Hedley, D. M. Bird, F. Benabid, J. C. Knight and P. St. J. Russell, *Conference on lasers and electro-optics* (Baltimore) (2003).

[8] J. von Neumann and E. Wigner, *Physik. Zeitschr.* **30**, 465 (1929).

[9] P. St. J. Russell, *Science* **299**, 358 (2003).

[10] JCMwave GmbH, www.jcmwave.com

[11] G. Humbert, J. C. Knight, G.Bouwmans, P. St. J. Russell, D. P. Williams, P. J. Roberts and B. J. Mangan, *Opt. Express* **12**, 1477 (2004).

[12] F. H. Stillinger, D. R. Herrick*, Phys. Rev. A* **11**, 446 (1975).

[13] P. Yeh, A. Yariv, and E. Marom, "Theory of Bragg fiber," *J. Opt. Soc. Am.* **68,** 1196-1201 (1978).

[14] Y. Fink, D. J. Ripin, S. Fan, C. Chen, J. D. Joannepoulos, and E. L. Thomas, *J. Lightwave Tech.* **17**, 2039(1999).

Chapter 8

Multi-Octave Frequency Comb Generation in Kagomé Fibre

In this final chapter, molecular hydrogen confined in a Kagomé fibre is used for the generation and guidance of a higher-order stimulate Raman scattering comb-like spectrum spanning three optical frequency octaves (325-2300 nm). Up to 45 high-order Stokes and anti-Stokes lines are generated by coherently exciting the confined gas with a simplified pumping system consisting of a single, moderately powerful infra-red nanosecond pulsed laser. The system requires no cryogenic system to achieve maximum molecular coherence of the Raman active gas and cuts the required laser power for efficient conversion by six orders of magnitude compared to current Raman sidebands generation techniques. The process opens up a robust, inexpensive and straightforward route to finding viable alternatives to high harmonic generation in synthesizing attosecond pulses.

8.1 Introduction

The most promising alternative to high harmonic generation (HHG) for the creation of attosecond pulses is the technique based on Raman sidebands by adiabatically driving the Raman medium to maximum molecular coherence (see chapter 1). This technique, suggested and demonstrated by Harris and co-workers [1,2], achieves high conversion efficiency and an ultra-broad spectrum consisting of a large number of mutually phase

locked high-order Stokes and anti-Stokes fields over a very large frequency span. The coherence and the broadband nature of the spectrum mean that it should be possible to synthesize sub-femtosecond optical pulses. However, it has been argued qualitatively that one could obtain a coherent high order Stimulated Raman Scattering (HSRS) spectrum using a single pump laser, provided one operates in the transient and high-gain regime of Raman amplification [3-5]. So far, this requirement meant the frequency comb was only generated using GW-power, transform-limited sub-picosecond lasers.

The results presented in Chapter 4 and Chapter 5 clearly indicate that the transient regime of rotational SRS could be extended to low-power nanosecond pulses by use of a photonic band gap HC-PCF. Nevertheless, the fibre itself would hinder the number of generated frequency components, due to its modest ~70THz available bandwidth. This is far away from the ~1000THz bandwidth required to generate attosecond pulses in the IR-UV domain. The new type of guidance achieved in Kagomé-lattice fibre and reported in Chapter 7, lifts these bandwidth limitations by offering a transmission spectrum spanning from UV to mid-IR with low dispersion and relatively low loss.

The generation of the spectral comb was first observed experimentally by the author. The simultaneous generation of the Stokes lines indicates a parametric process, implying that the comb components could be Fourier-synthesized into attosecond pulses. This suggestion was theoretically confirmed by studying the expected evolution of the Raman lines from spontaneous emission (the theoretical investigation was conducted by F. Benabid from the University of Bath, UK and by M. G. Raymer from the University of Oregon, USA).

8.2 Theory of Frequency Comb Generation in Kagomé Fibre

As demonstrated in Chapter 5, the HC-PCF offers the possibility to extend the transient regime of Raman amplification to pulse length much longer than T_2 and with a peak-power level lower than experiments in free-space or using hollow fibres. By using one metre of single-cell defect core Kagomé-lattice fibre (with ~20µm core diameter), one could use pulses as long as 700 times T_2 with peak powers as low as 10kW, whilst remaining in the transient regime of amplification, creating a new and favourable situation for the generation of coherent SRS for pulses >10ns. Indeed, the extension of the pump pulses to much longer durations would enhance the still-transient Raman gain and would weaken

the damaging effect of dispersion in the generation process. In the case of SRS in hydrogen with 10ns pulses, the dispersion length (Eq (4.14)) largely exceeds the 1km length-scale.

The broadband low-loss light guiding and confining features of the Kagomé fibre means that a single pump laser configuration can be used for the Raman amplification and frequency comb generation. The one-pump scheme can be viewed qualitatively as the combination of the spontaneously seeded SRS process to produce the first Stokes line, followed by parametric four-wave Raman mixing to produce the anti-Stokes and the higher-order Stokes Raman sidebands [4]. This system also offers flexibility in the choice of Raman medium used and the pump wavelength, lifting the limitation of previous dual-pump techniques, restricted to using Deuterium as the Raman medium and to Nd:YAG and Ti:Sapphire lasers due to the high laser power necessary for to achieve efficient conversion.

Due to the major role of the quantum noise in the initiation of the SRS process (as discussed in Chapter 4), the issue of the mutual phase coherence of these many sidebands generated by a single pump is subtle and should be addressed theoretically within the quantum framework. Quantum analysis of spontaneously initiated single-Stokes generation has been previously made for the case of broadband, multi-line pump lasers, and those results showed that there is automatic phase coherence of the generated Stokes lines with the pump, even when initiated by spontaneous emission [6,7], in corroboration with previous work reported by Carman et al. using the classical approach [8]. In order to deal with the present case of a single-frequency pump and several Stokes and anti-Stokes (S/AS) lines, a new quantum analysis (i.e. SRS initiation from spontaneous emission) generalized to include an arbitrary number of Stokes and anti-Stokes lines is required. The quantum theory stems from two previous works that dealt with limited cases; one on the generation of the first Stokes line [6] and the other on joint generation of the first pair of Stokes and anti-Stokes [9]. Full details of this analysis are given in Reference [10].

The results of the theory, applied to an isolated vibrational (or rotational) Raman transition, predict that in the high-gain transient regime, all Stokes/Anti-Stokes sidebands carry phases that are automatically correlated in a deterministic fashion (i.e. phase-locked). First, the pump pulse, short enough to be in the transient regime, spontaneously generates a first-Stokes (S1) pulse. The optical phase of the spontaneous seed for the S1 pulse is temporally and spatially randomly fluctuating during the generation process, corresponding to a thermal distribution of the temporal-spatial modes (TSM) of the molecular excitation [6]. Remarkably, and crucially, this initial noise is heavily filtered out under the high-gain transient conditions to produce a Stokes field determined solely by the

dominant TSM that corresponds to the highest Raman gain; in other words, it has the form of a transform-limited wave packet with a single overall phase which is random but reproducibly created on each laser shot when SRS is in the high-gain transient regime [11]. Furthermore, concomitantly with the generation of S1, there is a rise of a first anti-Stokes (AS1) field and a molecular excitation, which are determined by the same phase that arises spontaneously [9,11,12]. This result is ascertained by calculating the degree of mutual coherence between the Stokes and anti-Stokes fields [10].

A further result from the new theory shows that the higher order S/AS pairs retain the same key features of sharing a common phase related to that of the first S/AS pair. Similarly, the net molecular-excitation builds up constructively as more S/AS pairs are generated and excite substantial molecular coherence despite it been initiated from quantum noise. As in the case of single S/AS pair generation, the molecular coherence shares a (random) overall phase with the higher-order sidebands. In analogy with the previous results in the adiabatic regime [2], the results of the new theory can be viewed as the generation of a coherent molecular spatial excitation, which modulates the first S/AS pair by adding S/AS sidebands. In turn, these sidebands then get modulated to generate sidebands of their own, and so on.

To summarize, the use of Kagomé fibre filled with a Raman active medium in a single, low power driving laser configuration is expected to efficiently generate a broad frequency comb composed of mutually phase-locked sidebands even though the first Stokes line is generated from the quantum noise.

8.3 Experimental Setup

Figure 8.1 shows a schematic diagram of the simplified HSRS experimental set-up using 40cm of the Kagomé fibre filled with natural hydrogen at a pressure of 20bars. The fibre is coupled to a single Nd:YAG laser operating at 1064nm, which generates pulses of duration τ_p=12ns at 50Hz repetition rate, with a linewidth ~40MHz. Care is taken so that the fundamental core-mode (HE_{11}) is predominantly excited and any coupling to cladding modes, or higher order modes is avoided. The power and polarisation of the laser is controlled by a set of wave plates and a polarising beam splitter.

The fibre output beam is collected onto the detection bench where a combination of a multi-channel UV/visible spectrometer (200-800nm), an OSA (400-1700nm) and an IR

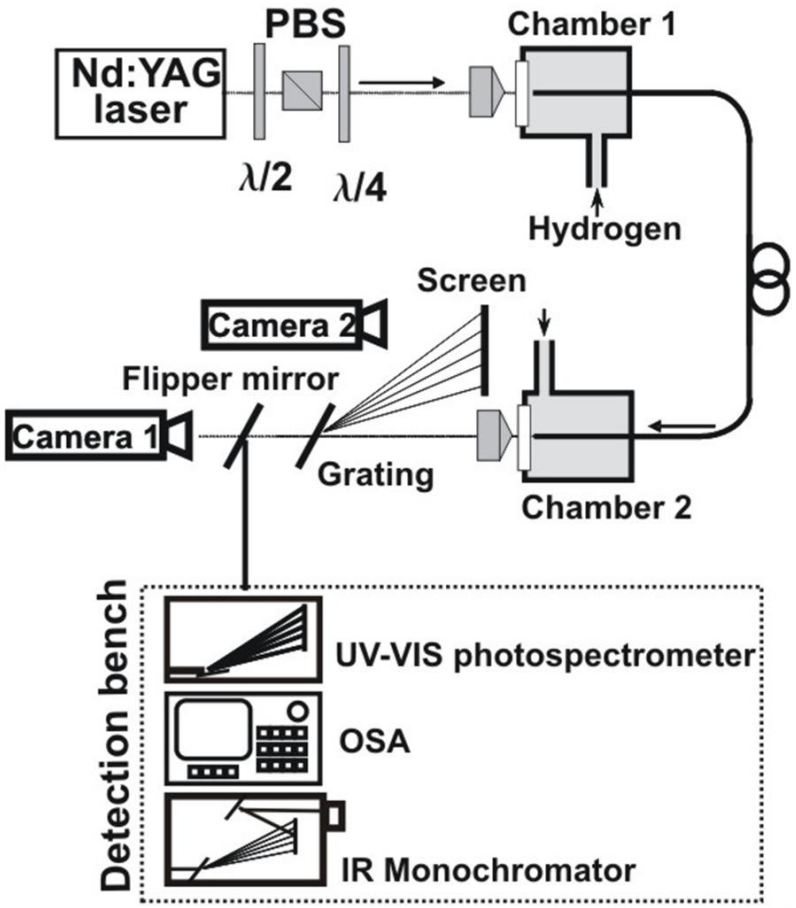

Fig. 8.1 Experimental setup for the generation of higher-order stimulated Raman scattering.

monochromator (1600-3000nm) ensure that all the lines are recorded. The overall spectrum is then deduced by combining the spectra from the three spectrometers after they have been relatively calibrated. Alternatively, a grating is placed in the path of the beam and projected onto a screen for direct visualisation.

8.4 Experimental Results

Due to the large number of anti-Stokes lines in the visible region of the spectrum, the comb generation process is clearly visible experimentally as green/yellow light escaping from the side of the fibre (Fig 8.2A). The output of the fibre also becomes bright white as the input power is increased above threshold (Fig 8.2B).

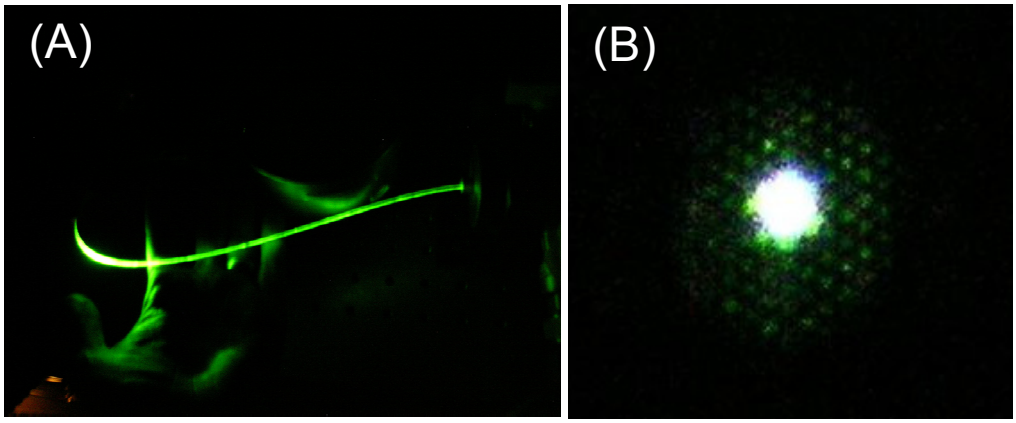

Fig. 8.2 (A) View of the fibre from the side. The laser is coupled into the fibre on the left-hand side of the picture. The fibre output is on the right. The total fibre length is 40cm. (B) Output end of the fibre, showing a bright white light guided in the core.

8.4.1 Raman Spectrum

Figure 8.3B show the typical transmitted spectrum obtained at 40kW pump peak power and for a linearly polarized input. In addition to the pump line, the spectrum contains six strong spectral lines consisting of one Stokes (S) (~1892nm) and five anti-Stokes (AS) components; the fifth anti-Stokes being in the UV (~332nm). The lines are equally spaced by ~125THz which corresponds to the frequency of the vibrational Raman-transition $Q_{01}(1)$ of ortho-hydrogen. The spatial-mode images of the observed anti-Stokes spectral lines can be directly observed by using a diffraction grating and projecting the modes onto a screen (Fig 8.3A). Due to the variable sensitivity of the camera with wavelength, the strength of the lines is not well reproduced in the picture.

When the laser polarisation is changed from linear to circular in order to favourably excite the $S_{00}(1)$ rotational transition, a spectrum of 45 spectral components (Fig 8.3D) can be observed. Once again, the anti-Stokes lines are individually visualised using a grating (Fig 8.3C). The spectrum consists of the vibrational HSRS components observed above, with additional strong rotational sidebands on either side of them, spaced by the 17.6THz of the S00(1) transition. Careful measurement of the spectral line positions indicates that all lines involve only a single vibrational shift and a single rotational shift. That is, other excitations of rotation and vibration do not occur in the molecules.

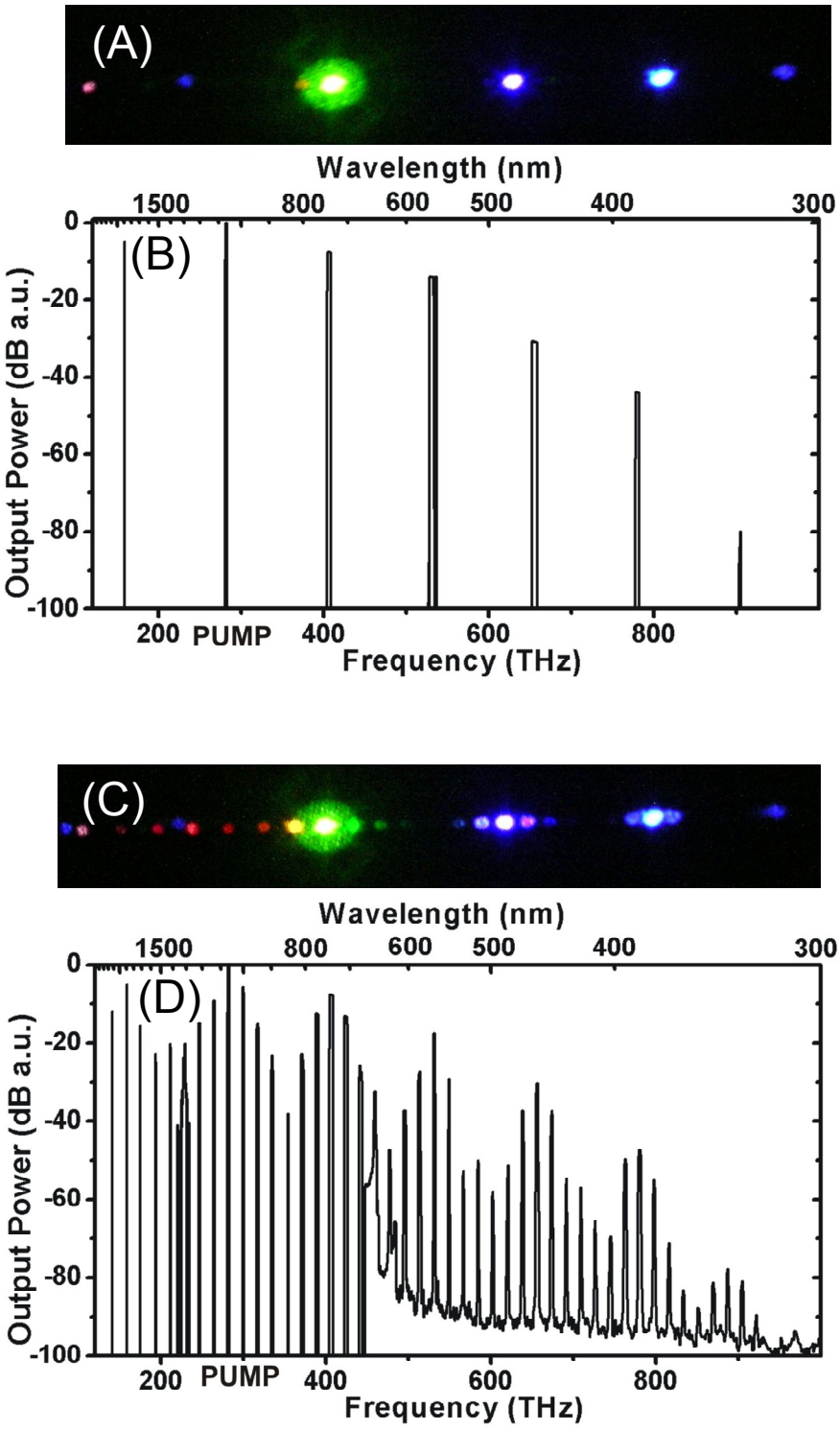

Fig. 8.3 (A) Diffracted output and (B) optical spectrum of the generated and transmitted higher-order SRS through 40cm of hydrogen filled Kagomé fibre for a linearly polarized laser input. (C-D) same as (A-B) for a circularly polarized laser input.

The final spectrum spans from ~325nm in the UV to ~2300nm, therefore covering nearly 1000THz of bandwidth with more than 53% of the input pump energy being converted to higher order Stokes and anti-Stokes spectral lines. Each line is well separated, with no spectral broadening generated between the lines [5], thanks to the relative low power threshold and the high light-in-air fraction of the Kagomé fibre's guided modes.

The present spectra contrast with the previously reported results using HSRS in both the impulsive [3] and the transient regimes [4,5,13] by possessing higher conversion efficiency into the higher order Raman lines and a wider spectral span, despite pumping at a longer wavelength [13]. The conversion from the pump to the comb components is much higher than for HHG and is comparable to the Raman sidebands technique using the adiabatic regime [2]. Additionally, the spectral bandwidth is similar even though it is obtained with a peak power almost four orders of magnitude lower. Most remarkably, the experimental conditions do not satisfy neither the requirements for adiabatic preparation, as the SRS is seeded from the quantum noise, nor impulsive preparation, which requires laser pulses shorter than the period of the Raman molecular excitation. This makes the technique one of the most potentially efficient for frequency comb generation.

8.4.2 Near field profile of generated Stokes lines

The observation of the dispersed Raman lines near-field profile gives some insight into the mechanism behind the generation of the lines. Direct near field imaging of the H_2 filled Kagomé fibre's output has been performed for the first Stokes and the first three anti-Stokes vibrational lines using a diffraction grating and a Vidicon camera (Camera 2 in Fig 8.1). As can be seen in Fig 8.4, the pump laser is coupled into the fundamental-like core-mode. The generated Stokes and anti-Stokes output field intensities all exhibit higher order transverse spatial modes despite the fibre supporting a low-loss HE_{11}-like mode at the same wavelength, indicating the parametric nature of the interactions. This can occur if more optimal phase matching of the four-wave mixing process is achieved for the higher order modes, provided they show sufficiently low loss.

The second AS field (AS2) is particularly odd as it coincidently corresponds to the mode hybridization between core and cladding also observed in the transmission spectrum of the Kagomé fibre (Fig 7.18C). This enhanced coupling between guided core mode and "leaky" cladding mode is strikingly illustrated in the colour image shown as Fig 8.4 and explains the green/yellow colour of the side-scattering light presented in Fig 8.2.

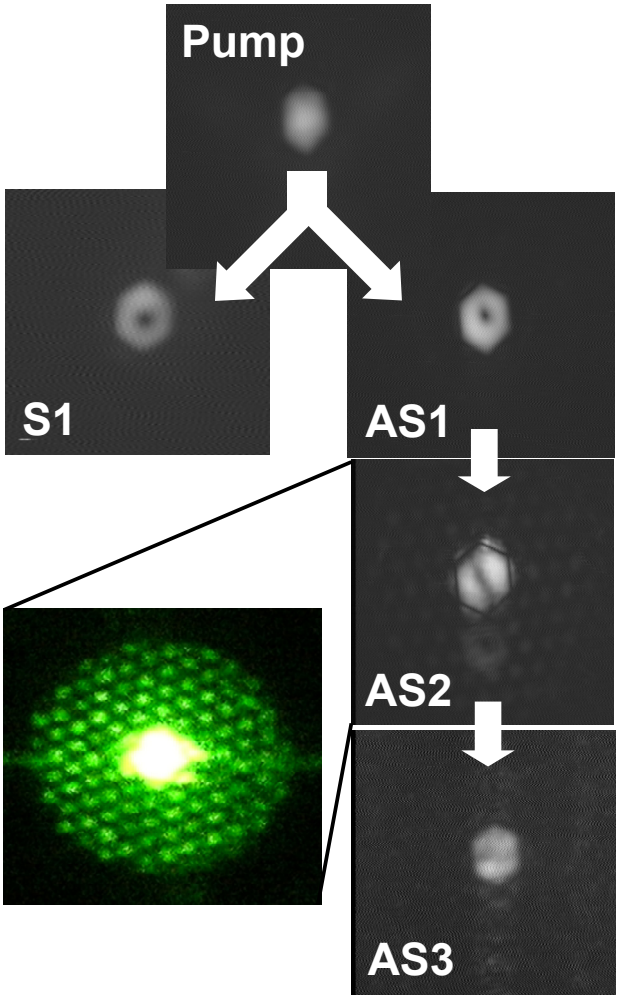

Fig. 8.4 Near field profile of the output from the H_2-filled Kagomé fibre. The Stokes (S) and anti-Stokes (AS) frequencies are separated from the pump by means of a diffraction grating. The transverse profile of AS2 is also shown in colour (left hand-side picture). This anti-Stokes line lies in the low transmission band of the Kagomé fibre. One could see that the AS2 light also couples to cladding holes via linear phase-matching between the core-mode and the cladding hole-modes.

8.4.3 Experimental indications of the parametric process

In order for the sidebands to comprise a coherent field suitable for sub-femtosecond pulse synthesis, all spectral lines should be mutually coherent, as would be expected in the case of parametric wave mixing processes. As discussed in Section 8.2, one would expect the Stokes and anti-Stokes lines to be mutually coherent, despite the fact that they are initiated by spontaneous Raman scattering.

Experimentally, several indications point toward a high degree of coherence. The parametric process was highlighted above by the high-order transverse modes of the Stokes and anti-Stokes lines at the output of the fibre. But the most striking indication of

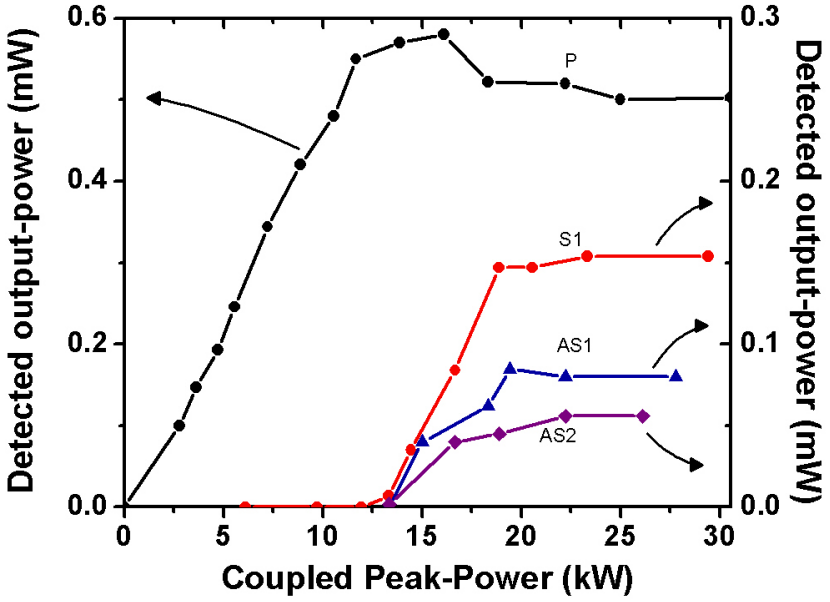

Fig. 8.5 Detected output power from the pump (black circles and line), first Stokes (red circles and line), first anti-Stokes (blue triangles and line) and second anti-Stokes components (purple diamonds and line), as a function of the coupled peak power. Each component is taken from a fraction of the output beam diffracted on a grating.

the parametric process is the observed simultaneous rise of all the spectral lines for both the vibrational and ro-vibrational spectra in accordance with [13], thus ruling out the possible incoherent cascaded SRS process. This is illustrated in Fig 8.5 where the evolution of the output power of the transmitted pump, the 1st Stokes (S1) and the 1st and 2nd anti-Stokes (AS1 and AS2) of the vibrational transition is plotted as the input power is increased. The plot shows the rise of all three generated lines occurring around a pump peak power of 13 kW.

It is noteworthy that the spectrum generated with circular polarization contains both rotation and vibration generated lines. Consequently there is a second coherent molecular excitation, which implies the introduction of one additional random phase. This, in itself does not destroy the phase-coherence of either the pure vibrational or the pure rotational spectra, but, to experimentally produce sub-fs pulses, these degrees of freedom need to be relatively controlled, or phase compensation methods need to be developed to correct for this additional random phase. Also, one could optimize the medium pressure so to suppress completely the vibrational lines [4], leaving only the mutually coherent rotational lines (Chapter 4).

8.5 Summary

A frequency comb spanning 1000THz has been generated and guided through a H_2-filled Kagomé lattice HC-PCF. Theoretical and experimental results point toward the mutual coherence of the spectral components.

The extension of using this HC-PCF to other Raman excitation regimes is straightforward. For example, its combination with the adiabatic preparation technique would enhance the conversion efficiency and further reduce the required pumping powers involved whilst ensuring a better control on the spectral components' phases. This would enable the generation and synthesis of attosecond pulses with much lower pumping powers.

References

[1] S. E. Harris and A. V. Sokolov, *Phys. Rev. Lett.* **81**, 2894 (1998).

[2] A. V. Sokolov, D. R. Walker, D. D. Yavuz G. Y. Yin, and S. E. Harris, *Phys. Rev. Lett.* **85**, 562 (2000).

[3] A. Nazarkin, G. Korn, M. Wittmann and T. Elsaesser, *Phys. Rev. Lett.* **83**, 2560 (1999).

[4] H. Kawano, Y. Hirakawa, and T. Imasaka, *J. Quant. Elect.* **34**, 260 (1998).

[5] E. Sali, K. J. Mendham, J. W. G. Tisch, T. Halfmann and J. P. Marangos, *Opt. Lett.* **29**, 495 (2004).

[6] M. G. Raymer, J. Mostowski, *Phys. Rev. A* **24**, 1980 (1981).

[7] M.G. Raymer, L. A. Westling, *J. Opt. Soc. Am. B* **2**, 1417 (1985).

[8] R. L. Carman, F. Shimizu, C. S. Wang and N. Bloembergen, *Phys. Rev. A* **2**, 60 (1970).

[9] S. Y. Kilin, *Europhys. Lett.* **5**, 419 (1988).

[10] F. Couny, F. Benabid, P. J. Roberts and M. G. Raymer, *Science* **318**, 1118 (2007)

[11] M. G. Raymer, Z. W. Li, I. A. Walmsley, *Phys. Rev. Lett.* **63**, 1586 (1989).

[12] W. Wasilewski, M. G. Raymer, *Phys. Rev. A* **73**, 063816 (2006).

[13] H. Kawano, Y. Hirakawa, and T. Imasaka, *Appl. Phys. B* **65**, 1 (1997).

Chapter 9

Summary and Future Work

9.1 Summary

This thesis reported the experimental and theoretical results obtained in designing, fabricating and using photonic micro-cells based on gas-filled HC-PCF for the generation of Raman scattering. The main scope of the study was to create photonic tools towards the realisation of a compact, self-contained optical waveform synthesiser.

Hollow core photonic crystal fibre

Two classes of HC-PCF have been reported in this thesis. The photonic band gap HC-PCF offers a low optical loss over a narrow frequency range while the large pitch HC-PCF offers a large transmission bandwidth with modest optical transmission.

In chapter 2, innovative experimental tools probed the guidance mechanism in photonic band gap HC-PCF by directly identifying the resonators responsible for the PBG formation.

In chapter 7, the experimental and theoretical investigation of the large pitch Kagomé fibres optical properties led to the identification of a new guidance mechanism, akin to Von Neumann Wigner bound states observed in quantum electronics.

These results give a better understanding of the fibre's optical properties and help in designing new photonic band gap fibres with improved attenuation for ultra-low threshold

Raman scattering in the CW regime and new Kagomé fibre with improved transmission bandwidth for ultra-broad frequency comb generation and guidance such as Raman side bands.

Photonic micro-cells

The development of gas-laser devices based on the loading of gas inside HC-PCF was reported in Chapter 3. Thanks to an innovative process for hermetically splicing the HC-PCF to a conventional solid core fibre, photonic micro-cells with low insertion loss, compactness and optimum efficiency were reported for high internal pressure and vacuum pressure.

Stimulated Raman scattering

In order to demonstrate the possibility of Raman sideband generation inside the HC-PCF and optical waveforms synthesis, various regimes of Raman amplification were reported and studied in the gas-laser devices. Two key results emerged.

Firstly, the power threshold for the observation of the Raman process was reduced by a factor of 10^6 compared to previous techniques (Chapter 5). This property led to the realisation of a continuous wave compact and efficient Raman laser in a single pass configuration reported in Chapter 6.

Secondly, these photonic micro-cells provide accurate control over the transient regime of Raman amplification (Chapter 5). As a result, unusually long laser pulses (>10ns) can be used in a "single-pump" laser system whilst retaining a high degree of molecular coherence. In this configuration, a frequency comb spanning 1000THz was generated and guided in a Kagomé-based micro-cell. Experimental observations and theoretical considerations point toward a relatively high degree of mutual coherence of the spectral components.

9.2 Future Work

Towards optical waveform synthesis

The results obtained in this thesis hold the promise that optical waveform synthesis in HC-PCF via the generation of Raman sidebands in the CW regime could be realised in the foreseeable future.

Indeed, the two-pump CW source can be realised by using a high power CW fibre laser and combining it with the Raman converter reported in Chapter 6. Lower CW power

threshold could be achieved by designing and fabricating optimised HC-PCF, with lower optical attenuation. Improvements to the splicing technique would bring better conversion efficiency to the photonic micro-cells and would increase the finesse of the all-fibre cavities reported in Chapter 5 and Chapter 6.

Much work is still required, however, to demonstrate that the Raman medium trapped inside the HC-PCF fulfils the conditions on molecular coherence and adiabaticity necessary for efficient Raman sideband generation at cryogenic temperature. The Raman scattering results obtained at liquid nitrogen temperature in Chapter 5 indicated that the fibre's mechanical properties and optical guidance will not be the limiting factors. The ultra-broad spectrum obtained in Chapter 8 is also a sign that the coherence achieved inside these fibres can remain high for long periods.

As a matter of fact, the novel route for frequency comb synthesis reported in Chapter 8 still needs to be ascertained as an alternative to Raman sideband generation. For example, the exact degree of coherence of the spectral components needs to be assessed and the influence of the fibre's chromatic dispersion taken into consideration. The single transition excitation will also need to be confirmed.

Lastly, the new photonic guidance identified in large-pitch HC-PCF will enable the development of the next generation of hollow core fibre, with low loss over ultra-broad wavelength range that could revive gas-phased linear and non-linear optical applications.

These future developments would then emulate the start of the second phase of development of the optical waveform synthesiser, which consists of using the photonic tools presented above to generate, detect and synthesise waveforms.

List of Publications

Publications by the author related to the thesis:

1. F. Benabid, G. Bouwmans, J.C. Knight, P. St Russell, **F. Couny**, "Ultrahigh efficiency laser wavelength conversion in a gas-filled hollow core photonic crystal fibre by pure stimulated rotational Raman scattering in molecular hydrogen," Physical Review Letters **93**, 123903 (2004), Selected for publication in Virtual Journal of Ultra-fast Science 3, 10 (2004)
2. F. Benabid, **F. Couny**, J.C. Knight, T.A. Birks & P.S. Russell, "Ultra-compact, stable and efficient all-fibre gas cells using hollow-core photonic crystal fibre," Nature **434**, 488 (2005)
3. P. Roberts, **F. Couny**, H. Sabert, B. Mangan, D. Williams, L. Farr, M. Mason, A. Tomlinson, T. Birks, J. Knight, and P. St. J. Russell, "Ultimate low loss of hollow-core photonic crystal fibres," Optics Express **13**, 236 (2005)
4. **F. Couny**, H. Sabert, P. Roberts, D. P. Williams, A. Tomlinson, B. Mangan, L. Farr, J. Knight, T. Birks, and P. S. Russell, "Visualizing the photonic band gap in hollow core photonic crystal fibres," Optics Express **13**, 558 (2005)
5. P. Roberts, D. Williams, B. Mangan, H. Sabert, **F. Couny**, W. Wadsworth, T. Birks, J. Knight, and P. Russell, "Realizing low loss air core photonic crystal fibres by exploiting an antiresonant core surround," Optics Express **13**, 8277 (2005). Selected for publication in Virtual Journal of Biomedical Optics **1**, 12 (2006).
6. **F. Couny**, F. Benabid, P. S. Light, "Large-pitch Kagomé-structured hollow-core photonic crystal fibre," Optics Letters **31**, 3574 (2006), Selected for publication in Virtual Journal of Nanoscale Science & Technology **14**, 24 (2006) and in Virtual Journal of Ultra-fast Science **5**, 12 (2006)
7. **F. Couny**, F. Benabid, O. Carraz, "Enhanced SRS in H_2 filled hollow core photonic crystal fibre by use of fibre Bragg grating," Journal of Optics A - Pure and Applied Optics **9**, 156 (2007)
8. **F. Couny**, F. Benabid, P.J. Roberts, M.T. Burnett, S.A. Maier,"Identification of Bloch-modes in hollow-core photonic crystal fibre cladding," Optics Express **15**, 325 (2007)
9. **F. Couny**, F. Benabid, P. S. Light, "Reduction of Fresnel Back-Reflection at Splice Interface between Hollow Core PCF and Single Mode Fibre", Photonic Technology Letters **19** 1020-1022 (2007)
10. **F. Couny,** F. Benabid and P. S. Light, "Subwatt Threshold CW Raman Fibre-Gas Laser Based on H_2-Filled Hollow-Core Photonic Crystal Fibre" Phys. Rev. Lett. **99** 143903 (2007)
11. **F. Couny**, F. Benabid, P.J. Roberts, P.S. Light & M.G. Raymer, "Generation and Photonic Guidance of Multi-Octave Optical-Frequency Combs", Science **318** 1118-1121 (2007)

Publications by the author on other subjects:

1. G. Kakarantzas, A. Ortigosa-Blanch, T. A. Birks, P. S. J. Russell, L. Farr, **F. Couny**, and B. J. Mangan, "Structural rocking filters in highly birefringent photonic crystal fibre," Optics Letters **28**, 158 (2003)
2. D. Galea, **F. Couny**, S. Coupland, P. J. Roberts, H. Sabert, J. C. Knight, T. A. Birks, and P. S. J. Russell, "Selective mode excitation in hollow-core photonic crystal fibre," Optics Letters **30**, 717 (2005)
3. F. Benabid, P. Light, **F. Couny**, and P. Russell, "Electromagnetically-induced transparency grid in acetylene-filled hollow-core photonic crystal fibre," Optics Express **13**, 5694 (2005)
4. P. Roberts, **F. Couny**, H. Sabert, B. Mangan, T. Birks, J. Knight, and P. Russell, "Loss in solid-core photonic crystal fibres due to interface roughness scattering," Optics Express **13**, 7779 (2005)
5. J. D. Shephard, **F. Couny**, P. St. J. Russell, J. D. C. Jones, J. C. Knight, and D. P. Hand, "Improved hollow core photonic crystal fibre design for delivery of nanosecond pulses in laser micromachining applications" Applied Optics **44**, 4582 (2005)
6. P. Roberts., B. J. Mangan, H. Sabert, **F. Couny**, T. A. Birks, J. C. Knight, P. St. J. Russell, "Control of dispersion in photonic crystal fibres," Journal of Optical Fibre Communication Reports **2**, 435 (2005)
7. **F. Couny**, P. S. Light, F. Benabid and P. St. J. Russell, "Electromagnetically induced transparency and saturable absorption in all fibre devices based on $^{12}C_2H_2$ filled hollow core photonic crystal fibre," Optics Communications **263**, 28 (2006). Selected for publication in Virtual Journal of Biomedical Optics **1**, 10 (2006)
8. P. S. Light, **F. Couny**, F. Benabid, "Low optical insertion-loss and vacuum-pressure all-fibre acetylene cell based on hollow-core photonic crystal fibre," Optics Letters **31**, 2538 (2006)
9. G. S. Wiederhecker, C. M. B. Cordeiro, **F. Couny**, F. Benabid, S. A. Maier, J. C. Knight, C. H. B. Cruz, H. L. Fragnito, "Field enhancement within an optical fibre with a subwavelength air core" Nature Photonics **2**, 115 (2007)
10. P. S. Light, F. Benabid, **F. Couny**, M. Maric, and A. N. Luiten, "Electromagnetically induced transparency in Rb-filled coated hollow-core photonic crystal fibre," Opt. Lett. **32**, 1323-1325 (2007)

Publications by the author at international conferences:

B. J. Mangan, L. Farr, A. Langford, P. J. Roberts, D. P. Williams, **F. Couny**, M. Lawman, M. Mason, S. Coupland, R. Flea, H. Sabert, T. A. Birks, J. C. Knight, P. St. J. Russell, "Low loss (1.7

dB/km) hollow core photonic band gap fibre" 2004 Optical Fibre Communication Conference (OFC2004), PDP24 (**Post-deadline paper**)

B. J. Mangan, **F. Couny**, L. Barr, A. Langford, P. J. Roberts, D. P. Williams, M. Banham, M. W. Mason, D. F. Murphy, E. A.M. Brown, A. Sabert T. A. Birks, J. C. Knight, P. St. J. Russell, "Slope-matched dispersion-compensating photonic crystal Fibre", 2004 Conference on Lasers and Electro-Optics (CLEO2004), CPDDJ (**Post-deadline paper**)

F. Benabid, G. Bouwmans, **F. Couny**, J. C. Knight, P. St. J. Russell, "Rotational SRS in hydrogen gas filled hollow-core photonic crystal fibre with 3 nJ threshold and 92 % conversion efficiency," 2004 Conference on Lasers and Electro-Optics (CLEO2004), CThEE5

F. Benabid, **F. Couny**, J. C. Knight, T. A. Birks, P. St. J. Russell, "All-fibre single-mode hollow-core gas cells for stimulated Raman scattering and laser frequency stabilization," 2005 Conference on Lasers and Electro-Optics (CLEO2005), CMV4

P. J. Roberts, **F. Couny**, T. A. Birks, J. C. Knight and P. St. J. Russell B. J. Mangan, H. Sabert, D. P. Williams, L. Farr, "Achieving low loss and low nonlinearity in hollow core photonic crystal fibres," 2005 Conference on Lasers and Electro-Optics (CLEO2005), CWA7

T. A. Birks, P. J. Roberts, **F. Couny**, H. Sabert, B. J. Mangan, D. P. Williams, L. Farr, M. W. Mason, A. Tomlinson, J. C. Knight, P. St.J. Russell, "The fundamental limits to the attenuation of hollow-core photonic crystal fibres," Proceedings of 2005 7th International Conference on Transparent Optical Networks (ICTON2005), 1505762

P.S. Light, **F. Couny**, F. Benabid, P. St. J. Russell, "Electromagnetically-induced transparency and saturable absorption in all-fibre devices based on acetylene-filled hollow-core photonic crystal fibre," 2005 European Conference on Optical Communication (ECOC2005), Th 4.5.6 (**Post-deadline Paper**)

C. Xiong, S. G. Leon-Saval, **F. Couny**, W. J. Wadsworth, "Residual pump peak removal for ultra-flattened supercontinuum generation by photonic crystal fibres," 2006 Conference on Lasers and Electro-Optics (CLEO2006), CWO4

F. Couny, P. S. Light, F. Benabid, "Electromagnetically-induced transparency and saturable absorption in all-fibre devices based on acetylene-filled hollow-core photonic crystal fibre," 2006 Conference on Lasers and Electro-Optics (CLEO2006), CTuK7

F. Couny, F. Benabid, O. Carraz, "Enhanced stimulated Raman scattering in hollow core photonic crystal fibre by use of fibre Bragg grating," 2006 Conference on Lasers and Electro-Optics (CLEO2006), CFK3

P. S. Light, **F. Couny**, F. Benabid, "Electromagnetically-induced transparency decoherence sources in acetylene-filled hollow-core photonic crystal fibre," 2006 Conference on Lasers and Electro-Optics (CLEO2006), CMO6

F. Couny, F. Benabid and P.S. Light, "Large pitch Kagomé-structured hollow-core photonic crystal fibre," 2006 European Conference on Optical Communication (ECOC2006), Th 4.2.4 **(Post-deadline Paper)**

F. Couny, F. Benabid and P.S. Light, "Large pitch Kagomé-structured hollow-core photonic crystal fibre," 2007 Conference on Lasers and Electro-Optics (CLEO2007) CWF1

F. Couny, F. Benabid, P. J. Roberts, P. S. Light, "Fresnel zone imaging of Bloch-modes from a hollow-core photonic crystal fibre cladding," 2007 Conference on Lasers and Electro-Optics (CLEO2007) CWF5

F. Couny, F Benabid, P. J. Roberts, M. T. Burnett, S. A. Maier, "Identification of the band-edge cladding modes of a hollow-core photonic crystal fibre," 2007 Conference on Lasers and Electro-Optics (CLEO2007) CFE4

F. Couny, F. Benabid and P.S. Light, "Control of the transient regime of stimulated Raman scattering in hollow-core photonic crystal fibre," 2007 Conference on Lasers and Electro-Optics (CLEO2007) CWO1

P. S. Light, F. Benabid, **F. Couny**, G. J. Pearce and D. M. Bird, "EIT with counter propagating probe-coupling beams in acetylene filled HC-PCF," 2007 Conference on Lasers and Electro-Optics (CLEO2007) QMC7

P.S. Light, F. Benabid and **F. Couny**, "Low insertion-loss (1.8 dB) and vacuum-pressure all-fibre acetylene cell based on hollow-core PCF," 2007 Conference on Lasers and Electro-Optics (CLEO2007) CThKK4

P. S. Light, F. Benabid, **F. Couny**, G. J. Pearce and D. M. Bird, "Experimental study comparing EIT in V and Λ schemes in acetylene-filled HC-PCF," 2007 Conference on Lasers and Electro-Optics (CLEO2007) CMI2

G. S. Wiederhecker, C. M. b. Cordeiro, **F. Couny**, F. Benabid, S. A. Maier, J. C. Knight, C. H. b. Cruz, H. L. Fragnito , "Sub-Wavelength Intensity Profiles and Field Enhancement within an Optical Fibre," 2007 Conference on Lasers and Electro-Optics (CLEO2007) CWF6

F. Couny, F. Benabid and P. S. Light, "Sub-Watt Threshold CW Raman Fibre-Gas-Laser Based on H2-Filled Hollow-Core Photonic Crystal Fibre", 2007 European Conference on Optical Communication (ECOC2007), **(Post-deadline Paper)**